STUDIES OF MAGNETOTACTIC BACTERIA BY SOFT X-RAY

MICROSCOPY

STUDIES OF MAGNETOTACTIC BACTERIA BY SOFT X-RAY

MICROSCOPY

By

Xiaohui Zhu, M.Sc.

A Thesis

Submitted to the School of Graduate Studies

in Partial Fulfillment of the Requirements

for the Degree of

Doctor of Philosophy

McMaster University

DOCTOR OF PHILOSOPHY (2016)   McMaster University
(Chemistry)   Hamilton, Ontario

TITLE: Studies of Magnetotactic Bacteria by Soft X-ray Microscopy

AUTHOR: Xiaohui Zhu, M.Sc. (University of Science and Technology Beijing)

SUPERVISOR: Professor Adam P. Hitchcock

NUMBER OF PAGES: xx, 189

ABSTRACT

Magnetotactic bacteria (MTB) are ubiquitous in aquatic environments. They biomineralize membrane-bound magnetic nanoparticles (magnetosomes), which are magnetically single-domain, single crystals of either magnetite, Fe_3O_4, or greigite, Fe_3S_4. Magnetosomes are arranged in chains inside the cell. The chain is a strong magnetic dipole, which aligns the cell with the earth's magnetic field (magnetotaxis) and, together with chemical signatures (aerotaxis), is believed to increase the efficiency of the organism in finding an optimum oxygen concentration in the sediments which is at the interface of oxic and anoxic zones. As the simplest organism, in which biomineralization occurs, magnetotactic bacteria serve as an ideal model to study mechanisms of biomineralization. In addition, a good understanding of biomineralization by MTB is crucial to designing methods for *in vitro* formation of nanomagnetite.

In this thesis, soft X-ray STXM (scanning transmission X-ray microscopy) and ptychography were used to characterize the chemistry and magnetism of magnetotactic bacteria (MTB) on an individual cell and an individual magnetosome basis. The Fe $L_{2,3}$-edge X-ray absorption spectra (XAS) and X-ray magnetic circular dichroism (XMCD) of biogenic Fe_3O_4 magnetosomes and abiogenic Fe_3O_4 nanoparticles were measured and were used to clarify confusion in the literature as to the correct shape of the Fe L-edge XAS spectra of magnetite (Fe_3O_4). Reliable S L-edge XAS and Fe L-edge XAS and XMCD spectra of Fe_3S_4 nanoparticles synthesized via hydrothermal method were obtained, which were utilized to investigate the sulfur chemistry and magnetic properties of multicellular magnetotoactic prokaryotes (MMPs). In addition, as an extension of Kalirai et al.'s study in which anomalous reversed sub-chain magnetic orientation in a single *Candidatus Magnetovibrio blakemorei* strain MV-1 cell was

observed (Kalirai et al. 2013), a connection was made to proposed mechanisms of establishment of the single moment chain and how that moment is linked to the motile system in single-flagellum MV-1 species.

Since STXM has limited spatial resolution, an emerging coherent diffraction imaging technique, ptychography, which is not limited by the quality of the X-ray optics and has the potential to reach near atomic-scale spatial resolution with very short wavelength X-rays, was used to study biomineralization and magnetism of MTB cells. A spatial resolution of 7 nm below 1000 eV was achieved with ptychography, which is the highest in the soft X-ray region so far. Precursor-like and immature magnetosomes in intact MV-1 cells were observed with ptychography. A model for the pathway of magnetosome biomineralization for MV-1 was proposed. It was shown that XMCD spectra could be derived with both ptychography modulus and phase modes. Our results demonstrate that ptychography offers a superior means relative to STXM to characterize the chemical and magnetic properties of magnetotactic bacteria at the individual magnetosome level.

ACKNOWLEDGEMENTS

Furthermore, I am grateful to all of my past and current group members for sharing their ideas and suggestions and providing me with such a comfortable working environment. Thank you Dr. Vincent Lee, Dr. Glyn Cooper, Juan Wu, Lis Melo, Vinod Prabu, Zhsheng Qin, Sam Kalirai, and Karen Lam.

Thanks to all the people and friends for their kind assistance at McMaster University: Marcia West for TEM training and assistance, Fang Yuan for sample synthesis, and Victoria Jarvis for XRD analysis. Special thanks to Yujie Zhu who helped me set up the experiment and prepare samples at the beginning of my Ph.D. studies.

Finally, I would like to thank my families for their eternal support and unconditional love. My parents and my sister never hesitated to encourage and support me to achieve my goals even they had to make a lot of sacrifices. It is their constant support that makes me get through the hard time in my life. This thesis is dedicated to all of them.

Xiaohui Zhu
October 05, 2016

TABLE OF CONTENTS

LIST OF FIGURES

Chapter 1

Chapter 2

Chapter 3

Chapter 4

Chapter 5

Chapter 6

Chapter 7

Chapter 8

Appendix A

LIST OF TABLES

LIST OF ABBREVIATIONS AND SYMBOLS

Å	Angstrom
A_o	Distance between sample and order-sorting aperture
ALS	Advanced Light Source
CLS	Canadian Light Source
CXRO	Center for X-Ray Optics
δ_{rN}	Width of the Most Outer Zone (Nth) of a Zone Plate
Δr	Diffraction Limited Spatial Resolution
D	Zone Plate Diameter
E	Energy
emu	Electromagnetic Unit
erg	unit of energy or work (centimeter-gram-second system)
f	Focal Length
FOV	Field of View
G	Gauss
H	Magnetic Field Strength
I_t	Transmitted Photon Intensity
I_0	Incident Photon Intensity
K	Kelvin (unit of temperature)
k_B	Boltzmann constant, 1.38×10^{-16} erg/K
λ	Wavelength of light
LCP	Left Circular Polarization (Polarized Light)
LUMO	Lowest Unoccupied Molecular Orbital
M	Magnetic Moment
MC-1	*Magnetococcus sp.* (bacterial strain)
MFM	Magnetic Force Microscopy
$\mu(E)$	Energy Dependent Mass Absorption Coefficient
MMP	Multi-cellular Magnetotactic Prokaryote
MSR-1	*Magnetospirillum gryphiswaldense* (bacterial strain)
MTB	Magnetotactic Bacteria
MV-1	Marine Vibrio (bacterial strain)

NEXAFS	Near Edge X-Ray Absorption Fine Structure
NS	North-Seeking (bacterial motility)
OATZ	Oxic-Anoxic Transition Zone
OD	Optical Density
OSA	Order Sorting Aperture
PBS	Phosphate-Buffered Saline Solution
PGM	Plane-grating Monochromator
RCP	Right Circular Polarization (Polarized Light)
ROI	Region of Interest (in STXM images)
ρ	Sample Density
σ	Energy-dependent Mass Absorption Coefficient
s	Second
SGM	Spherical-grating Monochromator
SQUID	Superconducting quantum interference device
SS	South-Seeking (bacterial motility)
STXM	Scanning Transmission X-Ray Microscopy
SVD	Singular Value Decomposition
t	Sample Thickness
T	Temperature
TEM	Transmission Electron Microscopy
TEY	Total Electron Yield
UFRJ	Federal University of Rio de Janeiro
UNLV	University of Nevada, Las Vegas
XAS	X-ray Absorption Spectroscopy
XANES	X-ray Absorption Near Edge Structure
XMCD	X-Ray Magnetic Circular Dichroism
ZP	Fresnel Zone Plate

Chapter 1

Introduction

This chapter outlines the projects I have performed within this thesis. It then gives an overview of magnetotactic bacteria and their magnetic organelles, magnetosomes. This is followed by an introduction to X-ray Magnetic Circular Dichroism (XMCD), and its application to investigate magnetic properties of two types of minerals, magnetite (Fe_3O_4) and greigite (Fe_3S_4), in magnetosomes. Finally, this chapter concludes with the goals and outline of the thesis.

1.1 Overview of the thesis

Microorganisms have long been thought to play crucial roles in ecosystems as they are actively involved in the global cycles of principal elements necessary to life, such as, C, O, N, P, S, and Fe, etc. (Ehrlich, 1998; Nazaries et al., 2013). These living organisms selectively take up certain elements from the local environment, transform their chemical state and synthesize minerals inside or outside the cells under strict biochemical and genetic control, a process known as biomineralization. To date, over 60 different minerals of biological origin have been identified (Gargaud et al., 2011). One of the most fascinating examples of biomineralization is the formation of single-domain magnetic nanocrystals, termed magnetosomes, within magnetotactic bacteria (MTB) (Bazylinski and Frankel, 2004). The magnetosomes, made of magnetite (and less commonly, greigite), are surrounded by lipid membranes and organized in chains inside magnetotactic bacteria. The chain of magnetically aligned magnetosomes imparts a sufficiently large magnetic moment to the cells so that they are spatially oriented by the magnetic interaction

with the Earth's geomagnetic field (Bazylinski and Frankel, 2004). This alignment, coupled with

chemical aerotaxis, is believed to help magnetotactic bacteria locate and maintain position at the

oxic-anoxic transition zone, their preferred habitation (Bazylinski and Lefèvre, 2013).

Ferrimagnetic particles have also been found in other organisms such as algae (Torres de Araujo

et al., 1986), fish (Mann et al., 1988), insects (Maher, 1998), birds (Wiltschko and Wiltschko,

2005), and even humans (Kirschvink et al., 1992). As one of the simplest biomineralizing micro-

organisms, magnetotactic bacteria serve as a useful model for understanding the evolution and

mechanism of biomineralization (Komeili, 2012; Staniland et al., 2007). In addition, they

provide an easily accessible system to study the significance of biomagnetism for detection and

use of the local Earth's magnetic field in other living organisms.

Imaging and quantifying magnetic properties of magnetotactic bacteria has been achieved

with several techniques including superconducting quantum interference device (SQUID)

magnetometry (Qian, 2013), magnetic force microscopy (MFM) (Amemiya et al., 2005) , and

electron holography in transmission electron microscopes (TEM) (Dunin-borkowski et al.,

1998). However, SQUID microscopy only provides the integral properties of ensembles of

magnetic particles so that the magnetic characterization of individual particles is still inaccessible

(Sievers et al., 2012). MFM has a spatial resolution of better than 10 nm but the direct extraction

of quantitative information from MFM images is challenging (Freeman and Choi, 2001).

Although electron holography in transmission electron microscopes provides quantitative

information about magnetic structure of individual magnetosomes with high spatial resolution

(Dunin-Borkowski et al., 2001), radiation damage and the strict requirement for sample thickness

(less than 50 nm) limit its application. In addition, the presence of the magnetic field in electron

holography might also influence the internal magnetic structure of magnetotactic bacteria, and

there is no element or site specificity. In this context, synchrotron-based soft X-ray spectromicroscopy, which detects the intrinsic magnetism of a sample through the X-ray magnetic circular dichroism effect (Stöhr and Siegmann, 2006), is an ideal tool to probe valence state, site occupancy and element-specific magnetic moments in biologically generated magnetic structures with nanoscale spatial resolution (Hitchcock, 2012; Stöhr and Siegmann, 2006).

X-ray magnetic circular dichroism (XMCD) is the difference of X-ray absorption spectra (XAS) recorded with circularly polarized X-rays parallel and antiparallel to the magnetization direction. For the past few years, our group have been developing XMCD measured in a soft X-ray scanning transmission X-ray microscope (STXM) as a tool to study the chemistry and biomagnetism of MTB with a spatial resolution of 30 nm. The first, proof-of-principle measurement was reported in 2010 (Lam et al., 2010). An improved XMCD acquisition method was reported in 2012 (Kalirai et al., 2012). Motivated by these prior studies, this thesis aims at understanding MTB and its magnetosomes from a spectroscopic and biochemical point of view. The four specific projects performed in this thesis are described below:

Project 1: Spectroscopic study on biogenic and abiogenic Fe_3O_4:

Despite extensive studies, the published XAS and XMCD spectra of Fe_3O_4 are not consistent and often contradict each other. Specifically, some of the published Fe L_3 XAS spectra of Fe_3O_4 exhibit a low energy shoulder at ~708 eV (about 1.5 eV below the main $2p_{3/2} \rightarrow 3d$ peak), while others do not (Zhu et al., 2015a). The goal of this project was to clarify the confusion existing in the literature as to the correct Fe $L_{2,3}$ X-ray absorption spectra of Fe_3O_4. These results have been published (Zhu et al., 2015a) and are presented in Chapter 4.

Project 2: Chemical and magnetic study of greigite and Fe_3S_4 magnetosomes in multicellular magnetotactic prokaryotes (MMP)

There are only two prior studies of the application of XMCD to characterize the magnetic structure of Fe_3S_4 (Chang et al., 2012a; Letard et al., 2005), one of the two major magnetosome minerals in MTB cells. However, the Fe_3S_4 particles were identified as oxidized in both of these studies. One of the goals in this project is to gain a better understanding of the electronic and magnetic properties of Fe_3S_4 by means of the XAS and XMCD techniques. Multicellular magnetotactic prokaryotes (MMP) are one of the most interesting MTB due to their unique multicellular morphology (Balkwill et al., 1980) and capability to biomineralize Fe_3S_4 magnetosomes. The reliable reference spectra obtained from Fe_3S_4 nanoparticles can help to better understand sulfur metabolism, biomagnetism, and magnetosome biomineralization in bacteria (Keim et al., 2006). This material is the basis for Chapter 5.

Project 3: Cell division mechanism study of MV-1

In a recent study, Kalirai et al. (2013) showed that *Magnetovibrio blakemorei* strain MV-1 can have anomalous magnetosome chains in a single cell in which there are gaps separating sub-chains of opposite magnetic orientation. These results contradict previous understanding that all the magnetosomes in a single chain would have the same magnetic alignment. More important, magnetic reversal within the magnetosome chain of a single cell may also raise questions regarding the cell division process in MV-1. For example, depending on the position of the new flagellum and magnetic polarity in parent MV-1 cells, the daughter cells after division may adopt the same or opposite magnetite polarities as their parent. Following up on this earlier study, I performed a statistical measurement on the magnetic polarity of MV-1 cells in 3

different cultures to probe the relation between establishment of magnetic moment and the

flagellum motile system during the cell replication process. This is discussed in Chapter 6.

Project 4: Spectro-ptychograhy studies on extracellular and intracellular magnetosomes

With respect to the mechanism(s) of magnetosome biomineralization in MTB cells, the

existence of intra-cellular mineral precursors has been debated. It is notable that an immature

magnetosome phase was observed previously using conventional STXM (Kalirai et al., 2013;

Lam et al., 2010). However, characterization by conventional STXM is very challenging,

particularly when the region of interest is smaller than 10 nm. Ptychography is an emerging

coherent diffractive imaging (CDI) technique (Thibault et al., 2014). Unlike conventional lens-

based microscopic imaging techniques such as STXM, ptychography is not limited by the quality

of the X-ray optics used, and has the potential to reach near atomic-scale spatial resolution with

very short wavelength X-rays (Edo et al., 2013). In this project, I applied the emerging soft X-ray

spectro-ptychography technique, which combines high spatial resolution and chemical

sensitivity, to study extracellular magnetosomes and intact MV-1 cells. I measured Fe $L_{2,3}$ XAS

and XMCD spectra in ptychography mode from extracted magnetosomes and intact MV-1 cells.

This work achieved the most detailed spectral information to date from soft X-ray ptychography,

and also it is the highest spatial resolution for X-ray microscopy of any type at a photon energy

below 1 keV. The results of these studies are presented in Chapter 6.

1.2 Magnetotactic Bacteria (MTB)

1.2.1 Discovery

Magnetotactic bacteria (MTB) were first documented in 1963 by Salvatore Bellini, a

medical doctor at University of Pavia in Italy (Bellini 2009a, Frankel, 2009). Bellini observed

that some bacteria constantly swam towards and accumulated at the north edge of the water drop on microscope slides, which he thought was a response to the geomagnetic field. He called these bacteria "magnetosensitive bacteria" (Bellini, 2009a). He also observed: a) the swimming direction of the bacteria could be determined by an external magnetic field larger than the geomagnetic field; b) dead bacteria still oriented in the magnetic field but did not move; c) bacteria could lose magnetosensitivity when cultured in demineralized water but exhibited magnetosensitivity again with the addition of soluble iron. Based on these observations, Bellini proposed that some iron compound was present in these cells and functioned as a "biomagnetic dipole" which caused the cells to swim downward in the northern hemisphere (Bellini, 2009a; Frankel, 2009). In a further study of these magnetosensitive bacteria, Bellini (Bellini, 2009b) showed that both magnetosensitivity and oxygen levels in the environment affected the swimming behavior and growth of these organisms.

However, Bellini's reports of magnetosensitive bacteria (Bellini, 2009a, 2009b) were not easily accessed, so the discovery was "effectively lost" (Frankel, 2009) until Richard P. Blakemore independently discovered these organisms from a salt marsh in Woods Hole (Massachusetts, US) (Blakemore, 1975). Much like Bellini, Blakemore microscopically observed a group of bacteria that rapidly swam in the same direction, which he described as a tactic reaction to local geomagnetic field. He termed this behavior "magnetotaxis" (Blakemore, 1975). Using transmission electron microscopy (TEM), which was inaccessible to Bellini at the time, Blakemore visualized bundles of flagella attached to the cell surface and chains of iron-rich particles enclosed within membrane vesicles (see **Figure 1.1**). He also claimed that these intracellular iron-rich organelles might function as magnetic dipoles which imparted a magnetic moment on the cell such that the cell could be aligned them in an external magnetic field
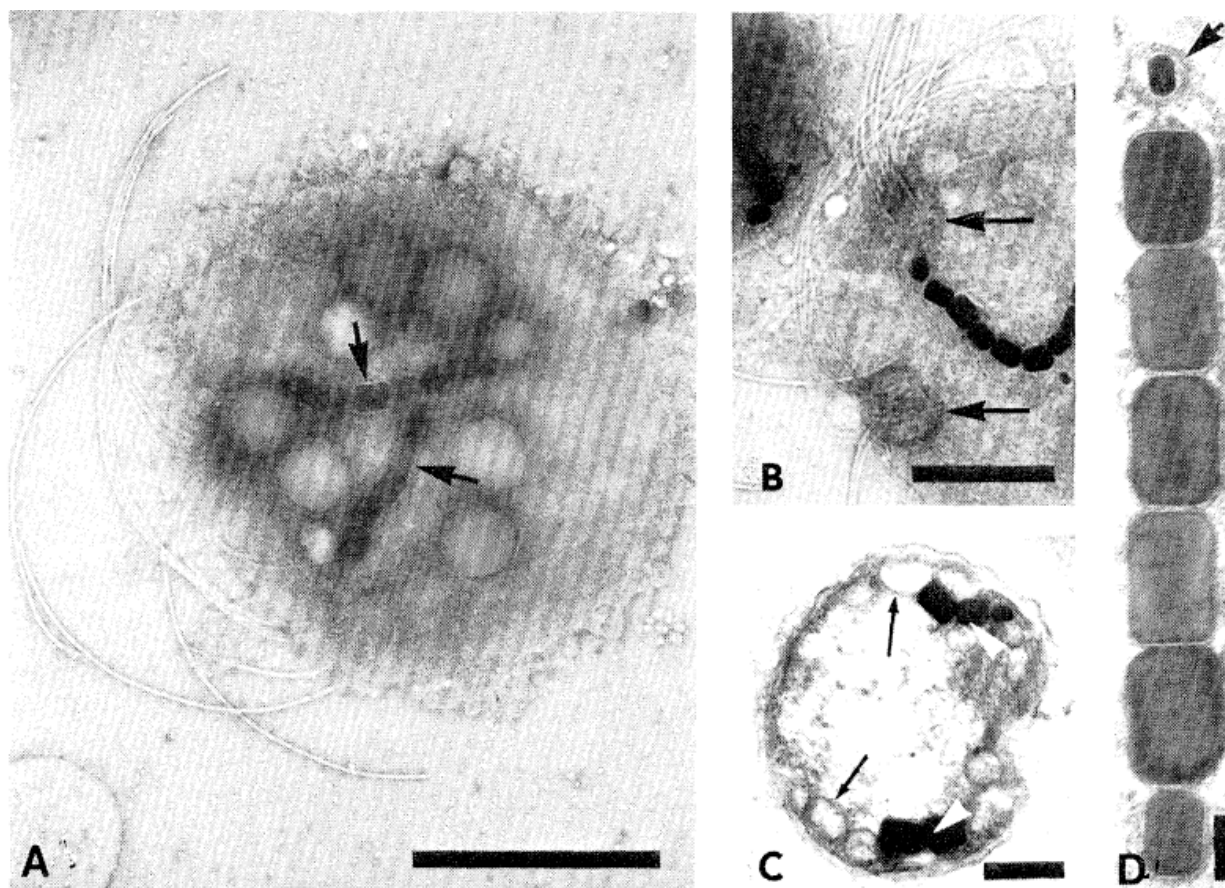
Figure 1.1 TEM images of a magnetotactic bacterium observed by Blakemore in 1975.(A) Two bundles of flagella insert at one side of the cell. Two chains of iron-rich particles are present (arrows). The scale bar represents 0.5 μm; (B). A portion of a magnetotactic bacterium showing the two disks (arrows) into which flagella insert. The scale bar represents 0.25 μm; (C). A chemically fixed and thin-sectioned magnetotactic bacterium stained with lead and uranyl salts. The iron-rich particles (white arrowheads) have been unintentionally displaced during thin-sectioning revealing intracytoplasmic membranes arranged as vesicles (black arrows) adjacent to the cell plasma membrane. The scale bar represents 0.25 μm; (D). A single chain of particles containing iron present in a cell prepared as described for (C). The scale bar represents 0.07 μm; (Blakemore, 1975); Figure reproduced with permission from the *American Association for the Advancement of Science (AAAS).*

(Blakemore,1975). By means of [57]Fe Mössbauer resonance spectroscopy, Frankel et al. (Frankel et al., 1979) first identified these iron-rich inclusions in the strain MS-1 to be magnetite (Fe_3O_4).

7

The particles were later termed "magnetosomes" (Balkwill et al., 1980). Later on, another type of

magnetosome, greigite (Fe_3S_4), was observed in a motile multicellular aggregate of bacteria in

the Southern Hemisphere (Farina et al., 1990). Up to the present, magnetite (Fe_3O_4) and greigite

(Fe_3S_4) are the major mineral phases of magnetosomes that have been identified in magnetotactic

bacteria (Bazylinski et al., 1994). In addition, several non-magnetic iron-sulfide minerals such as

mackinawite (tetragonal FeS) and cubic FeS were also found in iron-sulfide

magnetosomes(Lefèvre et al., 2011a; Pósfai et al., 1998)

There is no doubt that Bellini was the first to discover and document magnetotactic

bacteria. However, it was Blakemore who introduced these unique microorganisms to the

scientific community worldwide (Komeili, 2012). Thus, both Bellini and Blakemore should be

acknowledged as their discoverers. Subsequent work on MTB has proved to continuously impact

a large number of scientific fields such as geology, mineralogy, biochemistry, physics,

oceanography and astrobiology (Bazylinski and Schübbe, 2007).

1.2.2 General features of MTB

Magnetotactic Bacteria (MTB) are morphologically diverse and distributed worldwide.

Generally, MTB can be found in aquatic habitats such as, freshwater, sediments, marine,

brackish, marshes, etc. (Bazylinski and Frankel, 2004). Very rarely, they had also been observed

in soil (Fassbinder et al., 1990). Although MTB are known for biomineralizing Fe-bearing

magnetosomes (Fe_3O_4 and Fe_3S_4), the distribution of MTB is independent of the concentration of

Fe in the environment but rather dependent on the existence of an oxic-anoxic transition zone

(OATZ) (Bazylinski et al., 2000; Prozorov et al., 2013). For example, relatively high numbers of

MTB are usually found at OATZ, or the anoxic regions of the environment, or both (Bazylinski

and Moskowitz, 1998; Bazylinski et al., 1995). Sometimes the concentration of MTB can

reach10^5~10^6/ml (Spring et al., 1993). In addition, different species of MTB may occupy different habitats which have specific and different chemical conditions. For example, only Fe_3O_4 producing MTB are found in freshwater environments while both Fe_3O_4 and Fe_3S_4 producers are observed in marine environments (Lefèvre et al., 2011a). However, although one strain of Fe_3S_4-producing MTB, BW-1, has been isolated and grown in axenic culture (Lefèvre et al., 2011b), most remain resistant to attempts at culturing. Therefore, much less is known about Fe_3S_4-producing MTB compared to their Fe_3O_4-producing counterparts.
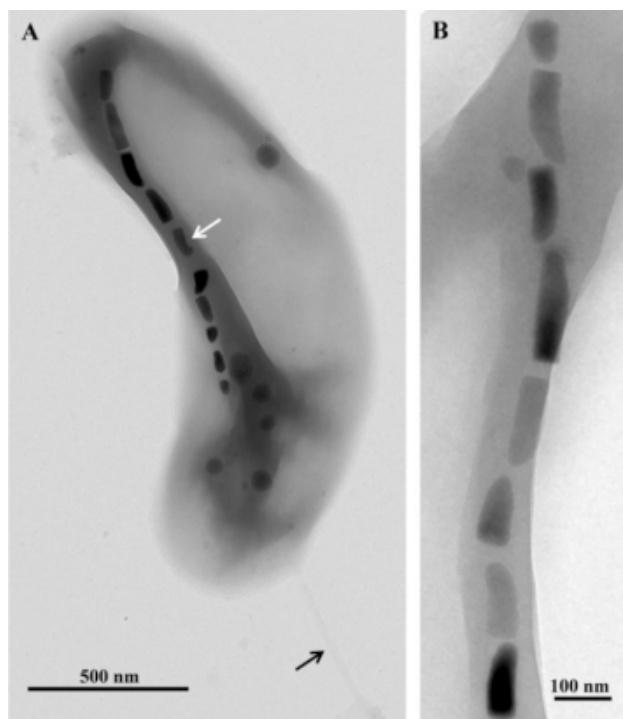
Figure 1.2 TEM images of cells and magnetosomes of the thermophilic magnetotactic bacterium strain HSMV-1 (*Candidatus* Thermomagnetovibrio paiutensis). (A) TEM image of a cell of HSMV-1 showing a single polar flagellum (black arrow) and a single chain of bullet-shaped magnetosomes (white arrow). (B) High magnification TEM image of a magnetosome chain of strain HSMV-1. Figure reproduced from (Bazylinski and Lefèvre, 2013) with permission from the *Multidisciplinary Digital Publishing Institute (MDPI)*.
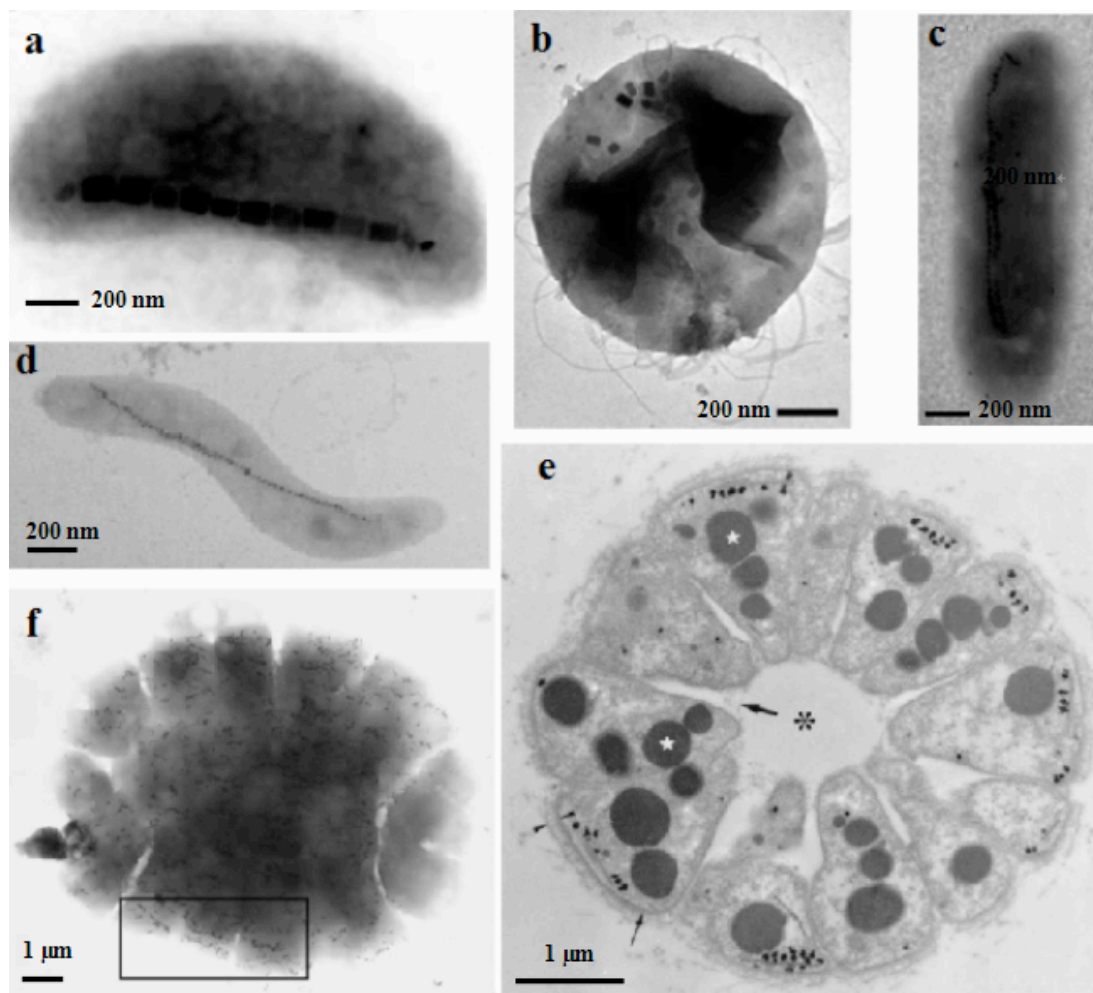
Figure 1.3 TEM images of various morphological forms of MTB. (a). vibros; (b) cocci; (c). rod-shaped; (d). spirilla; (e) mulberry-shaped and (f) pineapple-shaped multicellular magnetotactic prokaryotes (MMPs). Figure a reproduced from (Keim et al., 2006), b and c from(Lefèvre et al., 2011a) with permission from *Springer*. Figure d reproduced from (Schüler, 2008) with permission from *Oxford University Press*. Figure e reproduced from (Keim et al., 2004) with permission from *Elsevier*. Figure f reproduced from (Zhou et al., 2012) with permission from *John Wiley and Sons*.

Until recently, no MTB cells were identified as extremophilic as their growth generally requires some restricted conditions such as ambient temperature, neutral pH, specific oxygen level, etc. (Bazylinski and Lefèvre, 2013). However, an uncultured magnetotactic bacterium,

designated HSMV-1 (*Candidatus* Thermomagnetovibrio paiutensis, see **Figure 1.2**), was recently found in the Great Boiling Springs (GBS) in Nevada where the temperatures range from 32°C to 63°C (Bazylinski and Lefèvre, 2013). In addition, large numbers of MTB have been found to grow in highly alkaline aquatic environments (Mono Lake, California) with pH 9.0-9.5 (Lefèvre et al., 2011c). Since some MTB can survive/grow in high-temperature and high-basicity environments (Bazylinski and Lefèvre, 2013; Lefèvre et al., 2011c) it is possible that MTB may exist in other extreme environments such as extraterrestrial planets like Mars (Bazylinski and Lefèvre, 2013; McKay et al., 1996; Thomas-Keprta et al., 2001).

The great biodiversity of MTB can be exemplified with various morphological forms of MTB observed in both freshwater and marine habitats, which mainly includes vibros, cocci, rod, and spirilla (see **Figure 1.3a~d**). In addition, some MTB exhibit a unique multi-cellular feature and thus are referred to as magnetic multicellular prokaryotes (MMPs) (Balkwill et al., 1980; Keim et al., 2006, 2004). Until now, two kinds of MMPs have been observed: one mulberry-shaped (**Figure 1.3e**) (Keim et al., 2006) and the other with pineapple-like morphology (**Figure 1.3f**) (Zhou et al., 2012). Although the morphology may vary among different species, all known MTB are motile by means of one or more flagella whose attachment can be polarly monotrichous (single flagellum on one end), bipolar (single flagellum on each of opposite ends), and lophotrichous (bundles of flagella on the surface) (Lefèvre et al., 2011a; Matheron and Caumette, 2015). **Table 1.1** presents a few physical parameters of several magnetotactic bacteria. It can be observed that the size, velocity of swimming speed, magnetic moments, etc. vary among different species. For example, *Candidatus* Magnetobacterium bavaricum move with a velocity of ~40 μm/s while some cocci strains can move with a velocity up to 1000 μm/s (Frankel et al., 2007).

Table 1.1 Lengths, swimming speeds, and magnetic dipole moments of selected motile microorganisms. Magnetotactic bacterial species are designated with an "*" in front of their name. Reproduced from (Frankel et al., 2007) with permission from *Springer*.

Organism	Average cell length (μm)	Observed swimming speed(μm/s)	Magnetic Moment (Am^2)
* *Magnetospirillum* magnetotacticum strain MS-1	3	44	5.0×10^{-16}
* *Candidatus* Magnetobacterium bavaricum	9	40	3.2×10^{-14}
* Many-celled Magnetotactic Prokaryote (MMP)	8	170/100	
* *Candidatus* Bilophococcus magneticus	1	69	7.0×10^{-16}
* Unidentified Woods Hole Coccus	1	159	
* Coccus "ARB-1"	1	1000	
* Strain MV-1	2		7.0×10^{-16}
* Morro Bay greigite-containing Rod Anisonema	3.6		9.0×10^{-16}
Anisonema platysomum (protist)	20		7.0×10^{-13}
Escherichia coli	2	20	
Psuedomonas aeruginosa	1.5	55	
Vibro comma	4	200	
Thiovulum Majus	15	600	

1.2.3 Magneto-aerotaxis

In most unicellular MTB cells, magnetosomes are arranged in chains and along the long axis of the cell. This arrangement maximizes the magnetic moment which in turn, optimizes the preferred orientation of the cells in an aquatic environment (Frankel, 1984). It is thought that the chain-like arrangement of magnetosomes imparts a magnetic dipole moment that passively aligns the MTB cell with magnetic field as it swims by means of the flagella (Bazylinski and Frankel, 2004), a behavior referred to "magnetotaxis". Previous studies showed that MTB in the northern hemisphere migrate preferentially in a direction parallel to the Earth's magnetic field lines (north-seeking, NS), whereas those in the southern hemisphere migrate anti-parallel with Earth's magnetic field lines, (south-seeking, SS), (Blakemore et al., 1980). Because of the inclination, the Earth's magnetic field is directed downward in the northern hemisphere and upward in the southern hemisphere. Thus, the natural orientation of the magnetic moment of MTB is with the earth's magnetic field such that MTB migrate downward in either hemisphere (see **Figure 1.4**). Therefore, the function of magnetotaxis was initially thought to make MTB favorably swim downward, away from toxic higher oxygen concentrations at the water surface and towards microaerobic or anaerobic sediments (Blakemore, 1975; Blakemore et al., 1980). However, some MTB cells such as MC-1 and MO-1 were shown to have behaviors inconsistent with this model (Frankel et al., 1997; Zhang et al., 2010). For example, cells of MC-1 reverse their swimming direction when encountering different oxygen levels (Frankel et al., 1997). Later on, a new model, which combined the function of magnetotaxis with aerotaxis (sensitivity to the oxygen level) (Mazzag et al., 2003), namely "magneto-aerotaxis", was proposed to help understand how MTB locate and main their positions at the OATZ in the water column (Frankel et al., 1997). Recently, analysis of the *Magnetospirillum gryphiswaldense* genome revealed at
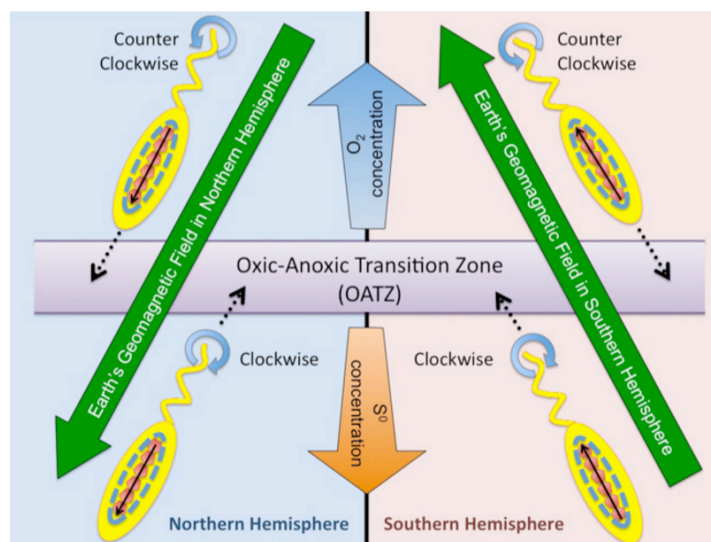
Figure 1.4 Diagram showing how magnetotactic bacteria use magnetotaxis to swim to the OATZ in the Northern versus the Southern Hemisphere on Earth. Figure reproduced from (Chen et al., 2012) with permission from *Nature Education*.

least 56 genes that encode putative chemoreceptors, known as methyl-accepting chemotaxis proteins (MCPs), and four putative chemotaxis operons, designated *cheOp 1-4* (Popp et al., 2014).

According to the model of magneto-aerotaxis, the swimming direction of MTB is determined by the sense of flagellar rotation, which in return is determined by the aerotactic response of the cell (Frankel et al., 2007, 1997). Two different magneto-aerotaxis mechanisms have been proposed for *Magnetospirillum magnetotacticum* strain MS-1 and *Magnetococus marinus* strain MC-1(Frankel et al., 1997). For strain MS-1, the magnetic field **B** only provides an axis but not a direction such that cells of MS-1 swim along **B** but with frequent reversals of swimming directions. This mechanism is called axial magneto-aerotaxis. For strain MC-1, the role of **B** is polar, which provides both axis and direction for cell mobility. Therefore, MC-1 is found to swim persistently in a specific direction (either parallel or antiparallel to **B**) along the O_2
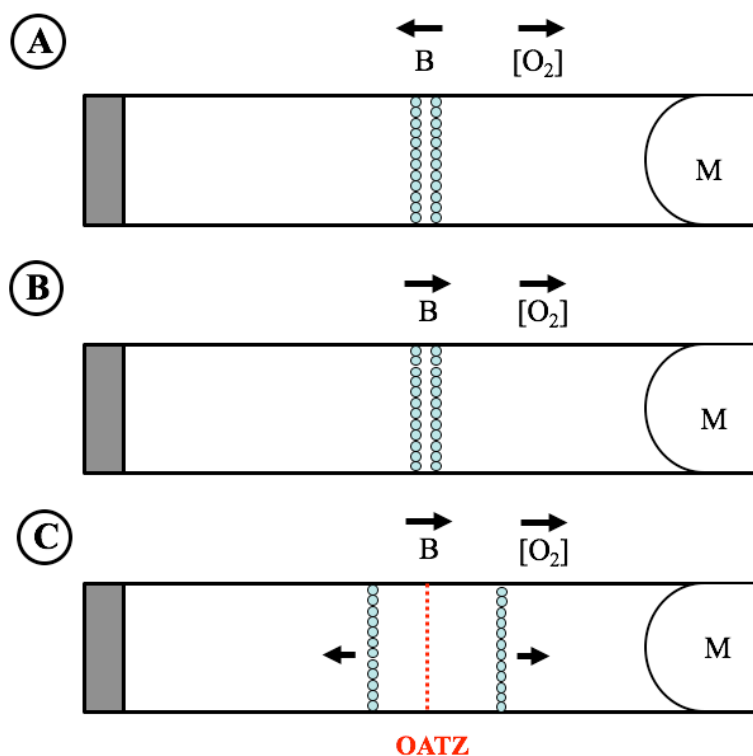
Figure 1.5 Demonstration of axil and polar magneto-aerotaxis in MTB. (A). Schematic drawing of a flat capillary with one end closed and the other end open to air. Cell suspensions are transferred to the capillary under a magnetic field **B**. A meniscus (M) formed at the open end and oxygen diffused into the middle from this end. Results showed that all the MTB cells formed a microaerobic band at an [O$_2$] concentration less than 25 μM (B). For axial magneto-aerotaxis, the initial band still remained intact after **B** was reversed. (C). For polar magneto-aerotaxis, the initial band dispersed and separated into two groups, which swam towards opposite directions. (Lefèvre et al., 2014).

gradient, a mechanism called polar magneto-aerotaxis (Frankel et al., 1997). An effective way to distinguish polar and axial magneto-aerotaxis is to transfer these cells into a microcapillary with an oxygen gradient and watch the cell motion under a specific magnetic field. Polar and axial cells behave significantly different when the applied magnetic field is reversed (see **Figure 1.5**).

Figure 1.5 illustrates an experimental setup to distinguish axial and polar cells. **Figure 1.5 A** demonstrates a flat capillary with one end closed and the other one open to the air. A cell

suspension was transferred to the capillary and formed a meniscus (M) in the open end. The

oxygen level increased from the center to the open end of the capillary, opposite to the applied

magnetic field **B**. Using a similar setup, Lefèvre et al. (2014) reported that 12 different species of

MTB all formed a well-defined microaerobic band (oxygen concentration lower than 25μM) 15

to 45 minutes after the transfer. The cells still continued to swim back and forth along the

magnetic field within the band. However, when the original magnetic field was reversed,

different species of MTB exhibit different behaviours. For axial magneto-aerotaxis, MS-1 cells

rotated 180° when the magnetic field was reversed but the band still remained intact (see **Figure
1.5B**). For polar magneto-aerotaxis, MC-1 cells also rotated 180° with the inversion of magnetic

field but the band further split into two subgroups of cells which swam in opposite directions

(see **Figure 1.5C**) (Frankel et al., 1997). This suggests that the mechanism for connecting

magnetic orientation and mobility is different for the two different types of magneto-aerotaxis

shown in Figure 1.5.

Axial magneto-aerotaxis is consistent with a sensory mechanism (Frankel et al., 1997;

Segall et al., 1986), in which cells can sense the oxygen gradient over a period of time. They

should also be able to compare whether the present oxygen level is above or below their

preferred levels (Lefèvre et al., 2014). For example, when the cells sense that they are moving

away from their preferred $[O_2]$, they can reverse their swimming direction and then return to the

preferred location. In this way, the band is kept intact even when the external magnetic field is

reversed (Figure 1.5B).

Polar magneto-aerotaxis fits a model of a two-state aerotactic sensory system proposed

by Frankel et al. (1997), as shown in **Figure 1.6**. In this model, the sense of flagella rotation is

directly determined by the O_2 concentration, $[O_2]$. When the present $[O_2]$ is higher than preferred
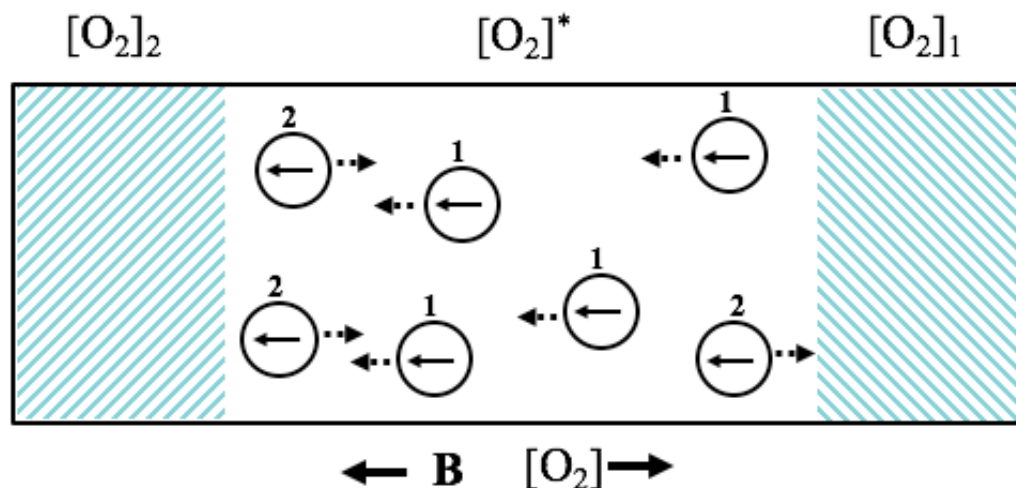
Figure 1.6 Illustration of two-state aerotactic sensory mechanism. Cells are thought to have two sensory states,1 and 2, which cause the opposite direction of flagella rotation and lead to opposite swimming direction along magnetic field B. Figure reproduced from (Frankel et al., 1997) with permission from *Elsevier*.

level, the cells are in the "oxidized" state or state 1 in Figure 1.6. In this case, cells would rotate their flagella counterclockwise (CCW) and swim parallel to magnetic field. When the present $[O_2]$ is lower than the preferred level, the cells are in the "reduced" state or state 2 in Figure 1.6, which causes them to rotate their flagella clockwise (CW) and leads to migration antiparallel to the external magnetic field. When the magnetic field was reversed, the cell in either state would continue to swim parallel (state 1) or antiparallel to magnetic field **B** (state 2), which causes them to move away from their preferred $[O_2]$ and leads to a dispersal of the band, as shown in Figure 1.5C (Frankel et al., 1997). Lefèvre et al. (2014) further proposed that cells with polar behaviour sensed the oxygen gradient only when the oxygen gradient was antiparallel to the magnetic field, which was also the natural environmental condition for these cells. When the initial magnetic field was reversed and made parallel to the oxygen gradient (Figure 1.5C), these cells might turn

off their sensory mechanism in such non-natural conditions and only rely on the magnetic field

to direct their movement.

Although only aerotaxis is discussed in this section, it is noted that the navigation of

MTB does not rely only on oxygen levels. Multiple chemical gradients and light (Alexandre et

al., 2004; Shapiro et al., 2011) also play roles in the movement of MTB, particular in complex

environments (Faivre and Schuler, 2008). Up to now, it is still unclear how aerotaxis, chemotaxis

and phototaxis are combined and how they transmit signals to the flagellar motor.

1.3 Bacterial Magnetosomes

1.3.1 Magnetosome membrane

Bacterial magnetosomes are intracellular inclusions in MTB that help them detect and align

themselves with external magnetic field. They consist of two main parts: the inorganic Fe-

bearing magnetic crystals (Fe_3O_4 or Fe_3S_4) and an organic phospholipid bilayer (Prozorov et al.,

2013). In most unicellular MTB cells, the magnetosomes are enclosed by a bilayer lipid

membrane and arranged in chains along the long axis of the cell such that the magnetic moment

can be maximized. The resulting magnetic moment and strength of the earth's magnetic field are

then sufficient to prevent the random orientation of the cells in aquatic environment (Frankel,

1984). **Figure 1.7A** presents a TEM image of magnetosome chains extracted from

Magnetovibrio blakemorei strain MV-1 and **B** shows the image of red square region in Figure

1.7A. The membrane can mainly be found at both ends, side surfaces and possibly upper surface

of each magnetosome.
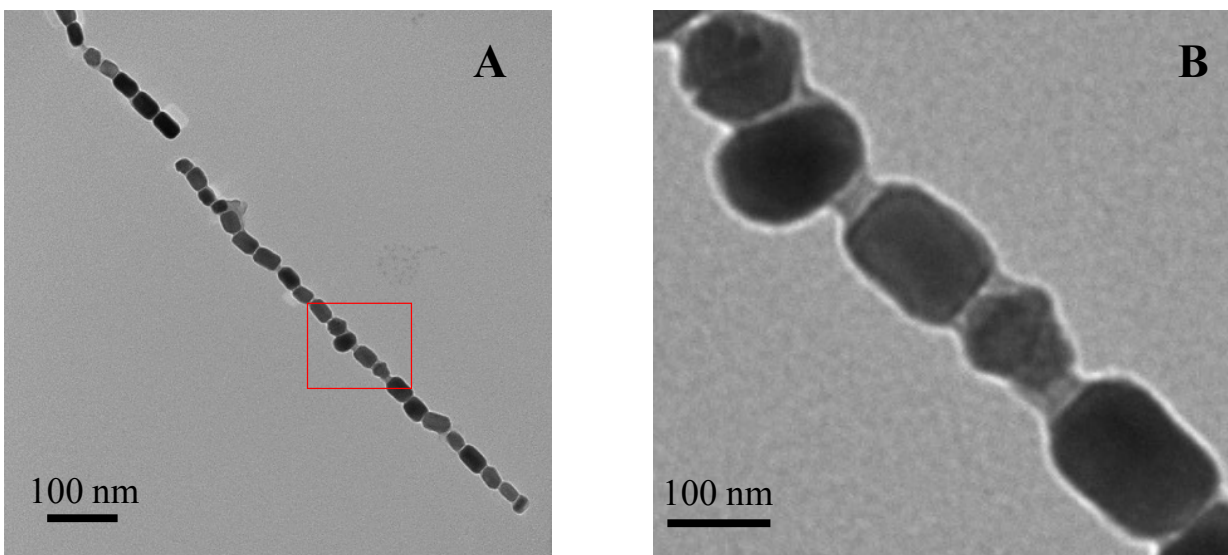
Figure 1.7 (A).TEM image of magnetosome chains extracted from MV-1 MTB cell; (B). Magnified TEM image corresponding to the red square in (A).

1.3.2 Biologically controlled mineralization of magnetosomes

The formation of minerals by prokaryotic microorganisms can be mainly divided into two categories: biologically controlled mineralization (BCM) and biologically induced mineralization (BIM) (Lowenstam and Weiner, 1989; Lowenstam, 1981). BIM refers to a mineralization process where minerals are generally produced extracellularly and considered as an unintended and uncontrolled consequence of the metabolic activity of the organism (Frankel and Bazylinski, 2003). However, in BCM, the synthesis of minerals mainly occurs within the cell or on the cell surface, and is subjected to a high degree of crystallographic and chemical control (Bazylinski and Frankel, 2003).,The formation of magnetosomes in MTB is one of the most clear-cut examples of BCM. It involves: tight genetic control (Schüler and Frankel, 1999): certain elements (mainly iron) uptaken by the cell from the environment; nucleation and growth of magnetosomes taking place at specific locations within the cell and only under certain chemical conditions; well-defined magnetosomes ultimately formed with high chemical purity, consistent

morphology, narrow size distribution, and specific arrangements, etc. (Bazylinski and Frankel, 2003).

1.3.2.1 Chemical purity of magnetosomes

Up to now, magnetite (Fe_3O_4) and greigite (Fe_3S_4), have been identified as two primary mineral phases of magnetosomes (Bazylinski et al., 1994) in MTB cells. However, several other iron-oxides and iron-sulfides, which appear to be precursors to magnetosomes, are also observed in MTB. For example, Frankel et al. (1983) reported that an amorphous ferrihydrite ((Fe^{3+})$_2O_3 \cdot 0.5H_2O$) precursor was formed prior to Fe_3O_4 magnetosome formation. Staniland et al. (2007) observed that a non-magnetic hematite (α-Fe_2O_3) phase acted as the precursor of Fe_3O_4. In the case of Fe_3S_4-producing MTB cells, several iron-sulfides including cubic FeS and tetragonal FeS (mackinawite) were identified and attributed as the precursors to Fe_3S_4 (Pósfai et al., 1998).

In most cases, MTB biomineralize either Fe_3O_4 or Fe_3S_4 but not both. However, a large rod-shaped bacterium, designated as strain BW-1, was isolated and grown in axenic culture, which was found to synthesize Fe_3O_4 and Fe_3S_4 in the same chain (see **Figure 1.8**) (Lefèvre et al., 2011b). In addition, it has been found that magnetic multicellular prokaryotes (MMPs) sometimes synthesize both magnetite and greigite crystals in the same chain (Lins et al., 2007). The fact that both types of magnetosomes can be biomineralized in Fe_3O_4 and Fe_3S_4 producers suggests that the mechanism of chain assembly is independent of the type of mineral, as proposed by Bazylinski et al. (1995).
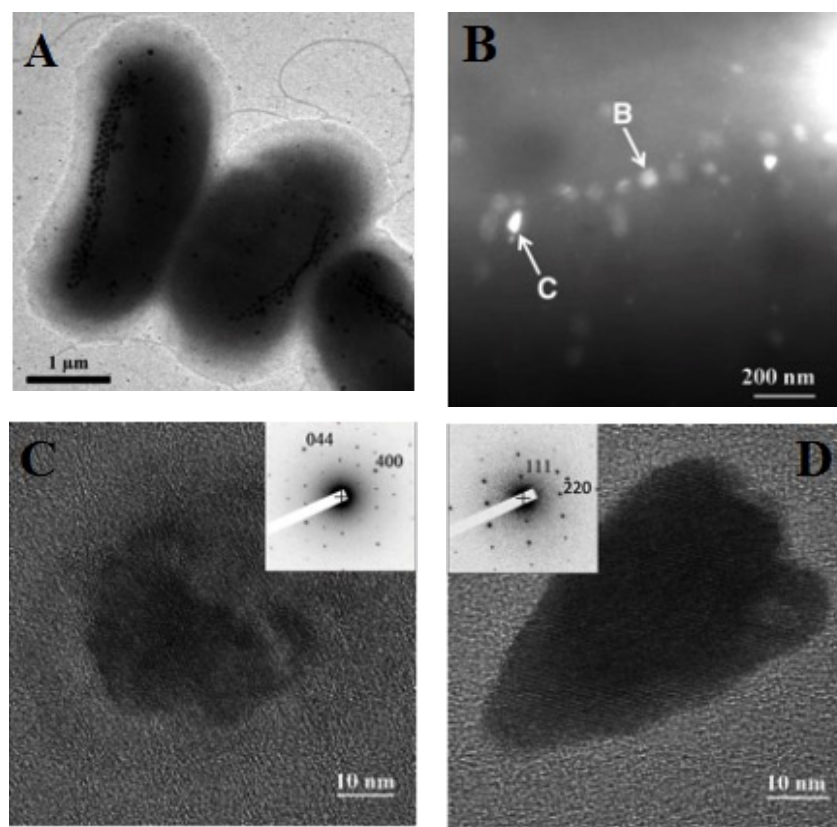
Figure 1.8 TEM and selected area electron diffraction (SAED) of BW-1 cell. (A) TEM image of large and rod-shaped strain BW-1. (B) Darkfield scanning TEM image of a magnetosome chain containing both greigite (labeled B) and magnetite (labeled C). (C) High-magnification TEM image of greigite crystal labeled in (A). (Inset) SAED of crystal viewed along the [0 −1 1] zone axis. Pattern is consistent with greigite. (C) High-magnification TEM image of magnetite crystal labeled in (A). (Inset) SAED pattern of crystal viewed along the [−1 −12] zone axis. Figure A~D reproduced from (Lefèvre et al., 2011b) with permission from the *American Association for the Advancement of Science (AAAS)*.

With respect to the composition of magnetosomes, another interesting observation is that some trace elements such as titanium (Ti) (Towe and Moench, 1981) and copper (Cu) (Bazylinski et al., 1993) can be doped into magnetosomes in environmental MTB cells. Staniland et al. (Staniland et al., 2008) successfully controlled cobalt doping (between 0.2 and 1.4 at%) in *Magnetospirillum* MTB cells *in vivo* by replacing iron quinate (FeQ) with cobalt quinate (CoQ)

in the growth medium. In addition, Keim et al. (Keim et al., 2009) showed that some manganese

(Mn) can be incorporated into magnetosomes (up to 2.8 at%) in uncultured magnetotactic coccus

when $MnCl_2$ is added to microcosms. These results may open possibilities of designing

biologically synthesized nanoparticles with tailored properties (Staniland et al., 2008).

1.3.2.2. Morphology of magnetosomes

The shapes of Fe_3O_4 and Fe_3S_4 magnetosomes varies in a species-specific manner. Three

general morphologies of mature magnetosomes have been observed in MTB: cubo-octahedral

(**Figure 1.9a**) (Balkwill et al., 1980; Mann et al., 1984), elongated prismatic, (roughly

rectangular, **Figure 1.9b, d, e, f**) (Meldrum et al., 1993; Towe and Moench, 1981), and tooth-,

bullet-, or arrowhead-shaped (**Figure 1.9c**) (Mann et al., 1987; Spring et al., 1993; Thornhill et

al., 1994).

Both Fe_3O_4 and Fe_3S_4 are spinel minerals with *Fd3m* space group (Devouard et al., 1998).

The crystal habits of magnetosome crystals are based on octahedral {111}, dodecahedral {110},

and cubic {100}forms (Devouard et al., 1998). For example, the idealized habits of cubo-

octahedral magnetosomes (Figure 1.9a) are composed of {100} and {111} with roughly equal

development of the six faces of the {100} form and eight faces of the {111} form (**Figure

1.10A**). However, most of the magnetosomes found in MTB cells appear to be elongated along

one face, leading to non-isometric and anisotropic morphologies (Figure 1.9b~f). The habits of

these non-equidimensional crystals are described as combinations of {100},{111} and {110}

forms (**Figure 1.10B~D**). Devouard et al. (1998) proposed that the morphologic anisotropy

observed in magnetosomes is linked to magnetic anisotropy, which allows for an easy axis of

magnetization and thus helps to align magnetic moments along the long axis of the cell.
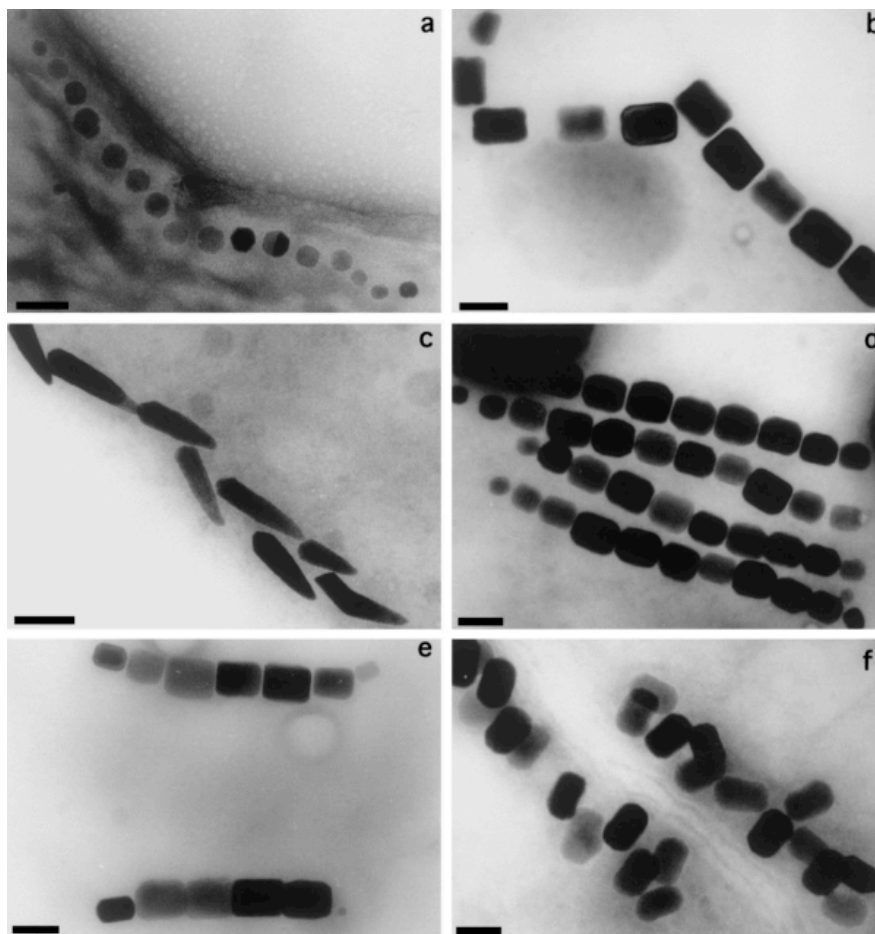
Figure 1.9 a~f. TEM images of crystal morphologies and intracellular organization of magnetosomes found in various magnetotactic bacteria. Shapes of magnetotactic crystals include cubo-octahedral (a), elongated hexagonal prismatic (b,d,e,f) and bullet-shaped morphologies (c). The particles are arranged in one (a,b,c), two (e) or multiple chains (d) or irregularly (f). Bar represents 100 nm. Figure a~f reproduced from (Schüler and Frankel, 1999) with permission from *Springer*.

Generally, elongated growth can occur either because of anisotropy in the growth environment or anisotropy in the growth site (Devouard et al., 1998). In the case of magnetosomes, the shape anisotropy was attributed to an anisotropic flux of iron through the surrounding membrane during magnetosome growth (Gorby et al., 1988). Interestingly, although elongated Fe_3O_4 crystals have been synthesized via simple inorganic processes in the laboratory (Piepho and

Williams, 2010), most of these unusual magnetic crystals are observed in ancient and recent
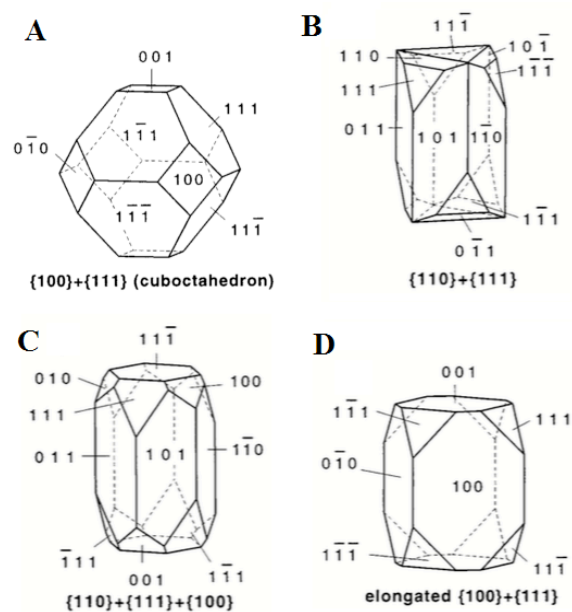
Figure 1.10 Combinations of forms compatible with *Fd3m* symmetry. A. cuboctahedron observed in both Fe_3O_4 and Fe_3S_4 magnetosomes; Elongated habits found in Fe_3O_4 magnetosomes (B and C), and in Fe_3S_4 magnetosomes (D). Figure 1.10A~D reproduced from (Devouard et al., 1998).

sediments or in the Martin meteorite ALH84001 (McKay et al., 1996), and are referred to as 'magnetofossils' (Chang, 1989). The presence of magnetofossils is considered as evidence for past existence of MTB in aquatic environments (Chang, 1989; Stolz et al., 1986) and even life on ancient Mars (McKay et al., 1996; Thomas-Keprta et al., 2001).

1.3.2.3 Size distribution of magnetosomes

In addition to composition and morphology, the size distribution is another parameter subjected to a tight control by MTB. The size of a magnetic crystal has a great effect on its magnetic properties. MTB optimize the magnetic dipole moment on an individual magnetosome basis by controlling its size (Muxworthy and Williams, 2006). Several results have shown that

almost all Fe_3O_4 and Fe_3S_4 magnetosomes are distributed in a very narrow size range, which is

between 35-120 nm (**see Figure 1.11**)(Bazylinski and Moskowitz, 1998; Jandacka et al., 2013).
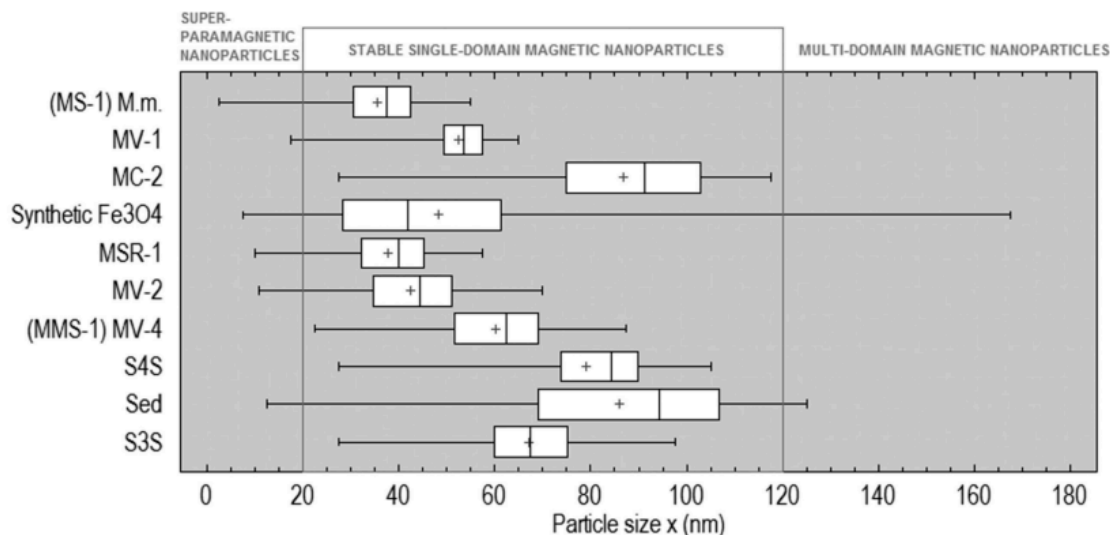
Figure 1.11 Box-plot for bacterial and inorganic magnetic nanoparticles (Jandacka et al., 2013).

When the size of magnetic crystals is 20~120 nm, they are single-domain (SD) particles,

meaning that they can be uniformly magnetized and have the maximum possible magnetic

moment per unit volume (Lins and Bazylinski, 2012). If the particles are larger than 120 nm,

they naturally create multiple magnetic domains, with the domain moments typically organized

to have a closed magnetic loop (Muxworthy and Williams, 2006). This prevents particles from

being uniformly magnetized and significantly reduces the magnetic moment. When the particles

are smaller than 20 nm, they are superparamagnetic particles (SPM). Although SPM particles are

SD, their magnetic moments can be reversed by thermal induction, which results in a time-

averaged moment of zero (Muxworthy and Williams, 2006). Therefore, it is clear that the

preference for stable SD particles facilitates the orientation of magnetosome chains in

geomagnetic field

1.3.2.4 Magnetosome formation and arrangement

The hypothesized mechanism of magnetosome formation is a complex process, which generally includes: iron uptake from the environment by the cell; magnetosome vesicle formed intracellularly; iron transport into the magnetosome vesicle; and protein-mediated Fe_3O_4 or Fe_3S_4 formation inside magnetosome vesicles (Bazylinski and Schübbe, 2007). It should be noted that current study of the mechanism of magnetosome formation has mainly focused on *Magnetospirillum* species (Yan et al., 2012) because they can be cultivated more readily than most other MTB (Schüler, 2002). However, even among closely related *Magnetospirillum* species, such as AMB-1 and MSR-1, the formation and assembly of magnetosomes in these organisms differs (Komeili, 2012). For example, in AMB-1, it has been observed that empty magnetosome vesicles are already localized and organized into chains prior to magnetosome formation (Komeili et al., 2006, 2004). Contrary to AMB-1, magnetosomes in MSR-1 nucleate in widely-spaced vesicles and then move along a cytoskeletal filament to form tight chains through magnetic interactions (Faivre et al., 2010; Scheffel et al., 2006). Recently, a special genomic region was identified, one where genes for magnetosome formation in MTB cells are located. The sequence is more or less conserved among a large number of MTB species. This region is known as the "magnetosome gene island (MAI)" (Ullrich et al., 2005). The discovery of MAI may allow people to classify genes associated with magnetosome formation and promises to understand mechanisms of magnetosome chain assembly in different MTB cells. Some of the knowledge on functional analysis of genes in MAI is summarized below.

With electron cryotomography (ECT), some distinct filaments were observed around the magnetosome chain (**Figure 1.12A~C**) (Komeili et al., 2006; Scheffel et al., 2006). These cytoskeletal filaments are composed of protein MamK. They are thought to function as structural scaffolds for magnetosome chain organization. Green fluorescent protein (GFP)-tagged MamK
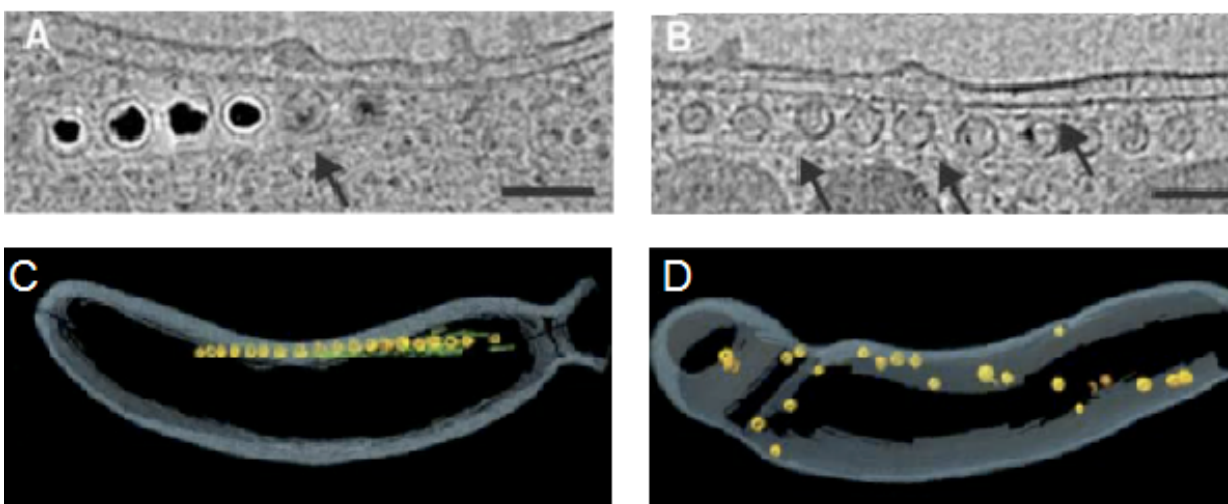
Figure 1.12 Magnetosome chains are flanked by long cytoskeletal filaments. (A) Larger view of the magnetosome chain in Fig. 1A. (B) Similar view of a magnetosome chain grown in the absence of iron, which prevents the formation of magnetite crystals. Arrows point to the long filaments. Scale bars, 100 nm. (C) Three-dimensional organization of magnetosomes (yellow) and their associated filaments (green) shown in (B) with respect to the whole cell (blue). (D) mamK mutant, where magnetosomes appear disordered and no filaments are found in their vicinity. Figure reproduced from (Komeili et al., 2006) with permission from *American Association for the Advancement of Science (AAAS)*.

also appeared to form linear filaments along the curvature of the cell (Komeili et al., 2006). In the absence of mamK, AMB-1 still produces proper magnetosomes with the same features as the wild-type strain. However, the cytoskeletal filaments disappeared in this mutant and magnetosomes did not assemble as one chain but were scattered throughout the whole cell (**Figure 1.12D**) (Komeili et al., 2006). Another protein that relates to magnetosome chain organization is MamJ, which is an acidic protein and considered as a candidate MamK regulator (Greene and Komeili, 2012). It is proposed that MamJ may anchor magnetosomes into the cytoskeletal filament to stabilize the magnetosome chain and prevent it from collapsing (Faivre and Schuler, 2008; Keim et al., 2006). When the mamJ gene in strain MSR-1 is deleted, the
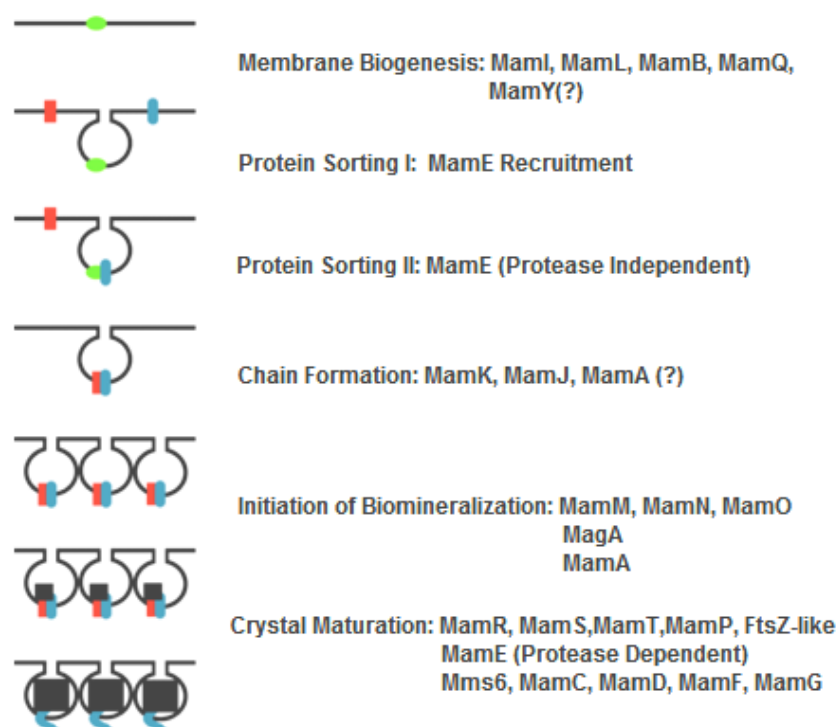
Figure 1.13 A model for magnetosome formation under genetic control. Figure reproduced from (Komeili, 2012) with permission from *Oxford University Press*.

magnetosomes do not organized into chains but aggregate into clusters (Scheffel et al., 2006). The agglomeration occurs at a later stage of crystal growth and is probably caused by the increasing magnetic attractions between magnetosomes once they are in close proximity (Scheffel et al., 2006).

Based on numerous genetic and biochemical analyses of genes in MAI, Komeili (2012) proposed a model for magnetosome formation (**Figure 1.13**): First, protein MamI, MamL, MamQ, MaMB and other factors (green) reshapes the inner cell membrane and creates the magnetosome membrane; second, protein MaME (blue) is recruited to the nascent magnetosome; third, MamE recruits other proteins (red) to the magnetosome in manner independent of its protease activity; fourth, proteins MamJ and MamK assist to assemble magnetosomes into chains; fifth, biomineralization is initiated and small magnetite crystals start to form; finally, magnetite

crystals continue to grow into mature ones, which requires the protease activity of MaME and

other factors including the Mms protein, etc.

1.4 X-ray Magnetic Circular Dichroism (XMCD)

1.4.1 Theory of XMCD

X-ray magnetic circular dichroism (XMCD) is a synchrotron-based technique, which

provides quantitative information about elemental and site-specific magnetism in magnetic

materials (Stöhr and Siegmann, 2006). The XMCD effect was first discovered by Schütz et al.

(1987) at the Fe K absorption edge in the hard X-ray region. The first XMCD spectrum in the

soft X-ray region was measured at the Ni $L_{2,3}$ edge of nickel metal by Chen et al. (1990). Hard

X-rays typically probe K-edge levels, where the XMCD signal is in the order of 10^{-3} of the

absorption signal or even less in saturation conditions (Mathon et al., 2004). In contrast, XMCD

at the $L_{2,3}$ edge for 3d transition metal element or $M_{4,5}$ edge for rare earth elements can be as

high as 30%. Such edges are located in the 500~3000 eV energy range and thus XMCD

measurements are mainly performed in the soft X-ray region. The advent of high-brilliance 3rd

generation synchrotron facilities equipped with elliptically polarizing undulator, which can

change from left to right circular polarization with a switching rate in the 0.1Hz regime, has

greatly improved the accuracy of XMCD measurements (Kang et al., 2005).

The XMCD signal is defined as the difference of the two X-ray absorption spectra (XAS)

recorded with circularly polarized X-rays when the photon spin and magnetic moment in the

sample are aligned parallel and anti-parallel. In these conditions, the photon spin and magnetic

moment vectors are either parallel or anti-parallel aligned. This can be achieved equivalently by

either switching circular polarizations for a fixed sample magnetization direction or changing the

magnetization direction of the sample and using a single circular polarization. A good starting

point to explain the mechanism of XMCD is the interaction between X-rays and the matter.

According to the Lambert-Beer law, the intensity of X-rays, I_z, decreases exponentially with the

distance, d, travelled in the sample:

$$I_z = I_0 \cdot e^{-\mu d} \quad \text{with} \quad \mu = \rho \cdot \sigma \qquad (1.1)$$

where I_0 is the intensity of the incident X-rays, μ is the absorption coefficient, ρ is the sample

density and σ is the absorption cross section. The absorption cross section σ is defined as the

number of excited states created per unit time divided by the number of incident photons I_0 per

unit time and per unit area:

$$\sigma = \frac{P_{i \to f}}{I_0} \qquad (1.2)$$

where $P_{i \to f}$ refers to the transition amplitude between the inititial state i and the final state f. The

transition amplitude $P_{i \to f}$ can be calculated from Fermi's golden rule:

$$P_{i \to f} = \frac{2\pi}{\hbar} \left| < f |\overline{V}| i > \right|^2 D(E_f) \qquad (1.3)$$

where $\left| < f |\overline{V}| i > \right|$ is the transition matrix element and $D(E_f)$ is the energy density of electric-

dipole copuled final states. Thus, the absorption coefficient μ can be determined by

$$\mu \propto \left| < f |\overline{V}| i > \right|^2 \cdot D(E_f). \qquad (1.4)$$

Here, the transition matrix element remains constant for mutual polarizations but the density of

final states varies with different polarizations, which causes the XMCD contrast.

The origin of XMCD can be understood with the so-called two-step model (Stöhr, 1995), which

is described in **Figure 1.14A**. In the first step, a circularly polarized photon is absorbed and an

inner-shell electron is excited into empty states above the Fermi level. For a left or right

circularly polarized photon, it also has a defined angular momentum, $\hbar$ or $-\hbar$. If the

photoelectron originates from a spin-orbit split state, for example the $2p_{3/2}$ or $2p_{1/2}$ state in Figure

1.13a, the angular momentum added by the absorbed photon is partly transferred to the electron

spin via spin-orbit coupling (Stöhr, 1999, 1995). This leads to a preferential absorption of

photons with $\hbar$ momentum in the $2p_{3/2}$ state (L_3 edge) and preferential absorption of photons

with $-\hbar$ momentum in the $2p_{1/2}$ state (L_2 edge) (Stöhr, 1995). Magnetic properties of the sample

would then play roles
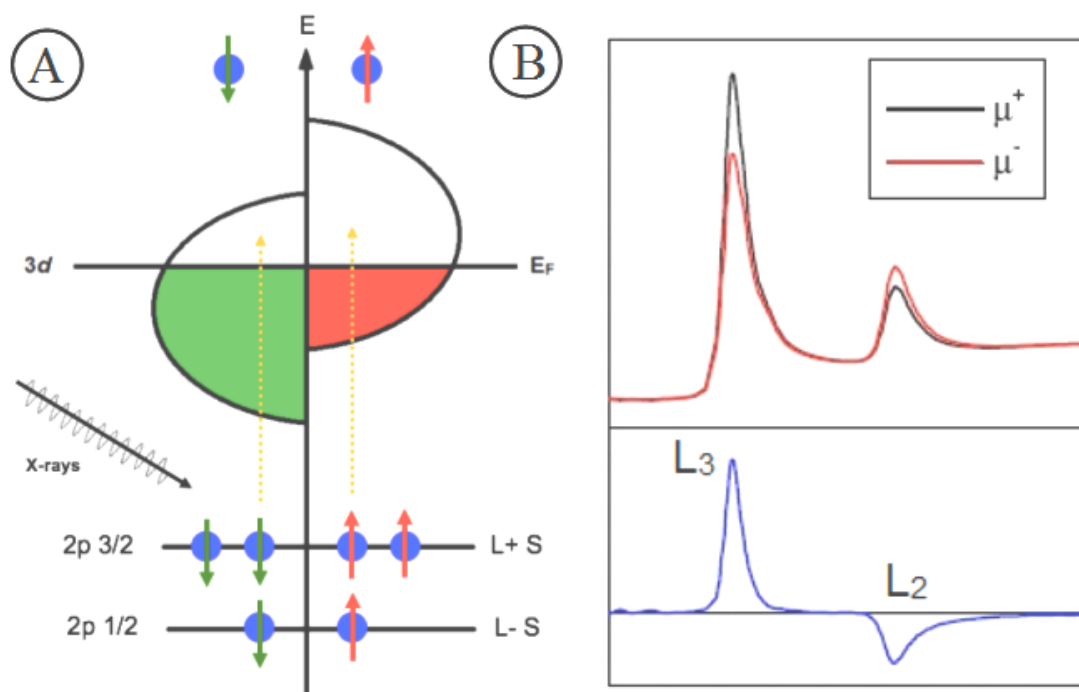
Figure 1.14 Illustration of origin of XMCD contrast. (A). A two-step model of the XMCD
effect where circularly polarized light excites 2p electrons to empty 3d states. The unbalanced
density of final states leads to an XMCD contrast. (B). X-ray absorption spectra of a magnetic
materials recorded with two polarized light (top panel) and the derived XMCD spectrum
(bottom panel). Course of A.Scholl,
http://xraysweb.lbl.gov/peem2/webpage/Project/TutorialContrast.shtml

in the second step. For the magnetized materials, an imbalance in empty spin-up and spin-down

states exists in the valence band, which makes the valence shell act as a "spin-detector" (Stöhr,

1995). As shown in Figure 1.14A, due to the conservation of the spin in the absorption process,

the spin-up photoelectrons only occupy the empty spin-up final states while spin-down photoelectrons only fill the empty spin-down final states. This means the density of empty final states, $D(E_f)$, in a magnetized material is different for the two types of spin-polarized photoelectrons, which causes different absorption coefficients for different circularly polarizations (see **Figure 1.14B**) . This is the orgin of the XMCD contrast. It should be noted that since 2p$_{3/2}$ and 2p$_{1/2}$ have opposite spin-oribt coupling, *l+s* and *l-s*, respectively, the XMCD contrast at L$_3$ and L$_2$ edge is inverted, as shown in Figure 1.14B.

1.4.2 XMCD of Magnetite (Fe$_3$O$_4$) at the Fe L$_{2,3}$ edge

Magnetite, Fe$_3$O$_4$, is ferromagnetic with an inverse spinel structure with space group *Fd3m* (227) and a lattice constant of 8.3941 Å (Fleet, 1981). It is a mixed valence compound with a Fe(II)/Fe(III) ratio of 0.5. The relatively large O^{2-} ions form a face-centered cubic (fcc) lattice where different Fe ions are located in interstitial sites (Stöhr and Siegmann, 2006). As shown in **Figure 1.15**, the tetrahedral sites (*A*) are occupied by Fe(II) ions while the octahedral sites (*B*) are occupied by a random distribution of Fe(II) and Fe(III) ions. Due to its unique properties, Fe$_3$O$_4$ has been used in biomedical application (Mohapatra and Anand, 2010), magnetic storage media (Yamaguchi et al., 1990), catalysts (Zhang et al., 2005), etc. Therefore, a good understanding of theelectronic and magnetic structure of Fe$_3$O$_4$ is of great importance.
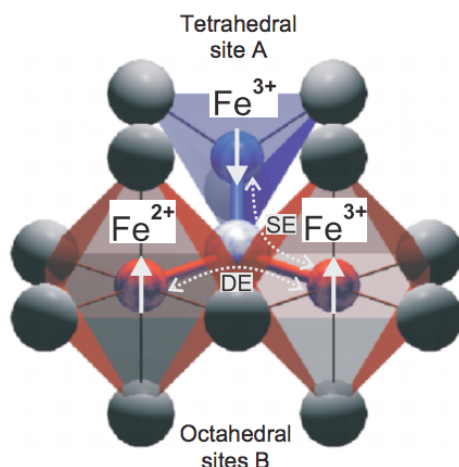
Figure 1.15 Crystallographic and magnetic structure in Fe_3O_4, near tetrahedrally (site A) and octahedrally (site B) coordinated Fe atoms. Figure reproduced from (Stöhr and Siegmann, 2006) with permission from *Springer*.

Figure 1.16 A shows the Fe $L_{2,3}$ X-ray absorption (XAS) spectra of a magnetized magnetite thin film for two different magnetizations (Goering et al., 2007). The XMCD spectrum, the difference between these two XAS spectra, is also shown. The Fe $L_{2,3}$ XAS spectrum exhibits two main bands which are the L_3 ($2p_{3/2}$) and L_2 ($2p_{1/2}$) peaks separated by the spin-orbit coupling of the 2p hole. Each band has a fine structure which is determined by a complex interplay of ligand field splitting, covalent interactions and atomic multiplets for each of the distinct electronic/magnetic sites in magnetite (Antonov et al., 2003; Kuiper et al., 1997; Pattrick et al., 2002). The XMCD spectrum of Fe_3O_4 consists of three distinct peaks in the L_3 region, which are typically located at 708.1 eV (peak B_1), 709.1 eV (peak A), and 709.9 eV (peak B_2). Multiplet calculations showed that each of these three peaks has its major contributions from states with the promoted electron associated with Fe ions in three different sites (Crocombette et al., 1995; Pattrick et al., 2002): d^6O_h (octahedral Fe(II)site, peak B_1), d^5T_d (tetrahedral Fe(III)site, peak A), and d^5O_h (octahedral Fe(III) site, peak B_2) (see **Figure 1.16B**).

Another prominent feature of the Fe L_3 XMCD of Fe_3O_4 is the "negative-positive-negative"

sense of the structure in the L_3 region. The Fe (II) and Fe(III) ions in the octahedral
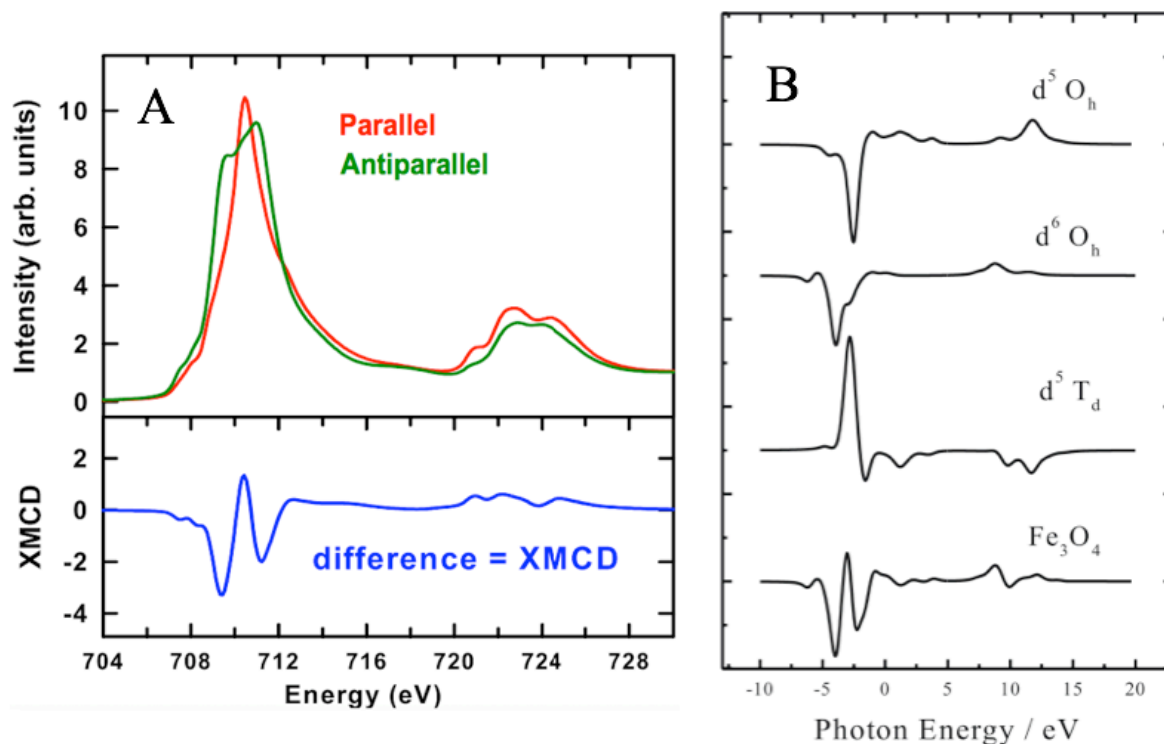
Figure 1.16 Experimental and calculated Fe $L_{2,3}$ XMCD spectra of Fe_3O_4. (A). Fe $L_{2,3}$ X-ray absorption (XAS) spectra of thin film magnetite recorded using total electron yield detection, with two circularly polarized X-rays (data courtesy of Goering et al. (Goering et al., 2007); (B) Calculated XMCD spectra of Fe components in different sites. Figure adapted from Pattrick et al (2002).

sites are parallel coupled while the two Fe(III) in the tetrahedral and octahedral sites are anti-

parallel coupled. Thus, the calculated XMCD spectrum of d^5O_h site has the same sign with $d^6 O_h$

but opposite to d^5T_d, as shown in Figure 1.16B. In addition, due to the antiferromagnetic

coupling between $d^5 T_d$ and $d^5 O_h$ sites, their magnetic moments of $\pm 5\mu_B$ cancel each other which

leaves a net magnetic moment of 4 μb from the $d^6 O_h$ site (Stöhr and Siegmann, 2006).

1.4.3 XMCD of Greigite (Fe₃S₄) at the Fe L₂,₃ edge

Greigite (Fe_3S_4) is a thiospinel of iron with a lattice constant of 9.876 Å (Rickard and

Luther, 2007). Like Fe_3O_4, Fe_3S_4, is ferrimagnetic with a mixed valence compound with Fe(II)

and Fe(III) occupying octahedral and tetrahedral sites (see **Figure 1.17**). However, the site

distribution of Fe(II) and Fe(III) in Fe_3S_4 is not well understood (Chang et al., 2012a; Letard et

al., 2005).
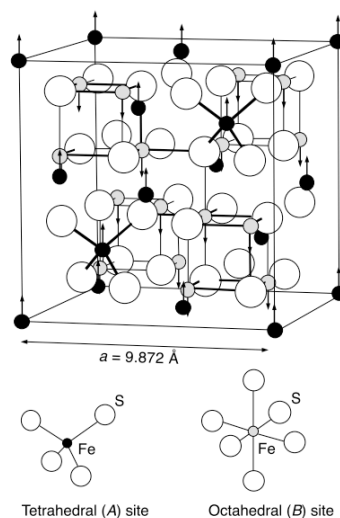
Figure 1.17 Crystallographic and magnetic structure for greigite (Fe_3S_4). Fe^{3+} occupies
tetrahedral (*A*) sites; both Fe^{2+} and Fe^{3+} occupy octahedral (*B*) sites. The octahedral and
tetrahedral ions are anti-ferromagnetically coupled with arrows representing the magnetic
moment direction at each Fe ion. Figure reproduced from Roberts et al. (2011) .

Greigite and the pyrrhotites ($Fe_{1-x}S$, 0<x<0.13) are the two major ferromagnetic iron-

sulfide minerals (Letard et al., 2005). Because Fe_3S_4 was thought to be thermodynamically

metastable and to transform to pyrite (FeS_2) under sedimentary, reducing conditions with excess

sulfide, its geological importance in sediments was previously underestimated (Berner, 1984;

Roberts, 1995; Roberts et al., 1996). However over the last few decades, increasing evidence has

demonstrated that greigite can persist in the geological record of sediments for long periods of

time (Porreca and Mattei, 2010; Porreca et al., 2009; Roberts et al., 2011; Snowball and Thompson, 1988). Thus, if greigite can be preserved in environments such as soils, rocks and sediment, they may provide information regarding the history, properties and behavior of the geomagnetic field (Roberts, 1995; Roberts et al., 2011).

The magnetic properties of Fe_3S_4 have been characterized using several techniques including Mössbauer spectroscopy (Lin et al., 2014), ferromagnetic resonance (FMR) spectroscopy (Chang et al., 2012b) and superconducting quantum interference device (SQUID) magnetometry (Feng et al., 2013). Neutron powder diffraction and polarized neutron diffraction also demonstrated that Fe_3S_4 has a collinear ferrimagnetic structure with antiferromagnetic coupling between Fe ions in tetrahedral and octahedral sites (Chang et al., 2009a) (see Figure 1.16). However, to date, there are only two published studies reporting on application of XMCD to characterize magnetic structures of Fe_3S_4 (Chang et al., 2012a; Letard et al., 2005).

Figure 1.18 A presents one XAS and XMCD study on Fe_3S_4 nanoparticles reported by Chang et al. (2012a). For the XAS spectrum, two main bands are also observed due to the spin-orbit splitting of the Fe 2p core level into the L_3 ($2p_{3/2}$) and L_2 ($2p_{1/2}$) components, which is similar to that of Fe_3O_4. However, a two-peak feature with an energy separation of 1.5 eV in the L_3 energy region was also observed. This is not consistent with the spectrum of Fe_3O_4, which only shows one peak in the L_3 region. Chang et al. (Chang et al., 2012a) attributed the high-energy peak in the XAS spectrum to the presence of a non-magnetic, oxidized layer on the Fe_3S_4 crystal surface, which dominated the Fe $L_{2,3}$ XAS signal as the surface-sensitive TEY (total-electron-yield) detection mode was used to acquire XAS spectra in their study. Recently, Bauer et al. (Bauer et al., 2014) reported a different Fe $L_{2,3}$ XAS spectrum of Fe_3S_4, which only showed

a single peak in the L_3 region and shared similar features as Fe metal (**Figure 1.18B**). In XMCD

spectrum of Fe_3S_4 reported by (Chang et al., 2012a), as shown in Figure 1.18A, it is significantly

different from the XMCD spectrum of Fe_3O_4 which shows three characteristic peaks in the L_3

region (Goering et al., 2007). Chang et al. (2012a) reported that the experimental XMCD

spectrum of Fe_3S_4 can be fit well only by using O_h Fe^{2+} and O_h Fe^{3+} peaks obtained by multiplet

calculations, but without using a calculated T_d Fe^{3+} peak. However, neutron diffraction patterns

indicated that the same Fe_3S_4 sample (Chang et al., 2012a) had almost full Fe occupancy (Chang

et al., 2009a). This literature survey shows that, Fe_3S_4 is a complicated system whose electronic

and magnetic structure is highly complex and not understood well.
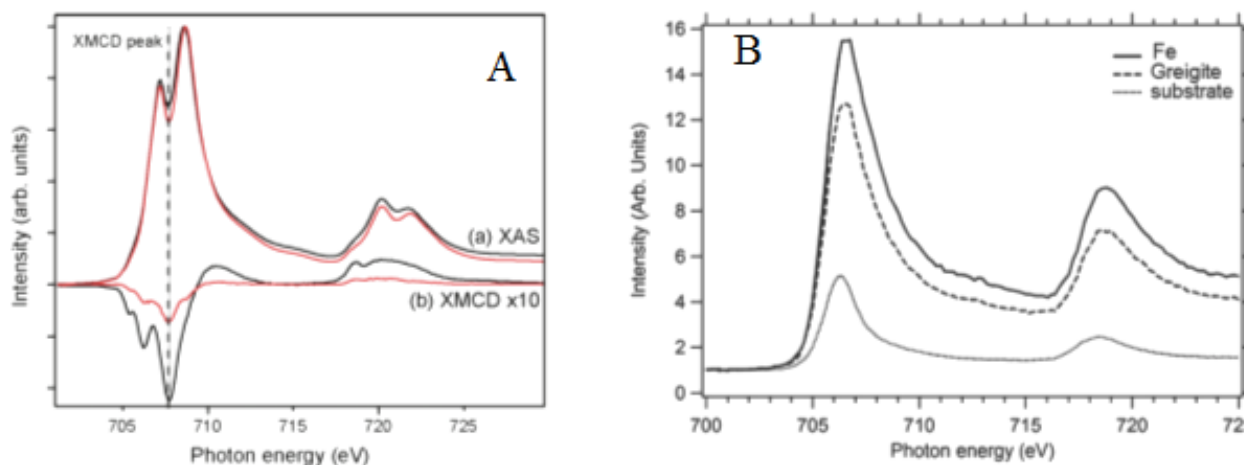
Figure 1.18 Comparison of published Fe $L_{2,3}$ XAS and XMCD spectra of Fe_3S_4. (A): Fe $L_{2,3}$
XAS and XMCD spectra of fresh natural and synthetic Fe_3S_4; (Chang et al., 2009b); (B): Fe
$L_{2,3}$ XAS spectra of Fe_3S_4 and Fe;(Bauer et al., 2014).

1.5 Outline of the thesis

Chapter 2 describes the principles of synchrotron radiation and the technique of scanning transmission X-ray microscopy (STXM), including its principles, instrumentation, performance, etc. Chapter 2 concludes with a description of ptychography, an emerging coherent diffraction based imaging technique. The instrumentation, reconstruction algorithm and current status are covered.

Chapter 3 describes the methods used for preparing MTB samples, performing STXM and STXM-XMCD measurements, and data analysis.

Chapter 4 presents results of a spectroscopic study on biogenic and abiogenic Fe_3O_4. The goal of this project is to clarify the confusion existing in the literature as to the correct Fe $L_{2,3}$ X-ray absorption spectra of magnetite and maghemite. We used STXM, powder X-ray diffraction and chemical modification to show that magnetosomes extracted from MV-1 are stoichiometric magnetite while as-received synthetic nano-magnetite was partly oxidized, with a powder pattern closer to that of γ-Fe_2O_3 than that of Fe_3O_4. Our results suggest that one of the reasons for differing literature XAS spectra of Fe_3O_4 and γ-Fe_2O_3 is due to differences in the samples. This chapter is presented in as-published format (Chapter 4: X.Zhu, S.S.Kalirai, A.P.Hitchcock, D.A.Bazylinski, Journal of Electron Spectroscopy and Related Phenomena, 2015, 199, 19-26).

Chapter 5 presents results of chemical and magnetic study of Fe_3S_4 magnetosomes in multicellular magnetotactic prokaryotes by STXM. We first measured XAS and XMCD spectra of Fe_3S_4 nanoparticles synthesized via hydrothermal method. We showed that, although the XAS spectra of abiotic Fe_3S_4 nanoparticles and biotic magnetosome Fe_3S_4 crystals in MMPs are slightly different, the XMCD spectra of these two types of Fe_3S_4 were in good agreement, indicating that the Fe_3S_4 crystals in magnetosomes biomineralized by MMPs are close to

stoichiometric. In addition, two other sulfur species, sulfate and sulfide, were also identified in

MMPs, both of which are likely involved in sulfur metabolism in MMPs.

Chapter 6 presents the results of a study of the cell division mechanism in MV-1 cells. This

project is built on the Master thesis work of S. Kalirai (Kalirai et al., 2013), which reported

anomalous magnetic orientations of magnetosome sub-chains in a single MV-1 MTB cell. We

first observed a couple of MV-1 cells with a single flagellum on each of two opposite ends,

indicating it is in the division state. Magnetic reversal of magnetosome sub-chains was observed

in this cell. We then performed XMCD mapping on MV-1 cells which were extracted from

culture medium at different time intervals and thus were at different growth states. In a sampling

of 110 cells, only ~ 2% cells have magnetically reversed magnetosome sub-chains. Based on

these results, a mechanism of how parent MV-1 pass on magnetic polarities to their daughter

cells is proposed.

Chapter 7 presents results of spectro-ptychograhy studies of extracellular and intracellular

magnetosomes in MV-1 cells. The high spatial resolution (7 nm) achieved with spectro-

ptychography allowed visualization and measurement of the Fe 2p spectra of precursor-like and

immature magnetosome phases in an intact MV-1 cell. A model for the pathway of

magnetosome biomineralization for MV-1 is proposed. In addition, The Fe L_3 XAS and XMCD

spectra of individual magnetosomes were obtained with ptychographic modulus and phase mode.

Chapter 8 summarizes the results and significant contributions of this thesis. It also gives

suggestions for future work.

Chapter 2

Methods

Chapter 2 describes the principles of synchrotron radiation and the technique of scanning transmission X-ray microscopy (STXM), including its principles, instrumentation, performance, etc. Chapter 2 includes a description of ptychography, an emerging coherent diffraction based imaging technique, which provides much improved spatial resolution. The instrumentation, reconstruction algorithm and current status are covered.

2.1 Synchrotron radiation

Synchrotron radiation refers to a phenomenon in which relativistic charged particles emit electromagnetic radiation when accelerated along curved paths by external magnetic fields (Balerna and Mobilio, 2015). Due to its unique characteristics, synchrotron radiation has become one of the most powerful techniques for investigating matter at the molecular and atomic level. Typically, a synchrotron facility consists of the main components (Willmott, 2011) shown in **Figure 2.1**. These are the vacuum system (metal pipe), injection system (e.g. a electron source, a low energy linear accelerator and a booster synchrotron), bending magnets (BM), quardupole, hexapole and other steering magnets, a radiofrequency cavity, insertion devices, beam position monitors and beam controls (Riekel et al., 2009). Briefly, an electron source, such as a heated filament in an electron gun or a photocathode, emits electrons which are then accelerated by microtrons or linear accelerators (linac). The electrons are injected into a booster ring in which they are further accelerated and finally injected into a storage ring. There are several bending

magnets per arc sections in the ring which are used to modify the trajectory of electrons and

force them to move in a closed path. For example, the Advanced Light Source (ALS) uses a

triple bend achromat design (3 BM/sector) while the Canadian Light Source (CLS) uses a double

bend achromat design (2 BM/sector). In addition, insertion devices (ID) such as wigglers and

undulators, which are placed in the straight sections between bending magnets along the orbit,

are used to provide brighter radiation. Brightness is defined as the number of photons per unit

time (second), per unit source size (mm^2), per unit angular divergence ($mrad^2$) in a given energy

bandwidth (0.1% of E) (Weckert, 2015). Both BM and ID produce radiation, but bending-

magnet radiation is significant lower in brightness than radiation produced by insertion devices.

In part this is because undulators concentrate all the radiation into a few narrow, intense peaks

(with an energy and polarization controlled by the physical structure of the undulator), while

bend magnets give a continuous distribution over a very wide energy range. Due to the emission

of radiation, the electrons lose energy which needs to be compensated by a radiofrequency (RF)

cavity where an electromagnetic field acts in synchronism with the arrival of electrons and

boosts the energy of the electrons every time they pass through the RF cavity. Finally, the

synchrotron radiation emitted from insertion devices and bending magnets travels downstream

along evacuated metallic pipes, called beamlines. A beamline usually consists of gratings,

mirrors, slits, etc., which are optimized for a specific photon energy range and type of

experimental technique (diffraction, spectroscopy, microscopy, crystallography, etc).

Experimental end stations, such as diffractometers or microscopes are attached at the end of the

beamline (Willmott, 2011)
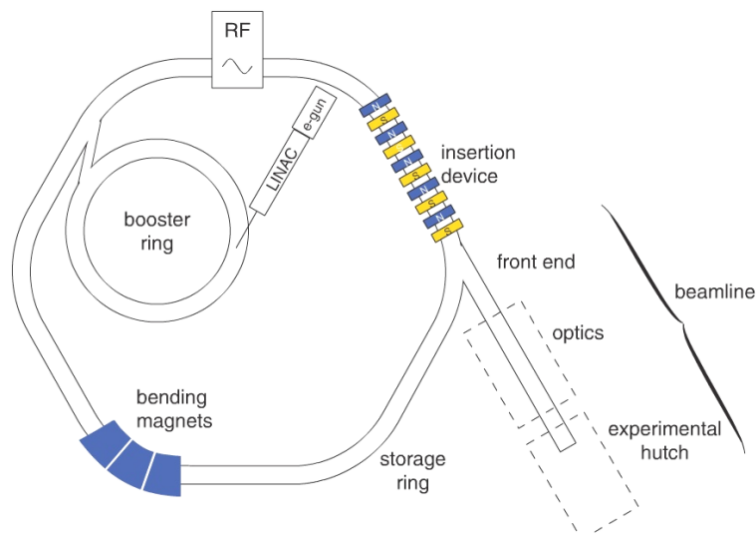
Figure 2.1 Schematic of the main components of a modern synchrotron source. Figure reproduced from Willmott (Willmott, 2011) with permission from *John Willey & Sons*.

2.1.1 Properties of synchrotron radiation

Although any charged particle which is accelerated (increase in speed, or moving in a curved path at a constant speed) will emit electromagnetic radiation, the property of the emitted radiation largely depends on the velocity of the particle. If the electron moves at a velocity (v) much smaller than the speed of light (*c*), v $<<c$, the emitted radiation has a dipole distribution with a frequency comparable to the angular frequency (*w*) of the electron (see **Figure 2.2a**). However, in the case of high kinetic energy particles where the electron speed (v) approaches the speed of light (e.g. v $\leq c$, relativistic condition), the radiation pattern is compressed into a narrow cone in the forward direction, with a larger frequency on the order of $\gamma^3 w$ due to relativistic effects, as shown in **Figure 2.2b**. γ is the Lorentz factor:

$$\gamma = \frac{E}{mc^2} \tag{2.1}$$
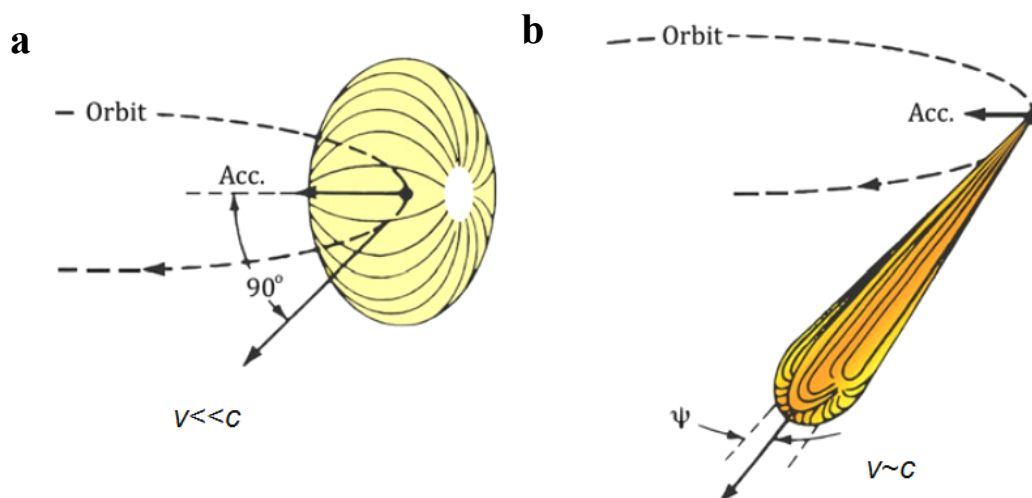
Figure 2.2 Qualitative radiation patterns related to charged particles moving in a circular orbit. The dipole pattern achieved for slow particles (Figure 2.2a) *(v << c)* is distorted into a narrow cone when v~c (Figure 2.2b) Figure reproduced from Balerna et al. (Balerna and Mobilio, 2015) with permission from *Springer*.

where mc^2 is the rest mass energy of electron, equal to 511 keV, and E is the kenetic energy of electron. Thus, γ can be rewritten as:

$$\gamma = 1957 \cdot E \ (GeV) \tag{2.2}$$

In addition, the half-opening angle of the narrow radiation cone, ψ, in Figure 2.1b is given by:

$$\psi \approx \frac{mc^2}{E} \approx \gamma^{-1} \tag{2.3}$$

For example, for a synchrotron storage ring with an energy of 1 GeV, ψ is roughly equal to 0.5 mrad (0.029º). Synchrotron radiation is highly collimated, and increasingly so as the ring energy increases (ALS operates at 1.9 GeV, CLS operates at 2.9 GeV). Compared with other natural and laboratory-based light sources, synchrotron radiation has many advantages such as:

(1). High brightness. For example, for an undulator-based synchrotron source, the brightness can reach larger than 10^{18} photons/s/mm^2/mrad^2/0.1%BW while it is only 10^8~10^{10}

photons/s/mm^2/mrad^2/0.1%BW for a typical X-ray tube (Nuhn, 2004). Note that lab sources

are typically single line in the hard X-ray region so they can not be used to perform

spectroscopy.

(2). High collimation, i.e. narrow angular distribution of the beam

(3). High degree of linear polarization from BM and also, pure linear, circular and elliptical

polarized X-rays with controllable directions from suitable insertion devices.

(4). Broad and continuous range of photon energies from infrared to hard x-ray region.

(5). Pulsed photon emission with pulse widths of $10 - 100$ ps, which allows for study on

dynamic processes with similar temporal scale.

2.2 Beamline instrumentation

The schematic diagram and photos of beamline 10ID-1 (Spectromicroscopy (SM)

beamline) at Canadian Light Source (CLS) are shown in **Figure 2.3** (Kaznatcheev et al., 2007).

At this beamline, the X-rays are generated by an Apple II type elliptically polarized undulator

(EPU), which consists of four magnet assemblies (**Figure 2.4**). By moving the girders holding

the magnet arrays relative to each other, the magnetic field is varied and radiation with various

polarizations can be generated. One particular feature of the EPU at CLS BL10ID1 is that it can

deliver 100% linearly polarized light with an orientation from -90° to 90° relative to horizontal,

which allows one to easily control the angular relationship between the electric field of X-rays

and the sample. In addition it can produce left and right circular polarized light, which makes it a

suitable tool to study magnetic structures in magnetotactic bacteria (MTB) by means of X-ray

magnetic circular dichroism (XMCD).
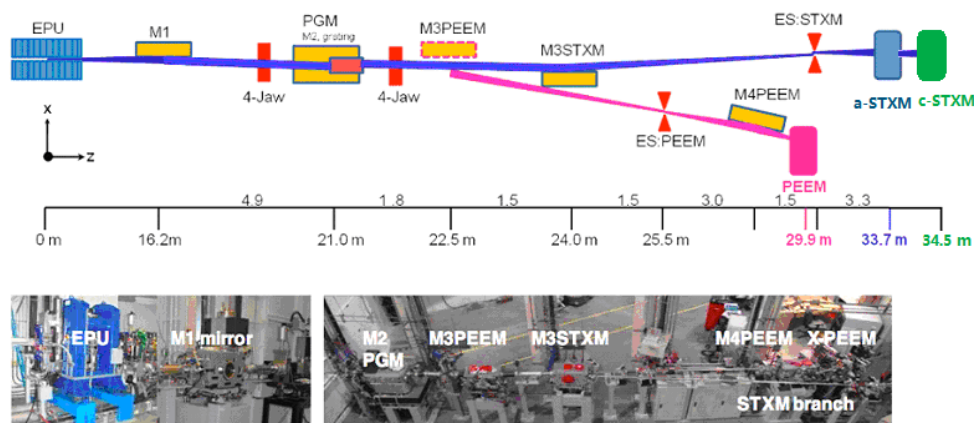
Figure 2.3 Schematic diagram (top) and photos (bottom) of 10ID-1 beamline at CLS.
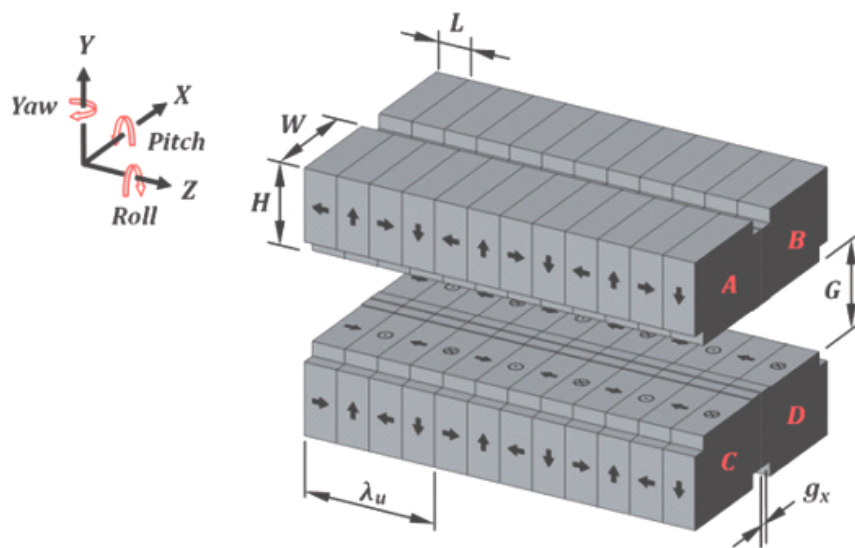
Figure 2.4 Schematic diagram of Apple II EPU. Figure reproduced from Chang et al. (Chang et al., 2012c) with permission from *Taylor & Francis*.

X-rays emitted from the EPU impinge on the M1 mirror inside a radiation protection hutch which deflects the beam horizontally. A plane grating monochromator (PGM) is used to monochromate the synchrotron radiation, which disperses the soft X-rays (100~3000 eV) vertically with a resolving power between ~3000 to ~10,000, depending on the size of the

45

vertical exit slit. After the PGM, the beamline has two slower diverging paths: one leading to a toroidal mirror, an exit slit, and the two scanning transmission X-ray microscope (STXM) endstations; and the other one leading to a toroidal mirror, exit slit, a refocusing ellipsoidal mirror and then into a commercial photoemission electron microscope (PEEM). The M3STXM mirror which directs the beam into the STXM branch is fixed, while M3PEEM, which deflects the beam into the PEEM branch, can be moved in or out of the beam.

2.3 *Scanning transmission X-ray microscopy (STXM)*

Scanning transmission X-ray microscopy (STXM) is a synchrotron-based technique which is able to identify and quantitate electronic, chemical and magnetic structures of samples at a high spatial resolution. The primary contrast mechanism is near edge X-ray absorption fine structure (NEXAFS) spectra (Hitchcock, 2015) of the chemical or magnetic components of the sample. Compared with non-spatially resolved spectroscopies and other spectromicroscopies, STXM has many advantages including good spatial resolution, high sensitivity to chemical structure, high energy (spectral) resolution and radiation damage that is ~ 100-fold less than the directly comparable technique of core level electron energy loss spectroscopy in a transmission electron microscope (TEM) (Wang et al., 2009). This makes STXM a suitable tool to study biogeochemical and environmental samples (Hitchcock et al., 2012; Lawrence et al., 2012; Rema et al., 2014) as well as radiation-sensitive nanostructures (Zhu et al., 2015b). With the advent of elliptically polarizing undulators (EPU) in modern synchrotron facilities, linearly, left and right circularly polarized light can be generated by adjusting the relative positions of rows of magnets in the EPU. The CLS-SM EPU is particularly powerful since all four quandrants can be translated (most EPUs only provide for moving 2 of the 4 quadrants), which gives greater

flexibility in setting the polarization of the light (Kaznatcheev et al 2007) This makes the

XMCD measurement convenient since one can keep the sample fixed and easily alternate the

two circular polarizations with the EPU.

XMCD measured with STXM has been successfully applied as a tool to study chemistry,

magnetism, and biomineralization mechanism of magnetotactic bacteria on an individual

magnetosome basis (Kalirai et al., 2013, 2012; Lam et al., 2010). In this thesis, I have used

STXMs from three beamlines, beamline 10ID-1 at the Canadian Light Source (CLS) in

Saskatoon, and beamlines 5.3.2.1. and 11.0.2 at the Advanced Light Source (ALS) in Berkeley,

to study magnetotactic bacteria.

2.3.1 STXM principles

Figure 2.5 shows a schematic of STXM, in which the monochromated X-rays generated

by bending magnet or insertion devices are focused to a spot (30~50 nm) on the sample by a

Fresnel zone plate. An image at each photon energy is generated by raster scanning the region of

interest of the sample through the X-ray focal spot while detecting the transmitted intensity in

single photon counting mode, using a phosphor to convert soft X-rays to visible light followed

by detection of the visible light using a high performance photomultiplier detector. Spectral data

are acquired by collecting a sequence of images over the energy range of interest. The image

sequences are also called a "stack" and was first implemented by Jacobsen et al. (2000).

As a zone plate based imaging technique, the spatial resolution of STXM depends on the illumination, numerical aperture (NA) of the zone plate, and the nature and thus contrast of the object (Chao et al., 2009). The zone plate (ZP) is the key component for STXM imaging. A ZP is a circular diffraction grating, which is capable of focusing the incident beam to a point. It consists of a series of concentric metal rings (typically gold or nickel) alternating with transparent circular slots mounted on a thin soft X-ray transparent substrate such as Si_3N_4, as shown in **Figure 2.6**. According to the trigonometry shown in Figure 2.6 (left), the interference condition of a zone plate is given by:

$$f^2 + r_n^2 = (f + \frac{mn\lambda}{2})^2 \tag{2.4}$$

where f is the focal length, n is the zone number, r_n is the radius of the nth zone, m is the diffraction order ($m=0, \pm1, \pm2, \pm3, \dots$) and λ is the wavelength of the X-rays being focused. Since zero order ($m=0$) light is un-diffracted while the first order light is the most intense
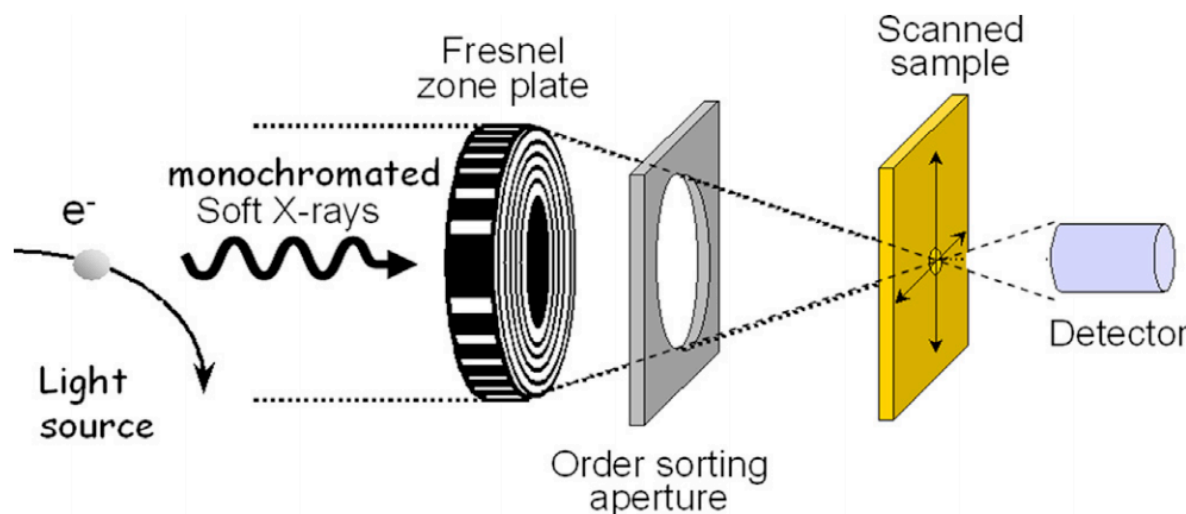
Figure 2.5 Schematic diagram of STXM microscope. Figure reproduced from Hitchcock et al. (Hitchcock et al., 2014) with permission from *Elsevier*.

diffracted light (~10-15 % of the total flux), an order-sorting aperture (OSA), typically 50-90 μm

in diameter, and a central stop centered on the ZP structure are used to isolate the first order

light, block zero order light, and reduce contributions from other higher order diffracted light

(see Figure 2.6, right).
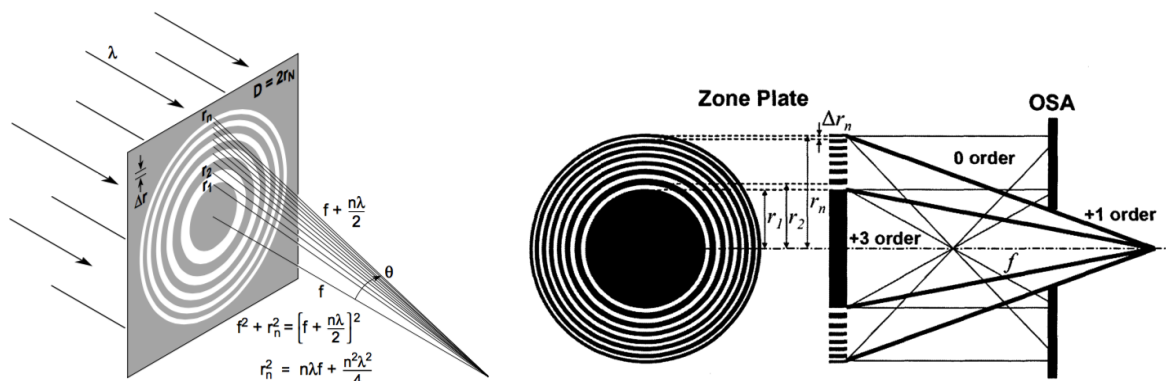
Figure 2.6 Schematic presentation of principles of zone plate. Left: A Fresnel zone plate lens with plane wave illumination, showing only the convergent (+1st) order of diffraction; Right: Schematic geometry of a zone plate and the focusing scheme of a STXM with a plane wave illumination of X-rays. (OSA: order sorting aperture). Figures reproduced from Attwood (Attwood, 1999).

Since only the first order diffracted light (m=+1) is used in most STXM measurements, equation 2.4 can be simplified to:

$$r_n^2 = \frac{\lambda^2 n^2}{4} + fn\lambda \approx fn\lambda \; (f \gg n\lambda) \tag{2.5}$$

and the focal length can be written as:

$$f = \frac{r_n^2}{n\lambda} \tag{2.6}$$

Because each zone in a ZP has equal area, the number of zones, n, can be calculated by:

$$n = \frac{\pi r_n^2}{2\pi r_n \cdot \Delta r_n} = \frac{r_n}{2\Delta r_n} \; (\Delta r_n = r_n\text{-}r_{n\text{-}1}) \tag{2.7}$$

Thus, equation 2.6 converts to:

$$f = \frac{2r_n \Delta r_n}{\lambda} \qquad (2.8)$$

Equation 2.8 shows that the focal length, f, is inversely proportionally to the wavelength of the

beam (λ) and thus linearly proportionally to the photon energy. This means, the ZP must move

upstream, away from the sample, as the photon energy increases.

The numerical aperture (NA) is defined as (Attwood, 1999):

$$NA = \frac{r_n}{f} = \frac{\lambda}{2\Delta r_n} \qquad (2.9)$$

The spatial resolution of a ZP, δ, can be calculated according to the Rayleigh criterion:

$$\delta = 0.61 * \frac{\lambda}{NA} = 1.22 * \Delta r_n \qquad (2.10)$$

Therefore, the diffraction-limited spatial resolution of a ZP is largely determined by its outer

zone width, although the alignment of the ZP relative to the X-ray beam, higher order diffraction

terms, and zone plate quality also play a role. With smaller outer zone width, a better spatial

resolution can be achieved in principle. The ZP should be sufficiently thick to provide reasonable

efficiency at the photon energy of interest (Sakdinawat and Attwood, 2010). The aspect ratio,

the ratio of zone thickness to the smallest lateral structural size, dramatically increases with

smaller outer zone width, which makes nanofabrication increasingly difficult. For a ZP to work

properly each zone has to be positioned with an accuracy of 1/3rd of the wavelength. Thus for a

240 μm diameter zone plate with 20 nm outer zone widths, the precision of placement of the

outer zone across the width of the zone plate (240 μm) has to be 0.2 nm at a photon energy of

2400 eV ($\lambda = 0.5$ nm) or 1 part in 10^6. Although the best spatial resolution of zone plate imaging

reported is 10 nm (Chao et al., 2012, 2009; Sakdinawat and Attwood, 2010) , in fact there are

very few examples of zone plates with less than 20 nm outer zone width. Recently ptychography,

a new coherent diffraction technique, is attracting more and more attention because it is not
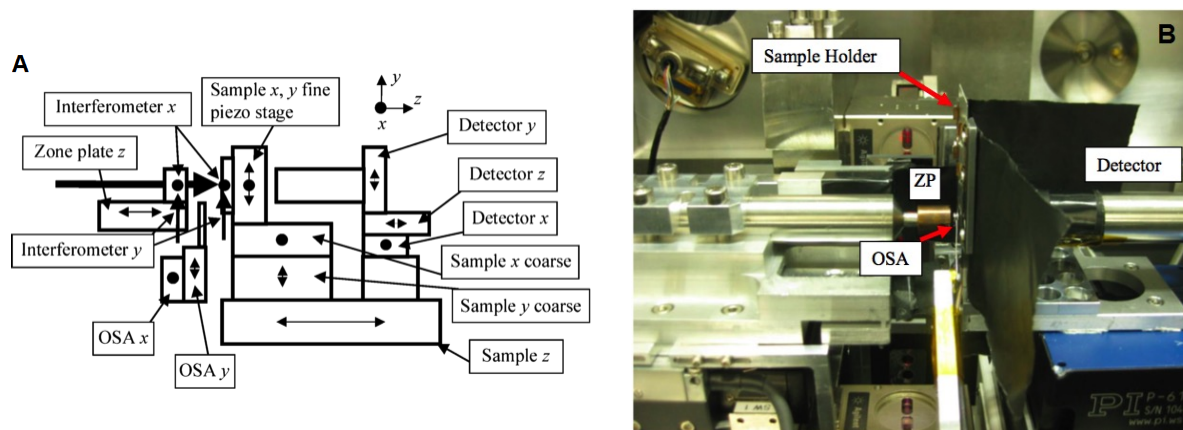
Figure 2.7 A. Schematic of the 5.3.2 STXM components. B. Layout of ZP, OSA, sample holder, and detector at the ambient STXM at CLS beamline 10ID1. Figure A reproduced from Kilcoyne et al. (2003). Figure B: Courtesy of 10ID-1 CLS STXM manual.

limited by the properties of the X-ray optics used. It is believed that ptychography has the potential to reach near atomic-scale spatial resolution with very short wavelength X-rays (Edo et al., 2013). The published record spatial resolution from ptychography is 3 nm at 1600 eV (Shapiro et al., 2014), with 2 nm at 1600 eV reported at a recent X-ray microscopy conference (Tyliszczak et al., 2014). Ptychography was also used in this thesis. It is described in section 2.4.

2.3.2 STXM instrumentation

Although the STXM microscopes located at beamlines 10ID-1 (CLS), 11.0.2 and 5.3.2.1 (ALS) are different, they share the same general features. **Figure 2.7A** is a schematic of the major STXM components including zone plate z stage, OSA x, y stages, sample x, y coarse stage, sample x, y fine piezo stage, sample z stage, detector x,y,z stage and interferometer system (Kilcoyne et al., 2003). **Figure 2.7B** shows a photograph of the ZP, OSA, sample holder and detector. Zone plates used in this thesis are provided by the Centre for X-ray Optics, Lawrence Berkeley National Lab. A zone plate with outer zone width of 25 nm, outer diameter of 240 µm

and 95 μm central stop is typically used, which provides a theoretical diffraction limited spatial

resolution of 31 nm. Note that the central stop is made sufficiently thick to block the X-rays over

the full photon energy range of the beamline (<0.1% transmission). The OSA is a thin metal

strip, which has a smaller diameter (usually 50 μm) than the diameter of the center stop

(typically 95 μm). By carefully aligning the OSA with the ZP, only first order diffraction light is

selected.

    While the ZP optics fundamentally limit the spatial resolution of STXM, many other

factors and parameters must be optimized to achieve the best possible resolution and

performance. These include beamline intensity, ring and beamline stability, precision of scanning

system, OSA position, ZP Z-scale calibration, sample focus, detector efficiency, accuracy of

energy scale, etc (Wang, 2008). Besides these factors, one of the critical aspects of STXM

measurements is how to stabilize the beam position as the ZP moves as a function of the photon

energy (Hitchcock, 2012). Deviations can arise from several sources including: misalignment of

the X-ray and ZP-z motion axes; misalignment of the interferometer mirrors; thermal drift; and

inadequate attachment of the sample to the sample support system. As shown in equation 2.8, the

focal length is linearly proportional to photon energy. When the energy is changed by 50 eV, the

width of a typical XAS spectrum, the ZP moves by several hundred microns. If the energy

changes from the carbon K edge (280 eV) to the iron $L_{2,3}$-edge (700 eV), the ZP moves by

several millimeters. However, in order to preserve the spatial resolution achieved at a single

photon energy, the alignment of the (X,Y) co-ordinates of the ZP (which determines the X-ray

beam position) and the sample must be kept much better than the size of the focused beam

(spatial resolution, 20~50 nm) (Tyliszczak and Chou, 2010). It is not possible to build a

mechanical stage which can scan 10-20 mm in one dimension, without there being significant

deviations in the two orthogonal directions (called run-out). During translations of a few mm, the

run-out can be in the order of several hundreds of nanometers (Kilcoyne et al., 2003). All of the

STXMs used in this thesis dramatically reduce this run-out by using a differential laser

interferometer feedback system to drive a fast scan piezoelectric stage to compensate for the ZP-

z stage run-out, and other factors such as thermal drift, and mechanical instabilities. The

interferometer system uses mirrors placed on the ZP and sample stages, carefully adjusted to

have their reflective surfaces parallel to the X-ray beam (see Figure 2.7A) (Kilcoyne et al.,

2003; Tyliszczak and Chou, 2010). The interferometer signal, which is read out at MHz rates, is

used as the feedback signal in an active control system which constantly adjusts the position of

the piezo fast scan sample stage to keep the desired position of the sample aligned with the

centre of the focused X-rays. The feedback system achieves a stabilization of better than 10 nm

over short times (see Figure 2.8). A positional stability of better than 50 nm can be achieved over

the full energy range of the ALS 5.3.2.2 beamline (150~1150 eV) (Kilcoyne et al., 2003).
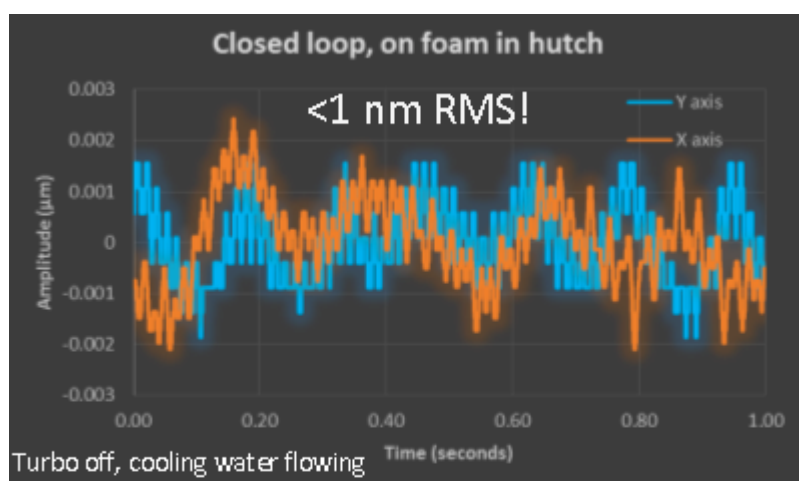
Figure 2.8 A stabilization of better than 5 nm in both X and Y axis over short time in the cryo-
STXM (in commissioning phase, as of Aug 2016). Courtesy of A. Leontowich and R.Berg.
Similar plot for ambient STXM has peak-to-peak excursions of ~10 nm.

The transmitted X-rays are converted to a burst of visible photons by a thin phosphor. The photon pulse is then detected using a high performance photomultiplier which, with associated electronics, can detect the X-rays in single event counting mode linearly up to 20 MHz. All threes beamlines can greatly exceed this intensity in the focused spot so it is essential when operating the beamline to reduce the exit slits to values which keep the signal at the most intense part of the energy range measured to less than 20 MHz.

2.4 Ptychography

Although synchrotron-based X-ray microscopy can routinely achieve a spatial resolution of a few tens of nanometers, the spatial resolution is limited by the quality of the image-forming optics, such as the zone plate in STXM. One of the approaches to address this issue is to perform coherent diffraction imaging (CDI), which does not rely on X-ray optics and holds promise for imaging with wavelength-limited resolution (Miao et al., 2012; Schroer et al., 2008). In CDI experiments, the transmission diffraction patterns, from a partially or fully coherent X-ray beam impinging on a sample, are measured and then reconstructed into high resolution images (Miao et al., 1999). A major challenge for all CDI methods is how to solve the phase problem because the phase information, unlike amplitude, can not be measured directly. Sayre (Sayre, 1952) once suggested that if the diffraction patterns can be sampled with enough precision, the phase information can be retrieved. This was later experimentally verified by Miao et al. (1999) who demonstrated that the phase shift when coherent X-rays scatter from a non-crystalline sample can be determined if the diffraction patterns are oversampled. In this work, Miao et al were able to reconstruct an images from the CDI signal with a spatial resolution of 75 nm using an iterative algorithm (Miao et al., 1997). However, there are still a few drawbacks with traditional CDI
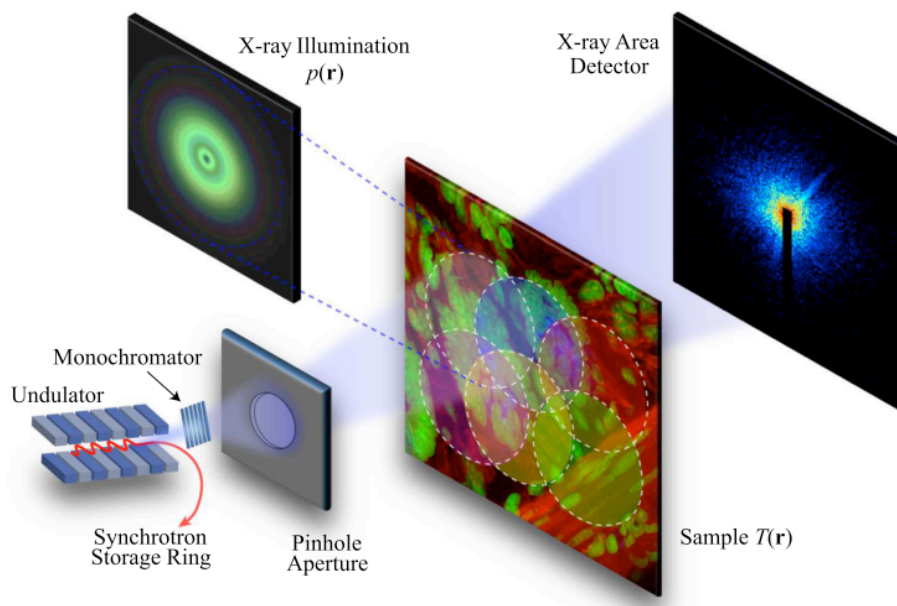
Figure 2.9 A. Schematic of a ptychographic measurement. An area X-ray detector is used to collect diffraction patterns while sample is scanned with overlapping illumination regions, represented by open circles in the figure (Tripathi et al., 2014).

techniques such as the requirement for sufficiently small and isolated sample to achieve oversampling (Thibault et al., 2009), difficulty in controlling the convergence of the reconstruction (Xiong et al., 2014), etc.

Ptychography is an emerging CDI technique (Thibault et al., 2014), in which coherent scattering patterns are measured from an array of spots in a region of interest. When the spots are chosen with sufficient spatial overlap, the complex-valued information of the sample can be retrieved from the the set of measured elastic scattering patterns with a ptychographical iterative algorithm (Thibault et al., 2014, 2008). **Figure 2.9** shows a schematic of the experimental setup of a ptychography measurement. An area X-ray detector, placed behind the sample, collects the diffraction patterns with high dynamic range. The beam or the sample is then raster scanned in a pattern which overlaps the sampled spots. There is no requirement for a small isolated object, as

is the case of other, non-ptychographic CDI techniques. More important, the overlapping regions

means there are multiple diffraction measurements sampling each region in the sample, which

greatly aids the reliability and speed of convergence of the image reconstruction and reduces

image artifacts (Tripathi et al., 2014). The substantial amount of overlap (typically 30-40%)

between different sampling spots can dramatically increase the success of reconstruction as it

requires the algorithm to find a solution where the phase and amplitude of the reconstructed

image must be the same in the overlapping parts of neighboring spots (Faulkner and Rodenburg,

2004; Guizar-Sicairos and Fienup, 2008).

In ptychography, the complex transmission function of the sample, $T(r)$ can be modeled

with the following approximation (Maiden et al., 2013):

$$T(r) = \exp\left[2\pi i(n(r)\text{-}1)t(r)/\lambda\right] \qquad (2.11)$$

where λ is the wavelength of the incident beam, *t(r)* is the sample thickness and *n* is the

complex-valued index of refraction. *n* can be written as:

$$n = 1 - \delta\text{-}i\beta \qquad (2.12)$$

where the real part δ is the phase and imaginary part β is the absorption term of the refraction

index. As pointed by Maiden et al. (2013), the phase contrast is proportional to $-\frac{2\pi\delta t}{\lambda}$ while the

natural log of the modulus image gives $-\frac{2\pi\beta t}{\lambda}$. Because the index of refraction, *n*, can be

determined in the reconstruction, one can quantitatively measure the phase and absorption

signals at the same time, as well as the phase and amplitude properties of the probe illumination

(Thibault et al., 2014).

Figure 2.10 presents recently published results from soft X-ray ptychography at the

Advanced Light Source (ALS) (Shapiro et al., 2014). **Figure 2.10A** and **Figure 2.10 B** present
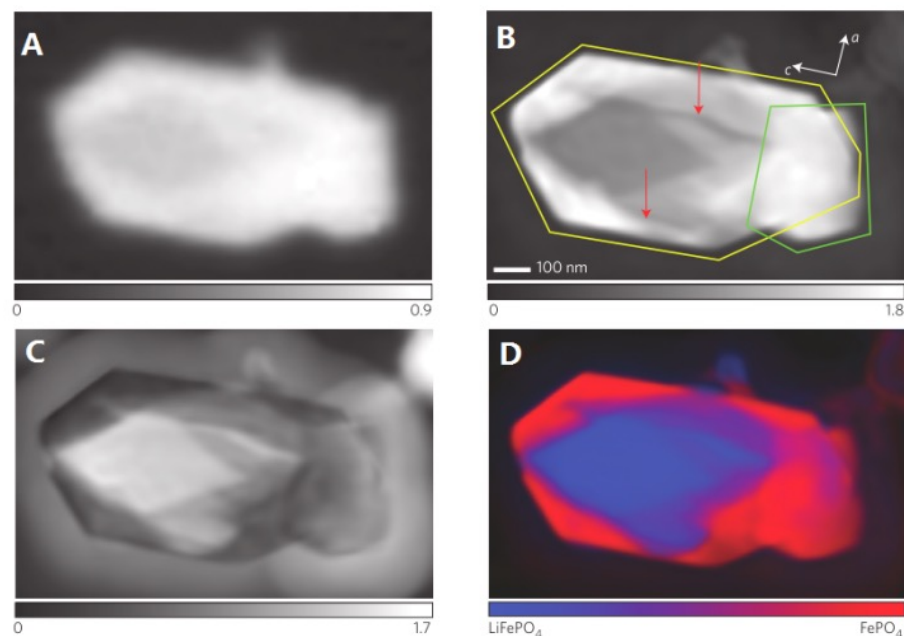
Figure 2.10 X-ray microscopy of partially delithiated LiFePO$_4$. A and B. Optical density maps from STXM (a) and ptychography (b) at 710 eV, showing maximum absorption contrast between the end members; C. Phase of the ptychographic reconstruction at 709.2 eV, showing maximum relative phase shift between the end members; D. Colourized composition map calculated by principal component analysis, clustering and singular value decomposition of the full complex refractive index. Figures reproduced from (Shapiro et al., 2014) with permission from *Nature Publishing Group (NPG)*.

conventional STXM and ptychography images of partially delithiated LiFeO$_4$ at 710 eV, respectively. Whereas STXM can only resolve the general shape of the particle, the ptychography image clearly shows cracks (red arrow) along the crystallographic axis c. **Figure 2.10C** presents the ptychography phase image of the same particle at 709.2 eV. **Figure 2.10D** shows a color coded composite of the component maps of LiFeO$_4$ (red) and FeO$_4$ (blue), which were derived by fitting the ptychographic Fe L$_3$ spectra with principal component analysis and singular value decomposition methods. Both the phase and amplitude components were used in

the analysis which effectively modeled the full X-ray - sample interaction, including the spatial

distribution of the illumination probe which is also generated in ptychography. The data was

recorded using a zone plate with outer zone width of 60 nm and achieved a spatial resolution of

the chemical component maps of ~18 nm, nearly an order of magnitude smaller than the spot

size (150 nm). With such high spatial resolution, the delithiation mechanism can be visualized in

fine details. The results showed that $LiFeO_4$ and FeO_4 coexist in small plates and suggests the

lithation/ delithiation processes probably occur in two steps. (Shapiro et al., 2014).

In a recent study, our group showed that ptychography can also be applied to image

intracellular magnetosomes and probe magnetic structures in individual MTB cells, as shown in

Figure 2.11 (Hitchcock, 2015). **Figure 2.11A** presents a conventional STXM optical density

image of two MV-1 MTB cells at 710 eV. **Figure 2.11B** shows the ptychography absorption

image of the magnetosome chain in a horizontal cell (indicated with a pink rectangle in Figure

2.11A. This image was measured at 708.2 eV where the XMCD signal is the strongest. Its spatial

resolution is estimated to be around 7 nm (Zhu et al., 2016), which allows for better visualization

of the gaps between magnetosomes (white arrow), and magnetosomes with various sizes. A

major outcome of my thesis work is to demonstrate this capability, which has tremendous

potential to lead to a better understanding of how magnetosomes are biomineralized in MTB

cells, as discussed in detail in chapter 7. **Figure 2.11C** presents the color coded composite of the

XMCD signal obtained by taking the difference between two ptychography modulus images

recorded with left and right circularly polarized lights, at 708.2 eV. The red and blue means

opposite magnetic polarities of magnetosomes. This is consistent with our previous study which

showed that, some magnetosome sub-chains in a single MTB cell have magnetic moments

pointing in opposite directions (Kalirai et al., 2013). It also showed that the biomagnetism in
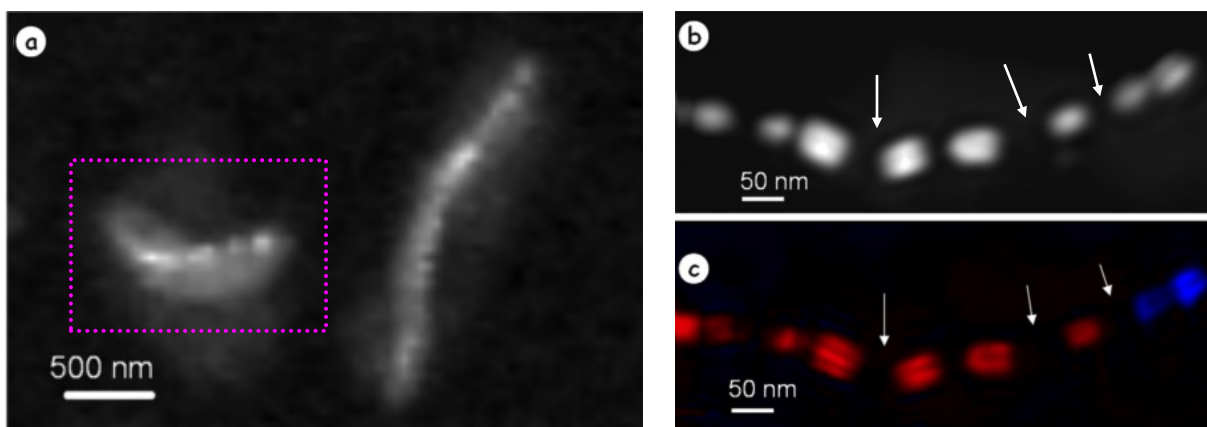
Figure 2.11 Conventional STXM and ptychography images of MV-1 cells. (A). Conventional STXM image of several MV-1 cells measured at 710 eV. The ptychography measurements were made on the intact cell indicated by the pink rectangular; (B). The ptychography absorption image of magnetosome chain at 708.2eV. The gaps are indicated by white arrows; (C). Magnetic map at 708.2 eV of the magnetosomes in this cell from single energy X-ray magnetic circular dichroism (XMCD)—the difference of ptychography OD images measured at 708.2 eV with the photon spin parallel and anti-parallel to the magnetic moment. There are gaps in the chain (white arrows) and the orientation of the magnetic vector is opposite on each side of the right most gap. The uneven distribution of intensity within individual magnetosomes is an artefact of the ptychographic data processing; Figures reproduced from Hitchcock (Hitchcock, 2015) with permission from *Elsevier*.

MTB cells can be probed with soft X-ray spectro-ptychography. Therefore, we launched a project that measures XMCD spectra from magnetosomes via ptychography, with the aim of probing biomineralization mechanism and magnetic properties of MTB simultaneously with high spatial resolution. This will be covered in chapter 7 in this thesis.

2.4.1. Ptychographic Iterative Engine

Ptychographic iterative engine (PIE) refers to a phase retrieval algorithm proposed by

Rodenburg and Faulkner (2004), which uses the redundant information of overlapping

diffraction patterns to retrieve the amplitude and phase of both object and the illumination probe.

Figure 2.12 presents a schematic for the PIE algorithm for data recorded at *N* different

illumination positions.
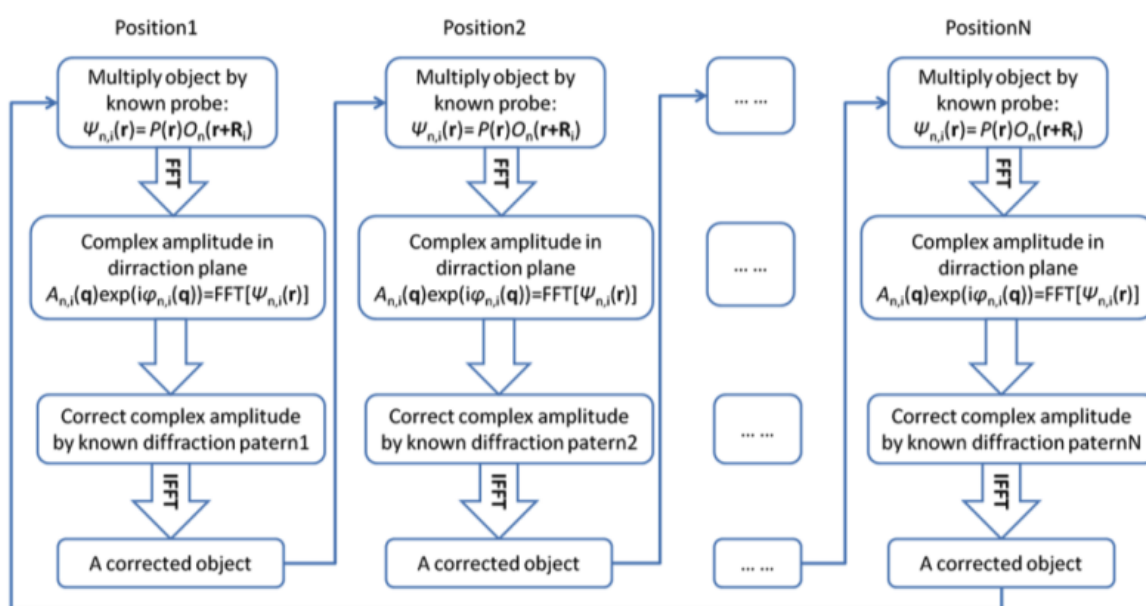
Figure 2.12 Flow chart of PIE algorithm for data recorded at *N* illumination positions. Figure
produced from Wang et al. (2013) with permission from *The International Society
of Optics and Photonics (SPIE)*.

As shown in Figure 2.12, the PIE algorithm generally works by executing the following

steps (Rodenburg and Faulkner, 2004):

1. It starts with an arbitrary guess at the object function $O_{g,n}$ (r), where *g* indicates it is a

    guessed function and *n* represents the *n*th iteration of the algorithm;

2. It assume the illumination probe $P(r)$ is known and the object function $O_{g,n}$ (r) and

    illumination probe $P(r)$ are positioned relatively to each other by a distance R. Then, the

    exit wave function can be produced by multiplying the object function with the

    illumination function:

$$\psi_{g,n}(r, R) = O_{g,n}(r)\, P(r\text{-}R) \tag{2.13}$$

3. Since the data is collected by an area detector in the diffraction plane, which is related to

    the object plane by a Fourier transform, the wave function in the diffraction plane can be

    obtained as:

$$\Psi_{g,n}(k, R) = \mathcal{F}[\psi_{g,n}(r, R)] \tag{2.14}$$

4. Next, the wave function in the diffraction plane can be rewritten as a function of

    amplitude and phase:

$$\Psi_{g,n}(k, R) = \left|\Psi_{g,n}(k, R)\right| e^{-i\theta_{g,n}(k,R)} \tag{2.15}$$

    where $\left|\Psi_{g,n}(k, R)\right|$ is the amplitude and $\theta_{g,n}(k, R)$ is the phase in the diffraction space at

    iteration n.

5. Because the amplitude of diffraction patterns, unlike phase, can be measured directly, the

    guessed amplitude in the diffraction plane can be replaced by the measured diffraction

    patterns, which gives a corrected wave function in the diffraction space:

$$\Psi_{c,n}(k, R) = \left|\Psi_{g,n}(k, R)\right| e^{-i\theta_{g,n}(k,R)} \tag{2.16}$$

6. An improved guess for the exit wave function can be obtained by inverse Fourier

    transform:

$$\psi_{c,n}(r, R) = \mathcal{F}^{-1}[\psi_{c,n}(k, R)] \tag{2.17}$$

7. Using the following update function, the object function can be updated:

$$O_{g,n+1}(r) = O_{g,n}(r) + \frac{|P(r\text{-}R)|}{|P_{max}(r\text{-}R)|}\frac{P^*(r\text{-}R)}{(|P(r\text{-}R)|^2 + \alpha)}$$

$$\times \beta(\psi_{c,n}(r,R)\text{-}\psi_{g,n}(r,R)) \tag{2.18}$$

where $P_{max}(r\text{-}R)$ is the maximum value of amplitude of $P(r)$, α and β are constants. α is used to prevent the denominator to be zero if $|P(r\text{-}R)|=0$ and β is the feedback parameter in the algorithm. Lower β increases the importance of the newest estimate of the objection function, while higher β values increase the importance of previous estimates. β can vary between 0.5~1 (Rodenburg and Faulkner, 2004)

8. Move to the next position, for which the illumination pattern partly overlaps with a previous position

9. Repeat previous steps (2~7) for all the sample positions. Sum squared error (SSE) is usually used to measure the convergence, which compares the measured amplitude with the calculated ones in the diffraction plane:

$$SSE = \frac{|\Psi(k,R)|^2\text{-}\left|\Psi_g(k,R)\right|^2}{N}$$

where N is the number of pixels in the array representing the wave function (Faulkner and Rodenburg, 2005).

As shown in Figure 2.10, PIE requires the algorithm to loop through all the illumination positions, from position 1 to position N, for one entire iteration and then repeat for other iterations until the image is reconstructed with satisfactory quality. Typically, multiple graphical processing units (GPU) on a host with adequate memory can efficiently carry out the reconstructions. For example, at ALS beamline 5.3.2.1, the nanosurveyor instrument is able to reconstruct the ptychography data in quasi-real time i.e., 1 s/μm^2 for data pre-processing time and 1.6 s/μm^2 for GPU reconstruction time.

Chapter 3

Experimental

Chapter 3 describes: the methods used to prepare MTB samples for STXM studies, detailed procedures for performing STXM and STXM-XMCD measurements, and how the resulting data was analyzed.

3.1 Magnetotactic bacterial samples

3.1.1 Sample sources

In the course of this thesis, both cultured and environmental MTB cells have been investigated. North-seeking MV-1 and BW-1 samples were provided by Professor Dennis Bazylinski from University of Las Vegas, Nevada. South-seeking MV-1 and MMP samples were provided by Professor Ulysses Lins and his graduate student, Pedro Leão, from Universidade Federal do Rio de Janeiro.

MTB samples were also collected from a local area, Cootes Paradise, in Hamilton, where bottles containing sediment and water were collected and brought to the lab for further study (**Figure 3.1**).

Figure 3.1 Collection of MTB from local environment. Left: The water area of Cootes Paradise.; Right: A clear glass bottle containing a sediment and water sample collected from Cootes Paradise.

In this project, a method called "capillary racetrack" was used to isolate MTB cells from crude sediment (Wolfe et al., 1987). Generally, the procedure of capillary racetrack involves the following steps (Oestreicher et al., 2012):

(1). One end of the capillary tube was sealed by Bunsen burner.

(2). Wetted cotton was plugged into the one-end-sealed capillary tube

(3). Environmental solution sampled from the area 1-2 cm above the sediment was added into the capillary tube.

(4). South pole of a stirring-bar magnet was placed at the closed end of the capillary.

Thus, MTB cells migrated quickly through the cotton and reached the closed end (**Figure 3.2**)
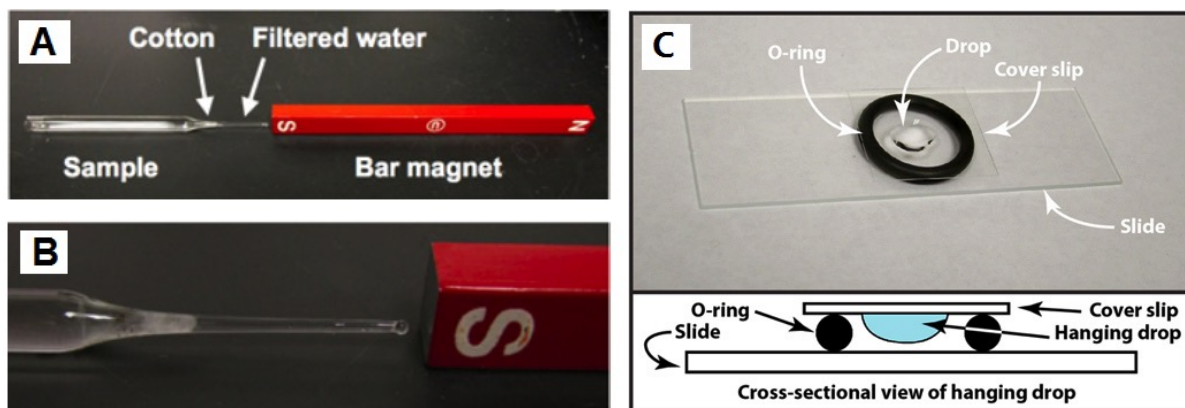
Figure 3.2 Capillary racetrack used to isolate MTB cells from environment. (A). A magnet is placed at the closed end of the capillary. MTB swim though a cotton plug (arrow) towards the south end of the bar magnet; (B). A close up view of the capillary racetrack showing the sample, cotton, filtered fluid, sealed end of the capillary tube and south end of a bar magnet. (C). Cross-sectional view of hanging drop; Figure reproduced from Oestreicher et al. (2012)

(5). Once the MTB have been enriched from the racetrack, the bottom part of the capillary, where MTB cells aggregated, was chopped off.

(6). One drop of the enriched solution obtained from the previous step was placed on a coverslip for "hanging-drop" visualization (see Figure 3.2C) with an optical microscope using differential interference contrast (DIC) or phase contrast.

(7) Finally, the drop was put on a TEM grid for TEM and STXM measurements.

Figure 3.3A~D show TEM images of MTB cells isolated from Cootes Paradise. Although most of the Cootes MTB cells are spirillum bacteria (Figure 3.3A~C), one cocci bacterium was observed (Figure 3.3D). Magnetosome chains can be clearly observed in these cells. This means MTB cells have been successfully isolated from the local environment. Further work such as genetic analysis, magnetic measurements, fluorescence labeling etc. can be conducted on these cells.
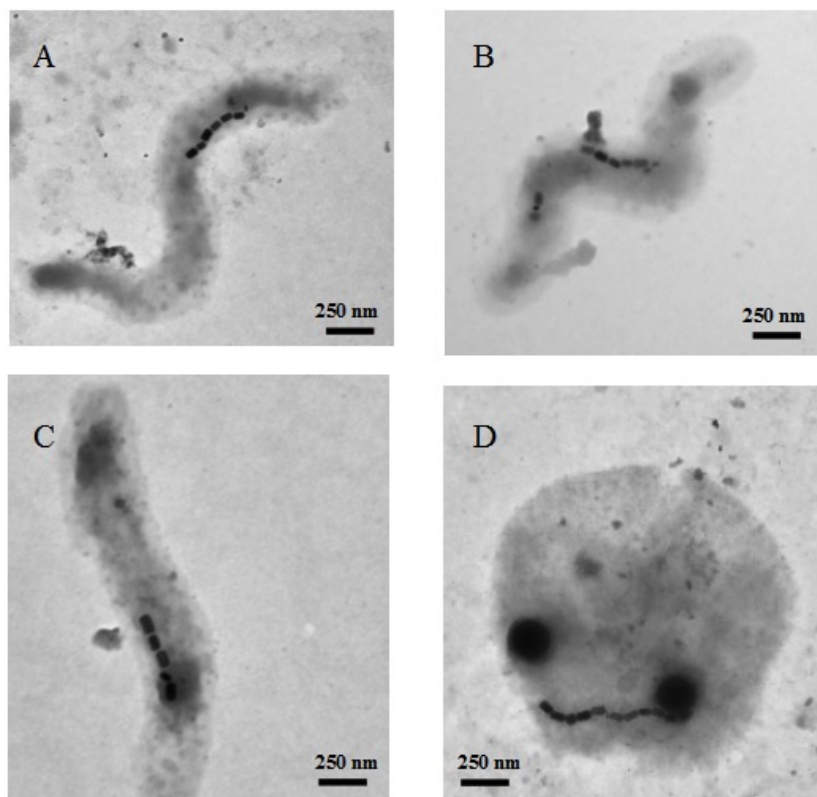
Figure 3.3 TEM images of MTB cells collected from Cootes Paradise **(**A~D).

3.1.2 Sample preparation for STXM

Samples for STXM measurement were prepared by placing MTB culture solution on a formvar-coated TEM grid or Si_3N_4 window. According to our Brazilian collaborator, Pedro Leão, the procedure to prepare MTB samples on formvar coated grids was:

(1) TEM Grid is glow discharged immediately before use to improve cell adherence

(2) 10 µl of sample culture solution is placed onto the grid for 5 minutes at room temperature

(3) The excess sample solution is gently removed with a filter paper placed at one side of the grid

(4) The grid is then placed with the sample side facing down on top of a 2% phosphotungstic acid (PTA) drop for 2 minutes for negative staining of cellular structures

(5) Excess PTA is wicked away with a filter paper placed at one side of the grid

(6) The grid is air-dried and stored in a desiccator until further measurements.

3.1.3 Sample mounting

Depending on the type of STXM measurement to be performed, various sample mounting strategies have been used (see **Figure 3.4**). For non-XMCD-type measurements, the samples are normally mounted on a standard flat plate. The sample plate used in ALS 11.0.2 has four holes evenly distributed in one row while that for 10 ID-1 STXM has 6 holes evenly distributed in 2 rows (**Figure 3.4A**). The diameter of each hole is 2.7 mm, a little smaller than a TEM grid (3 mm) such that the TEM grid centered on the hole has 0.15 mm overlap with the plate and can be attached with three small (~0.5 mm * 1 mm) strips of tape. A small drop of nail polish or epoxy is also used for a more secure mounting. In addition, the grid should be carefully mounted such that the orientation of the grid squares aligns with the x and y axes of the STXM to allow maximum access to the sample region with minimum scan area.
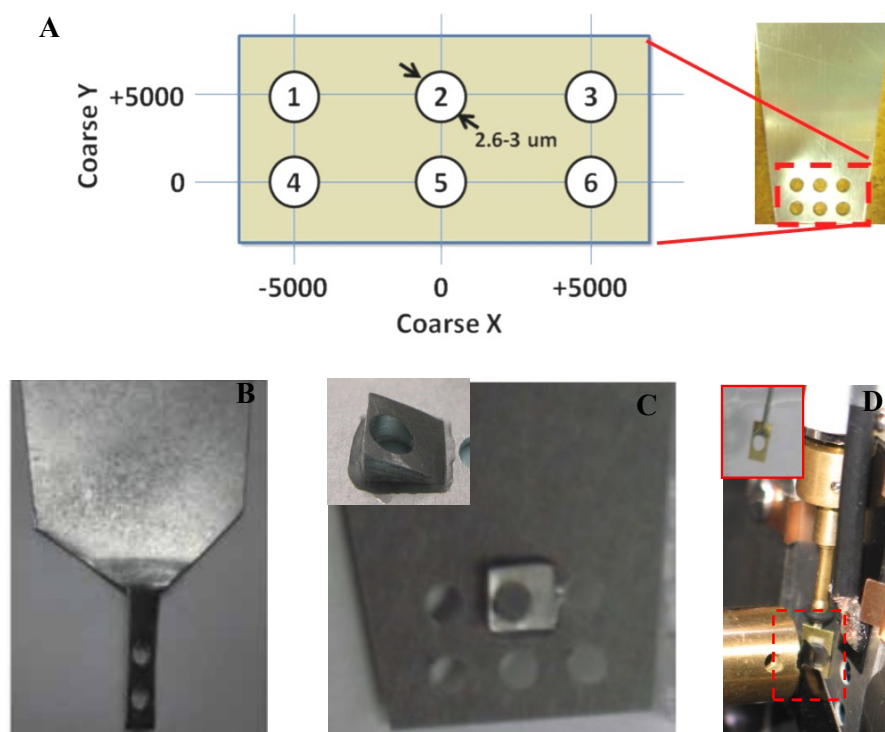
Figure 3.4 Various sample plates used for STXM and STXM-XMCD measurements. (A). A standard flat sample plate holder. Note for 11.0.2 STXM, holes#1, 2, and 3 are not accessible. Courtesy of 10ID-1 CLS STXM manual; (B) A twist plate; (C) A wedge (inset) mounted on a flat plate; (D). A tomography rotator placed into STXM chamber. Inset is a tomo-stub where a TEM grid can be attached with nail polish.

In contrast to many other types of STXM-XMCD measurements used in materials science (Lacour, et al, 2015), an external magnetic field is not used in the STXM chamber during these measurements since the goal of the study is to measure the intrinsic magnetic moment of the MTB without modification. Since the intrinsic magnetic moment of magnetosomes in MTB cells is almost always in the plane of the grid, a tilted or rotated mounting is used for STXM-XMCD measurements. When the sample plate is mounted such that its plane is tilted relative to the X-ray beam direction and the magnetic moment is horizontal, there is a projection of the sample magnetic moment on to the spin vector of the photon beam. The latter lies along the

direction of propagation of the X-ray beam. **Figure 3.5A** shows the situation for measurement in

the *normal* geometry, where the flat sample plate is orthogonal to the X-ray propagation

direction. In this geometry, neither horizontal nor vertical magnetic moments have a projection

along the X-ray propagation direction. Thus, in-plane magnetic moments can not be detected in

this geometry. **Figure 3.5B** shows the geometry when the sample plate is *tilted by* θ. In this case,

although vertical magnetic moments still have no projection along the X-ray propagation

direction, the horizontal magnetic moment, M, would have a projection component, M_z, $M_z=$

$M \cdot \sin\theta$, on to the X-ray beam axis. Therefore, XMCD signals can be detected from horizontal

magnetosome chains with this experimental geometry.
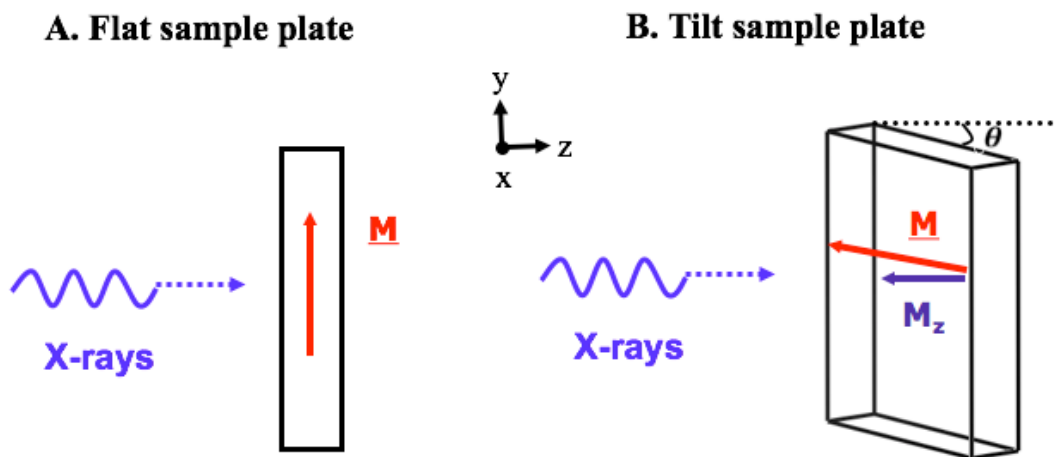
Figure 3.5 Illustration of need of a tilt geometry for XMCD detection. (A).The *normal* geometry, where the flat sample plate is orthogonal to the X-ray propagation direction (0 XMCD intensity for in-plane M in any orientation). (B). The geometry when the sample plate is tilted by θ degree ($M \cdot \sin\theta$ XMCD intensity for horizontal in-plane M).

Various sample mounting strategies were used to achieve the required tilted orientation, including the twist plate (**Figure 3.4B**), the wedge plate (**Figure 3.4C**), and the tomography stub (**Figure 3.4D**). In this thesis, the twist plate was used for STXM-XMCD measurements in most cases. With larger tilt angle, the projection of the MTB magnetic moment along the X-ray propagation direction increases. However, at higher tilt angles the plate can hit the OSA, particularly when a large motion in x axis is made. Considering the physical constraints in the STXM chamber, the sample plate was routinely rotated by ~30°, which means there is a $\sin(30^o)$ =0.5 (50%) projection of the magnetic moment onto the X-ray beam axis for completely horizontal moments.

3.2 Measurements of MTB

3.2.1 STXM measurements of MTB

In this thesis, all of the STXM measurements were performed using **STXM_control**, which provides full control of both the STXM microscope and the associated beamline and insertion device, as well as data acquisition, display and storage (Kilcoyne et al., 2003). The top level of the graphical user interface (GUI) for STXM_control is shown in **Figure 3.6**. STXM_control uses configuration files to adapt the software at run-time to allow it to operate many different STXMs and related instruments on different beamlines around the world (see **Table 3.1** for a list). STXM_control operates the microscope in many different modes, with some scan types used to align and verify the microscope set-ups (detector, OSA, OSA_focus, motor); and others used to acquire data using 1D, 2D, 3D, 4D and even 5D scanning. In the sample scan mode STXM_control can measure the sample transmission at 1 or more points,
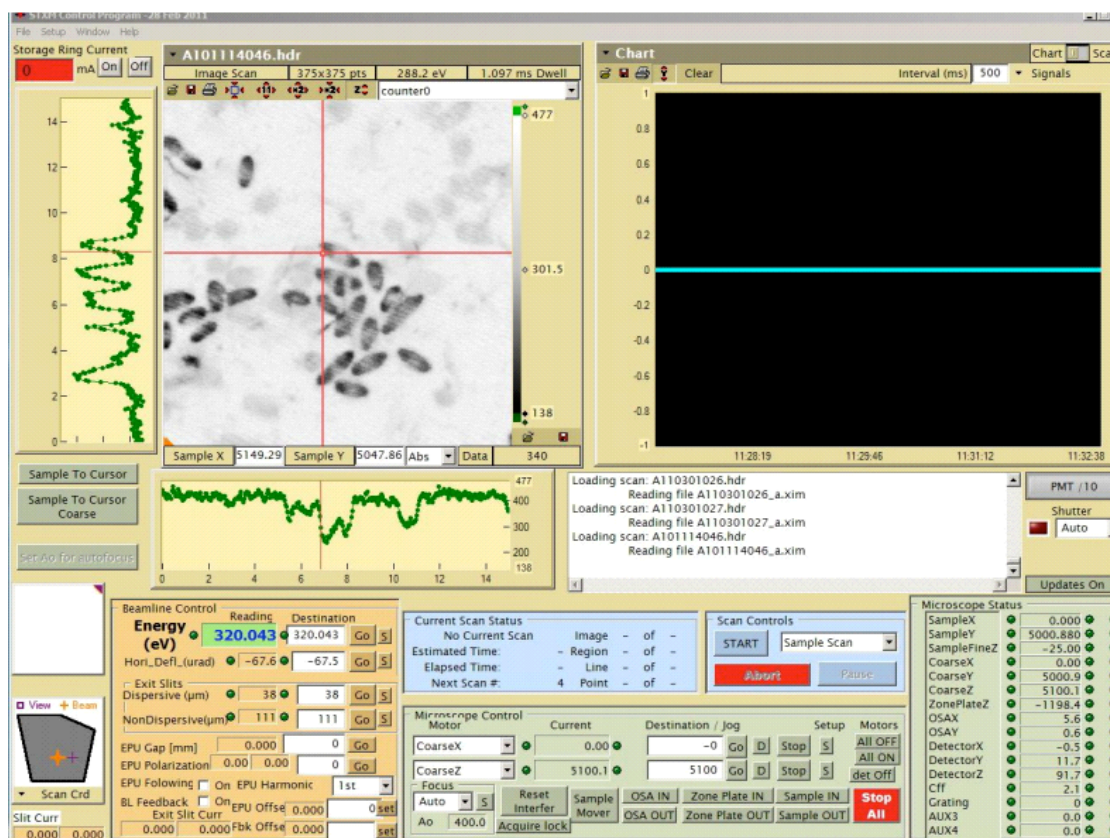
Figure 3.6 Graphical User Interface for STXM, which gives the user access to control photon energy, ZP, OSA, detector, beamline polarization, etc.

along a line, or over 1 or more 2D areas, at one energy or at a sequence of photon energies (image sequence or stack (Jacobsen et al., 2000). Other scan types include: XMCD-sample, DAC-sample, 2D motor, tomography, pattern generation, and ptychography. Among the many possible modes of using STXM_control, single energy images, stacks, XMCD-sample scans, and ptychography scans (image, stacks) are the major data acquisition modes used in this thesis.

Table 3.1 STXMs around the world (as of Aug. 2015)[a]

Facility	BL	location	Source	E-range (eV)	1st image	Status	software[b]	type[c]
ALS	5.3.2.2	Berkeley, US	BM	250-750	2001	op	STXM_control	HKT2003
ALS	11.0.2	Berkeley	EPU	100-2000	2002	op	STXM_control	HKT2003
ALS	5.3.2.1	Berkeley	BM	500-2500	2011	op	STXM_control	HKT2003
ALS	NS-1 on 5321	Berkeley	BM	500-2500	2011	op	STXM_control	HKT2003
ALS	NS-1 on 7.0.1	Berkeley	EPU	100-4000	2015	con	STXM_control	HKT2003
Australian SR		Melbourne	Und-L	100-2000	2014	op		Xradia
Bessy-II	MAXYMUS	Berlin, Germany	EPU	250 – 1500	2008	op	STXM_control	Bruker
CLS	10ID1	Saskatoon, Canada	EPU	130-2500	2006	op	STXM_control	HKT2003
CLS	10ID1	Saskatoon	EPU	130-2500	2015	com	pySTXM	HKT2003
Diamond	I08	Didcot, UK	EPU	250-2500	2015	op	pixelator	Bruker
Elettra	Twin-mic	Trieste, Italy	Und-L	250 - 2000	2002	op		custom
UVSOR	BL4U	Okazaki, Japan	Und-L	50-800	2013	op	STXM_control	Bruker
NSRRC	BL09A1	Hinschu, Taiwan	Und	60-1500	2017	des	STXM_control	Tyliszczak
PLS	nanoscopy	Pohang, Korea	EPU	100 - 2000	2014	op	STXM_control	Bruker
PF	Various BL	Tsukuba, Japan	BM	100-8000	2013	op		Atto-cube
SLS	PolLux	Villigen, Switz.	BM	250-750	2006	op	pixelator	Bruker
SLS	NanoXAS	Villigen, Switz.	BM	270-1800	2009	op		custom
Soleil	Hermes	Saint-Aubin, France	EPU	250 – 1500	2016	op	pixelator	Bruker
SSRF	SXS	Shanghai, China	EPU	200 - 2000	2011	op	pixelator	Xradia
SSRL	13-1	Stanford, USA	EPU	250 – 1000	2010	op	STXM_control	Atto-cube

a. adapted and updated from Hitchcock (2012)

b. **op**=operating, con=construction, **com**=commissioning, **des**=design

c. HKT2003-evolution from interferometer controlled STXM designed by Peter Hitchcock, David Kilcoyne and Tolek Tyliszczak (Kilcoyne et al., 2013); Bruker-commercial version of HKT sold by Accel (2004-2008), Bruker (2008-2014), Research instruments (2015-now) and Axilon (2015-now), Xradia-from their collaboration with APS (now part of Zeiss)

3.2.1.1 Single energy images

In order to record a single energy image (ie. an image taken at a specific photon energy), one needs to define the following parameters: photon energy, position of the center of the image, size of the image, point spacing (pixel size) in each dimension of the image, as well as the dwell time in each pixel. As shown in Figure 2.7 in Chapter 2, there are two sets of sample stages in STXM. When the x-dimension of the image is over a defined upper size limit (80 μm at CLS ID10.1, 30 μm at ALS 11.0.2, ALS 5.3.2.1-NS-1) a coarse scan stepper stage with a large travel (6-25 mm) is used. When the image size is smaller than the upper limit, a fine scan piezo stage is used. Compared with the coarse stepper stage, the piezo stage provides greater precision and better stability. In addition, the STXM image can be measured in two different modes: either using "line by line" mode (faster, but less precise as the interferometer feedback is disengaged while each line is scanned at a constant velocity), or "point" mode (slower, requires 2-4 ms settle time, but more precise, as the interferometer feedback is always engaged). **Figure 3.7A** and **3.7 B** shows STXM image of the same magnetosome chains with line-by-line and point mode, respectively. The dwell time for each image was 5ms. Clearly, the "point" mode generates better quality images, with better contrast and sharpness, greater precision and higher statistical quality. However, point mode images take a longer time to collect than "line-by-line" mode. In this work, "line-by-line" mode was used for large area imaging such as navigation. while "point" mode was used for imaging small areas (below 1 micron) with more detail and higher quality, as is required to apply STXM to study ~50 nm magnetosomes in MTB.
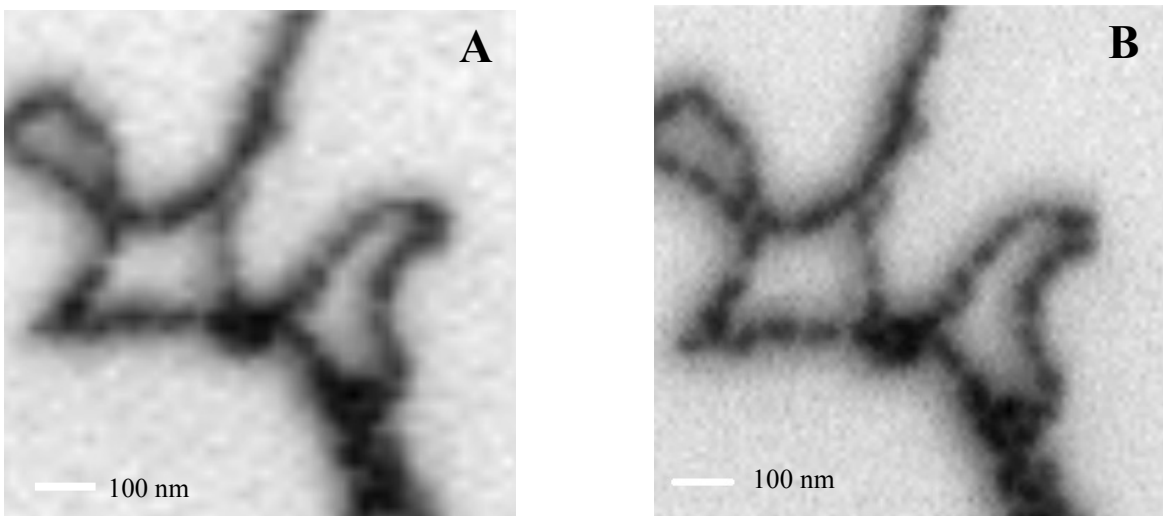
Figure 3.7 STXM transmission image of magnetosome chains measured with "line by line" (A) and "point" modes (B). The image was measured with a ZP with an outer zone width of 25 nm which has a diffraction limited spatial resolution of 31 nm. Images were measured at 11.0.2 STXM at ALS.

3.2.1.2 Image sequences (stacks)

In STXM, the spectral data can be obtained by recording a sequence of images, with defined image size, pixel size, dwell time and energy steps, over the energy range of interest. In order to probe the biochemical components of both Fe_3O_4-and Fe_3S_4- producing MTB cells, XAS spectra at various edges were measured in this thesis, including C 1s (270~320 eV), O 1s (520~560 eV), S 2p (150~200 eV), and Fe 2p (695~745 eV). Since the STXM control program allows users to set up to 10 energy ranges in one stack, one can use different energy increments for different energy regions. For example, a fine energy spacing (less than 0.2 eV) can be used for the main edge region while a coarse spacing (0.2~0.6 eV) can be used for pre-edge and post-edge regions - see **Figure 3.8** for the GUI used to define a multi-region, multi-energy, sample scan.
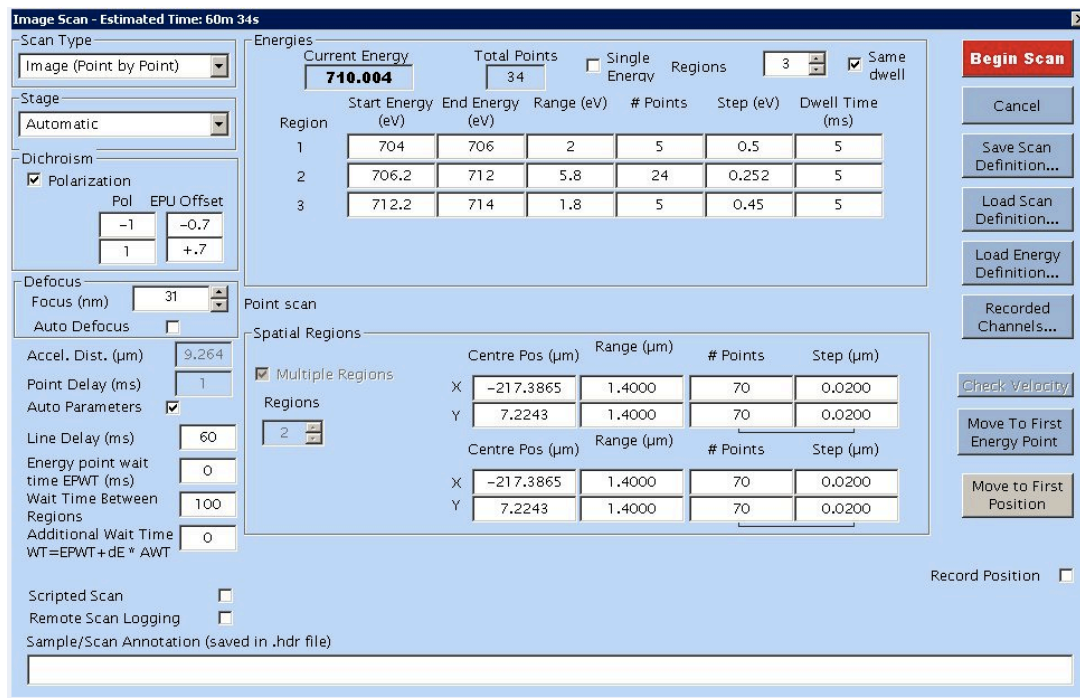
Figure 3.8 Example of scan parameters for an XMCD stack scan at Fe L_3 edge in STXM

The size of the individual single crystal magnetosomes in MTB cells range from ~40 to about ~80 nm, which makes imaging of individual magnetosomes in STXM rather challenging as the spatial resolution of STXM (routinely 30 nm) is similar to the size of magnetosomes. Therefore, it is challenging to visualize individual magnetosomes with high statistical quality. One way to improve the image quality is by over-sampling, which means using sufficiently small pixel size (~5-8 nm) and a long dwell time at each pixel (6-10 ms). Since the "line-by-line" scanning mode only works with pixel sizes > 10 nm and dwell times < 5 ms, the point mode was typically used to image individual magnetosomes. Although point mode generally improves the image quality, it requires longer time to collect data. Therefore, the image size has to be restricted to small dimensions (1~2 μm) in this mode. Spatial drifting was often a problem, such that a multi-hour stack would need to be split into 3 or 4 separate measurements, with re-centering of the image area to keep the object of interest in the field of view.

Unlike magnetosomes, over-sampling is not necessary for imaging the biochemical components in MTB cells. For example, the pixel size for a C 1s stack can range from 20~50 nm and the dwell time can be 1~2 ms with "line-by-line" scanning mode. Since organic molecules are more sensitive to radiation damage than the inorganic magnetosomes, stacks used to investigate the biological components (S 2p, C 1s, N 1s, O 1s) were measured before measuring Fe 2p XAS and XMCD.

3.2.1.3 STXM-XMCD measurements of MTB

XMCD measurements of MTB were carried out using a twist sample plate (see Figure 3.4A). Compared with a conventional STXM stack, XMCD is a polarization dependent signal, which will have a non-zero signal only when the in-plane magnetic moment is horizontal and has a projection along the X-ray propagation direction (Lam et al., 2010). Therefore, XMCD measurements were performed on MTB cells with horizontal chains instead of those with vertical chains. In order to make XMCD measurements, the XAS signals need to be recorded with left and right circularly polarized light. By putting different codes into the sample scan interface of STXM_control, the EPU can be automatically switched between the two circular polarizations. There are two modes to collect XMCD data. One is successive mode, in which the complete stack is first measured with one polarization before reversing the polarization and measuring a second stack. The other one is concurrent mode, in which the two different polarizations are alternated at each energy point. For XMCD, the left and right polarizations are alternated. However, in other cases, two different linear polarizations can be used (Zhu et al 2015). According to a previous study (Kalirai et al., 2012), XMCD measurements of magnetosomes using the successive mode is much more dependent on beamline stability and is

very sensitive to artefacts associated with carbon build-up on the sample. Therefore, the

concurrent mode was always used to acquire the STXM-XMCD stacks reported in this thesis.

Unfortunately at the time of the XMCD-ptychography measurements, due to software limitations,

it was not possible to use concurrent mode so sequential mode was used.

3.3 Data Analysis

All the STXM data ws analyzed with the software aXis2000, which is written in

Interactive Data Language (IDL). It is available free for non-commercial use from

http://unicorn.mcmaster.ca/aXis2000.html.

3.3.1 Stack and XMCD maps

A stack map refers to a measurement of images at two photon energies, which are

converted to optical density and subtracted. The difference of the signal at a characteristic X-ray

absorption energy (on-resonance) and at a pre-edge energy (off-resonance) can determine if a

certain element or chemical component exists in a sample. Stack maps can also be used to give a

quantitative distribution of the elements or chemical component. **Figure 3.9A** and **3.9B** presents

a STXM optical density image of a MV-1 cell at 710 eV and 700 eV, respectively. **Figure 3.9 C**

is a stack map derived by the difference between Figure 3.9 A and B, which cancels out the

background absorption from non-iron components and only demonstrates the distribution of Fe

components. **Figure 3.9D** is a color coded composite of the pre-edge image (purple, 700 eV) and

the stack map (green, Figure 3.9C), which shows the relative distribution of organic matter

relative to the magnetosome chains.
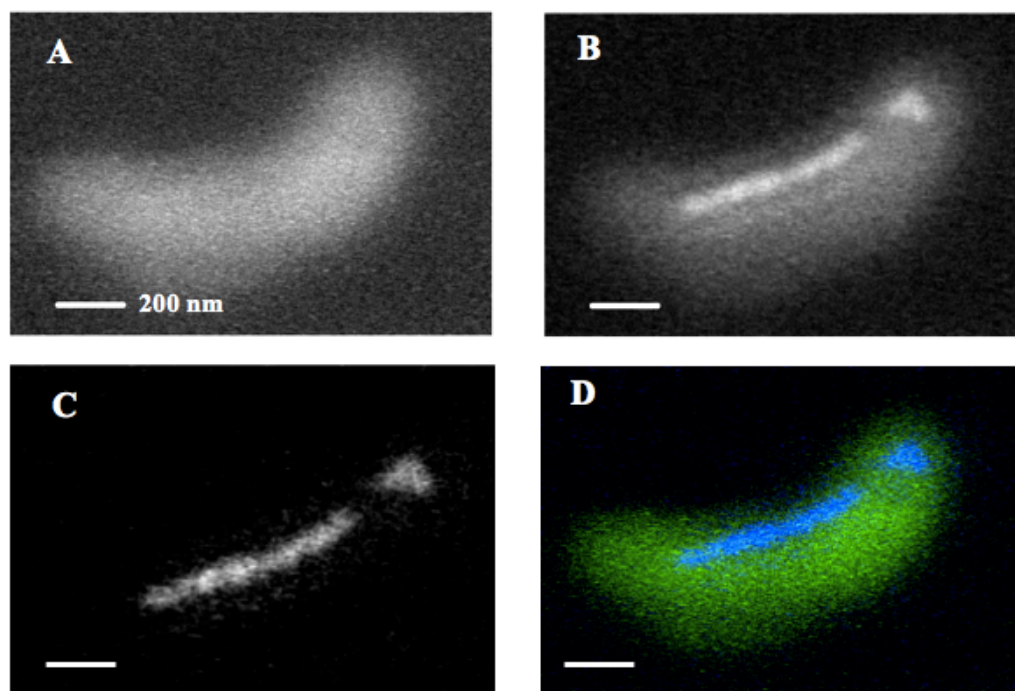
Figure 3.9 Single component map of Fe in MV-1 cells. (A) and (B), STXM optical density images of a MV-1 cell measured at 700 eV and 710 eV, respectively; (C). Stack map derived the difference between Figure 3.9B and 3.9A, revealing the area containing Fe components; (D) Color coded map of organic matter (green) and Fe components (blue)

XMCD mapping is performed by taking the difference between two STXM optical density images recorded with left circularly polarized light (LCP) and right circularly polarized light (RCP) at a specific photon energy where the maximum XMCD signal is located. In the case of magnetite (magnetosome), XMCD maps are measured at 708.2 eV. **Figure 3.10** presents an example of an XMCD map of a MV-1 cell. It should be notable that the LCP and RCP optical density images appear the same, as shown in **Figure 3.10A**. The only difference between them is the maximum optical density values: 0.249 for LCP and 0.254 for RCP. **Figure 3.10 B** shows two contrast levels (bright and dark) in the XMCD map, indicating there are magnetosome sub-chains in this cell which have opposite magnetic polarities. This is consistent with a previous

study which showed that some MV-1 cells contain magnetosome sub-chains with opposite

magnetic polarities (Kalirai et al., 2013).
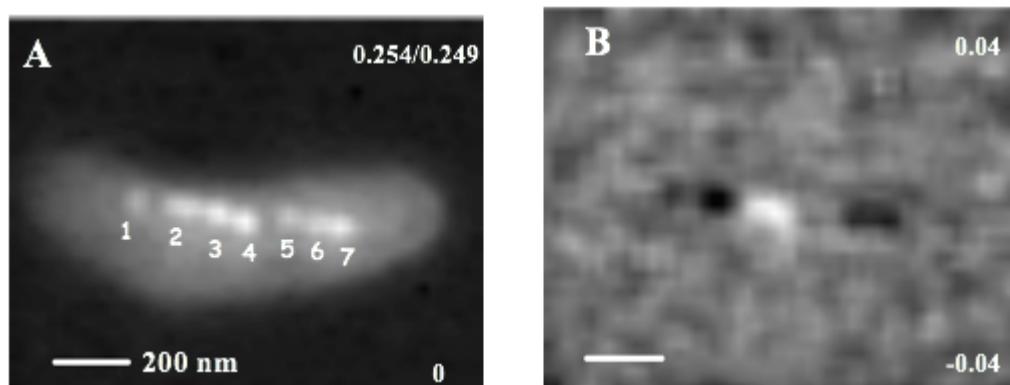
Figure 3.10 STXM optical density (OD) image and XMCD mapping of a MV-1 cell. (A). STXM optical density image of a MV-1 MTB cell recorded with either left circularly polarized light (LCP) or right circular polarized (RCP) light. (B). XMCD map of the difference between LCP and RCP optical density images. The bright and dark contrast in the XMCD map indicates magnetic polarities of magnetosomes are not the same: magnetosome 1, 2, 5 and 6 have one magnetic polarity while magnetosome 3 and 4 have the opposite

XMCD mapping was routinely used in thesis because of its advantages relative to full stacks:

1. An XMCD mapping usually takes 5~10 minutes which gives a quick "glimpse" to check if the region of interest has potential for a full XMCD stack which usually takes several hours.

2. The contrast in XMCD mapping can be used to determine the magnetic polarity.

3. XMCD mapping allows for efficient statistical studies of magnetic polarity in sampling sizes of hundreds of cells.

3.3.2 Analysis of stacks

Stacks are analyzed using aXis2000. It generally includes the following steps: pre-processing, alignment, conversion to optical density, and spectromicroscopy analysis.

3.3.2.1 Pre-processing

Before the actual analysis, it is important to check that each image in a stack is analyzable. It is common that some images are corrupted because of instability in the storage ring, beam injection, interference or vibration from outside environment, etc. Sometimes the region of interest drifts out of the field of view. There are multiple functions in aXis2000, such as filter, deglitching, and histogram, which can be used to correct the image. If issues still exist, images are deleted if deletion will not pose problems to the further analysis.

3.3.2.2 Stack alignment

A normal stack usually takes 30 minutes and a full XMCD stack can take several hours. Thus, misalignment inevitably occurs due to temperature changes in the STXM chamber, instrumental drift, sample drift, etc. Meaningful spectral data can be acquired only if the signal is extracted from exactly the same location in each image in a stack. Therefore, it is necessary to align all the images in a stack before extracting spectra. There are several routines in aXis2000 that can be used to align the images ("Zimba", "Jacobsen stack_analyze"). Auto-alignment is generally performed first. Multiple iterations are executed until a convergence is reached. In some cases, one may need to manually align images to obtain a good alignment. One way to monitor the alignment quality is to average all the images of the stack and check if there is any 'halo'surrounding cells or magnetosomes which is indicative of misalignment.

Good alignment is particularly crucial to XMCD analysis since it is a difference between two polarization stacks. In concurrent mode the images from the left and right circular

polarization (RCP, LCP) are stored separately. In order to get both stacks aligned in the same way, the two polarization stacks are merged into one stack (using an energy shift to keep the images from the 2 polarization modes separate) and then align the appended stack. This ensures that when a single region of interest (ROI) is used to extract spectra from two polarization stacks the XMCD spectrum is derived from exactly the same region.

3.3.2.3 Conversion to optical density

Once the stack is aligned, the STXM transmission images need to be converted to optical density (OD) using the Lambert-Beer Law:

$$OD = \ln \left(\frac{I_0}{I} \right) \tag{3.1}$$

where I_0 and I represents the incident and transmitted x-ray photon intensity, respectively. The choice of I_0 is usually a region close to the ROI but free of the cell and magnetosomes, i.e. the polymer supporting membrane of the TEM grid or a bare area of a silicon nitride window. In the case of XMCD stacks, it is important to use the same ROI to extract the I_0 from exactly the same area of each of the aligned polarization stacks.

3.3.2.4 Spectral analysis

Since various elements are present in MTB cells, such as C, Fe, O, S, etc., it is important to quantitatively probe the distribution of different chemical components. aXis2000 provides two methods to derive chemical component maps from energy stacks. Both procedures, called SVD and stack fit in the aXis2000 menu, use a single-pass matrix procedure called Singular Value Decomposition (SVD) (Koprinarov et al., 2002), which is equivalent to an optimized least squares fitting for over-determined data sets (typically there are 10^3 - 10^5 spectra in a stack which can be represented by less than 6 different independent spectra). The SVD method fits each spectrum of a stack to a set of reference spectra of different chemical
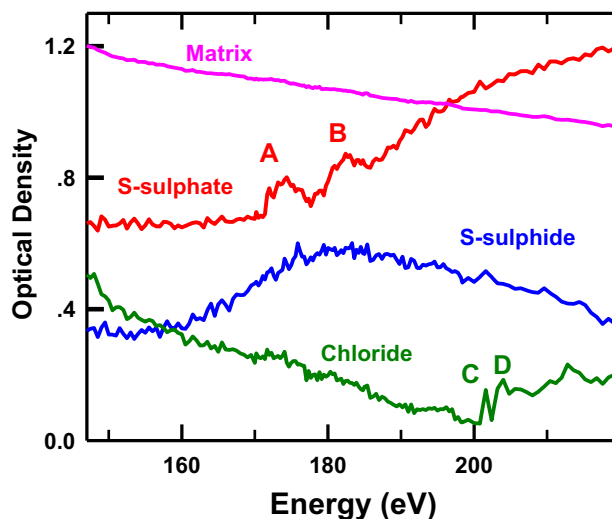
Figure 3.11 Four spectral models, including sulphide phase (S-sulphide), sulphate phase (S-sulphate), chloride and matrix (no S signals), which are used to derive the component map of each species from the S2p stack of a MMP.

components provided by the user (typically from independent measurements, or extracted from the stack being analyzed). Stack fit is the same as SVD except that an additional constant term (an intensity without a spectral variation) is included. With either approach, the fitting coefficient for each reference spectrum is proportional to the amount of each component at a given pixel. A set of fitting coefficient constitutes a chemical component map. **Figure 3.11** plots four spectra, including sulphide phase (S-sulphide), sulphate phase (S-sulphate), chloride and matrix (no S signals), which were used to derive component maps of each sulphur species inside a multicellular magnetotactic prokaryote (MMP) cell using the stack fit method. **Figures 3.12a~d** present the derived component maps of sulphide, sulphate, chloride and matrix in the MMP cell. After generating chemical component maps the user can combine them to form color coded composites to examine spatial correlations (see **Figure 3.12e and f**). aXis2000 also allows for generating ROI masks based on the intensities of individual component maps. The spectra from ROIs can then be examined and the quality of a given analysis can be evaluated in 'spectral

space'. In many cases, multiple analysis procedures are explored to build confidence in the final result.
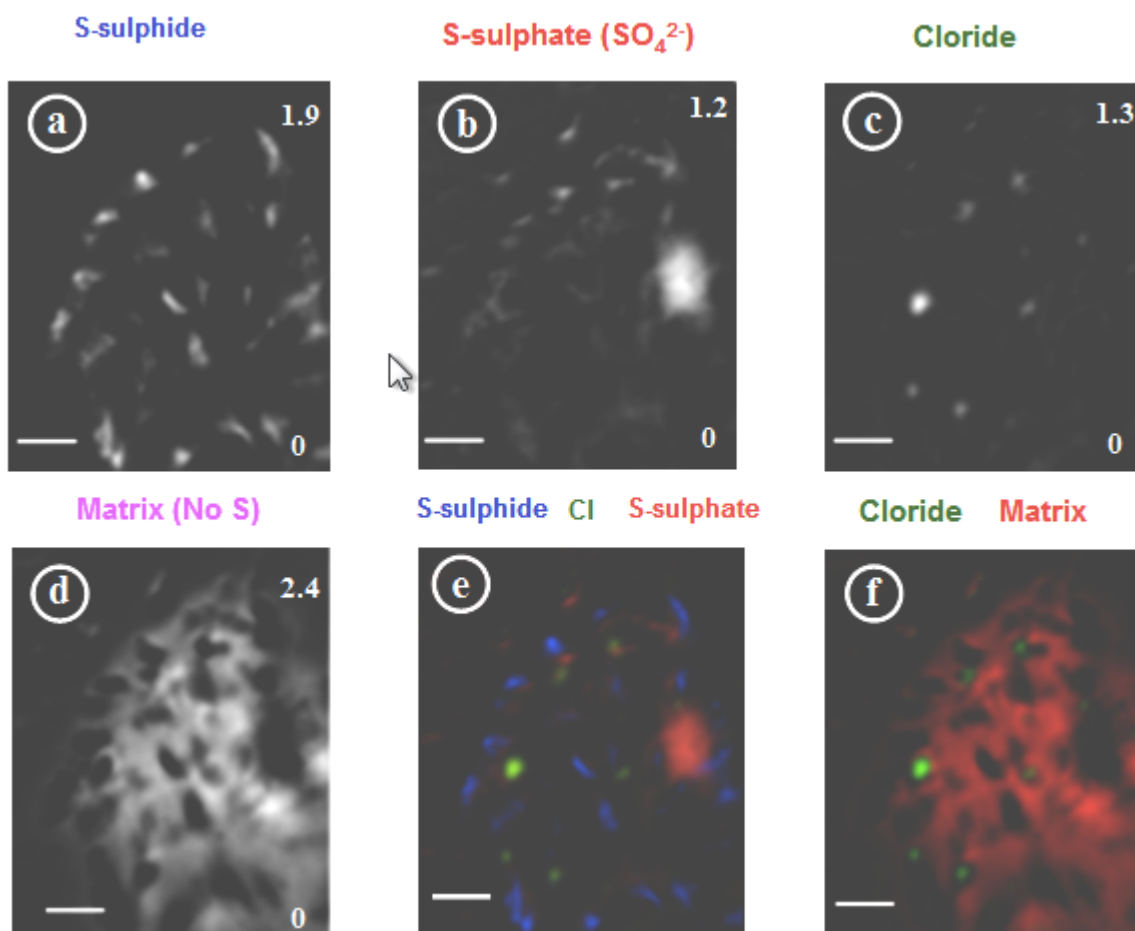
Figure 3.12 The derived sulphur component maps using stack fit method. Sulphide (a), sulphate (b), chloride (c) and matrix regions (d) regions in a MMP cell derived with stack-fit method using the spectra in Figure 3.11; (e) Scaled color composite of S-sulphide (Figure 3.12a), S-sulphate (Figure 3.12b) and cloride map; (f) Scaled color composite of chloride (Figure 3.12 c) and matrix (Figure 3.12d). The scale bar represents 1 μm

Chapter 4

What is the correct Fe $L_{2,3}$ X-ray absorption spectrum of magnetite?

This paper presents results of spectroscopic study of biogenic and abiogenic magnetite, with the aim of clarifying the confusion existing in the literature as to the correct Fe $L_{2,3}$ X-ray absorption spectra of magnetite and maghemite.

MV-1 cultures were grown by Prof. Dennis Bazylinski. Samanbir S. Kalirai made the STXM-XMCD measurements of abiogenic magnetite powder purchased from Sigma Aldrich company. The author of this thesis extracted magnetosomes from the MV-1 cells and chemically modified the biogenic magnetosomes and abiogenic magnetite powder. The powder X-ray diffraction and STXM-XMCD of these samples were measured by the author. The data was analyzed by the author and Prof. Adam P. Hitchcock. This paper was drafted by the author and edited and revised by the author, Prof. Adam P. Hitchcock and Prof. Dennis A. Bazylinski This paper has been published: 10.1016/j.elspec.2014.12.005

What is the correct Fe L_{23} X-ray absorption spectrum of magnetite?

Xiaohui Zhu [a], Samanbir S. Kalirai [a,1], Adam P. Hitchcock [a,*], Dennis A. Bazylinski [b]

[a] Department of Chemistry and Chemical Biology, McMaster University, Hamilton, ON L8S 4M1, Canada
[b] School of Life Sciences, University of Nevada at Las Vegas, Las Vegas, NV 89154-4004, USA

ARTICLE INFO

ABSTRACT

Various groups have reported Fe L_{23} X-ray absorption spectra (XAS) of magnetite (Fe_3O_4), each claiming to be that of magnetite, but which contradict each other. Here we report an XAS study of two kinds of magnetite: one is biogenic magnetite nanocrystals extracted from the magnetotactic bacterium *Magnetovibrio blakemorei* strain MV-1; the other is synthetic, abiogenically produced nano-magnetite. We see significantly different XAS spectra of these two materials. Only when the abiogenic magnetite was reduced under H_2 did it give the same spectrum as the biogenic sample. Extensive heating of the biogenic magnetite in air produced spectra similar to that of the abiogenic magnetite. These two spectra are typical of the range of published Fe L_{23} spectra of magnetite. X-ray diffraction confirmed that the biogenic material is stoichiometric Fe_3O_4, and showed that the as-received or partly reduced abiogenic material is a non-stoichiometric oxide, intermediate between magnetite and maghemite (γ-Fe_2O_3). When the membrane which surrounds magnetosome chains was intact, the biotic magnetite single crystals were surprisingly resistant to oxidation. This study clarifies a significant confusion existing in the literature as to the correct Fe L_{23} X-ray absorption spectra of magnetite and maghemite.

© 2014 Elsevier B.V. All rights reserved.

1. Introduction

Iron oxides, a group of minerals consisting of iron and oxygen and/or hydroxide, include some of the most important transition metal oxides [1]. To date, there are sixteen known phases of iron oxides differing in composition, Fe valence, and crystal structure [2]. Among them, magnetite (Fe_3O_4) and maghemite (γ-Fe_2O_3) are two particularly important members based on their unusual properties. For example, they are the only magnetic materials approved for use in biomedical applications [3,4]. They are also used in magnetic storage media [5], gas sensing materials [6], as catalysts [7], and they are being evaluated as electrodes in Li-ion batteries [8]. Fe_3O_4 and γ-Fe_2O_3 are of strong fundamental interest due to their interesting physical and chemical properties. Fe_3O_4 has an inverse spinel structure with space group Fd3 m and a unit cell edge length of 8.3941 Å [9]. It is a mixed valence compound with a Fe(II)/Fe(III) ratio of 0.5. In each unit cell, the tetrahedral sites are occupied by 8 Fe(II) ions while the octahedral sites are occupied by a random distribution of 8 Fe(II) and 8 Fe(III) ions. γ-Fe_2O_3 is iso-structural with Fe_3O_4 but has a slightly smaller lattice constant of 8.3474 Å [2]. It

has no divalent Fe ions and the trivalent Fe ions are positioned in the tetrahedral and octahedral sites.

Due to the structural similarities between Fe_3O_4 and γ-Fe_2O_3, it is difficult to distinguish these two oxides. The Fe 2p photoelectron spectra of these two species are very similar but distinguishable [10]. Acidic dissolution, Mössbauer spectroscopy and powder X-ray diffraction are common approaches to address the issue of stoichiometry in magnetite [11–13] but they all have limitations [14]. The acidic dissolution method cannot be applied to natural or mixed-phase samples which contain other redox active components or functional groups. Mössbauer spectroscopy and powder X-ray diffraction are limited by the effect of impurities which could influence results obtained by these two methods. Thus, additional methods are required for characterizing magnetite samples, particularly for nanoparticle samples.

Over the past two decades, synchrotron-based soft X-ray spectroscopy and imaging techniques, in particular X-ray absorption spectroscopy (XAS) with circularly polarized light, have been used to measure electronic properties of samples, through the near edge structure, and magnetic properties, through the X-ray magnetic circular dichroism (XMCD) signal. XAS is a suitable technique since the near edge fine structure is an excellent probe of valence state, local bonding and structure, while XMCD provides element and crystal site-specific magnetic moments of transition-metal ions [15–17]. Many different groups have reported X-ray absorption spectra of materials which are claimed to be magnetite (Fe_3O_4

---

* Corresponding author. Tel.: +1 905 525 9140x24749; fax: +1 905 521 2773.
E-mail address: aph@mcmaster.ca (A.P. Hitchcock).
[1] Present address: Inorganic Chemistry and Catalysis, Utrecht University, 99 Universiteitweg, Utrecht, The Netherlands.

Table 1
Summary of published L-edge XAS spectra of Fe_3O_4 and γ-Fe_2O_3.

Sample	Synthetic method	Shoulder at 708 eV (Y/N)	Detection method	Reference
Fe_3O_4 thin film	Epitaxy on MgO	Partly	TEY	[18]
Fe_3O_4 ultrathin film	Epitaxy on Pt (1 1 1)	N	TEY	[19]
Fe_3O_4 colloid	Co-precipitation	Y	TEY	[20]
Fe_3O_4	Unspecified	Y	TEY	[21]
Fe_3O_4 nanoparticles	Reacting iron salts in microemulsion reactors	N	TEY	[22]
Fe_3O_4 thin film	Pulsed laser deposition	N	TEY	[23]
Fe_3O_4 single-crystalline sample	–	N	TEY	[24,25]
Fe_3O_4 nanoparticles	Solution based	Y	TEY	[26]
Fe_3O_4 nanoparticles	From Alfa Aesar	Y	Transmission	[27]
Fe_3O_4 nanoparticles	Solution based	Y	TEY	[28]
Fe_3O_4 film	Epitaxy on GaAs (0 0 1)	N	TEY	[29]
γ-Fe_2O_3 film	Oxygen-plasma-assisted molecular beam epitaxy	N	TEY	[30]
γ-Fe_2O_3 nanoparticles	Solution based	N	TEY	[31]
γ-Fe_2O_3 nanoparticles	Soft chemistry in a two-step process	N	TEY	[32]
γ-Fe_2O_3 nanoparticles	Sono-chemistry	Y	TEY	[33]
γ-Fe_2O_3 nanoparticles	Solution based	Y	TEY/TFY	[34]
γ-Fe_2O_3 nanoparticles	Solution based	Y	TEY	[35]
γ-Fe_2O_3 nanoparticles	Biomineralized by *Helicobacter pylori*	Y	TEY	[36]
γ-Fe_2O_3 nanoparticles	Wet synthesis method	Y	TEY	[37]

TEY, total electron yield; TFY, total fluorescence yield.

[18–29]) or maghemite (γ-Fe_2O_3 [30–37]). Miedema and de Groot [38] have recently published a comprehensive overview of Fe 2p spectroscopy of Fe oxides and other Fe compounds. These authors maintain a web site (www.anorg.chem.uu.nl/xaseels/) which provides a complete listing and links to all references reporting Fe 2p spectra. Despite the extensive studies, the published X-ray absorption spectra of magnetite are not consistent and often contradict each other. A representative sample of this literature is summarized in Table 1 where the reported spectra are categorized as falling into one of two shapes. Specifically, some of the published Fe L_3 spectra of Fe_3O_4 exhibit a low energy shoulder at $\sim$708 eV (about 1.5 eV below the main $2p_{3/2} \rightarrow 3d$ peak), while the others do not. Similarly, some of the published Fe L_3 spectra of γ-Fe_2O_3 exhibit a low energy shoulder at $\sim$708 eV, while the others do not. This raises the question, *what is the correct spectrum of each of these important materials?*

Here, we report a detailed investigation of the Fe L_{23} XAS of magnetite. We used scanning transmission X-ray microscopy (STXM) to measure XAS spectra of the bulk material and thus reduce the sensitivity to surface oxidation, while at the same time using the high spatial resolution of STXM (30 nm) so that particles in the few hundred nm size scale can be measured in order to avoid absorption saturation. Two representative types of magnetite were studied: one type is magnetite nanocrystals extracted from the magnetotactic bacterium (MTB), *Magnetovibrio blakemorei* strain MV-1 [39]; the other type is chemically synthesized nano-magnetite, obtained commercially from Sigma–Aldrich. A detailed comparative study of the Fe L_{23} XAS and XMCD of biogenic versus abiogenic magnetite nanoparticles was published by Carvallo et al. [40]; our results are compared to theirs. The organization of the paper is as follows. After describing materials and experimental techniques (Section 2), the existence of an extra shoulder in the low-energy side of L_3 spectrum of abiogenically produced nano-magnetite, as compared with the L_3 spectrum of biogenic magnetite, is documented (Section 3.1). Powder X-ray diffraction (Section 3.2) is used to show that the biogenic magnetite is stoichiometric Fe_3O_4 and that the abiogenic nano-magnetite is an intermediate phase between Fe_3O_4 and γ-Fe_2O_3. We then show that the extra shoulder on the low-energy side of the Fe L_3 spectrum can be "switched off" by H_2 reduction (Section 3.3) or "switched on" by air oxidation (Section 3.4). We also document that the membrane enveloping the magnetite crystals in cells of *M. blakemorei* can protect magnetite crystals from air oxidation for a surprisingly long period of time. Our results are

compared to those of Carvallo et al. [40] in Section 4, followed by a summary in Section 5.

2. Experimental methods

Nano-magnetite powder (average particle size of 5 nm, stated purity of >95%) was purchased from Sigma–Aldrich [41]. The biogenic magnetite crystals were extracted from cells of *M. blakemorei* strain MV-1, which were grown anaerobically in liquid cultures with nitrous oxide as the terminal electron acceptor as previously described [42]. Cells were harvested from cultures at mid- to late-exponential phase of growth. By using the procedure described by Alphandéry et al. [43], the membrane-encased magnetite crystals, referred to as magnetosomes, were extracted from cells of MV-1. For some studies the membranes enclosing the magnetosomes were removed to accelerate oxidization by suspending extracted magnetosomes in 1% aqueous sodium dodecyl sulfate (SDS) and sonicating for 15 min at a power of 15 W. Finally, these stripped magnetosomes were heated at 600 °C in air for 3 h. The samples were imaged with a JEOL Model JEM 1200 EX transmission electron microscope. The phase composition was determined by powder X-ray diffraction (XRD) using a Bruker D8 Advance instrument with Co Kα or Cu Kα radiation.

STXM measurements were performed at the soft X-ray spectro-microscopy (SM) beamline (10ID1) at the Canadian Light Source (CLS), Saskatoon, Canada [44]. The beamline was operated at an energy resolving power $E/\Delta E > 3000$. The source point for the CLS SM beamline is an elliptically polarizing undulator (EPU) which provides nearly 100% circularly polarized light at the Fe L_{23} edge. The samples were mounted on a flat sample plate. The bottom 20% of the plate (that to which the grid sample was attached) was cut to generate a narrow strip which could be twisted by 30° about the long axis of the plate in order to achieve a 50% projection of the magnetization vector onto the direction of the incident X-ray beam. The tilt sample plate was mounted on an interferometrically controlled piezo stage, without any additional applied magnetic field. Images were measured in transmission mode by raster scanning the sample over the region of interest while detecting the transmitted signal. Spectral data was acquired by collecting a sequence of images over the energy range of interest, called a "stack" [45]. In order to measure the Fe L_3-edge XMCD, image sequences were recorded with both left circularly polarized light (LCP) and right circularly polarized light (RCP), with alternation

of the circular polarization at each photon energy. This concurrent acquisition mode [46] results in higher quality spectral data than when the full RCP and LCP spectra are recorded sequentially [47]. Data analysis was performed using aXis2000 [48]. The RCP and LCP stacks were combined and aligned together. The transmission signals were converted to optical densities using the incident flux signals through a region free of Fe but adjacent to the region under study. The acquired stacks (after alignment and conversion to optical density) consist of a near edge X-ray absorption fine structure (NEXAFS) spectrum at each pixel. The X-ray magnetic circular dichroism (XMCD) stack was obtained from the difference of the signals recorded with the two types of circular polarization. The L_3 and L_2 signals are only presented for some samples due to limited beam time to make measurements. The L_2 signal provides complementary information to the L_3 signal. However the L_2 signal is ~3 times weaker than the L_3 signal. Thus ~10 times more beam time would be needed to define the L_2 signal to the same quality as measured for the L_3 signal. Since measurement of just the L_3 edge take several hours per spectrum due to the very small amount of material being examined, it was not practical to record complete Fe L_{23} spectra in all cases, especially considering that access to the beam time on the high performance STXM beamlines needed for this work is very competitive.

3. Results

3.1. X-ray absorption spectroscopy

Fig. 1a shows the Fe L_{23} spectrum of a magnetized magnetite thin film recorded with the photon polarization parallel (red) and antiparallel (green) to the sample magnetization using total electron yield (TEY) detection [24]. That sample was very carefully prepared and is believed to be stoichiometric Fe_3O_4. Its spectrum agrees with that we measure from the biogenic MV1 magnetite [46], which supports the use of the spectra reported by Goering et al. [24] as the true spectrum of magnetite – see below. The XMCD spectrum (blue), the spectrum recorded with the photon polarization parallel minus that recorded with the photon polarization antiparallel to the sample magnetization, is also shown. The XMCD intensity of the Goering et al. [24] data has been reduced by a factor of 2 to make a valid comparison to the XMCD derived from the STXM-XAS spectra, since the magnetization of the MV-1 magnetosomes is in the plane of the sample which is tilted 30° from the normal to the X-ray beam and thus only 50% of the magnetic moment of the chain is aligned along the photon polarization vector [47]. Fe L_{23} XAS spectra exhibit two main bands which are the L_3 ($2p_{3/2}$) and L_2 ($2p_{1/2}$) peaks separated by the spin-orbit coupling of the 2p hole. Each band has a fine structure which is determined by a complex interplay of ligand field splitting, covalent interactions and atomic multiplets for each of the three distinct electronic/magnetic sites in magnetite [18,49,50]. Fig. 1b presents the Fe L_{23} spectra and XMCD of a chain of magnetite magnetosomes inside a single cell of the magnetotactic bacterium *M. blakemorei* strain MV-1, recorded using transmission detection in STXM [46]. The inset indicates the magnetosome chain from which the spectra were obtained. Fig. 1c shows the Fe L_{23} spectrum and XMCD of the as-received Sigma–Aldrich nano-magnetite powder. The inset is a STXM optical density image of the aggregate of Sigma–Aldrich nano-magnetite particles from which the XAS signals were extracted. In contrast to the spectra reported by Goering et al. [24] or the spectra of the magnetosomes [46], the L_3 spectrum of the abiogenic nano-magnetite exhibits an additional peak at 708 eV, which was not observed in biogenic magnetite synthesized by magnetotactic bacteria [46,47]. We note that the XAS spectrum of nano-magnetite presented in Fig. 1c matches well with
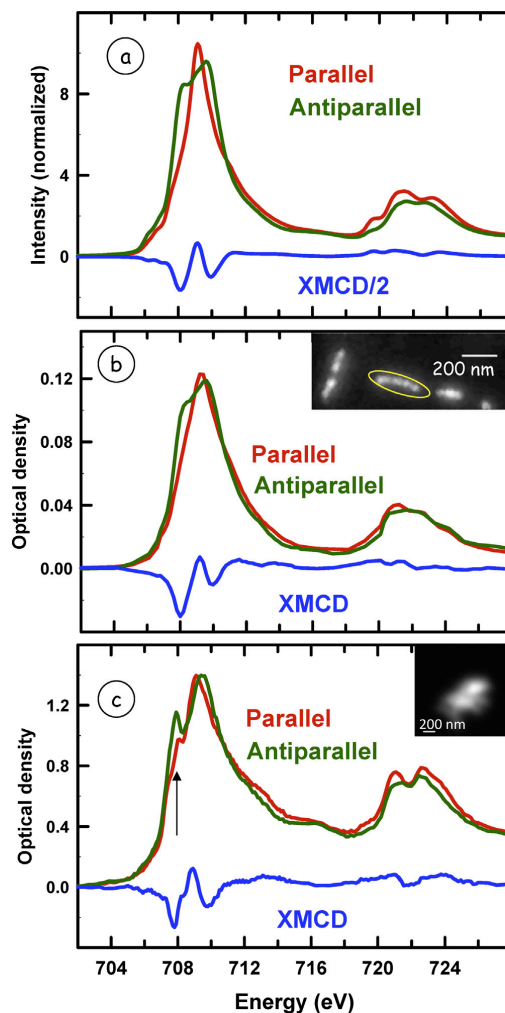
Fig. 1. (a) Fe L_{23} X-ray absorption (XAS) spectra of thin film magnetite recorded using total electron yield detection, with circularly polarized X-rays parallel (red) and antiparallel (green) with respect to the sample magnetization (data courtesy of Goering et al. [24]). A polynomial was fit to the pre-edge signal and the intensity at 730 eV was unit-normalized. The difference signal (parallel minus antiparallel), the X-ray magnetic circular dichroism (XMCD, blue) is plotted using the same vertical scaling. The XMCD in (a) is divided by two, as the XMCD measured in the STXM is only ½ of the full amount due to use of a 30° sample tilt angle [47]. (b) Fe L_{23} spectra of a chain of magnetite magnetosomes from *Magnetovibrio blakemorei* strain MV–1, recorded in STXM with circularly polarized X-rays parallel (red) and antiparallel (green) to the magnetization of the sample. The inset is a STXM image of the magnetosomes from which the spectra were obtained. (c) Fe L_{23} XAS spectra of the as-received Sigma–Aldrich nano-magnetite powder recorded in STXM with circularly polarized X-rays parallel (red) and antiparallel (green) to the magnetization of the sample. The inset is a STXM optical density image of the agglomerate of nano-magnetite particles from which the XAS signals were extracted. In each case, the XMCD spectrum (blue), the difference signal (parallel minus antiparallel), is shown below the spectral curves. (For interpretation of the references to color in this figure legend, the reader is referred to the web version of this article.)
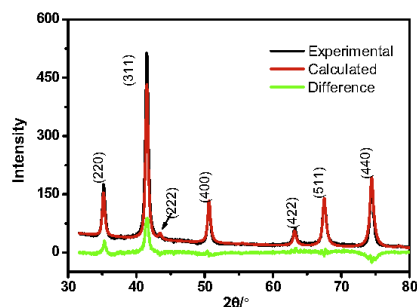
Fig. 2. XRD powder pattern of nano-magnetite as-received from Sigma–Aldrich, recorded using Co Kα radiation. The experimental (black) and calculated (red) powder patterns (for magnetite, but with modified unit cell parameters, as discussed in the text) are plotted, along with the difference (experimental minus calculated patterns) (green). The peaks are labeled with their corresponding crystallographic planes. (For interpretation of the references to color in this figure legend, the reader is referred to the web version of this article.)
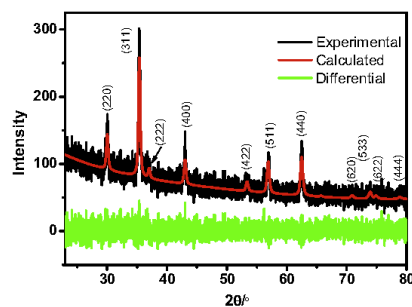
Fig. 3. XRD powder pattern of nano-magnetite reduced with H₂. For technical reasons, this signal was recorded using Cu Kα radiation, which resulted in a larger noise level due to Fe Kα fluorescence, which is excited by the Cu Kα but not the Co Kα line. The experimental (black) and calculated (red) powder patterns (for magnetite, with unit cell parameters similar to that for magnetite, as discussed in the text) are plotted, along with the difference (experimental minus calculated patterns) (green). The peaks are labeled with their corresponding crystallographic planes. (For interpretation of the references to color in this figure legend, the reader is referred to the web version of this article.)

that which has been reported for maghemite by several groups, such as that reported by Kim et al. [33].

Total electron yield (TEY) is a common detection mode used to measure X-ray absorption spectra. Nolle et al. [51] applied both TEY and transmission mode detection to measure XAS and XMCD spectra of FePt/FeO$_x$. They observed a higher oxidation state at the surface of the sample when the detection mode was switched from transmission to TEY. The Fe L$_{23}$ spectra of biogenic magnetite synthesized extracellularly by *Shewanella oneidensis* MR-1 were found to exhibit the lower energy 708 eV shoulder in the L$_3$ region when TEY detection mode was used [52] but not when transmission detection was used (see Fig. 3 in Ref. [53]). Likewise, Peak et al. [54] observed the 708 eV shoulder in Fe L$_3$ spectra of synthetic magnetite when TEY detection mode was employed. TEY is highly surface sensitive and heavily influenced by surface oxidation. Previous studies have shown that brief exposure (<1 day) of Fe$_3$O$_4$ films to the atmosphere does not affect the XAS and XMCD measurements, whereas longer exposures would oxidize the surface of the films [18,55]. This could explain the lower energy shoulder in the L$_3$ region that is often, but not always – see Table 1, observed with TEY detection. In the present work transmission detection in STXM was used, which is more bulk sensitive and less likely to be affected by surface oxidation. Thus, our spectra, measured in transmission mode, are more likely to reflect the intrinsic spectrum of a sample than TEY mode measurements on the same sample. It should be noted that the STXM samples need to be quite small to avoid absorption saturation. The magnetosomes examined in this work are typically 50 nm in diameter, while the nano-magnetite samples are in the range of 20–30 nm. At this size scale the particle surface is still an insignificant fraction of the total sample. At 50 nm diameter, assuming a surface modification over ~1 nm at the surface, the surface contribution would be of the order of 10^{-4}. However, for nanoparticle samples with diameters below 5 nm where a 1 nm zone at the surface contains about 10% of the material, the differences between transmission and TEY detection would be minimal.

3.2. Powder diffraction

Fig. 2 presents powder X-ray diffraction (XRD) patterns of the as-received Sigma–Aldrich nano-magnetite sample. The peaks are labeled according to their crystallographic planes. Although the XRD patterns of nano-magnetite and nano-maghemite are nearly identical due to their structural similarities, the unit-cell length obtained from the XRD can be used to distinguish these two oxides

[14]. The unit-cell length of the Sigma–Aldrich nano-magnetite was determined to be 8.3638± 0.0004 Å (a=b=c) using the Rietveld method. This value lies between the cell length of pure magnetite (8.3941 Å) and that of pure maghemite (8.3474 Å). This suggests that the as-received Sigma–Aldrich nano-magnetite sample was not pure magnetite, but rather a nonstoichiometric magnetite, an intermediate phase between magnetite and maghemite. The ratio of Fe(II) to Fe(III) oxidation states can be determined by an equation developed by Gorski and Scherer [14]:

$$a = 0.1094x_{\rm d} + 8.3424 \tag{1}$$

where a is the unit-cell length and $x_{\rm d}$ is the ratio of the amount of total Fe(II) in the octahedral sites to that of total Fe(III) in both octahedral and tetrahedral sites. Based on this equation the Fe(II)/Fe(III) ratio in the as-received Sigma–Aldrich nano-magnetite sample was 0.2, which is considerably smaller than the value of 0.5 for pure magnetite. Oxidation of magnetite (Fe$_3$O$_4$) to maghemite (Fe$_2$O$_3$) causes the Fe(II)/Fe(III) ratio to decrease. If magnetite was completely oxidized to maghemite, the Fe(II)/Fe(III) ratio would be 0. Thus, the powder diffraction data suggests that almost half of the total Fe(II) ions in as-received Sigma–Aldrich nano-magnetite had been oxidized to Fe(III). In other words, the Sigma–Aldrich nano-magnetite was actually partially oxidized magnetite, or an intermediate phase between magnetite and maghemite. *Is the additional peak observed at 708 eV in the Fe-L$_3$ XAS of Sigma–Aldrich nano-magnetite related to this partial oxidization?*

3.3. Generating pure magnetite from the commercial sample

To investigate this hypothesis, the as-received Sigma–Aldrich nano-magnetite powder was heated under a H$_2$ atmosphere at 309 °C for 0.5 h. Fig. 3 shows the XRD pattern of a Sigma–Aldrich nano-magnetite sample after reduction by H$_2$. The data is significantly noisier than that in Fig. 2 due to Fe Kα fluorescence background since Cu Kα rather than Co Kα radiation was used. The peaks are labeled with their corresponding crystallographic planes. The unit-cell length of H$_2$-reduced Sigma–Aldrich nano-magnetite, extracted by the Rietveld method, was 8.4058 ± 0.0007 Å. This value is in a good agreement with the reported unit-cell length of pure magnetite (8.3941 Å) [9], indicating that the previously partial oxidized Sigma–Aldrich nano-magnetite had been successfully reduced to pure magnetite.
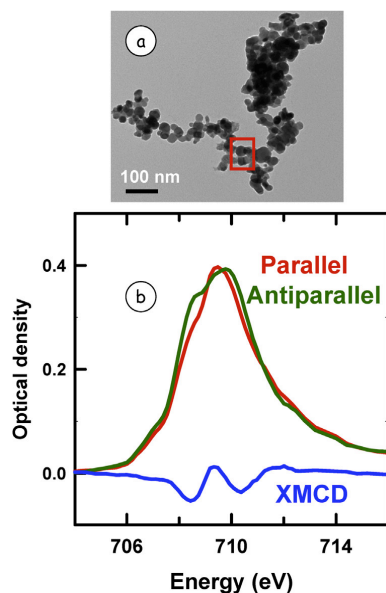
Fig. 4. (a) TEM image of H_2-reduced Sigma–Aldrich nano-magnetite powder. The red square indicates the area from which the Fe L_{23} XAS spectra were extracted. (b) Fe L_{23} XAS and XMCD spectra of the H_2-reduced Sigma–Aldrich nano-magnetite powder recorded with circularly polarized X-rays parallel (red) and antiparallel (green) to the magnetization of the sample. (For interpretation of the references to color in this figure legend, the reader is referred to the web version of this article.)

Fig. 4a is a transmission electron microscopy (TEM) image of H_2-reduced Sigma–Aldrich nano-magnetite powder. The Fe L_{23} XAS spectrum was measured from the area in the red square. Fig. 4b shows the Fe L_{23} XAS spectra of the H_2-reduced Sigma–Aldrich nano-magnetite powder recorded using X-rays with parallel (red) and antiparallel (green) polarization relative to the sample magnetization, along with the derived XMCD (blue). Fig. 4b shows that the peak previously observed at 708 eV in the Fe L_{23} XAS spectrum of the as-received Sigma–Aldrich nano-magnetite (Fig. 1c) was eliminated by H_2 reduction. Thus, the additional peak at 708 eV in the Fe L_{23} XAS spectra of as-received Sigma–Aldrich nano-magnetite is caused by partial oxidization. Thus we assume that similar peaks observed in the Fe L_3-edge XAS of Fe_3O_4 reported by Garcia et al. [21] and Pool et al. [26] (among others) are also due to partial oxidation, either at the surface, and sensed preferentially due to the TEY detection, or from the bulk, due to a non-stoichiometric synthesis or the overall sample being partially oxidized.

3.4. Generating oxidized magnetite from magnetosomes

Fig. 5a presents a TEM image of a biogenic magnetite chain extracted from a cell of *M. blakemorei* (MV-1). Fig. 5b shows the Fe L_3 XAS spectra of biogenic magnetite magnetosomes extracted from cells of *M. blakemorei* (Fig. 5a). The parallel (red), antiparallel (green) spectra and the XMCD (blue) all appear similar to the spectra of intracellular magnetosomes in cells of *M. blakemorei* (Fig. 1b) [46,47], and the spectra of H_2-reduced Sigma–Aldrich nano-magnetite (Fig. 4b). X-ray diffraction determined the unit-cell length of these extracted biogenic magnetite crystals to be 8.402 Å, indicating that magnetite crystals biomineralized by magnetotactic bacteria are stoichiometric, as determined and reported
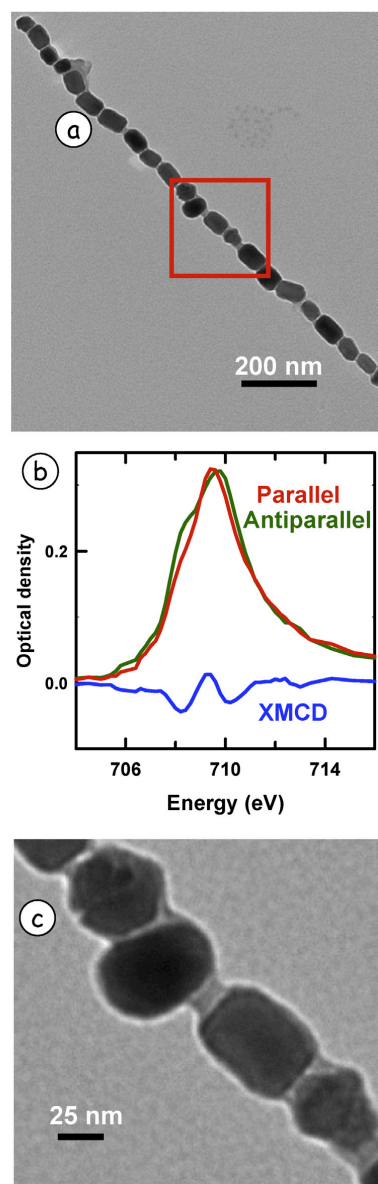
Fig. 5. (a) TEM image of the biogenic magnetite chain extracted from cells of the magnetotactic bacterium *Magnetovibrio blakemorei* strain MV-1. (b) Fe L_3 XAS spectra and XMCD of the biogenic magnetite chain extracted from MV-1 recorded with circularly polarized X-rays parallel (red) and antiparallel (green) to the magnetization of the sample. (c) Magnified TEM image corresponding to the red area labeled in (a). (For interpretation of the references to color in this figure legend, the reader is referred to the web version of this article.)

elsewhere [56]. Careful comparison of the magnitude of the XMCD signal from intact MV-1 cells with that from the Goering et al. [24] data has shown that intracellular magnetosomes are fully magnetized [46]. Thus, the Fe L_{23} XAS and XMCD spectra measured from

biogenic magnetite can be considered as the standard spectrum of magnetite.

The extracted magnetosome chain sample experienced significant air contact between the time it was extracted and the time it was measured, yet there is little or no evidence of oxidation. *Why are the long time air-exposed extracted biogenic magnetosomes still stoichiometric?* Note that transmission X-ray detection was used for the spectra reported in both Figs. 4 and 5 and thus they are characteristic of the bulk of the sample, not the surface. Fig. 5c shows a magnified TEM image corresponding to the red area labeled in Fig. 5a. A dense membrane tightly adhering to these magnetite crystals is observed. This membrane may limit air contact, thereby effectively protecting the magnetic crystals from being oxidized.

In order to probe the protective character of the membrane, the biogenic magnetite extracted from cells of a magnetotactic bacterium, *M. blakemorei* strain MV-1, was investigated after prolonged oxidation. Fig. 6a–c present Fe L_3 spectra of magnetosome chains extracted from *M. blakemorei* recorded over an extended time period. These magnetosome chains were enclosed by membranes, as shown in the inset in each panel, and were exposed to air for 1 week, 2 months, and 8 months, respectively. As shown in Fig. 6c, the magnetosome chain which was exposed to air for 8 months still does not exhibit any extra peak on the low energy side of the Fe L_3-edge XAS spectra, but rather its spectrum is similar to the magnetosome chain exposed in air for only one week (Fig. 6a). This indicates that the membrane enclosing the magnetosomes effectively protects the magnetite single crystals from oxidation by air for a relatively long time. In order to further quantify the proportional changes of Fe ions in these stripped magnetosome chains, we compare the three XMCD spectra obtained from stripped magnetosome chains with the one acquired from the intracellular magnetosome chain, and with the reference XMCD spectrum reported by Goering et al. [24] (see Fig. 6d). All the XMCD spectra in Fig. 6d are similar, indicating that the membrane allows these extracted magnetosome chains to effectively resist air oxidization under ambient conditions. The excellent match in the XMCD intensity (after correction for the 50% reduction due to the 30° tilt geometry we use) between all of the magnetosome signals (which are measured without an externally applied field) with that from a magnetite thin film in a strong external magnetic field [24] shows that both the intracellular magnetosomes [46] and the stripped magnetosomes are highly stoichiometric, and are fully magnetized.

Gao et al. [57] reported that Fe_3O_4 nanoparticles are partly transformed into γ-Fe_2O_3 after heating at 200 °C for 3 h in air and are completely transformed into γ-Fe_2O_3 if they are heated at 600 °C for 3 h. In order to investigate the corresponding transformation for biogenic magnetite, we took biogenic magnetite isolated from MV-1 bacteria, stripped it of its membrane with surfactant, and heated it in air at 600 °C for 3 h. Fig. 7a presents a TEM image while Fig. 7b shows the Fe L_3 XAS spectra of the air-heated biogenic magnetite crystals recorded with parallel (red) and antiparallel (green) polarization, and the associated XMCD (blue). A strong peak is observed at 708 eV (labeled by an arrow in Fig. 7b). This is similar to the structure observed at the low energy side of the Fe L_3-edge signal of as-received Sigma–Aldrich nano-magnetite (Fig. 1c). This supports our interpretation that the Sigma–Aldrich nano-magnetite was a partially oxidized phase. Also, the experimental results for oxidized magnetosomes match well with a theoretical prediction that the Fe L_{23}XAS of maghemite should exhibit a peak on the lower energy side of the L_3 peak [58]. Finally, we suspect the reason that Fe L_{23} XAS spectra of maghemite reported by Anders et al. [30] and Brice-Profeta et al. [32] did not exhibit a peak on the lower energy side of the L_3 peak was due to the fact that their supposed maghemite samples were not pure maghemite but rather a mixture with a large fraction of magnetite.
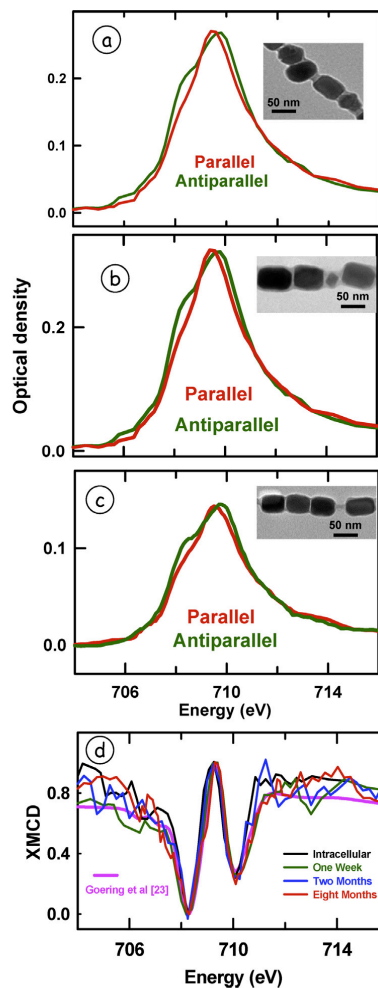
Fig. 6. Fe L_3 spectra of the extracted magnetosome chains, which have been exposed in air for (a) 1 week, (b) 2 months, and (c) 8 months, recorded with circularly polarized X-rays parallel (red) and antiparallel (green) to the magnetization of the sample. The insets in (a)–(c) indicate the magnetosome chains enclosed by the magnetosome membrane from which these spectra were obtained. (d) Comparison of the XMCD spectra, the difference signal (parallel minus antiparallel), for all three samples of the extracted magnetosome chains (1 week (green), 2 months (blue), 8 months (red)) and that of the intracellular magnetosome chain (black). The XMCD reported by Goering et al. [24] is also plotted, scaled by 50% (pink). (For interpretation of the references to color in this figure legend, the reader is referred to the web version of this article.)

4. Discussion

Carvallo et al. [40] presented a detailed study of the Fe L_{23} XAS and XMCD of biogenic magnetite (from *Shewanella putrefaciens* CIP 59.28) and abiogenic magnetite (nanoparticles prepared by adding 1 M NaOH to a suspension of lepidocrocite in an aqueous solution of $FeCl_2$). In that work the Fe L_{23} XAS spectra are very similar to each other and to the spectra of magnetosomes from MV-1 presented here, as well as to the spectra of abiogenic magnetite reported by Goering et al. [24]. (Note that the energy scale of the Carvallo et al.
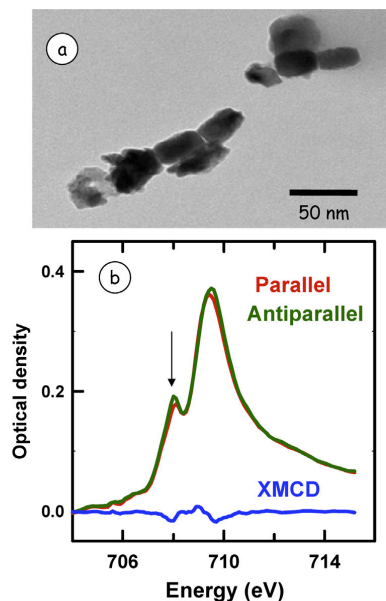
Fig. 7. (a) TEM image of the MV-1 derived magnetite heated in air at 600 C for 3 h. (b) Fe L$_3$ spectra of the air-heated magnetite recorded with circularly polarized X-rays parallel (red) and antiparallel (green) to the magnetization of the sample, and the associated XMCD. (For interpretation of the references to color in this figure legend, the reader is referred to the web version of this article.)

[40] spectra is displaced by almost 4 eV to higher energy – i.e. they claim the energy of the strongest XMCD signal is 712 eV, whereas our work, as well as that of Goering et al. [24] and many others, places the strongest XMCD signal at 708.2 eV.) Carvallo et al. [40] do see a small but reproducible difference in the XMCD spectra of their biogenic and abiogenic magnetite nanoparticles. By modeling the Fe L$_3$ XMCD signal with a linear combination of three Fe ion contributions in Fe$_3$O$_4$, they concluded that their (extracellular) biogenic nano-magnetite contained a higher amount of octahedral Fe(II) than their abiogenic nano-magnetite. In our study, we also observed differences in the XAS spectra between Sigma–Aldrich nano-magnetite and biogenic magnetite crystals biomineralized by cells of the magnetotactic bacterium *M. blakemorei*. Compared with the subtle XMCD difference investigated by Carvallo et al. [40], the difference between the XAS of biogenic and abiogenic magnetite reported in this work (Fig. 1a–c) is much larger. Based on the structural data obtained via XRD measurements (Section 3.2), it is clear that the difference between the XAS of biogenic and abiogenic magnetite found in this study is due to non-stoichiometry or partial oxidization in those samples showing the low energy L$_3$ peak. More importantly, we have shown that this XAS difference, the extra peak in the low energy side of L$_3$ region, could be "switched on" and "switched off" by using air oxidization and H$_2$ reduction methods, respectively. The small difference in XMCD reported by Carvallo et al. [40] may exist in our data set, but it is masked by the much larger difference due to a gross difference in the chemical nature of the two samples. Pattrick et al. [49] and Coker et al. [52] have used changes in the XMCD signal to study non-stoichiometric effects in bio-generated magnetite in a similar manner. While these results are completely credible, they are a more subtle effect than the effects reported in this work.

5. Summary

This work aimed at better understanding the reasons for inconsistencies in the literature regarding the shape of Fe L$_3$ XAS spectra claimed to be that of Fe$_3$O$_4$. We used STXM, powder X-ray diffraction and chemical modification to show that magnetosomes extracted from MV-1 are stoichiometric magnetite while as-received synthetic nano-magnetite was partly oxidized, with a powder pattern closer to that of γ-Fe$_2$O$_3$ than that of Fe$_3$O$_4$. Our results suggest that one of the reasons for differing literature XAS spectra of Fe$_3$O$_4$ and γ-Fe$_2$O$_3$ is due to differences in the samples. In particular, some samples that were considered to be either Fe$_3$O$_4$ or γ-Fe$_2$O$_3$ were most likely solid solutions of Fe$_3$O$_4$ and γ-Fe$_2$O$_3$. Other factors that can play a role are (i) differences in detection method, with surface-sensitive TEY being more likely to show the 708 eV feature characteristic of partial oxidation; and (ii) non-stoichiometry of Fe$_3$O$_4$ samples, in terms of modified site occupancies. X-ray absorption spectroscopy, using both the Fe L-edge spectral shape and detailed analysis of the XMCD, is a useful tool to probe site occupancies, as outlined in this work and exploited in detailed studies by Pattrick et al. [49] and Coker et al. [52]. Finally, we showed that the membrane enclosing the magnetite crystals in MV-1 magnetotactic bacteria can effectively protect magnetite crystals from being oxidized. At this point we are puzzled as to why the membrane in magnetosome extracts appears to be air-impervious, while that same membrane, inside the cell, is able to transport Fe ions and oxygen during magnetosome synthesis. Further studies are required to understand this phenomenon.

Acknowledgements

References

[1] H.I. Adegoke, F.A. Adekola, O.S. Fatoki, B.J. Ximba, Pol. J. Environ. Stud. 22 (2013) 7.
[2] R.M. Cornell, U. Schwertmann, The Iron Oxides: Structures, Properties, Reactions, Occurrences and Uses, Wiley VCH Press, Weinheim, Germany, 2003.
[3] R. Zboril, A. Bakandritsos, M. Mashlan, V. Tzitzios, P. Dallas, Ch. Trapalis, D. Petridis, Nanotechnology 19 (2008) 095602.
[4] M. Mohapatra, S. Anand, Int. J. Eng. Sci. Technol. 2 (2010) 127.
[5] K. Yamaguchi, K. Matsumoto, T. Fujii, J. Appl. Phys. 67 (1990) 4493.
[6] G. Neri, A. Bonavita, G. Rizzo, S. Galvagno, S. Capone, P. Siciliano, Sens. Actuators B: Chem. 114 (2006) 687.
[7] J. Zhang, Y. Wang, H. Ji, Y. Wei, N. Wu, B. Zuo, Q. Wang, J. Catal. 229 (2005) 114.
[8] Y. Shi, M. Shi, Y. Qiao, J. Tu, H. Chen, Nanotechnology 23 (2012) 395601.
[9] M. Fleet, Acta Crystallogr. B 37 (1981) 917.
[10] M. Descostes, F. Mercier, N. Thromat, C. Beaucaire, M. Gautier-Soyer, Appl. Surf. Sci. 165 (2000) 288.
[11] J. Jolivet, P. Belleville, E. Tronc, J. Livage, Clays Clay Miner. 40 (1992) 531.
[12] E. Schmidbauer, M. Keller, J. Magn. Magn. Mater. 297 (2006) 107.
[13] G. Da Costa, E. De Grave, P. De Bakker, R. Vandenberghe, Clays Clay Miner. 43 (1995) 656.
[14] C.A. Gorski, M.M. Scherer, Am. Mineral. 95 (2010) 1017.
[15] F. De Groot, J. Fuggle, B. Thole, G. Sawatzky, Phys. Rev. B 42 (1990) 5459.
[16] C. Chen, Y. Idzerda, H.-J. Lin, N. Smith, G. Meigs, E. Chaban, G. Ho, E. Pellegrin, F. Sette, Phys. Rev. Lett. 75 (1995) 152.

26   *X. Zhu et al. / Journal of Electron Spectroscopy and Related Phenomena 199 (2015) 19–26*

[17] A.P. Hitchcock, Soft X-ray imaging and spectromicroscopy, in: G.V. Tendeloo, D.V. Dyck, S.J. Pennycook (Eds.), Handbook of Nanospectroscopy, Wiley VCH Press, Weinheim, Germany, 2012, p. 745.
[18] P. Kuiper, B.G. Searle, L.-C. Duda, R.M. Wolf, P.J. van der Zaag, J. Electron Spectrosc. Relat. Phenom. 86 (1997) 107.
[19] F. Schedin, P. Morrall, V. Petrov, S. Case, M. Thomas, E. Dudzik, G. Van der Laan, G. Thornton, J. Magn. Magn. Mater. 211 (2000) 266.
[20] A. De Castro, P. Fonseca, J. Pacheco, J. Da Silva, E. Da Silva, M. Santana, J. Magn. Magn. Mater. 233 (2001) 69.
[21] J. García, G. Subías, J. Phys.: Condens. Matter 16 (2004) R145.
[22] Y. Lee, J. Lee, C.J. Bae, J.G. Park, H.J. Noh, J.H. Park, T. Hyeon, Adv. Funct. Mater. 15 (2005) 503.
[23] P. Thakur, W.K. Choi, K.H. Chae, J. Korean Phys. Soc. 53 (2008) 3694.
[24] E.J. Goering, M. Lafkioti, S. Gold, G. Schuetz, J. Magn. Magn. Mater. 310 (2007) e249.
[25] E. Goering, Phys. Status Solidi B 248 (2011) 2345.
[26] V. Pool, M. Klem, C. Chorney, E. Arenholz, Y. Idzerda, J. Appl. Phys. 109 (2011) 07B529.
[27] A. Michelin, E. Drouet, E. Foy, J. Dynes, D. Neff, P. Dillmann, J. Anal. At. Spectrom. 28 (2013) 59.
[28] Z. Wang, L. Wu, J. Zhou, W. Cai, B. Shen, Z. Jiang, J. Phys. Chem. C 117 (2013) 5446.
[29] P.J. Wong, W. Zhang, K. Wang, G. van der Laan, Y. Xu, W.G. van der Wiel, M.P. de Jong, J. Mater. Chem. C 1 (2013) 1197.
[30] S. Anders, M. Toney, T. Thomson, R. Farrow, J.-U. Thiele, B. Terris, S. Sun, C. Murray, J. Appl. Phys. 93 (2003) 6299.
[31] S. Sun, H. Zeng, D.B. Robinson, S. Raoux, P.M. Rice, S.X. Wang, G. Li, J. Am. Chem. Soc. 126 (2004) 273.
[32] S. Brice-Profeta, M. Arrio, E. Tronc, I. Letard, C.C. dit Moulin, P. Sainctavit, Phys. Scr. T 115 (2005) 626.
[33] D. Kim, H. Lee, G. Kim, Y. Koo, J. Jung, H. Shin, J.-Y. Kim, J.-S. Kang, Phys. Rev. B 79 (2009) 033402.
[34] B. Gilbert, J.E. Katz, J.D. Denlinger, Y. Yin, R. Falcone, G.A. Waychunas, J. Phys. Chem. C 114 (2010) 21994.
[35] R. Desautels, E. Skoropata, Y. Chen, H. Ouyang, J. Freeland, J. van Lierop, J. Phys.: Condens. Matter 24 (2012) 146001.
[36] E. Lee, D. Kim, J. Hwang, K. Lee, S. Yoon, B. Suh, K.H. Kim, J.-Y. Kim, Z. Jang, B. Kim, Appl. Phys. Lett. 102 (2013) 133703.
[37] C. Piquer, M.A. Laguna-Marco, A.G. Roca, R. Boada, C. Guglieri, J. Chaboy, J. Phys. Chem. C 118 (2014) 1332.
[38] P.S. Miedema, F.M.F. de Groot, J. Electron Spectrosc. Relat. Phenom. 187 (2013) 32.

[39] D.A. Bazylinski, T.J. Williams, C.T. Lefèvre, D. Trubitsyn, J. Fang, T.J. Beveridge, B.M. Moskowitz, B. Ward, S. Schübbe, B.L. Dubbels, Int. J. Syst. Evol. Microbiol. 63 (2013) 1824.
[40] C. Carvallo, P. Sainctavit, M.-A. Arrio, N. Menguy, Y. Wang, G. Ona-Nguema, S. Brice-Profeta, Am. Mineral. 93 (2008) 880.
[41] CAS Number: 1317-61-9; Assay: 95%; Particle Size: <5 μm (accessed January 2014).
[42] A.J. Dean, D.A. Bazylinski, Curr. Microbiol. 39 (1999) 219.
[43] E. Alphandéry, Y. Ding, A. Ngo, Z. Wang, L. Wu, M. Pileni, ACS Nano 3 (2009) 1539.
[44] K. Kaznatcheev, C. Karunakaran, U. Lanke, S. Urquhart, M. Obst, A. Hitchcock, Nucl. Instrum. Methods B 582 (2007) 96.
[45] C. Jacobsen, S. Wirick, G. Flynn, C. Zimba, J. Microsc. 197 (2000) 173.
[46] S.S. Kalirai, K.P. Lam, D.A. Bazylinski, U. Lins, A.P. Hitchcock, Chem. Geol. 300 (2012) 14.
[47] K.P. Lam, A.P. Hitchcock, M. Obst, J.R. Lawrence, G.D. Swerhone, G.G. Leppard, T. Tyliszczak, C. Karunakaran, J. Wang, K. Kaznatcheev, Chem. Geol. 270 (2010) 110.
[48] A.P. Hitchcock, aXis2000 is Written in Interactive Data Language (IDL), 2014, It is available free for non-commercial use from: http://unicorn.mcmaster.ca/aXis2000.html
[49] R.A. Pattrick, G. Van Der Laan, C.M.B. Henderson, P. Kuiper, E. Dudzik, D.J. Vaughan, Eur. J. Mineral. 14 (2002) 1095.
[50] V.N. Antonov, B.N. Harmon, A.N. Yaresko, Phys. Rev. B 67 (2003) 024417.
[51] D. Nolle, E. Goering, T. Tietze, G. Schütz, A. Figuerola, L. Manna, New J. Phys. 11 (2009) 033034.
[52] V.S. Coker, C.I. Pearce, C. Lang, G. van der Laan, R.A. Pattrick, N.D. Telling, D. Schüler, E. Arenholz, J.R. Lloyd, Eur. J. Mineral. 19 (2007) 707.
[53] V. Coker, J. Byrne, N. Telling, G. Van der Laan, J. Lloyd, A. Hitchcock, J. Wang, R. Pattrick, Geobiology 10 (2012) 347.
[54] D. Peak, T. Regier, Environ. Sci. Technol. 46 (2012) 3163.
[55] F. Schedin, E. Hill, G. Van der Laan, G. Thornton, J. Appl. Phys. 96 (2004) 1165.
[56] J. Li, Y. Pan, Geomicrobiol. J. 29 (2012) 362.
[57] M. Gao, W. Li, J. Dong, Z. Zhang, B. Yang, World J. Condens. Matter Phys. 1 (2011) 49.
[58] J. Crocombette, M. Pollak, F. Jollet, N. Thromat, M. Gautier-Soyer, Phys. Rev. B 52 (1995) 3143.

Further reading

[59] A.J.M. Kuipers, V.A.M. Brabers, Phys. Rev. B 14 (1976) 1401.

Chapter 5

Chemical and magnetic studies of greigite and greigite magnetosomes in multicellular magnetotactic prokaryotes

This chapter presents results of chemical and magnetic studies of multicellular magnetotactic prokaryotes (MMP) by means of STXM technique. Specifically, it investigates the difference of XAS and XMCD spectra between abiogenic Fe_3S_4 nanoparticles and Fe_3S_4 magnetosomes in MMP. The spectral difference between Fe_3O_4 and Fe_3S_4 is also discussed. It is demonstrated that two sulfur species are present inside MMP. These results are discussed in terms of possible sulfur metabolism mechanisms in MMP.

5.1 Introduction

Multicellular magnetotactic prokaryotes (MMPs) are one of the most interesting MTB due to their unique multicellular morphology (Balkwill et al., 1980). They have been detected in a large number of aquatic habitats (Bazylinski et al., 1990; Delong et al., 1993; Simmons et al., 2004; Farina et al., 1983). Most MMPs are roughly spherical shaped cell aggregates with a diameter varying between 3-12 μm (Keim et al., 2006). Typically they are composed of approximately 10-40 genetically-identical Gram-negative cells that are tightly bound to one another and radially organized around an internal acellular compartment located at the center of the whole organism (see Figure 1.3e in Chapter 1) (Balkwill et al., 1980; Keim et al., 2006, 2004). Recently, another kind of MMP with an ellipsoidal, rather than spherical, morphology was described, which is composed of ~40 cells but arranged in interlaced circles (see Figure 1.3f in Chapter 1) (Zhou et al., 2012).

Although a few non-magnetic iron-sulfide minerals such as mackinawite (tetragonal FeS) and cubic form of FeS have been identified in MMP, the dominant mineral phase in magnetosomes produced by MMPs is greigite (Fe_3S_4) (Anders et al., 1998; Pósfai et al., 1998). As the only known magnetotactic multicellular prokaryote, MMPs represent an important model for understanding cell evolution, multicellularity, sulfur metabolism, and magnetosome biomineralization in bacteria (Keim et al., 2006). In this study, the XAS and XMCD spectra of abiogenic Fe_3S_4 nanoparticles syntheized via hydrothermal method were measured. These spectra were then used as reference spectra to investigate the chemical and magnetic properties of MMP, with the aim of better understanding the magnetic microstructures as well as the Fe_3S_4 magnetosome biomineralization in this interesting microorganism.

5.2 Materials and Methods

5.2.1 Preparation of MMPs

Since the isolation and cultivation of MMPs in axenic cultures have not been successful, environmental MMP samples were used in this study. Water and sediment were collected at Araruama Lagoon (22° 50' S, 42° 13' W) in Rio de Janeiro State, Brazil. MMPs were magnetically isolated with a custom glass flask and home-made coil, as previously described (Lins et al., 2003). A droplet of enriched MMPs was deposited on formvar coated TEM copper grids. After several washes with distilled water, the grid is dried in air and then anaerobically transported to the synchrotron facility for STXM measurements.

5.2.2 Synthesis and characterization of Fe_3S_4 nanoparticles

The abiotic Fe_3S_4 nanoparticles were prepared by hydrothermal reactions of ferric chloride ($FeCl_3 \cdot 6H_2O$) with thiourea ($SC(NH_2)_2$) in ethylene glycol ($C_2H_6O_2$) solution at 180 °C for 12

hours, as described in (Zhang and Chen, 2009). The phase composition of the as-synthesized

Fe_3S_4 sample was determined by powder X-ray diffraction (XRD) using a Bruker D8 Advance

instrument with Co Kα radiation. The stoichiometric composition of the sample was further

confirmed with the energy-dispersive X-ray spectrometer (EDS) on a JEOL 7000F scanning

electron microscope (SEM). For STXM-XMCD analysis, the Fe_3S_4 nanoparticles were sonically

dispersed in ethanol and a droplet of the solution was deposited onto a formvar-coated copper

grid. The grid sample was anaerobically transported to synchrotron facility for further analysis.

5.3 STXM-XMCD Measurements

STXM measurements were carried out at 10ID-1 spectromicroscopy (SM) beamline at

the CLS and 11.0.2 beamline at the ALS. These two beamlines both use elliptically polarizing

undulator (EPU) as radiation source, which provides nearly 100% circularly polarized light at the

Fe $L_{2,3}$ region at 10ID-1 beamline (CLS) and about 90% circularly polarized light at 11.0.2

beamline (ALS). Details of the STXM instrumentation in these two beamlines have been

mentioned in section 2.3.2 in Chapter 2 and elsewhere (Kaznatcheev et al., 2007; Tyliszczak et

al., 2004). Data analysis was performed using aXis2000 software. The procedures to analyze

STXM and STXM-XMCD data using axis2000 have been described in section 3.3.

5.4. Results

5.4.1 S and Fe $L_{2,3}$ analyses of abiotically-produced Fe_3S_4 nanoparticles

Two mineral phases were identified from the powder X-ray diffraction (XRD) patterns of

the hydrothermally-produced, abiotic Fe_3S_4 nanoparticles (**Figure 5.1**). One was Fe_3S_4 (red

circle) and the other, mackinawite (tetragonal FeS) (blue rhombus). According to semi-
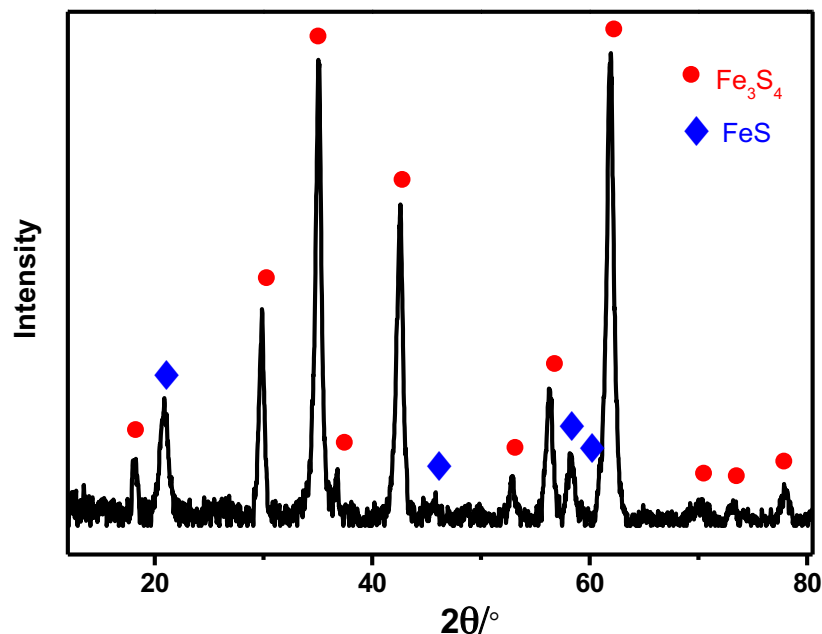
Figure 5.1 Powder X-ray diffraction (XRD) patterns of the as-synthesized Fe_3S_4 nanoparticles, recorded using Co Kα radiation. Two mineral phases are identified: one is Fe_3S_4 labeled with red circle; the other one is FeS phase (mackinawite) labeled with blue rhombus.

quantitative analysis, Fe_3S_4 was identified as the major phase while the percent mackinawite phase was estimated to be ~10% wt%. The presence of mackinawite in the sample may be due to decomposition of Fe_3S_4 which occurs about 190°C under hydrothermal conditions as reported by Uda (1967). However, since mackinawite is non-magnetic at ambient temperature, its presence likely does not have a detectable effect on the magnetic characterization of the abiotically-produced Fe_3S_4 nanoparticles.

Figure 5.2a presents a S 2p XAS spectrum of the abiotically-produced Fe_3S_4 nanoparticles and inset is the STXM image at 710 eV, where XAS and XMCD spectra are measured. As shown in Figure 5.2a, the S 2p spectrum of Fe_3S_4 shares similar features with other thiospinels

such as linnaeite (Co_3S_4) and carrollite ($CuCo_2S_4$) (Li et al., 1995). Generally, four well-defined peaks were observed, which are labeled A, B, C and D in Figure 5.2a. According to a previous study (Li et al., 1995), peak A corresponds to the transition of S 2p electron to S 3s-like states mixed with unoccupied Fe 3d crystal-field bands in the band gap; B is due to the transition of S 2p electron to S 3s-like states; and peaks C and D are attributed to transitions of S 2p electron to t_{2g} and e_g Fe 3d states.

Figure 5.2b shows Fe $L_{2,3}$-edge XAS spectra of hydrothermally-synthesized Fe_3S_4 nanoparticles recorded with circularly polarized X-rays parallel and antiparallel to the magnetic moment of the sample. The XMCD spectrum of Fe_3S_4 nanoparticles, obtained by taking the difference between two XAS spectra, is shown on the bottom panel. Two main peaks are present in the Fe $L_{2,3}$ XAS spectra and are due to the spin-orbit splitting of the Fe 2p core level into the L_3 ($2p_{3/2}$) and L_2 ($2p_{1/2}$) components. However, Chang et al. (2012a) reported an $L_{2,3}$ XAS spectrum of Fe_3S_4, which showed a two-peak feature with an energy separation of 1.5 eV in the L_3 energy region (see Fig. 1.18) instead of the single peak in these results. The authors claimed that the high-energy peak in the XAS spectrum was due to the presence of a non-magnetic, oxidized layer on the Fe_3S_4 crystal surface, which dominated the Fe $L_{2,3}$ XAS signal since the surface-sensitive TEY (total-electron-yield) detection mode was used to acquire XAS spectra in their study. Letard et al. (2005) also observed an amorphous shell surrounding Fe_3S_4 grains using electron energy loss spectroscopy (EELS) in a TEM. The shape of the EELS spectra of Fe_3S_4 they reported is similar to that of Chang et al. (2012a), but has a different energy scale. Recently, Bauer et al. (2014) reported an Fe $L_{2,3}$ XAS spectrum of Fe_3S_4 crystals which showed only a single peak in the L_3 region, similar to that presented in Figure 5.2b in this study. Besides the chemical purity of the Fe_3S_4, the detection mode used to determine XAS spectra might be
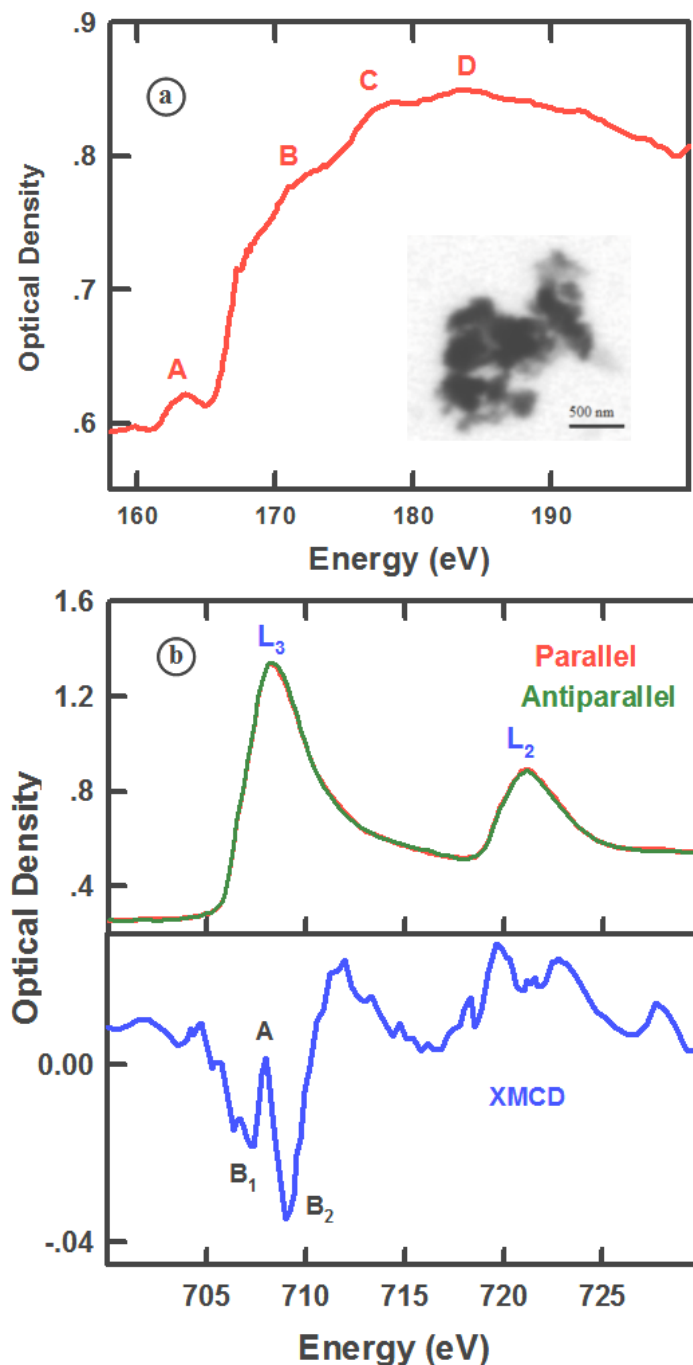
Figure 5.2 S 2p XAS (a) and Fe 2p XAS and XMCD spectra (b) of hydrothermally synthesized Fe_3S_4 nanoparticles. The inset in Figure 5.2a is a STXM image of Fe_3S_4 nanoparticles at 710 eV, where the XAS spectra are collected. The XMCD spectrum (blue) in Figure 5.2 b is obtained by taking two XAS spectra obtained with circularly polarized X-rays parallel (red) and antiparallel (green) to the magnetic moment of the sample.

another reason for the inconsistency among the published Fe $L_{2,3}$ XAS spectra of this mineral

(Bauer et al., 2014; Chang et al., 2012a; Letard et al., 2005). Although TEY is a common

detection mode used to collect XAS spectra, it is a surface-sensitive technique and generally has

a probing depth of only a few nm. Greigite is relatively easily oxidized when exposed to air and

oxidization first occurs at the crystal surface (Santos-Carballal et al., 2016). In this case, the XAS

spectra collected with TEY detection mode may be heavily influenced by surface oxidization and

surface cleaning. For example, Nolle et al.(2009) reported that a higher oxidation state of Fe was

observed at the surface of crystalline $FePt/FeO_x$ when the detection mode was switched from

transmission to TEY.

The XMCD spectrum of Fe_3S_4 (Figure 5.2 b) exhibits three characteristic peaks in the L_3

region located at 707.1 eV (feature B_1), 708.0 eV A) and 709.1eV (B_2). Since Fe_3S_4 is

structurally a ferrimagnetic inverse spinel (Pattrick et al., 2002; Rickard and Luther, 2007),

similar to Fe_3O_4, these three peaks are thought to correspond to three different iron sites in the

Fe_3S_4 crystal structure: $d^6 O_h$ (octahedral Fe^{2+} site, peak B_1), $d^5 T_d$ (tetrahedral Fe^{3+} site, peak A),

and $d^5 O_h$ (octahedral Fe^{3+} site, peak B_2). However, according to our previous study (Kalirai et al.,

2012; Lam et al., 2010; Zhu et al., 2015a), the three peaks in the Fe L_3 XMCD spectrum of Fe_3O_4

occur at 708.1 eV, 709.1 eV, and 709.9 eV. It is possible that the differences in bond lengths and

effective charges between Fe_3O_4 and Fe_3S_4 crystals are responsible for the negative shift in the

XMCD spectra (Chang et al., 2012a). In addition to the energy shift, the shape of Fe_3S_4 XMCD

spectrum is also different from that of Fe_3O_4. Letard et al. (2005) claimed the XMCD difference

was due to the presence of iron vacancies in Fe_3S_4. Chang et al. (2012a) reported a similar

XMCD spectrum of Fe_3S_4 and found that the experimental XMCD spectrum can be fit well only

by using $O_h Fe^{2+}$ and $d^6 O_h Fe^{3+}$ peaks obtained by multiplet calculations, but without using a

calculated $T_d Fe^{3+}$ peak. However, neutron diffraction patterns indicated that the same Fe_3S_4 sample (Chang et al., 2012a) had almost full Fe occupancy (Chang et al., 2009a). Regarding the electronic structure of Fe_3S_4, Spender et al (1972) reported that Fe_3S_4 is a semi-metal and proposed two alternative schemes for the electronic structures: one is it has an average of Fe(II) and Fe(III) on the octahedral sites; the other is it has only Fe(II) on octahedral sites. Later, the first scheme was supported by ab initio calculation (Devey et al., 2009). However, in a recent theoretical calculation of the electronic structure of Fe_3S_4, Zhang et al. (2012) reported that Fe_3S_4 is not half-metallic like Fe_3O_4 but is a normal metal with a complicated Fermi surface. This might be consistent with the Fe $L_{2,3}$-edge XAS spectra of Fe_3S_4 in Figure 5.2b, which show similar features as a Fe crystal (Bauer et al., 2014).

5.4.2 Distribution of other important elements in MMPs

In order to characterize the distribution of elements such as sulfur, oxygen and iron in whole MMPs, the "stack map" method was used in this study. A stack map is the difference of two STXM OD images recorded at a characteristic X-ray absorption energy (on-resonance) and a pre-edge energy (off-resonance). **Figures 5.3 a-c** show the stack maps of S, O and Fe within an MMP, derived from the difference of two STXM OD images at 173 and 168 eV, 540 eV and 528 eV, and 708.3 and 700 eV, respectively. The two numbers on the upper and lower right corner of each stack map refer to the OD limits of the gray scale display. **Figure 5.3d** shows the re-scaled color composite of the S (green), O (blue), and Fe (red) stack maps. In most unicellular MTB cells, magnetosomes are typically arranged in chains that lie along the long axis of the cell such that the magnetic moment of the chain is maximized, which provides preferred orientation of the cells in an aquatic environment (Frankel, 1984). However, in MMP, the magnetosomes (red in Figure 5.3d) inside MMP are not arranged as long chains but rather as aggregates or clumps and

short chains at multiple locations at the periphery of the cells (Keim et al., 2004). Winklhofer et al. (2007) once reported that the degree of magnetic optimization (DMO) of individual MMPs in vivo was consistently above 80%.
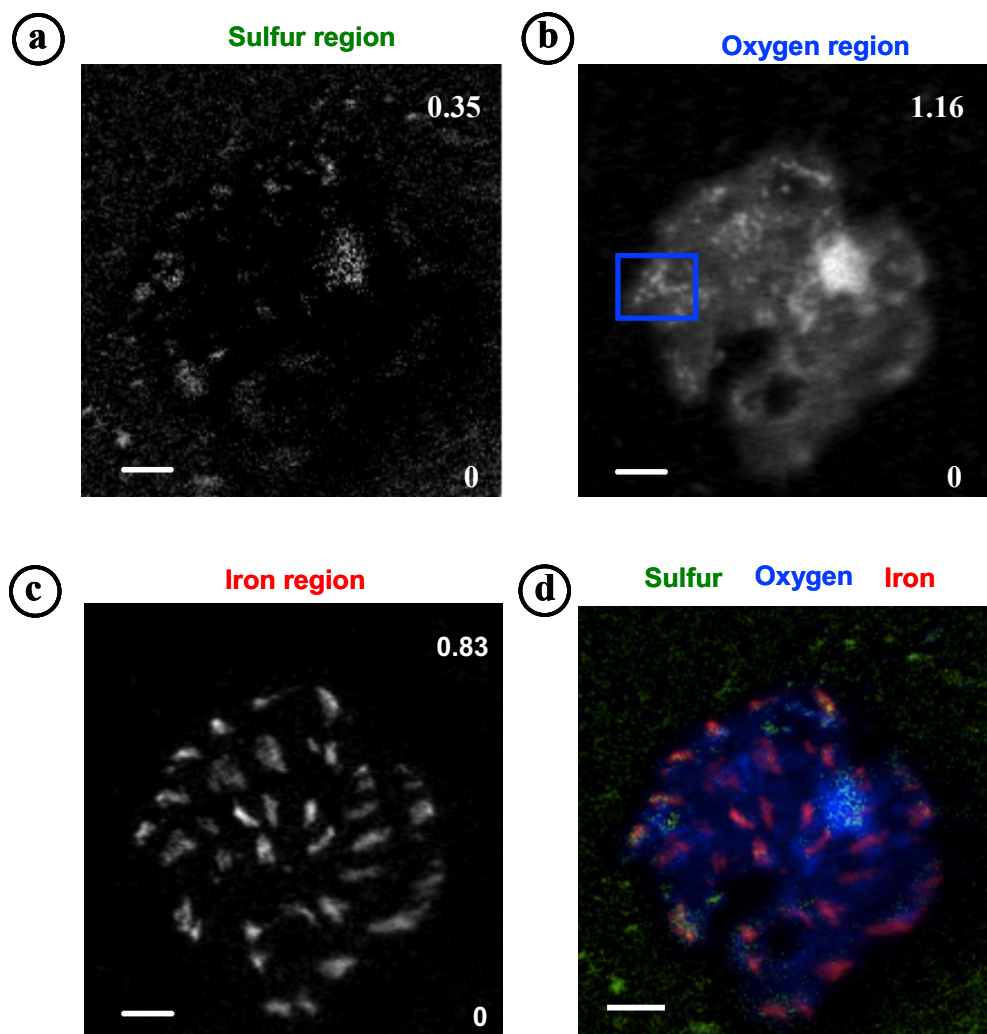
Figure 5.3 (a)~(c). Stack maps of S (a), O (b), and Fe (c) in a MMP cell, derived from the difference of two STXM OD images at 173 / 150 eV, 540 / 528 eV, and 708.3 / 700 eV, respectively; the blue rectangle in Figure 5.3b indicates some oxygen-rich region surrounding Fe_3S_4 magnetosome chains, which may be some intermediate oxides involved in the Fe_3S_4 biomineralization process (Farina et al., 1990).**(d).** A re-scaled colour composite of the S (green), O (blue), and Fe (red) stack maps. The scale bar in Figure 5.3 represents 1 μm.

As expected, the O signal is distributed throughout the cells of the MMP as shown in Figure 5.3d, most surely coming from the organic material of the cell (e.g., protein, lipids etc.) as well as other oxygen-containing molecules such as phosphate and sulfate. In addition, some oxygen-rich regions (labelled with a blue rectangle in Figure 5.3b) are also present surrounding Fe_3S_4 magnetosome chains, which may be some intermediate oxides involved in the Fe_3S_4 biomineralization process (Farina et al., 1990). A detailed analysis at the S 2p edge is described below.

Figure 5.4 plots four reference spectral, including sulphide phase (S-sulphide), sulphate phase (S-sulphate), chloride and matrix (no S signals), which are used to derive the component map of each species using the "stack fit" method based on singular value decomposition (SVD) analysis (Koprinarov et al., 2002). Each model spectrum in Figure 5.4 was measured from uniform regions in the S 2p image stack. However, because the general shapes of the S $L_{2,3}$ XAS spectra for mono-sulphides, di-sulphides and Fe_3S_4 are very similar (Li et al., 1995), it is challenging to accurately distinguish different sulphide species with the stack fit method at the S 2p edge. The component map of the sulphide phase (S-sulphide) derived with stack fit as shown in **Figure 5.5a**, appears to be mainly due to intracellular Fe_3S_4 magnetosomes. In addition, some sulphide phase, probably from the marine water and resulting salts from evaporation from the samples, is observed surrounding the MMPs outside of the cells. Compared with the S-sulphide spectrum (blue) in Figure 5.4, the S-sulphate spectrum (red) has two sharp features (A and B) due to the presence of SO_4^{2-} anion, which can be assigned to the transition of S 2p electrons to t_2 (S 3s-like) state and to S 3d-like states, respectively (Li et al., 1995). The component map of S-sulphate derived with stack fit is presented in **Figure 5.5b**. Figure 5.4 also indicates that some chloride is present inside MMPs, whose component map is shown in **Figure 5.5c**. The two sharp
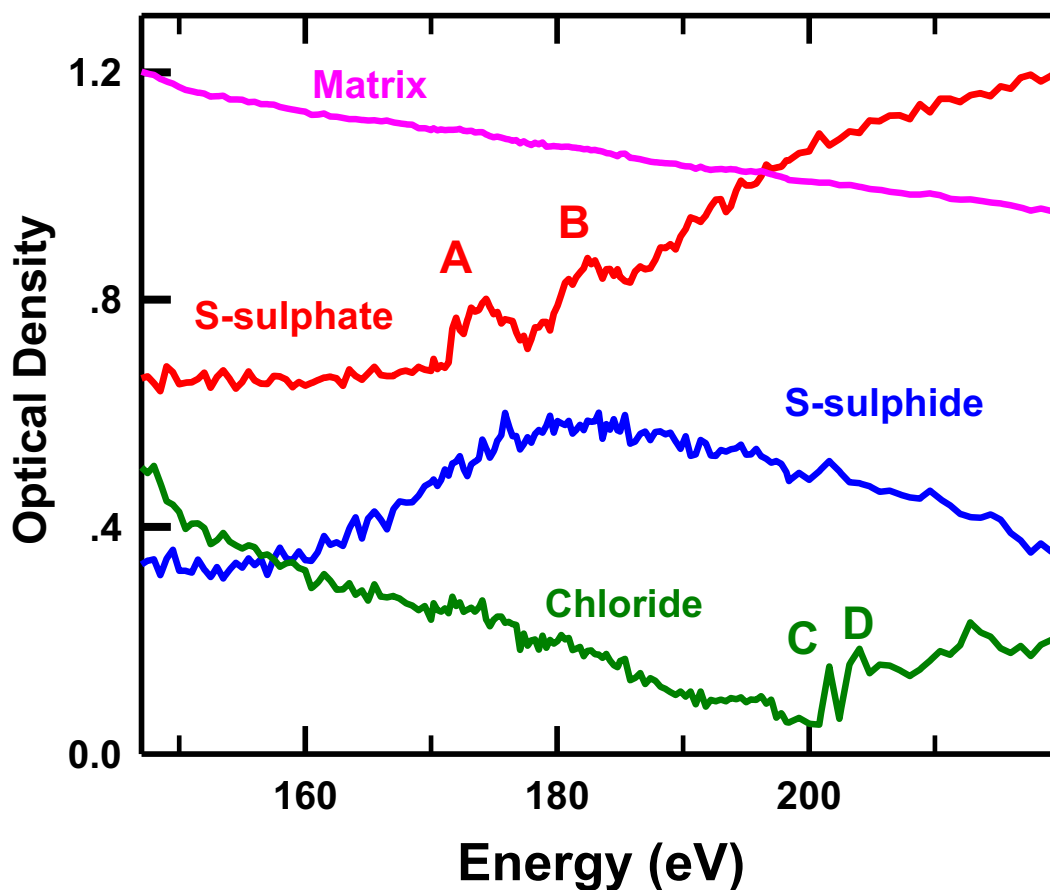
Figure 5.4 Four spectral models, including sulphide phase (S-sulphide), sulphate phase (S-sulphate), chloride and matrix (no S signals), which are used to derive the component map of each species from the S2p stack of a MMP.

features (C and D) in the energy range of 200~205 eV in the chloride spectrum (blue) in Figure

5.4 are attributed to the transition of Cl 2p electrons to 3d orbitals. **Figure 5.5d** presents the

component map of the region free of S in an MMP, which is derived using the "matrix" model

spectrum in Figure 5. 4. **Fig. 5.5e** shows a scaled color composite of the S-sulphide (Figure 5.5a),

S-sulphate (Figure 5.5b) and cloride map (Figure 5.5c). As shown in Figure 5.5c, the S-sulphide

(green) signal is spatially correlated with the Fe signal (Figure 5.3c) inside MMPs while the S-

sulphate signal (red) appears around the Fe signal in many areas. This suggests that sulphate is also involved in the Fe_3S_4 biomineralization process. Genomic and genetic evidence strongly indicates that MMPs are dissimilatory sulfate-reducing bacteria (Delong et al., 1993).
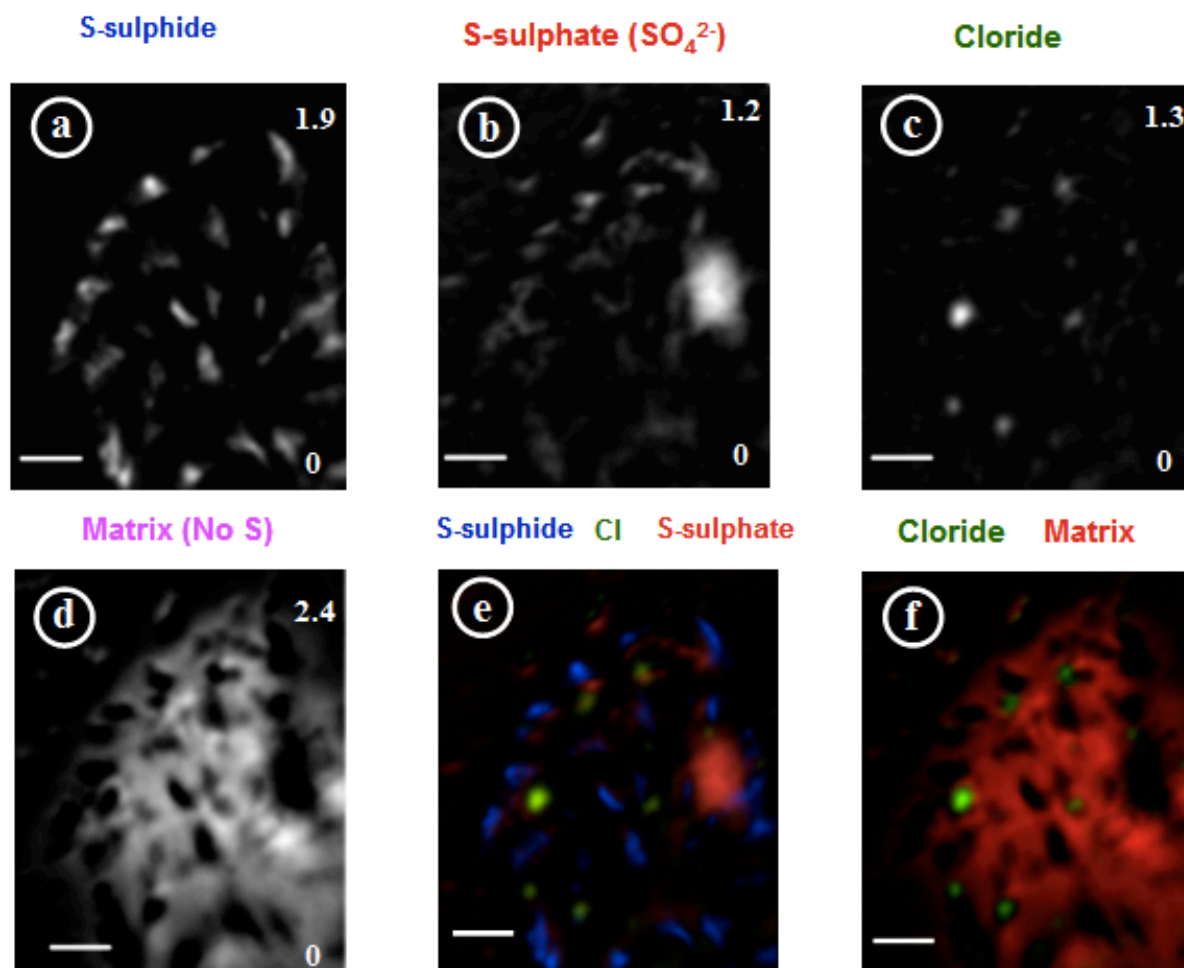
Figure 5.5 Sulphur component distribution in a MMP cell obtained by using stack fit method. Sulphide (a), sulphate (b), chloride (c) and matrix (d) regions in a MMP cell; (e) scaled color composite of S-sulphide (Figure 5.5a), S-sulphate (Figure 5.5b) and cloride map (Figure 5.5c); (e) scaled color composite of chloride (Figure 5.5c) and matrix (Figure 5.5d). The scale bar in Figure 5.5 represents 1 μm.

Figure 5.5 f is a color-coded composite of chloride (green, Figure 5.5c) and matrix (red, Figure 5.5e) component maps. As shown in Figure 5.5f, the chloride signal is roughly spherical in shape

and is distributed in multiple locations inside MMPs. It is most likely a remnant of the high amount of chloride ion in marine salts. However, chloride might also be associated with some intracellular inclusions in MMPs as chloride has also been observed in some phosphorus-containing granules in MMPs (Keim et al., 2005).

5.4.3 Magnetic measurements on MMPs

Figures 5.6a and 5.6b show a STXM OD image of a MMP cell at 707 eV but recorded with circularly polarized X-rays parallel and antiparallel to the magnetic moment of the sample, respectively. Note 707 eV is where the first XMCD peak of Fe_3S_4 magnetosomes occurs. **Figure 5.6c** shows the XMCD map difference between these two OD images, which indicates the intensity and polarity of XMCD signals. It should be notable that the XMCD polarity depends on the orientation of the spin polarization of X-ray photons relative to the magnetization of the sample. In a recent magnetic configuration model for one MMP, Acosta-Avalos et al. (2012) proposed that the cellular magnetic moment is given by the vector sum of the magnetic moments of each constituent cell, which is arranged in a spherical helix and aligns the organism along the magnetic field in the same way as other MTB species.
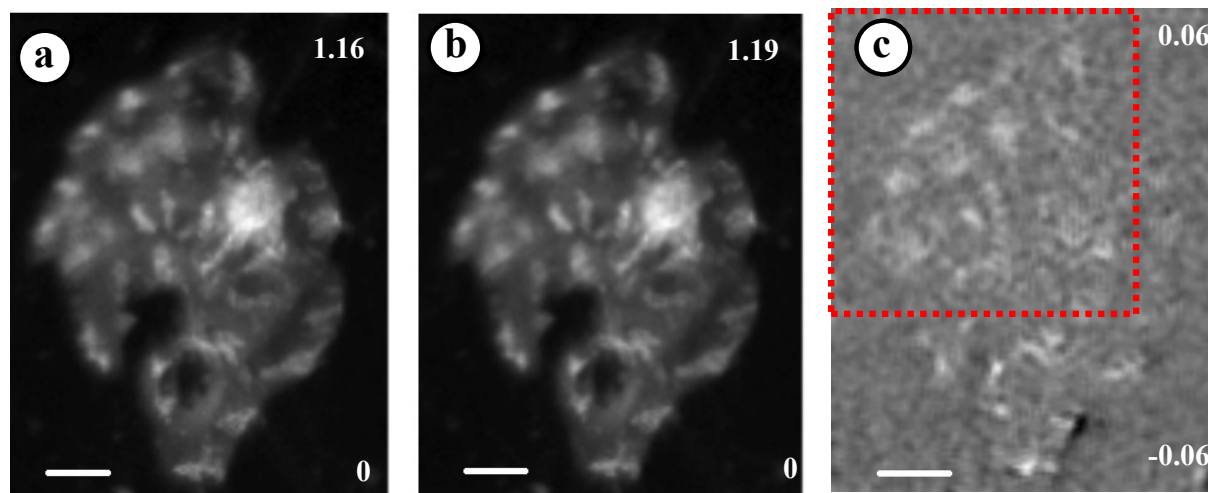
Figure 5.6 STXM OD images and XMCD map of a whole MMP cell. Two STXM OD image of a MMP cell at 707eV but recorded with circularly polarized X-rays parallel (a) and anti-parallel (b) to the magnetic moment of the sample, respectively. (c) XMCD map of the cell. The red region demonstrates where the XMCD spectra were collected. The scale bar in Figure 5.6 represents 1 μm.

An Fe $L_{2,3}$-edge XAS spectra of Fe_3S_4 magnetosomes in an MMP cell (red area labelled in Figure 5.6c) is shown in **Figure 5.7a** which was recorded with left and right circularly polarized X-rays, respectively. Compared with the Fe L_3 spectra of abiotic Fe_3S_4 nanoparticles in Figure 5.2a, which only show a single peak at about 708 eV, the spectra of biogenic Fe_3S_4 magnetosomes show an additional feature in the 708.5 eV to 710 eV energy range, which was indicated by the arrow in Figure 5.7a. Letard et al. (2007) reported a similar feature at a higher energy position than the main L_3 peak in pyrrhotite (Fe_7S_8) and found that this feature decreased when the sample surface was removed although the MCD signals did not change with the elimination of the sample surface. Letard et al. (2007) concluded this high-energy feature to be a result of the oxide layer surrounding the Fe_7S_8 surface and concluded that this surfacial oxide was not magnetic and thus did not contribute to the XMCD signals. **Figure 5.7b** shows a comparison between the Fe $L_{2,3}$-edge XMCD spectra of Fe_3S_4 nanoparticles and Fe_3S_4
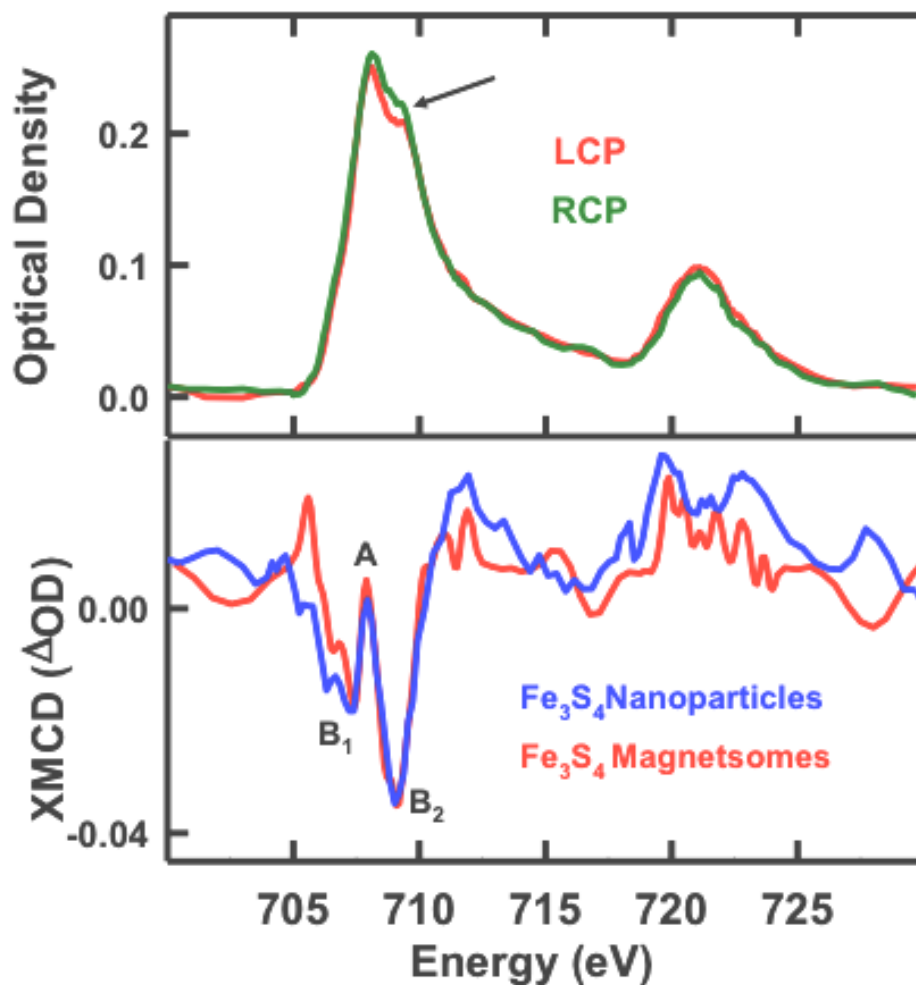
Figure 5.7 Fe $L_{2,3}$-edge XAS and XMCD spectra of biogenic Fe_3S_4 magnetosomes. (a). Fe $L_{2,3}$-edge XAS spectra of Fe_3S_4 magnetosomes in MMP cell recorded with circularly polarized X-rays parallel (red) and anti-parallel (green) to the magnetic moment of the sample. The arrow indicated the additional feature observed in Fe_3S_4 magnetosomes but not in Fe_3S_4 nanoparticles in Figure 5.2. (b) Comparison of XMCD spectra between abiotic Fe_3S_4 nanoparticles and biotic Fe_3S_4 magnetosomes.

magnetosomes. The two XMCD spectra in Figure 5.7b are rather similar although the XAS

spectra are different, suggesting that the XAS difference between abiotic and biotic Fe_3S_4 shown

in Figure 5.7a might also be caused by the surface oxidization of biotic Fe_3S_4 magnetosomes.

Previous study also showed that an amorphous phase which contained oxygen was present at the

surface but absent from the core of magnetosomes in MMP (Lins and Farina, 2001).

In order to probe the mechanism and kinetics of biotic Fe_3S_4 magnetosome oxidation in

MMPs, we tracked the spectral changes of the Fe_3S_4 as MMP cells were exposed to air over

time. **Figure 5.8** shows Fe L_3 XAS spectra of Fe_3S_4 magnetosomes in MMPs when exposed to

air for less than one week (fresh), three months, one year and over four years. Clearly, the

intensity ratio of peak B to peak A in Figure 5.8 greatly increases as the exposure time. This also
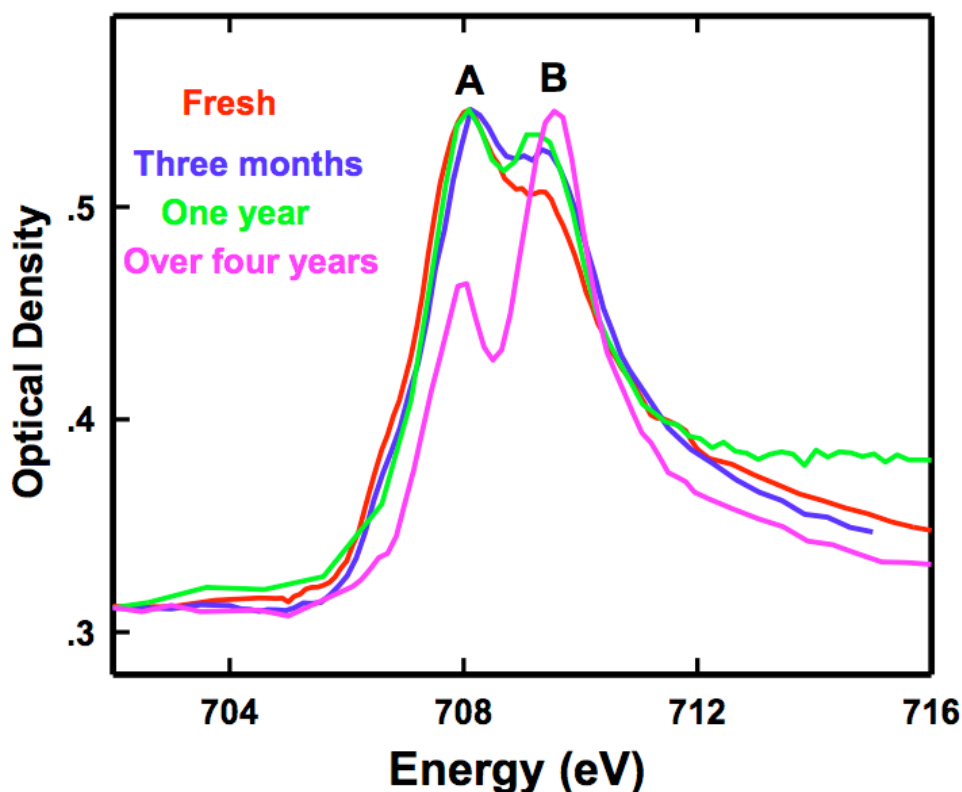
Figure 5.8 Comparison of Fe L_3 XAS spectra of Fe_3S4 magnetosomes in MMPs when they are
exposed in air for less one week (fresh), three months, one year and over four years.

confirms that the additional feature observed in biotic Fe_3S_4 magnetosomes but not in abiotic Fe_3S_4 nanoparticles in Figure 5.7a is indeed caused by surface oxidization of Fe_3S_4 stored in air. Another prominent spectral change occurred when MMPs were exposed to air for over four years because the peak B already dominated the Fe L_3 spectrum. Letard et al. (2005) once identified a surficial oxidized layer on Fe_3S_4 to be hematite (α-Fe_2O_3), whose L_3 XAS spectrum is very close to that obtained from Fe_3S_4 magnetosomes exposed to air for over four years. Thus, it seems likely that, Fe_3S_4 magnetosomes in MMPs stored under air slowly convert to the iron oxide hematite, which is a non-magnetic mineral.

5.5 Discussion

In this study, the STXM-XMCD technique was used to characterize the chemistry and magnetism of Fe_3S_4 magnetosomes in an unusual multi-cellular MTB species known as MMPs. Phylogenetically, MMPs belong to dissimilatory sulfate-reducing bacteria (dSRB) in the *Deltaproteobacteria* class of the *Proteobacteria* phylum (Delong et al., 1993). Figure 5.5 shows that two different forms of sulfur, sulfate and sulfide, are present in MMPs, whose spatial distribution and spectroscopic information might be helpful in understanding sulfur cycling in these organisms. Both these sulfur species are key components in the sulfur metabolism in dSRB. Sulfate is utilized by dSRB as a terminal electron acceptor and is reduced to sulfide (S^{2-}), which often reacts with many metal ions to form metal sulfides, such as FeS (Jong and Parry, 2003).

Pósfai et al. (1998a, 1998b) suggested that MMP did not synthesize greigite directly but initially produced either cubic FeS or mackinawite (tetragonal FeS). In addition, they reported that mackinawite could only be observed in relatively fresh samples because mackinawite crystals converted to greigite in ten days (Anders et al., 1998; Pósfai et al., 1998). In this study,

we did not observe the presence of any of the Fe_3S_4 precursors. One of the possible reason might be that the precursors had already transformed to Fe_3S_4 before the STXM measurements.

When compared with abiotic, chemically-produced Fe_3S_4 nanoparticles, the Fe $L_{2,3}$ edge XAS spectra of Fe_3S_4 magnetosomes have an additional spectral feature at a higher energy position than the main L_3 absorption peak. Otherwise, the XMCD spectra of these two Fe_3S_4 samples are generally in good agreement. This might suggest that the magnetic moment in Fe_3S_4 magnetosome chains is close to that of saturated abiotic Fe_3S_4 nanoparticles. However, because the abiotic Fe_3S_4 nanoparticles examined in this study were slightly oxidized, the magnetization of these nanoparticles might be underestimated. Nevertheless, these results demonstrate that STXM-XMCD has an excellent capability to probe both chemical and magnetic properties in MMPs. In addition, as more STXM-XMCD studies are acquired, analyzed and published, this technique promises to be applicable and of great value in understanding biomineralization in numerous organisms in the future.

Chapter 6

Probing magnetic property inheritance in cell division of

Magnetovibrio blakemorei strain MV-1

This chapter builds on previous work by Kalirai et al. (Kalirai et al., 2013), in which anomalous reversed sub-chain magnetic orientation in a single MV-1 cell was observed. In this chapter, the magnetic properties of a set of south-seeking (SS) MV-1 cells, which were in different growth states, were measured with STXM. Only one out of measured 110 MV-1 cells contain magnetically opposite magnetosome sub-chains despite a large population of cells which exhibited gaps and sub-chains. It was also observed in several cells that a new flagellum was assembled at the end opposite to the old flagellum. The significance of these results related to the two opposed mechanisms of magnetic property inheritance in cell division of MV-1 cells is discussed.

6.1 Introduction

According to the model of magnetotaxis (Blakemore, 1982), MTB organize magnetosomes in a chain all with the same magnetic orientation such that the magnetic moment will be stronger and interact more with the earth's magnetic field, which in turn spatially orients the cell and helps MTB search for their preferred OATZ environment more efficiently. However, it has been reported recently that some cells of cultured magnetotactic bacterium *Candidatus Magnetovibrio* blakemorei strain MV-1 contain magnetosome chains with gaps, and that, the magnetism of the

sub-chains on either side of the gap was opposed in some cases (Kalirai et al., 2013). Since this magnetic reversal significantly reduces the net magnetic moment of those cells, the existence of a sub-population of this type is a puzzle. Further study of its occurrence may help understand the mechanism and function of magnetic alignment in MTB cells. It raises some fundamental questions as to the process of replication in MV-1 cells, in particular, *"How do parent MV-1 cells pass on their magnetic polarity to their daughter cells during the replication?"*.

Here we report an extension of this earlier study. Several model mechanisms for establishing a single moment chain during replication are hypothesised. A connection is made between these models and the orientation of the magnetic moment relative to the motile system in the single-flagellum species MV-1 species. The hypothesized mechanisms were then tested by using a combination of high resolution transmission electron microscopy (to locate the flagellum, which is too fine to see with the current spatial resolution of STXM) and STXM-XMCD (to determine the orientation of the magnetic moment) to study the identical MV-1 cells. However, in contrast to the previous study (Kalirai et al., 2013), the frequency of magnetic reversal in a population of 150 MV-1 cells was found to be very low (~3%). Based on these results, the mechanism of magnetic property inheritance in cell division of MV-1 cells is discussed.

6.2 Materials and Methods

6.2.1 Preparation of MV-1

South-seeking (SS) MV-1 cells were prepared by Pedro Leão, a PhD student of Professor Ulysses Lins (Microbiology, Universidade Federal do Rio de Janeiro, Brasil). MV-1 cells were first grown in a culture medium that was free of iron. After these cells became completely non-magnetic (i.e. no magnetosomes), they were incubated with full culture medium, containing

Fe(II). Samples of the MV-1 cells were extracted from the culture medium after 9 hours, 18 hours, and 21 hours of incubation. Then, these cells were separated by a magnetic field and only SS MV-1 cells were collected. A droplet of the isolated sample solution was deposited on a formvar coated TEM copper grid. After several washes with distilled water to remove culture salts, the grid was dried in air and then transported to the synchrotron facility for STXM measurements.

6.3 STXM-XMCD Measurements

STXM measurements were carried out at beamline 11.0.2 at the ALS. This beamline uses an elliptically polarizing undulator (EPU) as the radiation source, which provides about 90% circularly polarized light at 11.0.2 beamline (ALS). STXM instrumentation and acquisition methods were described in section 2.3.2 in Chapter 2. Data analysis was performed using aXis2000 as described in section 3.3 in Chapter 3.

6.4. Results

6.4.1 Orientation dependent XMCD spectroscopy

X-ray magnetic circular dichroic (XMCD) spectra depend on the orientation of the magnetization vector of the sample relative to the spin polarization of the incident X-ray photon. **Figure 6.1A** and **6.1B** show the averaged STXM OD and XMCD signal of a magnetosome chain measured at 708.2 eV (peak of XMCD signal). **Figure 6.1C** and **Figure 6.1D** shows the STXM OD and XMCD images of the same chain after 180° rotation. Figure 6.1B and 6.1D clearly show opposite contrast (bright versus dark), a clear indication that the sense of the XMCD is inverted when the orientation of the magnetic moment of the magnetosome chain relative to the photon spin vector is changed by 180°. This is confirmed by **Figure 6.1E**, which compares the Fe L_3 XMCD spectrum of the magnetosome chain before and after 180° rotation. Before rotation, the
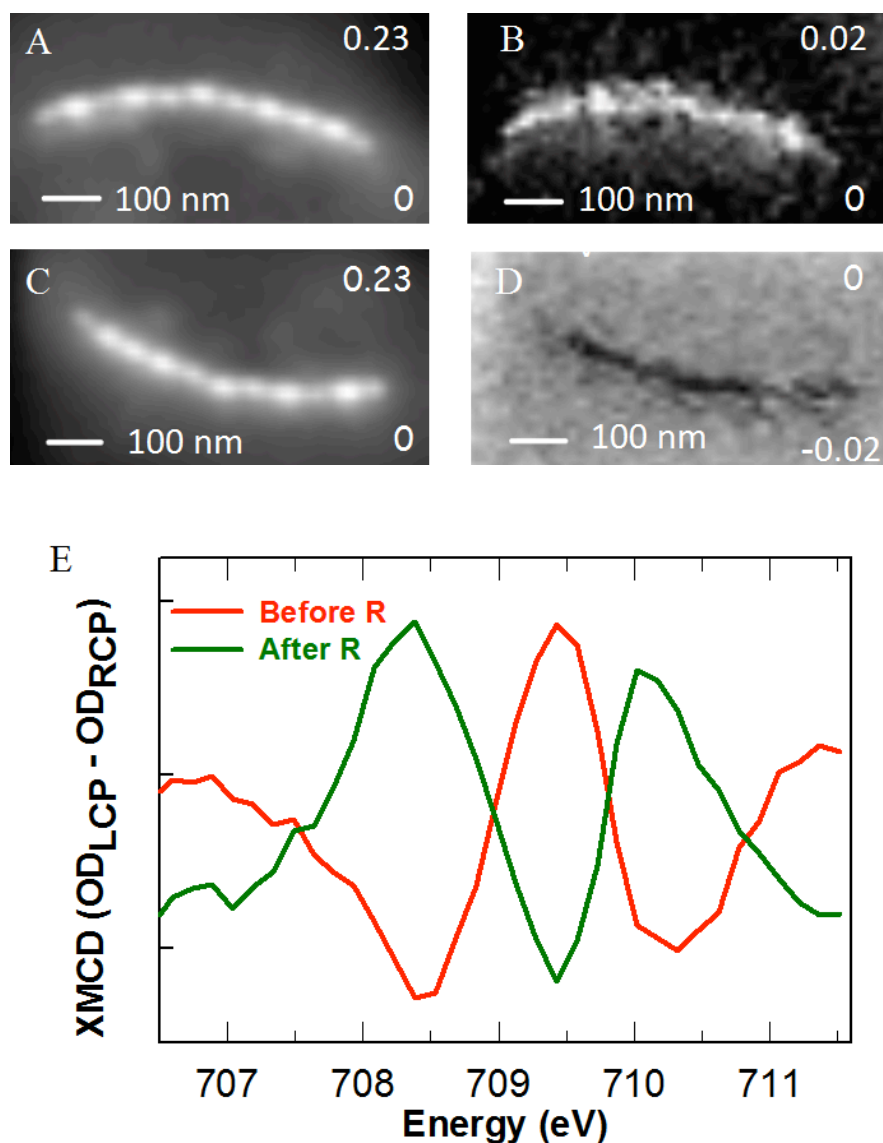
Figure 6.1 Illustration of the dependence of the XMCD spectrum on orientation of the magnetic moment relative to the polarization of incident X-ray beam. (A) Average of 60 STXM optical density (OD) images (699 - 712 eV) of a magnetosome chain in an MV1 magnetotactic bacterium. Numbers at upper and lower left are OD limits of the grey scale. (B) XMCD map, the difference of the images at 708.2 eV recorded with left and right circular polarized X-rays (C) Average of 60 STXM OD images (699 - 712 eV) of the same cell after rotation by 180°. (d) XMCD map of the cell in panel (C). (E) Plot of the XMCD spectra (difference of Fe L_3 spectra recorded with LCP and RCP X-rays) of the magnetosome chain (averaged over all magnetosomes) in the two orientations.

XMCD spectrum from 708 to 712 eV has a "down-up-down" character while it has a "up-down-up" character after 180° rotation. This demonstrates how XMCD spectroscopy, and associated XMCD imaging, can be used to determine the spatial orientation of magnetic moments. In order to investigate the role of the magnetic moment direction in magnetotactic bacteria, a "reference point" for this orientation is needed. A convenient reference point is a suitable structure in the cell, such as the flagellum of single flagella bacteria. In this study, MV-1 magnetotactic bacteria, which have a single polar flagellum, were used to investigate the relationship between magnetic polarity and magnetosome biomineralization.

6.4.2 Observation of MV-1 with one flagellum at each end during replication

During cell division, previous results have shown that most monotrichours bacteria (single flagellum on one end) assemble the new flagellum at the end opposite to the old flagellum (Green et al., 2009). **Figure 6.2A** presents a color coded composite of +ve (green) and -ve (red) XMCD maps of a SS MV-1 cell at 708.3 eV with the whole cell signal imaged at 700 eV (blue). **Figure 6.2B** shows a TEM image of the same cell with a single flagellum, labeled with a red arrow, at each end of the cell. Note that the body of the dividing cell is opaque (non-transparent to the electron beam) as it is too thick. There are five sub-chains (1 or more magnetosomes separated by gaps) inside this cell, which are labeled 1 to 5. The XMCD measurements clearly show that chains 1, 3 and 5 have the same magnetic polarity but opposite to that of chains 2 and 4. This can also be verified in **Figure 6.2c**, which shows the Fe L_3 XAS spectra and corresponding XMCD spectra of the different sub-chains. The XMCD signals in the 707 to 712 eV range demonstrate that sub-chains 1, 3 and 5 have a "down-up-down" character while chains 2 and 4 have a "up-down-up" character. This is similar to the previous study which reported two magnetically reversed sub-chains in a single NS MV-1 cell (Kalirai et al., 2013).
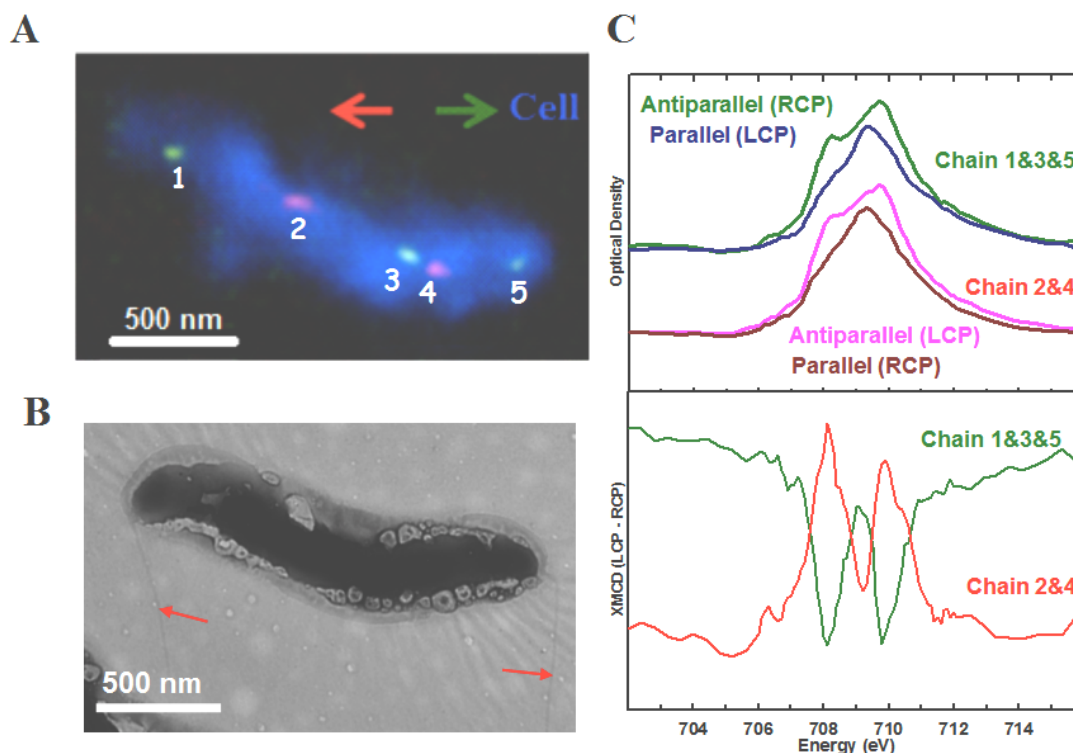
Figure 6.2 Example of a dividing MV-1 cell with a flagellum at each end. (A) Color coded composite of +ve (green) and -ve (red) XMCD map and the image at 702 eV (blue). (B) TEM bright field image of the cell. The arrows point to the flagella present at each end. (C) Fe L_3 XAS and derived XMCD spectra for the 5 magnetosomes in the dividing bacterium.

6.4.3 Mechanism of cell division in SS MV-1 MTB

The original model of north-seeking and south-seeking behavior of MTB cells proposed by Torres de Araujo et al. (1990) stated that these two polarity types can be differentiated by comparing whether it is the north-seeking pole or the south-seeking pole of the cellular magnetic dipole that is pointing forward (i.e. toward the opposite end of the cell relative to the flagellum). Torres de Araujo et al. (1990) also proposed that daughter cells inherit magnetosomes from their parents during cell replication such that they also inherit the parental polarity. However, with

respect to the cell division process, most studies assume all the magnetosomes in parent cells
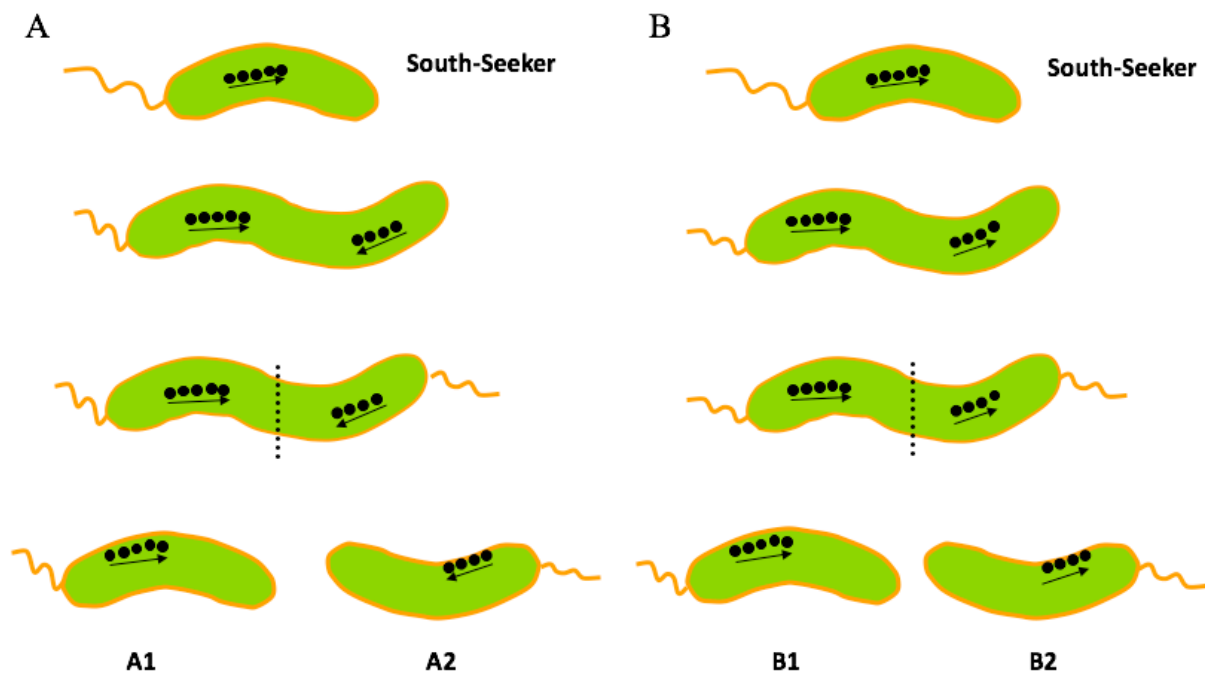
Figure 6.3 Cartoon of two different hypothetical cell division mechanisms for single flagellum species such as MV-1. (A) It there are two sub-chains and magnetic reversal in the parent cell then the parent and daughter cells will have the **same** magnetic moment relative to the flagellum. (B) It there is <u>no</u> magnetic reversal in the parent cell, then parent and daughter cells will have the **opposite** magnetic moment relative to the flagellum.

have the same magnetic polarity and neglect the possibility that they can also have opposite magnetic polarities in the same cell. **Figure 6.3 A** and **6.3B** present two possible hypothetical division processes in SS MV-1 cells. Note that the new flagellum is assumed to be positioned on the opposite end to the old flagellum as shown in Figure 6.2. In one case (6.3A) the parent cell has partial chains with opposite magnetic polarity. In the second case (6.3B) parent cell has all magnetosomes with the same polarity. During cell division, if the sub-chains in the parent cell have opposite magnetic polarities, both daughter cells (A1 and A2 in Figure 6.3A) end up with

the same magnetic polarity relative to the flagellum. If the sub-chains in the parent cell have the same magnetic polarities, the two daughter cells (B1 and B2 in Figure 6.3B) have opposite magnetic polarities relative to the flagellum.

6.4.4 Statistical study of magnetic polarity of SS MV-1 cells

In order to further study the magnetic polarity of MV-1 cells, XMCD maps were measured for 120 SS MV-1 cells, which were in different growth states. These MV-1 cells were extracted from the culture solution, after incubating non-magnetic cells in a full culture medium for 9, 18 and 21 hours, which were designated as SSMV-1 (9h), SSMV-1 (18h), and SSMV-1 (21h). **Table 6.1** presents the statistical results of the magnetic polarities of these MV-1 cells. In a previous study, Kalirai et al.(2013) reported the frequency of NS MV-1 cells containing two or more sub- chains of magnetosomes with opposite magnetic polarities was ~10% based on a sampling size of 150 cells. In this study, we only observed one cell from the sample of SS MV-1 (21h), which contained magnetically opposite sub-chains. This gives a frequency of magnetic reversal of 3% of the total cell population (35 cells), and a 4.2% frequency with respect to the population of cells with chain gaps (24 cells), where the gap was defined as a separation of 2 magnetosomes of more than 50 nm, which is much larger than typical separation distance among magnetosomes in a condensed chain (Kalirai, et al. 2013). In a comparative study between wild AMB-1 and AMB-1 ΔMamK cells, Komeili et al. (2006) showed that MamK deletion mutants have more widely dispersed magnetosomes in the cell. Klumpp and Faivre (Klumpp and Faivre, 2012) further simulated that, if gene mamK was deleted during the biomineralization process, the magnetosome transport would be "turned off", which produced small magnetosome chains typically with different magnetic polarities. Therefore, it is possible that the magnetic reversal in

the sample of SS MV-1 (21h) is a consequence of the large number of multiple and gap-

separated sub-chains in the SS MV-1 (21h) cell population.

Table 6.1 Statisticcal results of magnetic polarities of SS MV-1 cells

Cell type	Total cell measured	# of cells with magnetic reversal
SS MV-1 (9h)	43	0
SS MV-1 (18h)	31	0
SS MV-1 (21h)	35	1

6.4. Discussion

As shown in Table 6.1, the frequency of opposite magnetic polarities in a single MV-1

cell is much lower than that of the same magnetic polarities in a MV-1 cell. It would seem that

path B is the one that SS MV-1 cells choose to pass on their magnetic polarities to daughter cells.

Magnetotaxis (Blakemore, 1982) is believed to be an approach for MTB to locate and maintain

an optimal environment efficiently by reducing a three-dimensional search to a one-dimensional

search (Bazylinski and Frankel, 2004). Based on this model, if MTB can organize magnetosomes

in a chain and with the same magnetic orientation, the interaction with the earth's field can be

stronger and the search efficiency can be maximized (Mo et al., 2014). However, the statistical

results presented in Table 6.1 and Figure 6.2 show that there is a small fraction of SS MV-1 cells

containing magnetosome sub-chains with opposite magnetic polarities.

With respect to the origin of opposite magnetic polarity in a single MTB cell, Klumpp

and Faivre simulated a dynamic study on magnetosome chain organization (Klumpp and Faivre,

2012). They showed that the formation of magnetosomes into a chain is coordinated by both

magnetic interaction and biologically controlled magnetosome transport. According to their

simulations, if active magnetosome transport is removed and only the magnetic interaction exists

then small magnetosome sub-chains with opposite magnetic polarities are produced. They

propose such a defect in active transport as an analogy of the ΔmamK deletion mutant (Klumpp

and Faivre, 2012). In previous studies, cytoskeletal proteins MamK and MamJ have been shown

to play important roles in magnetosome chain formation. MamJ has been shown to link

magnetosomes to the filament which is formed by MamK. Without MamK or MamJ,

magnetosome chain is not observed (Komeili et al., 2006; Scheffel et al., 2006). In the case of

MV-1, it is known that magnetosomes are not adjacent to each other but commonly separated by

large gaps (Dunin-borkowski et al., 1998). Therefore, if the gaps between pre-existing sub-chains

and newly forming chains are large enough, the old sub-chains would have little effect on the

forming magnetosomes. There is about equal probability that the newly forming magnetosomes

adopt either the same or opposite polarity as the pre-existing magnetosomes (Kalirai, et al., 2013;

Torres de Araujo et al., 1990).

     If magnetic reversal occurs in a single MV-1 cell (Figure 6.3A) the two daughters would

have the same magnetic polarity relative to the flagellum orientation. As a result, in order for

each daughter cell to move toward the OATZ, they should rotate their flagella in the same way.

The flagellum rotation direction would then be coupled to the oxygen concentration sampled by

chemotaxis (Lefèvre et al., 2015). However, different magnetic orientations in the same cell

would definitely cancel with each other, leading to a reduced magnetic dipole moment and thus a

weaker magnetic interaction with the geomagnetic field, which in turn deteriorates their search

efficiency for the optimal environment.

One the other hand, if all magnetosomes in the parent cell have the same magnetic polarity, (Figure 6.3B), opposite magnetic polarities (relative to the flagellum location) would be passed on to the daughter cells after division. In order for these two daughter cells to achieve the same movement direction, they must rotate their flagellum in opposite directions. Bazylinski et al. (2013) reported that MV-1 cells swim in one direction with longer excursions than the opposite direction in the hanging-drop assays, suggesting that they exhibit polar magneto-aerotaxis behaviour (Frankel et al. 1997). According to the model proposed by Frankel et al. (1997), polar magneto-aerotaxis is a two-state aerotactic sensory system, in which O_2 concentration $[O_2]$ directly determines the sense of flagella rotation. In other words, such a sensory mechanism can control the direction of flagellum rotation of the daughter MV-1 cells and thus the swimming direction of daughter cells independent of the magnetic field.

According to the statistical results shown in Table 6.1, it appears that magnetic reversal in a single cell only occurs with a low frequency and that most of the cells synthesize magnetosome chains with the same magnetic polarity. Therefore, it is assumed that the majority of parent MV-1 cells would adopt mechanism B (Figure 6.3B) to pass on their magnetic polarities to daughter cells. This, in turn, would lead to a modified model for polar magneto-aerotaxis behavior for MV-1 (see **Figure 6.4**). According to the original polar magneto-aerotaxis model proposed by Frankel et al. (1997), the MTB cells have two sensory states, depending on the surrounding $[O_2]$. Frankel et al. (1997) proposed that if the $[O_2]$ is higher than the preferred level $[O_2]^*$, the cells are in state 1, which cause them to rotate their flagella counter clockwise (CCW). If the $[O_2]$ is lower than the preferred level $[O_2]^*$, the cells are in state 2, which cause them to rotate their flagella clockwise (CW). As shown in Figure 6.4A, the two daughter MV-1 cells contain magnetically opposite chains relative to the flagellum orientation, indicated by black and blue arrows in the
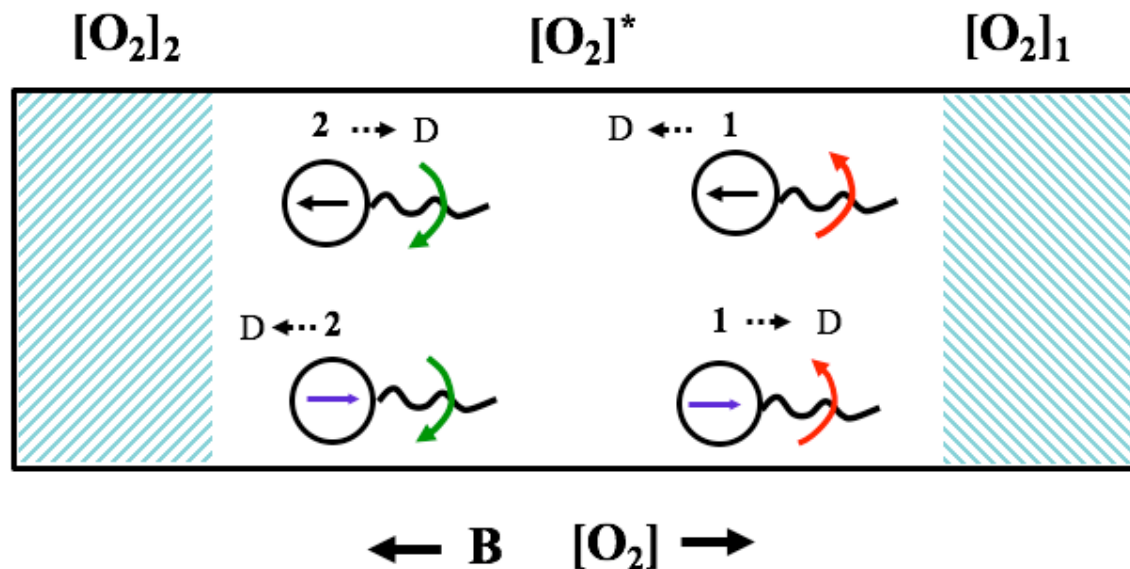
Figure 6.4 Illustration of the aerotactic sensory mechanism of MV-1 cells. $[O_2]^*$ represents the optimal O_2 level. $[O_2]_1$ means the O_2 level is higher than $[O_2]^*$ and $[O_2]_2$ represents O_2 level is higher than $[O_2]^*$. The magnetic field **B** is anti-parallel to the oxygen gradient $[O_2]$, similar to the natural environmental conditions for these cells. When the MV-1 cells are close to $[O_2]_1$ region, they are in state 1, which causes the cells to rotate the flagellum counter clockwise (CCW,red arrow); when the MV-1 cells are close to $[O_2]_2$ region, they are in state2, which causes the cells to rotate the flagellum clockwise (CW, green arrow). In either region, if the MV-1 cells contain magnetically opposite magnetosome chains, indicated with black and blue arrows inside the circle, relative to the flagellum orientation, these cells would swim in different directions.

circle in Figure 6.4. For example, if these two daughter cells are in the O_2 region ($[O_2]_1$ state), they both rotate their flagella CCW, which makes them swim towards the opposite directions (indicated by the dash arrow). This is also applicable to the situation when the daughter MV-1 cells are in the O_2-depleted region ($[O_2]_2$) state. The daughter cells would rotate the flagella CW, but also swim towards opposite directions. Therefore, it is expected that different MV-1 cells with opposite magnetic polarities can still swim towards the same direction (i.e. behave the north-seeking or south-seeking behavior) as long as they rotate their flagella in opposite ways. In

fact, aerotaxis controls the sense of rotation of the flagella which lets the cells locate the

preferred region more efficiently. Several methods which can be used to verify this model will be

described in Chapter 8.

Chapter 7

Measuring spectroscopy and magnetism of extracted and intracellular magnetosomes using soft X-ray ptychography

This chapter presents the application of spectro-ptychography at the Fe L edge to study magnetosomes from MV-1 magnetotactic bacteria both extracted and intracellularly. The Fe 2p XAS and XMCD spectra of individual magnetosomes were obtained with ptychographic modulus and phase modes. A world record spatial resolution of 7 nm was achieved. Precursor-like and immature magnetosome phases in an intact MV-1 cell were visualized and their Fe 2p spectra measured. Based on these new results, a model for the pathway of magnetosome biomineralization for MV-1 is proposed.

This chapter is extracted from a manuscript submitted to Proc. Natl. Acad. Sci. U.S.A and currently in revision. MV-1 cultures were grown by Prof. Dennis Bazylinski and Prof. Ulysses Lins. The author of this thesis did all the spectro-ptychography measurements. The data was analyzed by the author and Prof. Adam P. Hitchcock. Tolek Tyliszczak and David Shapiro helped to set up ptychography measurements and image reconstruction. This paper was drafted by the author and edited and revised by the author and Prof. Adam P. Hitchcock.

7.1 Introduction

In previous chapters, X-ray magnetic circular dichroism (XMCD) measured with a scanning transmission X-ray microscope (STXM) has been successfully applied as a tool to study chemistry, magnetism, and the biomineralization mechanism of magnetotactic bacteria on an individual magnetosome basis (Kalirai et al., 2013, 2012; Lam et al., 2010). However the spatial resolution of current STXMs is typically ~30 nm when generated by a 25 nm outer zone, Fresnel zone plate, and the monochromaticity and lateral coherence of the X-rays is such that the spot size is diffraction limited. This is just sufficient to resolve and measure XMCD of individual magnetosomes (Kalirai et al., 2013, 2012; Lam et al., 2010) but the size, morphology, and orientation of magnetosomes is not well resolved, which makes extraction of spectral information difficult.

Unlike conventional zone plate imaging techniques, ptychography is not limited by the properties of the X-ray optics used, has the potential to reach near atomic-scale spatial resolution with very short wavelength X-rays (Edo et al., 2013), and can image with Raleigh wavelength limited resolution in the soft X-ray region (at the Fe L_3 edge the wavelength is 1.8 nm). Ptychography has been applied to image biological cells (Giewekemeyer et al., 2010; Maiden et al., 2013), labyrinthine domains in magnetic multilayers (Tripathi et al., 2011) and 3D structure with 16 nm spatial resolution (Holler et al., 2014). Recently, soft X-ray spectro-ptychography was developed at the Advanced Light Source (Shapiro et al., 2014; Shi et al., 2016; Yu et al., 2015), which opens up the possibility of chemical speciation via X-ray spectroscopy with few-nanometer spatial resolution. Here, we present the first application of spectro-ptychography to measure X-ray absorption and XMCD spectra at the Fe $L_{2,3}$ edge to study spatially resolved

chemistry and magnetism of magnetosomes extracted from cells and inside intact magnetotactic bacterial cells.

7.2 Materials and Methods

7.2.1 Sample preparation

The cells of *Magnetovibrio blakemorei* strain MV-1 were cultured anaerobically in liquid cultures. The magnetosomes were extracted from MV-1 cells using the procedure developed by Alphandéry et al. (2009). A droplet of sample solution was deposited on formvar coated TEM copper grids. After several washes with distilled water, the grid was dried in air and then transported to synchrotron facility for STXM measurements.

7.2.2 Experimental Methods

Ptychographic measurements were carried out using the 5.3.2.1 bending magnet and 11.0.2 undulator beamlines at the ALS, Lawrence Berkeley National Laboratory. The ptychographic results shown in Figures 7.1, 7.4 and 7.5 were measured with the STXM on beamline 11.0.2 while the ptychographic results shown in Figures. 7.2 and 7.3 were measured using the Nanosurveyor I instrument at beamline 5.3.2.1. At beamline 11.0.2, a zone plate with outer zone width of 60 nm was utilized for illumination and a Princeton Instruments direct-sense X-ray camera was used for data collection. The sample was scanned in focus with a step size of 50 nm. A double exposure mode which combined 15 ms (short exposure)/150 ms (long exposure) was used at beamline 11.0.2 to extend the dynamic range as described by Shapiro et al. (2014). At beamline 5.3.2.1, a 100 nm outer zone width zone plate was used with a step size of 70 nm. A custom, high frame rate CCD detector, developed at LBNL and BNL, was used to record the diffraction data. At beamline 5.3.2.1 a single exposure time of 200 ms was used and a

partially transmitting silicon beam stop was used to increase dynamic range. In both systems, the incoherent background signal was measured at frequent intervals with the same CCD settings and the beamline shutter closed. This background was then subtracted in the data processing.

7.2.3 Ptychographic Reconstruction

The ptychography reconstruction provides a complex valued result, where the real part is related to elastic scattering and the imaginary part is related to absorption (Rodenburg, 2008). If we denote the exit wave reconstructed with ptychography as P, then the optical density (OD) can be calculated as:

$$OD = -\ln(|P|/|P\_0|)$$

where P_0 is the signal in the reconstruction in a region unobstructed by the sample, or from a measurement in a featureless region containing non-sample components, measured under the same instrumental conditions (zone plate, incident flux, sampling time, camera settings etc) and reconstructed in exactly the same way. In this paper we refer to this result as **ptychography absorption.**

The wave function P can be divided into a real part (Re[P]) and an imaginary part Im[P]. Then, a relative phase term ϕ, referred to **ptychography phase** in this study, can be calculated as:

$$\phi = \arctan(Im[P]/Re[P]) - \arctan(Im[P\_0]/Re[P\_0])$$

The measured ptychography images were reconstructed using 200 iterations of the RAAR algorithm implemented in the SHARP-CAMERA ptychography code (Marchesini et al., 2016; Donatelli et al., 2015; Luke, 2004). Illumination and incoherent background refinements were used every other iteration.

7.2.4 Image and spectral analysis

Individual ptychography modulus and ptychography phase images were assembled into stacks and analyzed in aXis2000. The stacks were aligned using Fourier correlation methods. A threshold masking procedure was used to establish regions of interest (ROI), including individual and chains of magnetosomes, as well as intracellular regions. These ROI masks were then applied to the ptychography stacks to generate XAS and XMCD spectra. The ptychography modulus and STXM transmission signals were converted to optical density signals using the intensity through an area free of iron and off the cell or extracted magnetosomes but close to the region under study.

7.3. Results

7.3.1 Fe 2p spectro-ptychography study of extracted magnetosomes

Figure 7.1A presents a conventional STXM image of a large region of a set of chains of magnetosomes extracted from *Magnetovibrio blakemorei* strain MV-1 cells. This image was measured with a zone plate with a 60 nm outer zone width and thus a 72 nm diffraction limited spot size. **Figure 7.1B** shows the ptychography modulus (amplitude) image of the area indicated by purple rectangular in Figure 7.1A, recorded using the same zone plate (ZP). The conventional STXM and ptychography modulus images were measured at 708.2 eV, which is the energy of the strongest XMCD signal. In the conventional bright field STXM image (Figure 7.1A), only the outline of magnetosome chains could be identified with the gaps between the individual magnetosomes only partially resolved. In contrast, the individual magnetosomes were spatially well resolved with ptychography using the same zone plate. After the STXM measurements, the
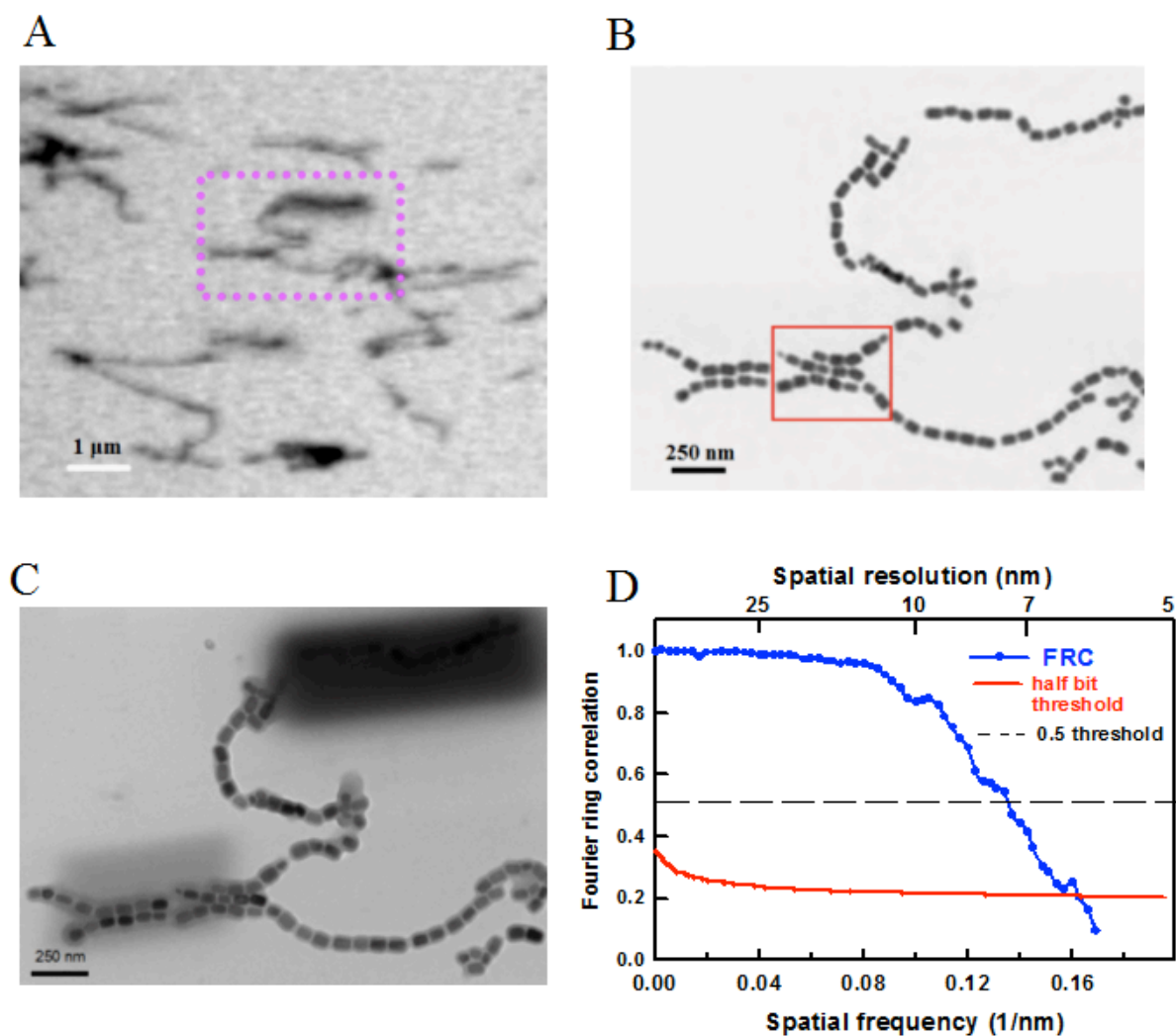
Figure 7.1 Ptychography reconstruction of magnetosomes extracted from MV-1 cells. (A) Conventional STXM image of extracted magnetosome chains. (B) Ptychography m dulus image of the same magnetosome chains in A. The ptychography data was measured using a photon energy of 708.2 eV, with an image size of 2 μm × 2 μm (40×40 points) and a dual sampling approach where at each pixel the diffraction pattern was measured with both 15 and 150 msec dwell time. A zone plate (ZP) with a 60 nm outer zone width was used. (C) TEM image of the same area as shown in A and B. (D) Fourier Ring Correlation analysis of the image in B. The spatial resolution is 6.8 nm if the half bit threshold is used.

same region of this sample was imaged by TEM. The TEM bright field image (see **Figure 7.1 C**) shows a pattern of magnetosomes with identical size, morphology and orientation as that seen in the ptychography modulus image. Note that the dark rectangular regions in Figure 7.1C are due to a build-up of carbon contamination produced by the long-exposure ptychographic measurements.

In order to quantify the spatial resolution of the ptychography images, several methods were used. **Figure 7.1 D** presents the calculated Fourier Ring Correlation (FRC) of the reconstructed image in Figure 1a. The FRC curve (blue) drops below the chosen threshold line of 0.5 (dashed grey line) at a spatial frequency of 0.147 nm^{-1}, which corresponds to a spatial resolution of 6.8 nm. A simple 10-90 % edge sharpness evaluation gave an estimate of 7 nm (Zhu et al., 2016), while a power spectral density (PSD) method estimated a spatial resolution of 5 nm. In a recent study, a spatial resolution of 6 nm, as measured by FRC, was achieved at the Fe $L_{2,3}$ absorption edge (Yu et al., 2015). A yet higher spatial resolution of 3 nm was reported in by Shapiro et al. (2014), but that was measured using X-rays with a considerably shorter wavelength (1500 eV, 0.85 nm) on a very high contrast one dimensional test pattern.

Another interesting observation is that some organic material surrounding the extracted chains can also be visualized with ptychography (see **Figure 7.2**). **Figure 7.2A** presents an expanded scale ptychography modulus image of part of the magnetosome chains plotted in Figure 7.1B (identified with a red rectangle), in which some organic material surrounding the extracted chains is indicated by red arrows. Although the amount of material is very small, it is possible to measure its C 1s spectrum using STXM (see **Figure 7.2B**). The C 1s spectrum indicates the material surrounding the magnetosomes is organic and that it has a lipid-like

signature, consistent with it being a residue of the lipid membranes which surround

magnetosome chains in MTB.
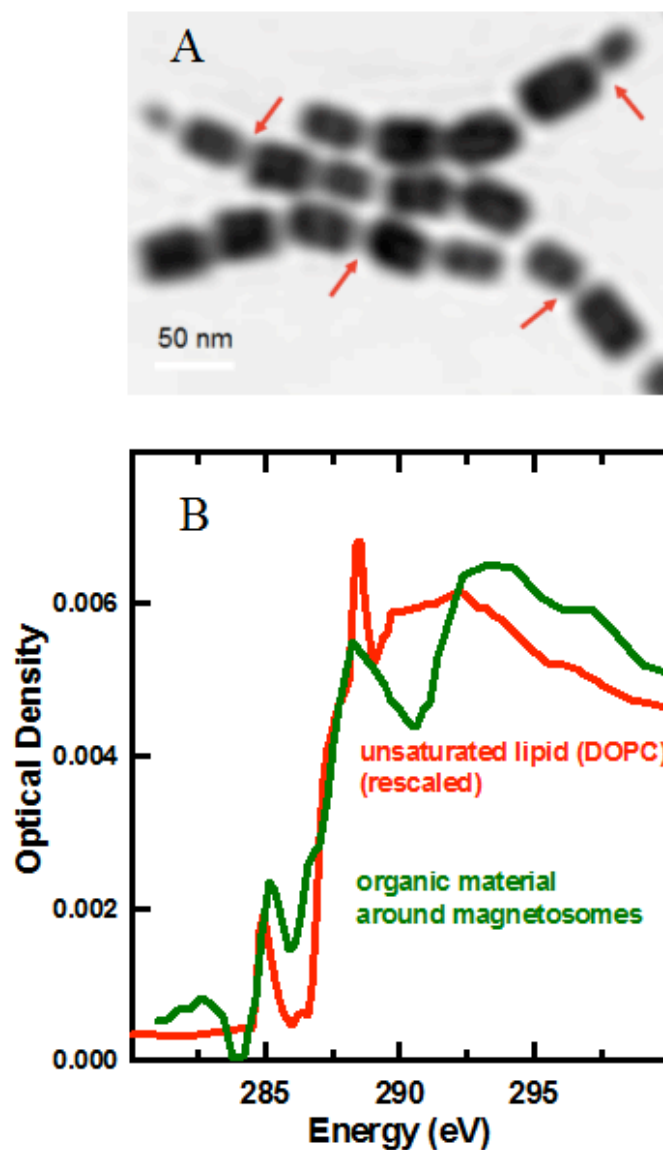
Figure   7.2   Observation of organic biomaterials surrounding magnetosomes by ptychography modulus mode. (A) Ptychography modulus image of extracted magnetosome chains, from the region indicated by a red rectangle in Figure 7.1B. The red arrows indicate regions showing the additional material located between magnetosomes. (B) Comparison of the C 1s spectrum of the organic material surrounding magnetosomes in Figure 7.2A with that of 1,2-dioleoyl-sn-glycero-3-phosphocholine (DOPC) lipid.

7.3.2 Fe 2p spectro-ptychography study of whole MV-1 cells

Figure 7.3 compares the conventional STXM transmission image (**Figure 7.3 A**) of multiple whole MV-1 cells with the ptychography modulus (**Figure 7.3B**) image of the same region. The data was measured at 710 eV (the peak around Fe L_3 absorption) using a 100 nm outer zone width zone plate. Here the typical morphology of chains of well resolved individual magnetosomes is observed in the ptychography modulus image, whereas the magnetosomes are
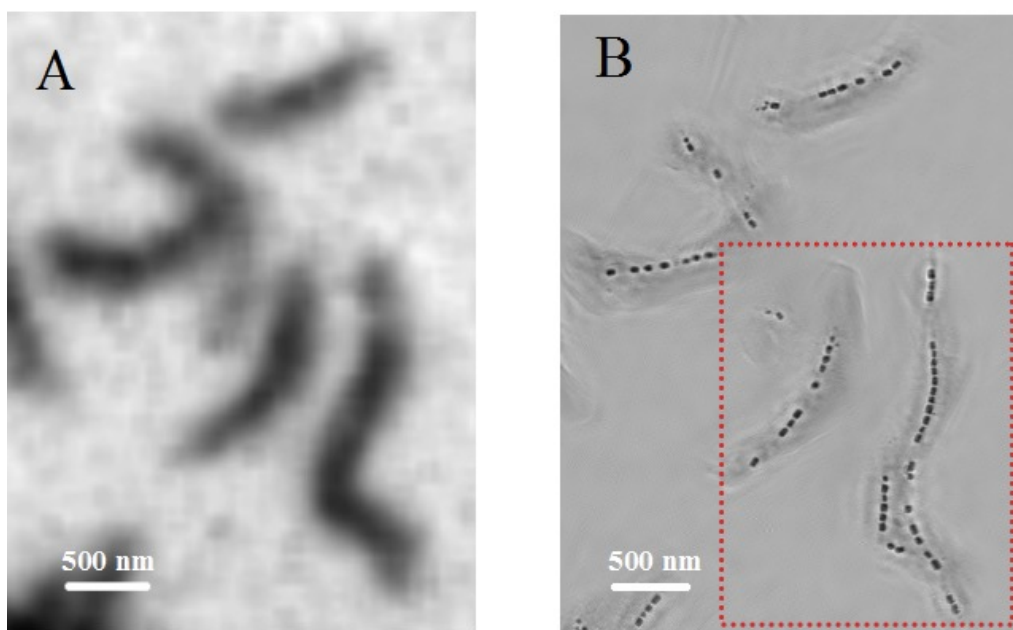
Figure 7.3 Comparison of intact MV-1 cells between conventional STXM and ptychography modulus images. (A) Conventional STXM image of multiple MV-1 cells using a 100 nm outer zone plate. (B) Ptychography modulus image of the same region. Both images were measured using the Nanosurveyor I instrument on beamline 5.3.2.1. The photon energy was 710 eV. A 100 nm outer zone ZP was used. The STXM image was recorded with 60×76 points and a dwell time of 5 ms while the ptychographic data was measured with 43×50 points and a dwell time of 300 ms. The red rectangle is the area where the detailed spectro-ptychography stack was measured.

not individually resolved and barely differentiated from the cell structure in the STXM image,

due to the low resolution zone plate used (120 nm diffraction limited resolution).
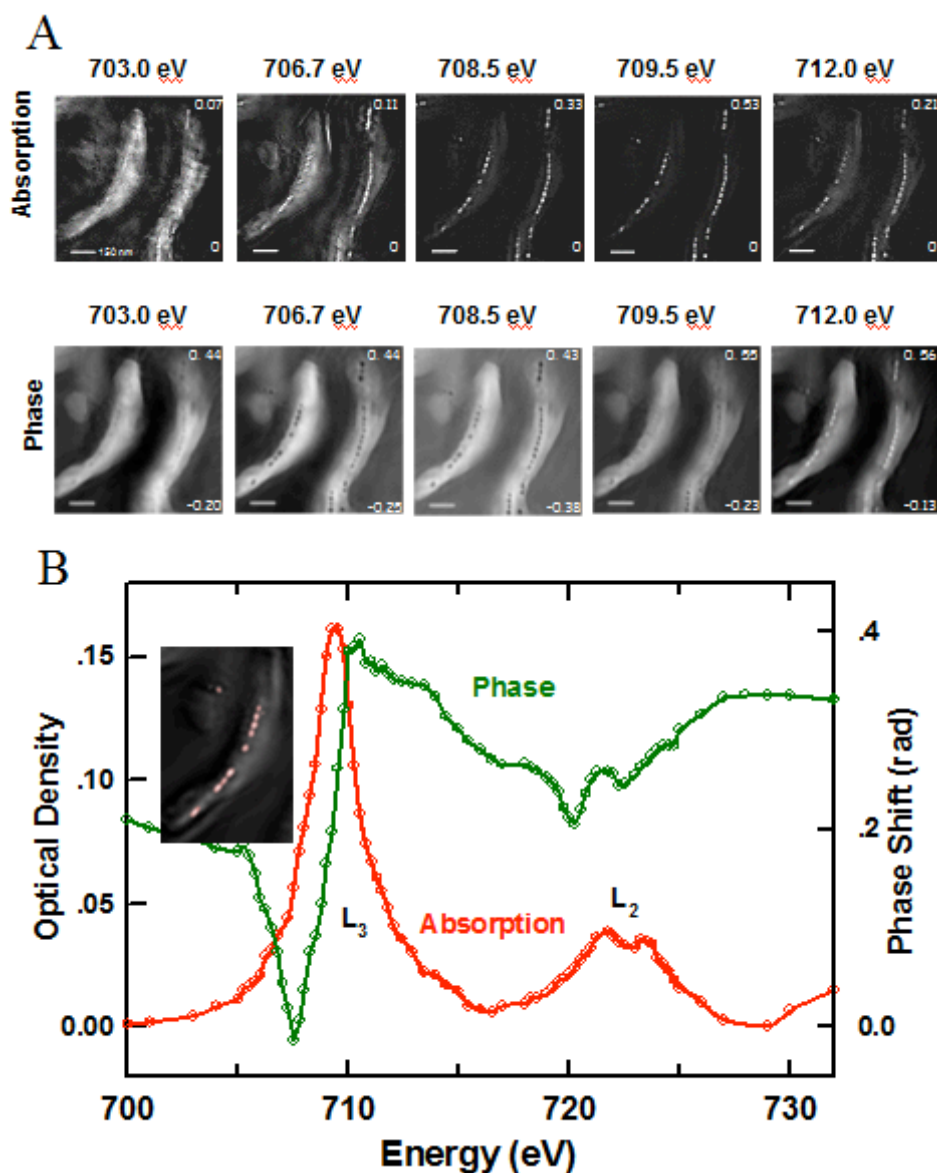
Figure 7.4 Spectro-ptychography of intact MV-1 cells at Fe $L_{2,3}$ edge. (A) Reconstructed ptychography absorption and ptychography phase images of intact MV-1 cells at five photon energies, 703.0, 706.7, 708.5, 709.5 and 712.0 eV. (B) Fe $L_{2,3}$-edge ptychographic absorption (red) and phase (green) spectra averaged over all the magnetosomes in the MV-1 cells in Fig. 3a. The inset image is the average of all ptychography absorption images in the stack, with the region from which the spectra are extracted indicated in red (BL 5.3.2.1)

Figure 7.4A presents ptychography absorption and ptychography phase images of the region outlined in red in Figure 7.3 B, at five of the 76 photon energies measured. The ptychography absorption images are obtained by converting the ptychography modulus images to optical density (OD) images. **Figure 7.4B** plots the ptychographic phase (green) and absorption spectra (red) over the full photon energy range, and averaged over all the magnetosomes in one cell (see inset for location). The ptychographic absorption spectrum (red in Figure 7.4B) corresponds to excitation of Fe 2p electrons to final states dominated by $(2p^{-1}$, Fe 3d) configurations. The maximum L_3 ptychographic absorption signal occurs at 709.5 eV, which is in good agreement with literature X-ray absorption spectra of magnetite (Goering et al., 2007; Kalirai et al., 2013, 2012; Lam et al., 2010; Zhu et al., 2015a). The ptychographic phase images (Figure 7.4A) show that magnetosomes can be clearly visualized in the phase signal in the pre-edge region (energies below 707 eV), at photon energies where the magnetosomes are barely visible in the ptychographic (or STXM) absorption signal. As the photon energy approaches the absorption peak, magnetosomes become less visible in the phase reconstruction, and increase in visibility in the absorption signal. The phase signal is minimum at 708.5 eV and then the contrast inverts after 709.5 eV, as shown in Figure 7.4B. Maiden et al. (2013) reported the ptychography phase spectrum of $CoFe_2O_4$ in the Fe 2p region and found the minimum around the same energy, while Shapiro et al. (2014) found the minimum in the ptychography phase spectrum at 708.0 eV in $LiFePO_4$ and 708.5 eV in $FePO_4$. The ptychography absorption spectrum of magnetosome chains tracks that of the X-ray absorption spectrum. The significant change in the contrast and morphology in the phase signal several eV below the absorption maximum means that the phase signal might offer advantages in terms of chemical differentiation and mapping. Often the changes in phase signal across an edge provides more detail, and clearer features than the

absorption signal (Maiden et al., 2013; Shapiro et al., 2014), at energies where the X-ray absorption is smaller, which gives advantages with respect to reducing radiation damage. In addition, analysis of the combined phase and absorption signals provides improved chemical contrast, as shown by Shapiro et al. (2014).

Figure 7.5A displays the average of 76 ptychography OD images of a single MV-1 cell recorded from 700 to 732 eV. Four different regions (A, B, C, D) are labelled. **Figure 7.5B** presents the ptychography absorption spectra extracted from these four areas, in comparison to reference spectra of Fe(II) and Fe(III) (Nagasaka et al., 2013). Region A corresponds to a gap between two magnetosome sub-chains. Here the absorption spectrum exhibits a two-peak feature in the L_3 region with the stronger peak at around 708 eV and the weaker one at 710 eV. The reference spectra of Fe(II) and Fe(III) (Figure 7.5B) clearly show that Fe(II) species have their main intensity around 708 eV while Fe(III) species have their main intensity around 710 eV (Chueh et al., 2013). This suggests that the gap region between two magnetosome sub-chains consists of both Fe(II) and Fe(III), with the Fe(II) character stronger than the Fe(III) character. Region B represents a region close to one end of a magnetosome chain, where a weak precursor-like structure can be visualized. Similar to that of region A, the spectrum of region B also has a two-peak feature in the L_3 region, but with an inversed intensity ratio of the 708 and 710 eV peaks. Although it is challenging to quantitatively determine the amount of Fe(III) and Fe(II) ions in region B, it is evident that there is more Fe(III) in precursor B than in gap area A. Region C corresponds to a single immature magnetosome, while region D represents a mature magnetosome. Compared with that of mature magnetosomes (D), the spectrum of the immature magnetosome (C) is rather different with a shoulder evident on the low energy side of the L_3 region, labeled with a red arrow, suggesting that these immature magnetosomes might be an
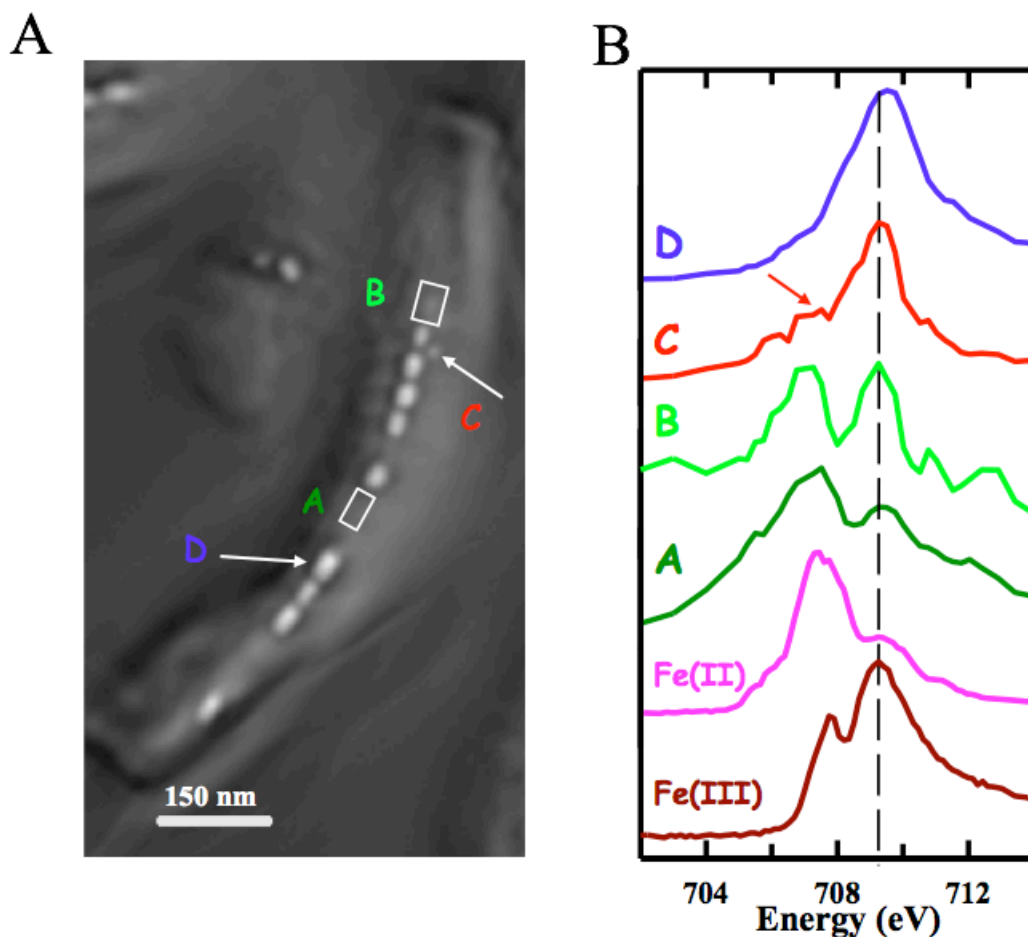
Figure 7.5 Chemical study of a single MV-1 cell with spectro-ptychography at Fe L_3 edge. (A). Average of 76 ptychography absorption images of a single MV1-cell from 700 to 732eV. Four regions, labelled A, B, C, and D, are identified. (B) Fe L_3 spectra from a gap in the magnetosome chain (region A), a precursor-like region (B), an immature magnetosome (C), and a mature magnetosome (D). The spectra of $FeCl_2.4H_2O$ [Fe(II)] and $FeCl_3.6H_2O$ [Fe(III)] are also plotted (Nagasaka et al., 2013). (BL 5.3.2.1)

Fe_2O_3 phase (Kim et al., 2009). In our previous study, we showed that these immature magnetosomes are non-magnetic as they have zero XMCD signals (Kalirai et al., 2013). Recently, in a real-time XMCD study of *Magnetospirillum gryphiswaldense*, strain MSR-1, Staniland et al (2007) reported that the non-magnetic phase found prior to mature magnetosomes

is hematite (α-Fe_2O_3), which covers the magnetic phase underneath and can convert to magnetite

in a very short time.

7.3.3 Ptychographic XMCD study of extracellular and intracellular magnetosomes

Figure 7.6A presents the ptychographic XMCD absorption signals of an extracellular

magnetosome chain measured at 708.2, 709.5 and 710.5 eV. The XMCD signal is generated by

taking the difference of two images, one recorded with the photon polarization parallel and the

other, antiparallel to the magnetosome magnetization. **Figure 7.6B** shows the Fe L_3 XAS spectra

of the extracellular magnetosome chain recorded with the photon polarization parallel (red) and

antiparallel (green) to the sample magnetization, which were extracted from the full sequence of

ptychographic absorption images. The corresponding XMCD spectra (blue), the difference of the

two ptychographic absorption spectra (parallel and antiparallel), is also plotted in Figure 7.6B.

The ptychographic XMCD absorption spectrum of the magnetosomes (Fe_3O_4) in Figure 7.6B has

three distinctive peaks, B_1 (708.2 eV), A (709.5 eV), and B_2 (710.5 eV), which are mainly

associated with Fe(II) in the octahedral site, Fe(III) in the tetrahedral site, and Fe (III) in the

octahedral site, respectively (Kuiper et al., 1997). In addition, the sign of each of these three

peaks is determined by the spin direction (spin up or spin down) of the Fe ions which is related

to antiferromagnetic coupling between the spins on the octahedral and tetrahedral sites (Kuiper et

al., 1997). As a result, the signs of B_1, and B_2 are negative while that of the A peak, is positive.

This is also verified by the contrast change in the ptychographic XMCD absorption images in

Figure 7.6A, which correspond to the energies of peaks B_1, A and B_2 and show an alternation of

contrast of magnetosomes as the energy increases from 708.2 to 710.5 eV. The extracted
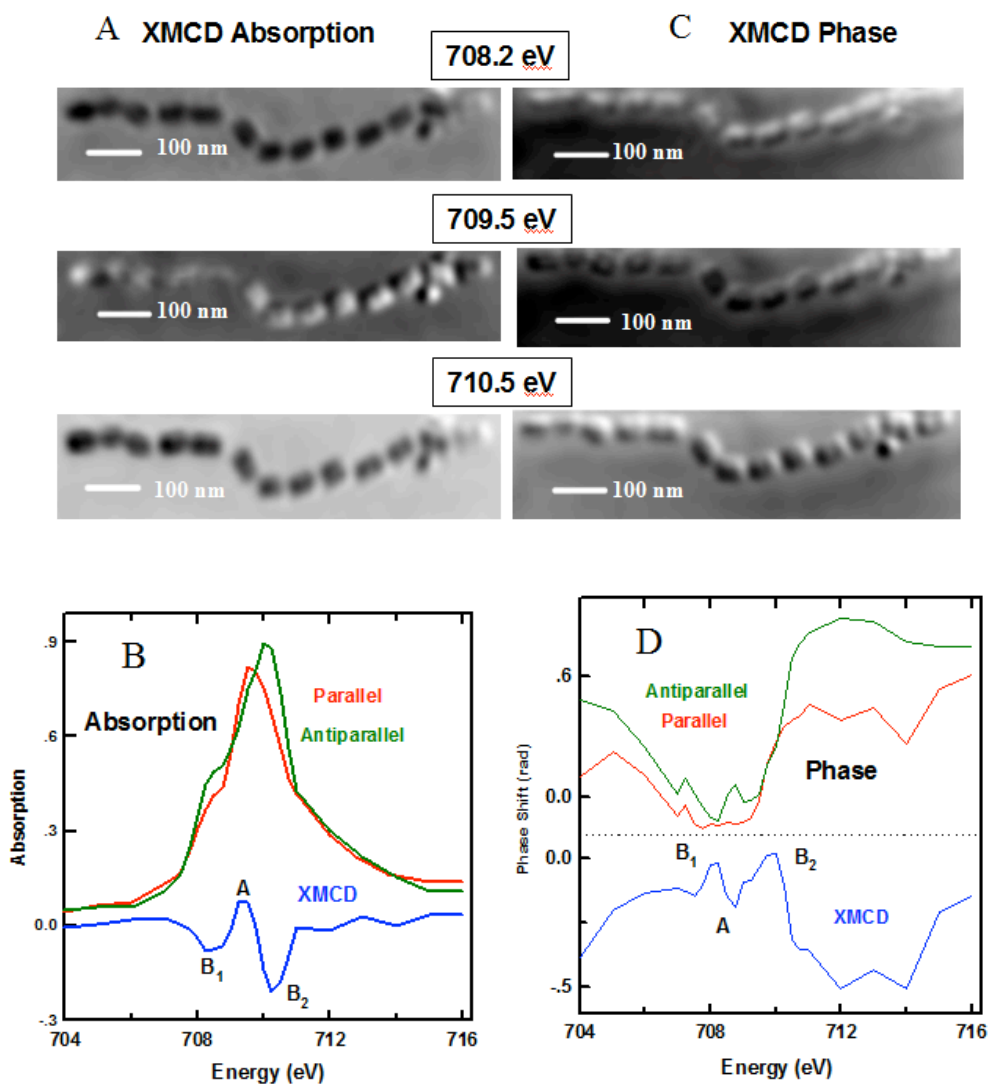
Figure 7.6 Ptychographic XMCD measurements of extracted magnetosome chains. (A) Ptychography absorption XMCD signals from an extracellular magnetosome chain measured at 708.2, 709.5 and 710.5 eV, respectively.**(B)** Ptychography phase XMCD signals from an extracellular magnetosome chain measured at 708.2, 709.5 and 710.5 eV, respectively. (c) Fe L_3-edge absorption and (D) phase signals integrated over the extracellular magnetosome chain in Figure 5a. The XMCD spectrum (blue) is also plotted in (b) and (c). (BL 11.0.2)

magnetosome sample was partly oxidized due to exposure to air over many months. As a result, the oxidized state of this sample leads to a shoulder at 708.5 eV in the ptychography absorption

spectrum and a much stronger B_2 peak in the XMCD absorption spectrum (Zhu et al., 2015a).

Figure 7.6C presents the ptychographic XMCD phase signals of the extracellular magnetosome chain measured at 708.2 eV, 709.5eV, and 710.5eV. **Figure 7.6D** shows the Fe L_3 ptychographic phase spectra of the extracellular magnetosome chain recorded with the photon polarization parallel (red) and antiparallel (green) to the sample magnetization, which were extracted from the full sequence of ptychographic phase images. Contrary to the "negative-positive-negative" contrast change of magnetosomes in ptychographic XMCD absorption signals, an almost reversed "positive-negative-positive" contrast change is observed in the ptychographic XMCD phase signals in Figure 7.6C. The interpretation of ptychography phase spectra is not well established. The phase spectra recorded with the two opposite elliptical polarizations do have different spectral fine structures. More importantly, the ptychographic XMCD phase spectrum (blue) derived from the difference of the two ptychographic phase spectra (parallel and anti-parallel) also exhibits a three-peak feature in the L_3 region but with an opposite sign to that in the ptychographic absorption spectrum in Figure 7.6B. In a previous study, Scherz et al. (Scherz et al., 2007) applied soft X-ray holography to magnetic Co/Pd multilayer samples using left and right circular polarization and they also observed that the absorption and phase differences had opposite signs in the resonance region. These results indicate that XMCD signals computed from ptychographic phase spectra contain information related to magnetic properties of the sample which can be used to probe site occupancy and magnetic moments of different Fe environments in magnetosomes. In addition, the spectral features in the range of 710 to 716 eV in the XMCD phase spectrum change more significantly than those in 708-710 eV region. One possible reason might be related to the successive mode used to collect XAS data. In this study, the complete image stacks were first measured with one polarization before elliptically

polarizing undulator (EPU) reverses the polarization. According to a previous study (Kalirai et al., 2012), measurements made using the successive mode are of lower quality and reliability, due to beamline instability and carbon build-up, than concurrent mode measurements, which alternate two opposite polarizations at each energy point.

Figure 7.7A compares the XMCD signals of an intracellular MV-1 magnetosome chain, as observed in the ptychography absorption and ptychography phase signals, respectively. These XMCD images were measured at 708.2, 709.5 and 710.5 eV, which correspond to the energies of the XMCD peaks B_1, A and B_2 respectively (see **Figure 7.7b**). **Figure 7.7B** and **7.7C** present the Fe L_3 XAS spectra of the intracellular magnetosome chain recorded with the photon polarization parallel (red) and antiparallel (green) to the sample magnetization, which were extracted from the full sequence of ptychographic absorption and phase images, respectively. The corresponding XMCD spectra (blue) are also plotted in Figures 7.7B and 7.7C. The measured XAS and XMCD ptychography absorption spectra are in a good agreement with reference XAS and XMCD spectra of magnetosomes recorded in conventional transmission mode (Kalirai et al., 2012; Lam et al., 2010; Zhu et al., 2015a), suggesting that the magnetic information is retrieved properly with ptychography absorption. As with the ptychographic XMCD absorption signals of extracellular magnetosome chain (Figure 7.6A), the intracellular magnetosome chain exhibits a "negative-positive-negative" contrast change as the energy increases from 708.2 to 710.5 eV (Figure 7.7A). However, the ptychography XMCD phase signals in Figure 7.7A do not show the alternating contrast change of magnetosomes with increasing energy. In addition, the ptychographic XMCD phase spectrum of intracellular magnetosome chain is ill-defined in the 708-711 eV region (Figure 7.7C). This is in contrast to the case of the extracellular magnetosome chain, where an XMCD phase spectrum with a reversed sign relative to the XMCD absorption

spectrum was observed in phase mode (Figure 7.6D). Possible reasons for this discrepancy are

discussed below.
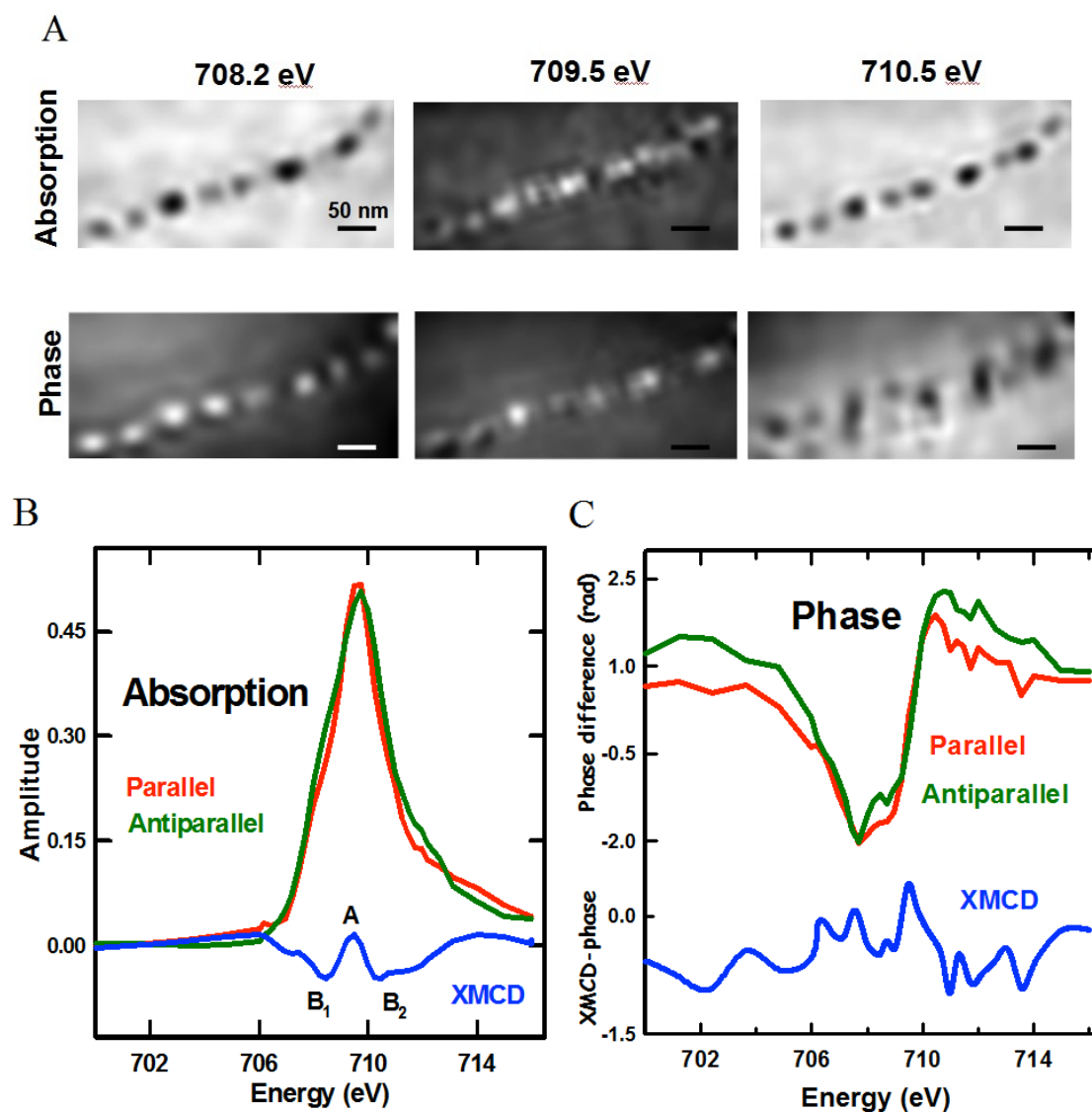
Figure 7.7 Ptychographic XMCD measurements of intracellular magnetosome chains. (A) Comparison of the XMCD signal from a single magnetosome chain in an individual MV-1 cell, in the reconstructed ptychography absorption and ptychography phase signals, respectively. The XMCD signal was measured at 708.2, 709.5 and 710.5 eV. (B) Fe L_3-edge OD and (C) phase signals of the intracellular magnetosome chain in Figure 7.7A. The XMCD spectrum (blue), the difference of two XAS spectra recorded with photon polarization parallel (red) and antiparallel (green) to sample magnetization, is shown below in each panel.

7.4. Discussion

The existence of mineral precursors in the process of magnetosome biomineralization in

MTB cells has been debated. Using Mössbauer spectroscopy, Frankel et al. (1983) reported that

an amorphous ferrihydrite $((Fe^{3+})_2O_3 \cdot 0.5H_2O)$ precursor was formed and then partially reduced

and dehydrated to Fe_3O_4. In contrast, Abe et al. (1999) have suggested that ferric hydroxyl

phases of goethite (α-FeOOH) and lepidocrocite (γ-FeOOH) are the precursor of Fe_3O_4 in a

process mimicking bacterial magnetosome synthesis. However, Faivre et al (Faivre et al., 2007)

reported that a mineral precursor was not observed in a time-resolved Mössbauer study and

suggested that Fe(II) and Fe(III) were quickly co-precipitated to Fe_3O_4 within magnetosome

vesicles. Recently, by using XAS combined with XMCD techniques, Staniland et al. (2007)

observed that a non-magnetic hematite (α-Fe_2O_3) phase acted as the precursor of Fe_3O_4, which

then rapidly converted to mature Fe_3O_4 in 15 minutes. It is notable that an immature

magnetosome phase was observed previously using conventional STXM (Kalirai et al., 2013).

However, characterization by conventional STXM is very challenging, particularly when the

region of interest is smaller than 10 nm. In this context, localization of mineral precursors and

the observation of a single immature magnetosome inside an MV-1 cell (Figure 7.5A), shows

that ptychography will be a valuable tool to study biomineralization process in MTB cells.

Figure 7.5B shows that the gap, precursor-like region, immature magnetosome and mature

magnetosome have different Fe L_3 absorption spectra, indicating that different iron species are

present in the MV-1 cell. These results, and further systematic ptychographic spectroscopy

studies as a function of magnetosome development, will provide a better understanding of how

these Fe phases are converted and mediated to form Fe_3O_4. Previous studies have shown that

Fe(II) is taken up from the environment and transported into magnetosome vesicles by several

types of MTB cells, including *Aquaspirillum magnetotacticum* MS-1 (Frankel et al., 1983),

Magnetospirillum gryphiswaldense MSR-1 (Faivre et al., 2007), and *Magnetospirillum* sp.

AMB-1 (Nakamure et al., 1995). In this study, over 70% of the iron in the culture medium used

to grow MV-1 cells is Fe(II) so it is assumed that Fe(II) is also the major Fe component that is

taken up by the MV-1 cell (Bazylinski and Frankel, 2004). This is consistent with the result that

there is more Fe(II) than Fe(III) in the gap area. However, the fact that the precursor-like region

has more Fe(III) than the gap area suggests that Fe(II) is probably oxidized to Fe(III) to form the

precursor phase. In addition, it is likely that the precursor is further oxidized to hematite (α-

Fe_2O_3) phase in the form of immature magnetosomes (Figure 7.5A). α-Fe_2O_3 can be considered

as an intermediate phase prior to Fe_3O_4 formation, as reported by Staniland et al. (2007). Based

on these observations we propose that the pathway of magnetosome biomineralization for the

MV-1 strain is as follows:

(i) Iron is taken up from the environment as Fe(II) or Fe (III)

(ii) Part of the Fe(II) is then oxidized to Fe(III) to form a precursor, either inside or as the Fe(II)
    enters the cell.

(iii) The precursor is further oxidized and transformed to α-Fe_2O_3, which is then ultimately
    converted to mature Fe_3O_4.

We have used soft X-ray spectro-ptychography to measure the X-ray absorption (XAS) and

X-ray magnetic circular dichroism (XMCD) spectra from individual magnetosomes within an

individual magnetotactic bacterium (MTB). Taking advantage of a fast CCD camera and the

Nanosurveyor-I instrument at ALS 5.3.2.1 beamline (Yu et al., 2015), Fe 2p XAS spectra (from

700 to 732 eV) were measured in ~8 hours on multiple MTB cells over an area of 2.5 μm × 2.5

μm. This allowed measurement of the full Fe L-edge ptychographic absorption and phase spectra

of magnetosomes in intact cells for the first time. Previously, other studies showed that chemical differentiating can be achieved through the phase signal derived from ptychographic measurements (Beckers et al., 2011; Maiden et al., 2013; Takahashi et al., 2011). However, the ptychographic data in those prior studies was only collected at a few discrete points so that the full ptychography spectra were missing. Recently, absorption and phase spectra over the full energy range of an absorption edge have been achieved (Shapiro et al., 2014; Yu et al., 2015). In this study, the ptychographic scan spanned from 700 to 732 eV with 76 points, which provided a detailed comparison of the absorption and phase signal over the full range of the Fe $L_{2,3}$ absorption and phase spectrum. The phase signal exhibited inverted contrast compared to the modulus signal in the pre-edge region but reversed its sign after the absorption edge (Figure 7.4). Because the phase signal changes more significantly than modulus signals through the absorption resonance, it might possess unique advantages over absorption signal in terms of chemical differentiation, especially around absorption resonance region. Using the high brightness and 90% circularly polarized light in 11.0.2 undulator beamline at ALS, we measured Fe L_3 XMCD spectra from both extracellular and intracellular magnetosomes. We showed that XMCD spectra could be derived from both isolated and intracellular magnetosomes and that the XAS is in a good agreement with absorption reference spectra (Kalirai et al., 2013, 2012; Lam et al., 2010). The ptychographic XMCD phase spectrum was measured from magnetosomes extracted from cells, and exhibited a "negative-positive- negative" feature from 708 to 712 eV, similar to the absorption and ptychographic modulus. However, the phase signal from intracellular magnetosomes differed. We speculate this difference may be due to the presence of surrounding poorly crystallized biomaterials. The results clearly indicate that both absorption and phase ptychography signal can probe magnetic dichroic information.

Chapter 8

Summary and Outlook

This chapter provides a summary of the thesis, followed by an outline of the major original contributions I have made. Suggestions are provided for the future studies of magnetotactic bacteria with soft X-ray microscopy

8.1 Summary

Soft X-ray STXM (scanning transmission X-ray microscopy) and ptychography were used to characterize the chemistry and magnetism of magnetotactic bacteria (MTB) on an individual cell and an individual magnetosome basis. The research can be divided into three categories: spectroscopy, biochemistry and biomineralization, and instrumentation.

For the spectroscopic aspects, the Fe L-edge X-ray absorption spectra (XAS) and X-ray magnetic circular dichroism (XMCD) of Fe_3O_4 were first investigated at the start of my thesis, as the published XAS and XMCD spectra of magnetite (Fe_3O_4) were not consistent and often contradicted each other. Specifically, some of the published Fe L_3 XAS spectra of Fe_3O_4 exhibited an additional low-energy shoulder at ~708 eV (about 1.5 eV below the main $2p_{3/2} \rightarrow 3d$ peak), while others did not (Zhu et al., 2015). By chemically modifying biogenic magnetosomes and abiogenic Fe_3O_4 nanopowder with air oxidization and H_2 reduction, I showed that the spectra with an additional peak at 708 eV are due to the existence of maghemite in the samples, in some cases emphasized by the use of a surface sensitive detection mode such as total electron yield (TEY). Regarding greigite (Fe_3S_4), its XAS and XMCD spectra were measured and found to be

very different than that of magnetite. As a matter of fact, the Fe L_{23} XAS spectrum of Fe_3S_4 appears to be rather similar to that of elemental Fe. With respect to the electronic structure of Fe_3S_4, some groups have stated it is semi-metal (Devey et al., 2009; Spender et al., 1972) while others claim it is metallic (Zhang et al., 2012). Although the electronic structure of Fe_3S_4 has yet been fully understood, our results may shed light on this issue.

In the area of the MTB biochemistry and biomineralization, two different species were examined: magnetotactic multicellular prokaryote (MMP), a greigite producer, and *Magnetovibrio blakemorei* strain MV-1, a magnetite producer. First, the XAS and XMCD spectra of MMP were extracted and compared to those of synthesized greigite nanoparticles. I showed that, although the XAS spectra of the synthetic Fe_3S_4 nanoparticles and Fe_3S_4 magnetosomes in MMP were slightly different, their XMCD spectra were rather similar, indicating that Fe_3S_4 magnetosomes biomineralized by MMPs were close to stoichiometric. In addition, two sulfur species, sulfate and sulfide, were identified in MMPs, both of which were likely involved in sulfur metabolism in MMPs. Second, as a follow-up to an earlier study (Kalirai et al., 2013), I performed a statistical study of magnetic polarities of south-seeking (SS) MV-1 cells. It was observed that only one out of 110 MV-1 cells exhibited magnetic reversal, and that the sub-population with gaps increased as the cell culture matured. This work showed that magnetic reversal in a single cell occurs with a low frequency and that most MV-1 cells produce magnetosome chains with the same magnetic polarity during cell replication. Based on these results, I proposed a modified model of polar magneto-aerotaxis behavior for MV-1, which took into account the effects of surrounding O_2 concentration, flagellum rotation, and magnetic polarity of magnetosome chains on the swimming behavior of SS MV-1 cells.

In the area of instrumentation and technique development, I showed that the spatial resolution of X-ray spectro-microscopy of MTB can be greatly improved by applying soft X-ray spectro-ptychography. Specifically, I used Fe L_{23} spectro-ptychography to record the first Fe L_3 XAS and XMCD spectra of individual magnetosomes in both ptychographic absorption and phase modes. With the high spatial resolution achieved (7 nm), precursor-like and immature magnetosome phases in an intact MV-1 cell were visualized and their Fe 2p spectra measured. Based on these new results, I proposed a model for magnetosome biomineralization byMV-1.

8.2 Original contribution of this thesis

Based on the observations, results, and conclusions, the major original contributions contained in this thesis are:

➢ Clarification of the confusion in the literature as to the shape of the Fe L-edge XAS spectra of magnetite (Fe_3O_4). Provided experimental verification of the link between spectral shape and degree of oxidization and crystal structure of Fe_3O_4

➢ Characterization of Fe_3S_4-producing MMP MTB with STXM-XMCD. Magnetic microstructures and sulfur metabolism were probed.

➢ Development of a method which combined TEM imaging and XMCD mapping to determine the magnetic polarity of magnetosome chains relative to the flagellum orientation.

➢ Performing a statistical study of magnetic polarity of MTB cells which resulted in a modified polar magneto-aerotaxis model for MV-1 MTB cells which explicitly applies to both single polarity cells and those with sub-chains of opposite magnetic polarities.

> ➢ Application of spectro-ptychography to study biomineralization and magnetism of MTB
>
> cells. A spatial resolution of 7 nm below 1000 eV was achieved with ptychography,
>
> which was the highest in the soft X-ray region so far. Observation of precursor-like and
>
> immature magnetosomes in intact MV-1 cells with ptychography. Proposing a model for
>
> the pathway of magnetosome biomineralization for MV-1.Demonstrating that XMCD
>
> spectra could be derived with both ptychography modulus and phase modes, and the
>
> phase and absorption mode XMCD were found to be very different.

8.3 Future work

8.3.1 Verification of the proposed polar magneto-aerotaxis model for MV-1

According to the statistical results in Table 6.1 (Chapter 6), magnetic reversal of two or

more sub-chains in a single cell only occurs with a low frequency. Based on this and the previous

polar magneto-aerotaxis model proposed by Frankel et al. (1997), a modified model for

magneto-aerotaxis behavior of MV-1 was proposed (see Figure 6.5). According to this model,

the flagellum rotation of MV-1 cells is mainly determined by the O_2 level, which in turn controls

the swimming direction. If this is true, MV-1 cells with opposite magnetic polarities can still

swim towards the desired direction (i.e. behave with north-seeking or south-seeking behavior) as

long as they rotate their flagella in opposite ways. I hypothesized that only the link of flagella

rotation direction and [O2] is meaningful; that the magnetic moment polarity is not relevant.

One approach to verify this hypothesis would be to collect north-seeking (NS) and south-

seeking (SS) MV-1 cells from the same culture and measure the magnetic polarity of these cells

with STXM-XMCD, using TEM to visualize the flagellum location relative to the magnetosome

chains. It is expected that NS and SS cells will exhibit opposite magnetic polarities relative to the

flagellum orientation because the O_2 level mainly determines the swimming direction according to the proposed model. However, since the flagellum is very fragile and can be dethatched from the cell body easily, extreme care must be taken when preparing these samples.

Another approach to verify the model is to directly probe the flagellum rotation in a single live MTB cell, which can be achieved in several ways. One way is to label the flagellum and the MTB cell with location-specific fluorescence dyes. **Figure 8.1** presents fluorescence
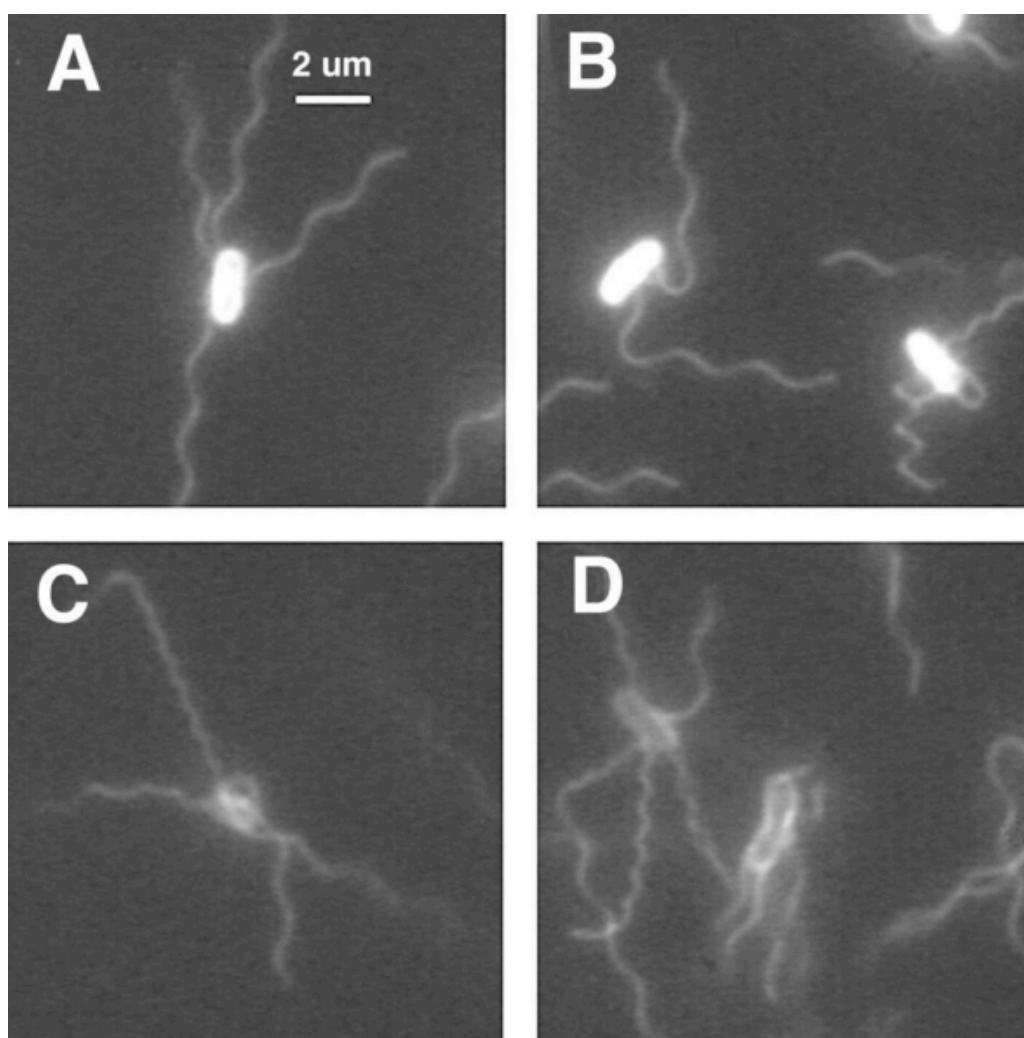
Figure 8.1 Cells of *E. coli* viewed labeled with Oregon Green 514 (A and B) and with Alexa Fluor 532 (C and D) (Turner et al., 2000).

images of *Escherichia coli* cells which are labeled with different fluoresce dyes (Turner et al.,

2000). If the flagellum and/or the MTB cell body can be tagged with fluorophores, one can

record the cell motion in real time with a video camera in a fluorescence microscope, which,

after measuring sufficient number of cells, can determine whether north-seeking cells rotate in

the same or in opposite directions relative to south-seeking cells. Another way to visualize the

flagellum rotation is to attach some fluorescence beads to the flagellum of the cell as described

by Cluzel et al. (2000). By monitoring the movements of the fluorescence beads, one can probe

the rotation of the flagellum.

8.3.2 Time-course biomineralization study on MTB cells with ptychography

In Chapter 7, I demonstrated that spectro-ptychography can measure Fe $L_{2,3}$ XAS and

XMCD spectra of different regions in an MV-1 cell and showed that different regions contain

different chemical signatures (see Figure 7.5). This helped to understand the biomineralization

process in MV-1 cells. Note that this measurement was performed on only one MV-1 cell under

a certain growth state. In the future, it will be worthwhile to perform a time-resolved study on

MTB cells, aiming to get more details regarding the mechanism of magnetosome

biomineralization. For example, we can continuously extract the MTB cells from the growth

medium at specific times after magnetosome synthesis starts (Staniland et al., 2007). The

extraction will cease when the mature magnetosome chain appears. Fe L-edge spectro-

ptychography measurements will be performed on the MTB cells in the different growth states.

The derived XAS absorption spectra from ptychography reconstruction would be measured from

the gaps, immature magnetosomes, cytoplasm, and mature magnetosomes inside individual cells.

These results can identify different Fe species and thus monitor how the ratio of Fe(II) to Fe(III)

changes, and how the different Fe species change, as the biomineralization of Fe_3O_4 proceeds.

The high spatial resolution and chemical sensitivity provided by spectro-ptychography can

provide new insights into magnetosome formation and the biomineralization mechanism.

8.3.3 Tomography study of MTB cell in the natural, hydrated state

In the past few years, cryo-electron tomography (cryo-ET) has been used to probe the 3D

internal structure of magnetotactic bacteria cell in three-dimensional space(Komeili et al., 2006,

2004). However, the relatively shallow penetration depth of electrons means that the cells can

only be imagined after they have been cut into sections less than 0.5 μm thick (McDermott et al.,

2012; Parkinson et al., 2008). There are significant concerns that the fidelity of the cell

ultrastructure is affected by the sectioning process. Because of more penetrating properties of X-

rays compared to electrons, thick biological specimens can be observed by soft X-ray

tomography (SXT) without sectioning. Thus 3-D imaging of whole intact magnetotactic bacteria

cells could be achieved with SXT. In this thesis, all measurements were performed on air-dried

samples. When the MTB cells are dried in air, it is inevitable that the cell shape changes and the

magnetosome chains are no longer arranged as they are in intact, fully hydrated MTB cells.

Although cell fixation can help to main cell morphology during the drying process, some

information regarding the orientation of organelles such as magnetosome chains may still not be

preserved well. Therefore, it is worthwhile to measure MTB cells in natural and hydrated states.

My colleague, Juan Wu, and I have tried to perform a tomography study of AMB-1 MTB cell in

the hydrated state using the approach developed by Schmid et al. (2014) (see **Figure 8.2**). Figure

8.2A presents a STXM transmission image of an AMB-1 cell in culture solution at 710 eV,

where a magnetosome chain is visualized. **Figure 8.2 B** and **C** presents the component image of

AMB-1 cell and H_2O while **Figure 8.2D** shows the overlap of these two images. These

component maps are derived by the stack fitting method using the O1s XAS spectra of AMB-1

cell and H_2O as the reference spectra (**Figure 8.2E**). As shown in Figure 8.2D, the AMB-1 cell

and surrounding H_2O can be easily differentiated based on their O 1s spectra. Since

magnetosomes have strong absorption signals in the energy range of 708~710 eV, it is relatively

easy to measure the Fe L_{23} spectra of magnetosomes in the presence of water. In future studies,

in addition to 2D spectromicroscopy, tomography studies of MTB cells at the O 1s and Fe 2p

edges should be measured in order to obtain the three dimensional structure of magnetosome

chains relative to the MTB cell body in the natural hydrated state.
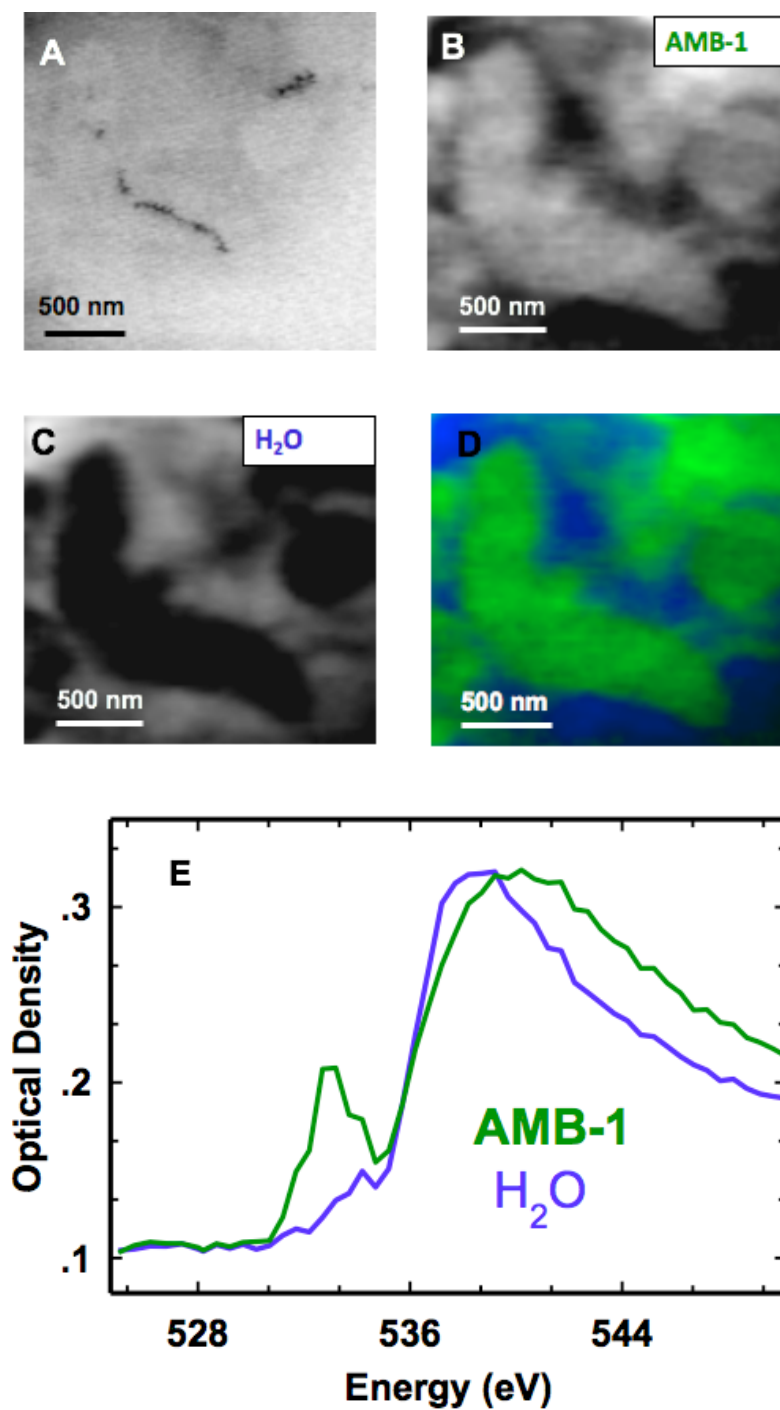
Figure 8.2 Projection images of an AMB-1 cell in culture solution. (A) STXM transmission image of an AMB-1 cell in solution. Component images of AMB-1 cell (B) and H_2O (C). (D) Overlay image of B and C. (E) The O1s XAS spectra of AMB-1 cell and H_2O used to derive the component images, B and C, in the stacking fitting procedure.

8.3.4 Spectroscopy of Fe$_3$S$_4$ and its application to characterize other Fe$_3$S$_4$ producers

It has been demonstrated that Fe$_3$S$_4$ nanoparticles have rather different XAS and XMCD spectra from those of Fe$_3$O$_4$, although Fe$_3$S$_4$ is generally considered as a sulfur analog of Fe$_3$O$_4$. A recent density functional theory (DFT) calculation showed that Fe$_3$S$_4$ is metallic (Zhang et al., 2012). This is consistent with the Fe XAS spectrum of Fe$_3$S$_4$ I measured (Figure 5.2 in Chapter 5), which is much more similar to elemental Fe than that of Fe$_3$O$_4$. From the point of view of crystal structure, the difference between Fe$_3$O$_4$ and Fe$_3$S$_4$ is the degree of covalence of iron with oxygen and sulfur. More spectroscopic measurements and theoretical calculation are needed to understand the o electronic properties and Fe L$_{23}$ spectra of greigite.

The XAS and XMCD reference spectra of synthesized greigite can be used as reference spectra to characterize more complicated MTB species, such as BW-1. BW-1 is the first Fe$_3$S$_4$-producing MTB that has been isolated and grown in axenic culture (Lefèvre et al., 2011b). It has been shown that BW-1 can synthesize both Fe$_3$O$_4$ and Fe$_3$S$_4$. However, the distribution of various elements (Fe, O, S, C, etc.), and how the magnetic particles are distributed in BW-1 cells have not yet been addressed, although they are key to understanding the mechanism of biomineralization and magnetosome chain assembly. By imaging the distribution of different chemical components in individual cells of BW-1, the biomineralization mechanism of this special magnetotactic bacterium will be better understood.

8.3.5 Studies of gene mutant and other MTB species

Up to now, about 20 magnetosome-specific proteins have been identified in MTB cells, which have specific functions in vesicle formation, iron transport, magnetosome crystallization, and magnetosome chain organization (Schüler, 2008). By comparing the features of

magnetosomes and magnetosome chains (size, morphology, chain length, magnetism, etc.) of individual MTB cells with and without a specific gene, the function of that gene may be understood.

All the samples studied in this thesis are wild type. It is notable that STXM-XMCD can also be applied to study gene defective mutant strains of MTB cells. In particular, STXM-XMCD can measure the magnetism (i.e. magnetic moment and magnetic polarity) of MTB cells. Previous Monte Carlo simulations show that if active magnetosome transport is removed and only the magnetic interaction exists then small magnetosome sub-chains with opposite magnetic polarities are produced. Such a defect in active transport is considered as an analog of the ΔmamK deletion mutant (Klumpp and Faivre, 2012). However, this hypothesis has not been verified experimentally. In this sense, if STXM-XMCD technique is used to compare wild type MTB and ΔmamK deletion mutant, it may be possible to verify the function of mamK gene in the process of magnetosome chain formation, in particular to determine whether it plays a role in the magnetic alignment of magnetosome sub-chains.In addition, since I have isolated some MTB cells from local area in Hamilton, further study such as cultivation, STXM-XMCD characterization, genetic analysis, would be interesting to perform.

Due to its excellent chemical sensitivity and high spatial resolution, STXM has become an indispensable technique for researchers addressing issues in various scientific fields. The methodology and results presented in this thesis will shed light on chemical, magnetic and biomienralization properties on MTB species and other biological systems in the future.

References

Abe, M., Ishihara, T., Kitamoto, Y., 1999. Magnetite film growth at 30 degrees C on organic monomolecular layer, mimicking bacterial magnetosome synthesis. J. Appl. Phys. 85, 5705–5707.

Alexandre, G., Greer-Phillips, S., Zhulin, I.B., 2004. Ecological role of energy taxis in microorganisms. FEMS Microbiol. Rev. 28, 113–126.

Alphandéry, E., Ding, Y., Ngo, A.T., Wang, Z.L., Wu, L.F., Pileni, M.P., 2009. Assemblies of aligned magnetotactic bacteria and extracted magnetosomes: What is the main factor responsible for the magnetic anisotropy? ACS Nano 3, 1539–1547.

Amemiya, Y., Tanaka, T., Yoza, B., Matsunaga, T., 2005. Novel detection system for biomolecules using nano-sized bacterial magnetic particles and magnetic force microscopy. J. Biotechnol. 120, 308–314.

Anders, E., Buseck, P.R., Bazylinski, D.A., Frankel, R.B., 1998. Reaction sequence of iron sulfide minerals in bacteria and their use as biomarkers. Science 280, 880–883.

Antonov, V.N., Harmon, B.N., Yaresko, A.N., 2003. Electronic structure and x-ray magnetic circular dichroism in Fe_3O_4 and Mn-, Co-, or Ni-substituted Fe_3O_4. Phys. Rev. B 67, 024417.

Attwood, D., 1999. Soft x-rays and extreme ultraviolet radiation: principles and applications. Cambridge University Press, Cambridge.

Balerna, A., Mobilio, S., 2015. Introduction to synchrotron radiation, in: Mobilio, S., Boscherini, F., Meneghini, C. (Eds.), Synchrotron Radiation. Springer-Verlag, Berlin Heidelberg, pp. 3–28.

Balkwill, D.L., Maratea, D., Blakemore, R.P., 1980. Ultrastructure of a magnetotactic spirillum. J. Bacteriol. 141, 1399–1408.

Bauer, E., Man, K.L., Pavlovska, A., Locatelli, A., Menteş, T.O., Niño, M.A., Altman, M.S., 2014. Fe_3S_4 (greigite) formation by vapor–solid reaction. J. Mater. Chem. A 2, 1903–1913.

Bazylinski, D. A., Frankel, R.B., 2003. Biologically controlled mineralization in prokaryotes. Rev. Mineral. Geochemistry 54, 217–247.

Bazylinski, D. A., Lefèvre, C., 2013. Magnetotactic bacteria from extreme environments. Life 3, 295–307.

Bazylinski, D.A., Frankel, R.B., 2004. Magnetosome formation in prokaryotes. Nat. Rev. Microbiol. 2, 217–230.

Bazylinski, D.A., Frankel, R.B., Garratt-Reed, A.J., Mann, S., 1990. Biomineralization of iron sulfides in magnetotactic bacteria from sulfidic environments, in: Frankel, R.B., Blakemore, R.P. (Eds.), Iron Biominerals. Plenum Press, New York, NY, USA, pp. 239–255.

Bazylinski, D.A., Frankel, R.B., Heywood, B.R., Mann, S., King, J.W., Donaghay, P.L., Hanson, A.K., 1995. Controlled biomineralization of magnetite (Fe_3O_4) and greigite (Fe_3S_4) in a magnetotactic bacterium. Appl. Environ. Microbiol. 61, 3232–3239.

Bazylinski, D.A., Garratt-Reed, A.J., Frankel, R.B., 1994. Electron microscopic studies of magnetosomes in magnetotactic bacteria. Microsc. Res. Tech. 27, 389–401.

Bazylinski, D.A., Garrattreed, A.J., Abedi, A., Frankel, R.B., 1993. Copper association with iron sulfide magnetosomes in a magnetotactic bacterium. Arch. Microbiol. 160, 35–42.

Bazylinski, D.A., Moskowitz, B.M., 1998. Microbial biomineralization of magnetic iron minerals: microbiology , magnetism and environmental significance. Rev. Mineral. Geochem. 35, 217-223

Bazylinski, D.A., Schlezinger, D.R., Howes, B.H., Frankel, R.B., Epstein, S.S., 2000. Occurrence and distribution of diverse populations of magnetic protists in a chemically stratified coastal salt pond. Chem. Geol. 169, 319–328.

Bazylinski, D.A., Schübbe, S., 2007. Controlled biomineralization by and applications of magnetotactic bacteria. Adv. Appl. Microbiol. 62, 21–62.

Bazylinski, D.A., Williams, T.J., Lefèvre, C.T., Trubitsyn, D., Fang, J., Beveridge, T.J., Moskowitz, B.M., Ward, B., Schübbe, S., Dubbels, B.L., Simpson, B., 2013. Magnetovibrio blakemorei gen. nov., sp. nov., a magnetotactic bacterium (Alphaproteobacteria: Rhodospirillaceae) isolated from a salt marsh. Int. J. Syst. Evol. Microbiol. 63, 1824–1833.

Beckers, M., Senkbeil, T., Gorniak, T., Reese, M., Giewekemeyer, K., Gleber, S.C., Salditt, T., Rosenhahn, A., 2011. Chemical contrast in soft X-ray ptychography. Phys. Rev. Lett. 107, 1–4.

Bellini, S., 2009a. On a unique behavior of freshwater bacteria. Chinese J. Oceanol. Limnol. 27, 3–5.

Bellini, S., 2009b. Further studies on "magnetosensitive bacteria." Chinese J. Oceanol. Limnol. 27, 6–12.

Berner, R.A., 1984. Sedimentary pyrite formation: An update. Geochim. Cosmochim. Acta 48, 605–615.

Blakemore, R., 1982. Magnetotactic bacteria. Annu. Rev. Microbiol. 36, 217–238.

Blakemore, R., 1975. Magnetotactic bacteria. Science 190, 377–379.

Blakemore, R.P., Frankel, R.B., Kalmijn, A.J., 1980. South-seeking magnetotactic bacteria in the Southern Hemisphere. Nature 286, 384–385.

Chang, L., Pattrick, R.A.D., van der Laan, G., Coker, V.S., Roberts, A.P., 2012a. Enigmatic X-

ray magnetic circular dichroism in greigite (Fe_3S_4). Can. Mineral. 50, 667–674.

Chang, L., Winklhofer, M., Roberts, A.P., Dekkers, M.J., Horng, C.S., Hu, L., Chen, Q., 2012b. Ferromagnetic resonance characterization of greigite (Fe_3S_4), monoclinic pyrrhotite (Fe_7S_8), and non-interacting titanomagnetite ($Fe_{3-x}Ti_xO_4$). Geochemistry, Geophys. Geosystems 13.

Chang, C.-H., Hwang, C.-S., Chang, C.-H., Chen, H.-H., Lin, F.-Y., Huang, J.-C., Wu, C.-M., Wu, C.-Y., Fan, T.-C., Hsu, K.-T., 2012c. Construction and performance of an elliptically polarized undulator of type Apple-II. J. Chinese Inst. Eng. 35, 63–68.

Chang, L., Rainford, B.D., Stewart, J.R., Ritter, C., Roberts, A.R., Tang, Y., Chen, Q., 2009a. Magnetic structure of greigite (Fe_3S_4) probed by neutron powder diffraction and polarized neutron diffraction. J. Geophys. Res. Solid Earth 114, 1–10.

Chang, L., Roberts, A.P., Rowan, C.J., Tang, Y., Pruner, P., Chen, Q., Horng, C.-S., 2009b. Low-temperature magnetic properties of greigite (Fe_3S_4). Geochem. Geophys. Geosyst. 10, 1-14

Chang, S., 1989. Magnetofossils, The magnetization of sediments, and the evolution of magnetite biomineralization. Annu. Rev. Earth Planet. Sci. 17, 169–195.

Chao, W., Fischer, P., Tyliszczak, T., Rekawa, S., Anderson, E., Naulleau, P., 2012. Real space soft x-ray imaging at 10 nm spatial resolution. Opt. Express 20, 9777-9783.

Chao, W., Kim, J., Rekawa, S., Fischer, P., Anderson, E.H., 2009. Demonstration of 12 nm resolution Fresnel zone plate lens based soft x-ray microscopy. Opt. Express 17, 17669–17677.

Chen, C.T., Sette, F., Ma, Y., Modesti, S., 1990. Soft-x-ray magnetic circular dichroism at the $L_{2,3}$ edges of nickel. Phys. Rev. B 42, 7262–7265.

Chen, L., Bazylinski, D.A., Lower, B.H., 2012. Bacteria that synthesize nano-sized compasses to

navigate using Earth's geomagnetic field. Nat. Educ. Knowl. 3, 5.

Chueh, W.C., El Gabaly, F., Sugar, J.D., Bartelt, N.C., McDaniel, A.H., Fenton, K.R., Zavadil, K.R., Tyliszczak, T., Lai, W., McCarty, K.F., 2013. Intercalation pathway in many-particle LiFePO$_4$ electrode revealed by nanoscale state-of-charge mapping. Nano Lett. 13, 866–872.

Cluzel, P., Surette, M., Leibler, S., 2000. An Ultrasensitive Bacterial Motor Revealed by Monitoring Signaling Proteins in Single Cells. Science 287, 1652–1655.

Crocombette, J., Pollak, M., Jollet, F., Thromat, N., Gautier-Soyer, M., 1995. X-ray-absorption spectroscopy at the Fe L$_{2,3}$ threshold in iron oxides. Phys. Rev. B 52, 3143–3150.

Dunin-borkowski, R.E., Mccartney, M.R., Frankel, R.B., Bazylinski, D.A., Posfai, M., Buseck, P.R., 1998. Magnetic microstructure of magnetotactic bacteria by electron holography. Science 282, 1868–1870

Delong, E.F., Frankel, R.B., Bazylinski, D. A, 1993. Multiple evolutionary origins of magnetotaxis in bacteria. Science 259, 803–806.

Devey, A.J., Grau-Crespo, R., De Leeuw, N.H., 2009. Electronic and magnetic structure of Fe$_3$S$_4$: GGA+U investigation. Phys. Rev. B 79, 1–7.

Devouard, B., Posfai, M., Hua, X., Bazylinski, D.A., Frankel, R.B., Buseck, P.R., 1998. Magnetite from magnetotactic bacteria: Size distributions and twinning. Am. Mineral. 83, 1387–1398.

Donatelli, J., Haranczyk, M., Hexemer, A., Krishnan, H., Li, X., Lin, L., Maia, F., Marchesini, S., Parkinson, D., Perciano, T., Shapiro, D., Ushizima, D., Yang, C., Sethian, J. A., 2015. CAMERA: The Center for Advanced Mathematics for Energy Research Applications. Synchrotron Radiat. News 28, 4–9.

Dunin-borkowski, R.E., Mccartney, M.R., Frankel, R.B., Bazylinski, D.A., Posfai, M., Buseck,

P.R., 1998. Magnetic microstructure of magnetotactic bacteria by electron holography. Science 282, 1868–1870.

Dunin-Borkowski, R.E., McCartney, M.R., Pósfai, M., Frankel, R.B., Bazylinski, D. A., Buseck, P.R., 2001. Off-axis electron holography of magnetotactic bacteria: magnetic microstructure of strains MV-1 and MS-1. Eur. J. Mineral. 13, 671–684.

Edo, T.B., Batey, D.J., Maiden, A.M., Rau, C., Wagner, U., Pesic, Z.D., Waigh, T.A., Rodenburg, J.M., 2013. Sampling in x-ray ptychography. Phys. Rev. A-At. Mol. Opt. Phys. 87, 1–8.

Ehrlich, H.L., 1998. Geomicrobiology: Its significance for geology. Earth Sci. Rev. 45, 45–60.

Faivre, D., Böttger, L.H., Matzanke, B.F., Schüler, D., 2007. Intracellular magnetite biomineralization in bacteria proceeds by a distinct pathway involving membrane-bound ferritin and an iron(II) species. Angew. Chemie - Int. Ed. 46, 8495–8499.

Faivre, D., Fischer, A., Garcia-Rubio, I., Mastrogiacomo, G., Gehring, A.U., 2010. Development of cellular magnetic dipoles in magnetotactic bacteria. Biophys. J. 99, 1268–1273.

Faivre, D., Schuler, D., 2008. Magnetotactic Bacteria and. Chem. Rev. 108, 4875–4898.

Farina, M., Esquivel, D.M.S., de Barros, H.G.P.L., 1990. Magnetic iron-sulphur crystals from a magnetotactic microorganism. Nature 343, 256–258.

Fassbinder, J.W.E., Stanjek, H., Vali, H., 1990. Occurence of magnetic bacteria in soil. Nature 343, 161–163.

Faulkner, H.M.L., Rodenburg, J.M., 2005. Error tolerance of an iterative phase retrieval algorithm for moveable illumination microscopy. Ultramicroscopy 103, 153–164.

Faulkner, H.M.L., Rodenburg, J.M., 2004. Movable aperture lensless transmission microscopy: A novel phase retrieval algorithm. Phys. Rev. Lett. 93, 023903–1.

Feng, M., Lu, Y., Yang, Y., Zhang, M., Xu, Y.-J., Gao, H.-L., Dong, L., Xu, W.-P., Yu, S.-H.,
    2013. Bioinspired greigite magnetic nanocrystals: chemical synthesis and biomedicine
    applications. Sci. Rep. 3, 2994.

Fleet, M.E., 1981. The structure of magnetite. Acta Crystallogr. Sect. B Struct. Crystallogr.
    Cryst. Chem. 37, 917–920.

Frankel, R.B., 2009. The discovery of magnetotactic/magnetosensitive bacteria. Chinese J.
    Oceanol. Limnol. 27, 1–2.

Frankel, R.B., 1984. Magnetic guidance of organisms. Annu. Rev. Biophys. Bioeng. 13, 85–103.

Frankel, R.B., Bazylinski, D.A., 2003. Biologically induced mineralization by bacteria. Rev.
    Mineral. Geochemistry 54, 95–114.

Frankel, R.B., Bazylinski, D.A., Johnson, M.S., Taylor, B.L., 1997. Magneto-aerotaxis in marine
    coccoid bacteria. Biophys. J. 73, 994–1000.

Frankel, R.B., Blakemore, R.P., Wolfe, R.S., 1979. Magnetite in freshwater magnetotactic
    bacteria. Science 203, 1355–6.

Frankel, R.B., Papaefthymiou, G.C., Blakemore, R.P., O'Brien, W., 1983. Fe_3O_4 precipitation in
    magnetotactic bacteria. BBA - Mol. Cell Res.763, 147–159.

Frankel, R.B., Williams, T.J., Bazylinski, D.A., 2007. Magneto-Aerotaxis, in: Schüler, D. (Ed.),
    Magnetoreception and Magnetosomes in Bacteria. Springer, Heidelberg, pp. 1-24.

Freeman, M.R., Choi, B.C., 2001. Advances in magnetic microscopy. Science 294, 1484–1488.

Gargaud, M., Lopez-Garcia, P., Martin, H., 2011. Origins and evolution of life, An
    Astrobiological Perspective. Cambrigde Univ. Press.

Giewekemeyer, K., Thibault, P., Kalbfleisch, S., Beerlink, A., Kewish, C.M., Dierolf, M.,
    Pfeiffer, F., Salditt, T., 2010. Quantitative biological imaging by ptychographic x-ray

diffraction microscopy. Proc. Natl. Acad. Sci. USA. 107, 529–534.

Goering, E.J., Lafkioti, M., Gold, S., Schuetz, G., 2007. Absorption spectroscopy and XMCD at
the Verwey transition of Fe_3O_4. J. Magn. Magn. Mater. 310, 249–251.

Gorby, Y.A., Beveridge, T.J., Blakemore, R.P., 1988. Characterization of the bacterial
magnetosome membrane. J. Bacteriol. 170, 834–841.

Green, J.C.D., Kahramanoglou, C., Rahman, A., Pender, A.M.C., Charbonnel, N., Fraser, G.M.,
2009. Recruitment of the earliest component of the bacterial flagellum to the old cell
division pole by a membrane-associated signal recognition particle family GTP-binding
protein. J. Mol. Biol. 391, 679–690.

Greene, S.E., Komeili, A., 2012. Biogenesis and subcellular organization of the magnetosome
organelles of magnetotactic bacteria. Curr Opin Cell Biol 24, 490–495.

Guizar-Sicairos, M., Fienup, J.R., 2008. Phase retrieval with transverse translation diversity: a
nonlinear optimization approach. Opt. Express 7076, 7264-7268.

Hitchcock, A.P., 2015. Soft X-ray spectromicroscopy and ptychography. J. Electron Spectros.
Relat. Phenomena 200, 49–63.

Hitchcock, A.P., 2012. Soft X-ray Imaging and Spectromicroscopy, in: Van Tendeloo, G., Van
Dyck, D., Pennycook, J.S. (Eds.), Handbook of Nanoscopy. Wiley, pp. 745–792.

Hitchcock, A.P., Berejnov, V., Lee, V., West, M., Colbow, V., Dutta, M., Wessel, S., 2014.
Carbon corrosion of proton exchange membrane fuel cell catalyst layers studied by
scanning transmission X-ray microscopy. J. Power Sources 266, 66–78.

Hitchcock, A.P., Obst, M., Wang, J., Lu, Y.S., Tyliszczak, T., 2012. Advances in the detection of
As in environmental samples using low energy X-ray florescence in a scanning transmission
X-ray microscope: Arsenic immobilization by a Fe(II)-oxidizing freshwater bacteria.

Environ. Sci. Technol. 46, 2821–9.

Holler, M., Diaz, a, Guizar-Sicairos, M., Karvinen, P., Färm, E., Härkönen, E., Ritala, M., Menzel, a, Raabe, J., Bunk, O., 2014. X-ray ptychographic computed tomography at 16 nm isotropic 3D resolution. Sci. Rep. 4, 3857.

Jacobsen, C., Wirick, S., Flynn, G.J., Zimba, C., 2000. Soft x-ray spectroscopy from image sequences with sub-100 nm spatial resolution. J. Microsc. 197, 173–184.

Jandacka, P., Alexa, P., Pistora, J., Li, J., Vojtkova, H., Hendrych, A., 2013. Size distributions of nanoparticles from magnetotactic bacteria as signatures of biologically controlled mineralization. Am. Mineral. 98, 2105–2114.

Jong, T., Parry, D.L., 2003. Removal of sulfate and heavy metals by sulfate reducing bacteria in short-term bench scale upflow anaerobic packed bed reactor runs. Water Res. 37, 3379–3389.

Kalirai, S.S., Bazylinski, D.A., Hitchcock, A.P., 2013. Anomalous magnetic orientations of magnetosome chains in a magnetotactic bacterium: *Magnetovibrio blakemorei* strain MV-1. PLoS One 8, 1–7.

Kalirai, S.S., Lam, K.P., Bazylinski, D.A., Lins, U., Hitchcock, A.P., 2012. Examining the chemistry and magnetism of magnetotactic bacterium *Candidatus Magnetovibrio blakemorei* strain MV-1 using scanning transmission X-ray microscopy. Chem. Geol. 300-301, 14–23.

Kang, B., Fischer, P., Kim, D., Attwood, D., Anderson, E., Cho, G., 2005. Bending magnet X-ray polarization modulation for magnetic full-field soft X-ray transmission microscopy. IPAP Conf. Ser. 7, 288–290.

Kaznatcheev, K. V., Karunakaran, C., Lanke, U.D., Urquhart, S.G., Obst, M., Hitchcock, A.P.,

2007. Soft X-ray spectromicroscopy beamline at the CLS: Commissioning results. Nucl. Instruments Methods Phys. Res. Sect. A Accel. Spectrometers, Detect. Assoc. Equip. 582, 96–99.

Keim, C.N., Abreu, F., Lins, U., De Barros, H.L., Farina, M., 2004. Cell organization and ultrastructure of a magnetotactic multicellular organism. J. Struct. Biol. 145, 254–262.

Keim, C.N., Lins, U., Farina, M., 2009. Manganese in biogenic magnetite crystals from magnetotactic bacteria. FEMS Microbiol. Lett. 292, 250–253.

Keim, C.N., Martins, J.L., de Barros, H.G.P.L., Lins, U., Farina, M., 2006. Structure, behavior, ecology, and diversity of multicellular magnetotactic prokaryotes, in: Schüler, D. (Ed.), Magnetoreception and Magnetosomes in Bacteria. Springer-Verlag, Heidelberg, pp. 103–132.

Keim, C.N., Solórzano, G., Farina, M., Lins, U., 2005. Intracellular inclusions of uncultured magnetotactic bacteria. Int. Microbiol. 8, 111–117.

Kilcoyne, A.L.D., Tyliszczak, T., Steele, W.F., Fakra, S., Hitchcock, A.P., Franck, K., Anderson, E., Harteneck, B., Rightor, E.G., Mitchell, G.E., Hitchcock, A.P., Yang, L., Warwick, T., Ade, H., 2003. Interferometer-controlled scanning transmission X-ray microscopes at the Advanced Light Source. J. Synchrotron Radiat. 10, 125–136.

Kim, D.H., Lee, H.J., Kim, G., Koo, Y.S., Jung, J.H., Shin, H.J., Kim, J.Y., Kang, J.S., 2009. Interface electronic structures of $BaTiO_3$ @X nanoparticles (X=α-Fe_2O_3, Fe_3O_4, γ-Fe_2O_3, and Fe) investigated by XAS and XMCD. Phys. Rev. B - Condens. Matter Mater. Phys. 79, 033402–1–4.

Kirschvink, J.L., Kobayashi-Kirschvink, a, Woodford, B.J., 1992. Magnetite biomineralization in the human brain. Proc. Natl. Acad. Sci. USA. 89, 7683–7687.

Klumpp, S., Faivre, D., 2012. Interplay of magnetic interactions and active movements in the formation of magnetosome chains. PLoS One 7, 1–11.

Komeili, A., 2012. Molecular mechanism of compartmentalization and biomineralization in magnetotactic bacteria. FEMS Microbiol. Rev. 36, 232–255.

Komeili, A., Li, Z., Newman, D.K., Jensen, G.J., 2006. Magnetosomes are cell membrane invaginations organized by the actin-like protein MamK. Science 311, 242–5.

Komeili, A., Vali, H., Beveridge, T.J., Newman, D.K., 2004. Magnetosome vesicles are present before magnetite formation, and MamA is required for their activation. Proc. Natl. Acad. Sci. USA. 101, 3839–44.

Koprinarov, I.N., Hitchcock, A.P., McCrory, C.T., Childs, R.F., 2002. Quantitative mapping of structured polymeric systems using singular value decomposition analysis of soft X-ray images. J. Phys. Chem. B 106, 5358–5364.

Kuiper, P., Searle, B.G., Duda, L.C., Wolf, R.M., VanderZaag, P.J., 1997. Fe $L_{2,3}$ linear and circular magnetic dichroism of Fe_3O_4. J. Electron Spectrosc. Relat. Phenom. 86, 107–113.

Lam, K.P., Hitchcock, A.P., Obst, M., Lawrence, J.R., Swerhone, G.D.W., Leppard, G.G., Tyliszczak, T., Karunakaran, C., Wang, J., Kaznatcheev, K., Bazylinski, D.A., Lins, U., 2010. Characterizing magnetism of individual magnetosomes by X-ray magnetic circular dichroism in a scanning transmission X-ray microscope. Chem. Geol. 270, 110–116.

Lawrence, J.R., Dynes, J.J., Korber, D.R., Swerhone, G.D.W., Leppard, G.G., Hitchcock, A.P., 2012. Monitoring the fate of copper nanoparticles in river biofilms using scanning transmission X-ray microscopy (STXM). Chem. Geol. 329, 18–25.

Lefèvre, C.T., Abreu, F., Lins, U., Bazylinski, D.A., 2011a. A bacterial backbone: magnetosomes in magnetotactic bacteria, in: Rai, M., Duran, N. (Eds.), Metal Nanoparticles

in Microbiology. Springer-Verlag, Berlin Heidelberg, pp. 75–102.

Lefèvre, C.T., Bennet, M., Klumpp, S., Faivre, D., 2015. Positioning the flagellum at the center of a dividing cell to combine bacterial division with magnetic polarity. MBio 6, 1–7.

Lefèvre, C.T., Bennet, M., Landau, L., Vach, P., Pignol, D., Bazylinski, D.A., Frankel, R.B., Klumpp, S., Faivre, D., 2014. Diversity of magneto-aerotactic behaviors and oxygen sensing mechanisms in cultured magnetotactic bacteria. Biophys. J. 107, 527–538.

Lefèvre, C.T., Menguy, N., Abreu, F., Lins, U., Posfai, M., Prozorov, T., Pignol, D., Frankel, R.B., Bazylinski, D.A., 2011b. A cultured greigite-producing magnetotactic bacterium in a novel group of sulfate-reducing bacteria. Science 334, 1720–1723.

Lefèvre, C.T., Frankel, R.B., Pósfai, M., Prozorov, T., Bazylinski, D.A., 2011c. Isolation of obligately alkaliphilic magnetotactic bacteria from extremely alkaline environments. Environ. Microbiol. 13, 2342–2350.

Letard, I., Sainctavit, P., Deudon, C., 2007. XMCD at Fe $L_{2,3}$ edges, Fe and S K edges on Fe_7S_8. Phys. Chem. Miner. 34, 113–120.

Letard, I., Sainctavit, P., Menguy, N., Valet, J.-P., Isambert, A., Dekkers, M.J., Gloter, A., 2005. Mineralogy of greigite Fe_3S_4. Phys. Scr. T115, 489–491.

Li, D., Bancroft, G.M., Kasrai, M., Fleet, M.E., Feng, X., Tan, K., 1995. S K-and L-edge X-ray absorption spectroscopy of metal sulfides and sulfates: applications in mineralogy and geochemistry. Can. Mineral. 33, 949–960.

Lin, C.-R., Tseng, Y.-T., Ovchinnikov, S.G., Ivantsov, R.D., Edelman, I.S., Fedorov, A.S., Kuzubov, A.A., Fedorov, D.A., Starchikov, S.S., Lyubutin, I.S., 2014. Fe_3S_4 and Fe_3O_4 magnetic nanocrystals: magneto-optical and Mössbauer spectroscopy study. Mater. Res. Express 1, 025033.

Lins, U., Bazylinski, D.A., 2012. Magnetotaxis, in: Schmidt, T.M., Schaechter, M. (Eds.), Topics in Ecological and Environmental Microbiology. Academic Press, pp. 251–263.

Lins, U., Farina, M., 2001. Amorphous mineral phases in magnetotactic multicellular aggregates. Arch. Microbiol. 176, 323–328.

Lins, U., Freitas, F., Keim, C.N., De Barros, H.L., Esquivel, D.M.S., Farina, M., 2003. Simple homemade apparatus for harvesting uncultured magnetotactic microorganisms. Brazilian J. Microbiol. 34, 111–116.

Lins, U., Keim, C.N., Evans, F.F., Farina, M., Buseck, P.R., 2007. Magnetite (Fe_3O_4) and greigite (Fe_3S_4) crystals in multicellular magnetotactic prokaryotes. Geomicrobiol. J. 24, 43–50.

Lowenstam, H., Weiner, S., 1989. On Biomineralization, Oxford University Press. Oxford University Press, New York.

Lowenstam, H.A., 1981. Minerals formed by organisms. Science 211, 1126–1131.

Luke, D.R., 2004. Relaxed Averaged Alternating Reflections for Diffraction Imaging. Inverse Probl. 37, 13.

Maher, B. A., 1998. Magnetite biomineralization in termites. Proc. R. Soc. B Biol. Sci. 265, 733–737.

Maiden, A.M., Morrison, G.R., Kaulich, B., Gianoncelli, A., Rodenburg, J.M., 2013. Soft X-ray spectromicroscopy using ptychography with randomly phased illumination. Nat. Commun. 4, 1669.

Marchesini, S., Krishnan, H., Daurer, B.J., Shapiro, D.A., Periano, T., Sethian, J.A., Maia, F.R.N.C., 2016. SHARP: a distributed GPU-based ptychographic solver. J. Appl. Cryst. 49, 1245.

Mann, S., Frankel, R.B., Blakemore, R.P., 1984. Structure, morphology and crystal growth of

    bacterial magnetite. Nature 310, 405–407.

Mann, S., Sparks, N.H., Walker, M.M., Kirschvink, J.L., 1988. Ultrastructure, morphology and

    organization of biogenic magnetite from sockeye salmon, Oncorhynchus nerka:

    implications for magnetoreception. J. Exp. Biol. 140, 35–49.

Mann, S., Sparks, N.H.C., Blakemore, R.P., 1987. Ultrastructure and Characterization of

    Anisotropic Magnetic Inclusions in Magnetotactic Bacteria. Proc. R. Soc. B Biol. Sci. 231,

    469–476.

Matheron, R., Caumette, P., 2015. Structure and functions of microorganisms: production and

    use of material and energy, in: Bertrand, J.-C. (Ed.), Environmental Microbiology:

    Fundamentals and Applications: Microbial Ecology. Springer, pp. 395–444.

Mathon, O., Baudelet, F., Itié, J.-P., Pasternak, S., Pollan, A., Pascarelli, S., 2004. XMCD under

    pressure at the Fe K edge on the energy-dispersive beamline of the ESRF. J. Synchrotron

    Radiat. 11, 423–427.

Mazzag, B.C., Zhulin, I.B., Mogilner, A., 2003. Model of bacterial band formation in aerotaxis.

    Biophys. J. 85, 3558–3574.

McKay, D.S., Gibson, E.K., Thomas-Keprta, K.L., Vali, H., Romanek, C.S., Clemett, S.J.,

    Chillier, X.D., Maechling, C.R., Zare, R.N., 1996. Search for past life on Mars: possible

    relic biogenic activity in martian meteorite ALH84001. Science 273, 924–930.

Meldrum, F.C., Mann, S., Heywood, B.R., Frankel, R.B., Bazylinski, D. A., 1993. Electron

    microscopy study of magnetosomes in two cultured vibrioid magnetotactic bacteria. Proc.

    R. Soc. B Biol. Sci. 251, 237–242.

Miao, J., Charalambous, P., Kirz, J., Sayre, D., 1999. Extending the methodology of X-ray

crystallography to allow imaging of micrometre-sized non-crystalline specimens. Nature 400, 342–344.

Miao, J., Sandberg, R.L., Song, C., 2012. Coherent X-Ray Diffraction Imaging. IEEE J. Sel. Top. Quantum Electron. 18, 399–410.

Miao, J., Sayre, D., Chapman, H.N., 1997. Phase retrieval from the magnitude of the Fourier transforms of nonperiodic objects. J. Opt. Soc. Am. A 15, 1662.

Mo, H., Liu, L., Geng, M., 2014. A New Magnetotactic Bacteria Optimization Algorithm, in: 2014 International Conference on Swarm Intelligence. pp. 103–114.

Mohapatra, M., Anand, S., 2010. Synthesis and applications of nano-structured iron oxides/hydroxides – a review. Int. J. Eng. Sci. Technol. 2, 127–146.

Muxworthy, A.R., Williams, W., 2006. Critical single-domain/multidomain grain sizes in noninteracting and interacting elongated magnetite particles: Implications for magnetosomes. J. Geophys. Res. Solid Earth 111, 3–9.

Nagasaka, M., Yuzawa, H., Horigome, T., Hitchcock, A.P., Kosugi, N., 2013. Electrochemical reaction of aqueous iron sulfate solutions studied by Fe L-edge soft X-ray absorption spectroscopy. J. Phys. Chem. C 117, 16343–16348.

Nakamure, C., Burgess, J.G., Sode, K., Matsunaga, T., 1995. An ironregulated gene,magA,encoding an iron transport protein of Magnetospirillumspm.strain AMB-1. J Biol Chem 270, 28392–28396.

Nazaries, L., Pan, Y., Bodrossy, L., Baggs, E.M., Millard, P., Murrell, J.C., Singh, B.K., 2013. Evidence of microbial regulation of biogeochemical cycles from a study on methane flux and land use change. Appl. Environ. Microbiol. 79, 4031–4040.

Nolle, D., Goering, E., Tietze, T., Schütz, G., Figuerola, A., Manna, L., 2009. Structural and

magnetic deconvolution of FePt/FeO$_x$-nanoparticles using x-ray magnetic circular dichroism. New J. Phys. 11, 033034.

Nuhn, H.-D., 2004. From storage rings to free electron lasers for hard x-rays. J. Phys. Condens. Matter 16, S3413–S3421.

Oestreicher, Z., Lower, S.K., Lin, W., Lower, B.H., 2012. Collection, isolation and enrichment of naturally occurring magnetotactic bacteria from the environment. J. Vis. Exp. e50123.

Pattrick, R. A. D., Van Der Laan, G., Henderson, C.M.B., Kuiper, P., Dudzik, E., Vaughan, D.J., 2002. Cation site occupancy in spinel ferrites studied by X-ray magnetic circular dichroism: developing a method for mineralogists. Eur. J. Mineral. 14, 1095–1102.

Piepho, H.P., Williams, E.R., 2010. Linear variance models for plant breeding trials. Plant Breed. 129, 1–8.

Popp, F., Armitage, J.P., Schüler, D., 2014. Polarity of bacterial magnetotaxis is controlled by aerotaxis through a common sensory pathway. Nat. Commun. 5, 5398.

Porreca, M., Mattei, M., 2010. Tectonic and environmental evolution of Quaternary intramontane basins in Southern Apennines (Italy): Insights from palaeomagnetic and rock magnetic investigations. Geophys. J. Int. 182, 682–698.

Porreca, M., Mattei, M., Di Vincenzo, G., 2009. Post-deformational growth of late diagenetic greigite in lacustrine sediments from southern Italy. Geophys. Res. Lett. 36, 1–6.

Pósfai, M., Buseck, P.R., Bazylinski, D.A., Frankel, R.B., 1998. Iron sulfides from magnetotactic bacteria: Structure, composition, and phase transitions. Am. Mineral. 83, 1469–1481.

Prozorov, T., Bazylinski, D.A., Mallapragada, S.K., Prozorov, R., 2013. Novel magnetic nanomaterials inspired by magnetotactic bacteria: Topical review. Mater. Sci. Eng. R Reports 74, 133–172.

Qian, L., 2013. Quantitative Magnetic Characterization of Single Cells. Standford University, Standford.

Rema, T., Lawrence, J.R., Dynes, J.J., Hitchcock, A.P., Korber, D.R., 2014. Microscopic and spectroscopic analyses of chlorhexidine tolerance in delftia acidovorans biofilms. Antimicrob. Agents Chemother. 58, 5673–5686.

Rickard, D., Luther, G.W., 2007. Chemistry of iron sulfides. Chem. Rev. 107, 514–562.

Riekel, C., Burghammer, M., Davies, R., Gebhardt, R., Popov, D., 2009. Applications of synchrotron light to scattering and diffraction in materials and life sciences, in: Ezquerra, T.A., Garcia-Gutierrez, M.C., Nogales, A., Gomez, M. (Eds.), Lecture Notes in Physics. Springer, pp. 91–104.

Roberts, A.P., 1995. Magnetic properties of sedimentary greigite (Fe_3S_4). Earth Planet. Sci. Lett. 134, 227–236.

Roberts, A.P., Chang, L., Rowan, C.J., Horng, C.-S., Florindo, F., 2011. Magnetic properties of sedimentary greigite (Fe_3S_4): an update. Rev. Geophys. 49, RG1002.

Roberts, P., Reynolds, L., Verosub, L., Adam, D.P., Authigenic, A., 1996. Environmental magnetic implications of greigite (Fe_3S_4) formation in a 3 m.y. lake sediment record from Butte Valley, northern California. Geophys. Res. Lett. 23, 2859–2862.

Rodenburg, J.M., 2008. Ptychography and related diffractive imaging methods. Adv. Imaging Electron Phys. 150, 87–184.

Rodenburg, J.M., Faulkner, H.M.L., 2004. A phase retrieval algorithm for shifting illumination. Appl. Phys. Lett. 85, 4795–4797.

Sakdinawat, A., Attwood, D., 2010. Nanoscale X-ray imaging. Nat. Photonics 4, 840–848.

Santos-Carballal, D., Roldan, A., de Leeuw, N.H., 2016. Early oxidation processes on the

greigite Fe_3S_4 (001) surface by water: A density functional theory study. J. Phys. Chem. C 120, 8616-8629

Sayre, D., 1952. Some implications of a theorem due to Shannon. Acta Crystallogr. 5, 843–843.

Scheffel, A., Gruska, M., Faivre, D., Linaroudis, A., Plitzko, J.M., Schüler, D., 2006. An acidic protein aligns magnetosomes along a filamentous structure in magnetotactic bacteria. Nature 440, 110–4.

Scherz, A., Schlotter, W., Chen, K., Rick, R., Stöhr, J., Lüning, J., McNulty, I., Günther, C., Radu, F., Eberhardt, W., Hellwig, O., Eisebitt, S., 2007. Phase imaging of magnetic nanostructures using resonant soft x-ray holography. Phys. Rev. B 76, 1–5.

Schmid, G., Zeitvogel, F., Hao, L., Ingino, P., Kuerner, W., Dynes, J.J., Karunakaran, C., Wang, J., Lu, Y., Ayers, T., Schietinger, C., Hitchcock, A.P., Obst, M., 2014. Synchrotron-based chemical nano-tomography of microbial cell-mineral aggregates in their natural, hydrated state. Microsc. Microanal. 20, 531–536.

Schroer, C.G., Boye, P., Feldkamp, J.M., Patommel, J., Schropp, A., Schwab, A., Stephan, S., Burghammer, M., Schöder, S., Riekel, C., 2008. Coherent X-ray diffraction imaging with nanofocused illumination. Phys. Rev. Lett. 101, 1–4.

Schtz, G., Wagner, W., Wilhelm, W., Kienle, P., Zeller, R., Frahm, R., Materlik, G., 1987. Absorption of circularly polarized X-rays in iron. Phys. Rev. Lett. 58, 737–740.

Schüler, D., 2008. Genetics and cell biology of magnetosome formation in magnetotactic bacteria. FEMS Microbiol. Rev. 32, 654–672.

Schüler, D., 2002. The biomineralization of magnetosomes in Magnetospirillum gryphiswaldense. Int. Microbiol. 5, 209–214.

Schüler, D., Frankel, R.B., 1999. Bacterial magnetosomes: Microbiology, biomineralization and

biotechnological applications. Appl. Microbiol. Biotechnol. 52, 464–473.

Segall, J.E., Block, S.M., Berg, H.C., 1986. Temporal comparisons in bacterial chemotaxis. Proc. Natl. Acad. Sci. USA 83, 8987–8991.

Shapiro, D.A., Yu, Y.-S., Tyliszczak, T., Cabana, J., Celestre, R., Chao, W., Kaznatcheev, K., Kilcoyne, A.L.D., Maia, F., Marchesini, S., Meng, Y.S., Warwick, T., Yang, L.L., Padmore, H.A., 2014. Chemical composition mapping with nanometre resolution by soft X-ray microscopy. Nat. Photonics 8, 765–769.

Shapiro, O.H., Hatzenpichler, R., Buckley, D.H., Zinder, S.H., Orphan, V.J., 2011. Multicellular photo-magnetotactic bacteria. Environ. Microbiol. Rep. 3, 233–238.

Shi, X., Fischer, P., Neu, V., Elefant, D., Lee, J.C.T., Shapiro, D.A., Farmand, M., Tyliszczak, T., Shiu, H.W., Marchesini, S., Roy, S., Kevan, S.D., 2016. Soft x-ray ptychography studies of nanoscale magnetic and structural correlations in thin $SmCo_5$ films. Appl. Phys. Lett. 108, 094103.

Sievers, S., Braun, K.-F., Eberbeck, D., Gustafsson, S., Olsson, E., Schumacher, H.W., Siegner, U., 2012. Quantitative measurement of the magnetic moment of individual magnetic nanoparticles by magnetic force microscopy. Small 8, 2675–2679.

Simmons, S.L., Sievert, S.M., Frankel, R.B., Bazylinski, D. A, Edwards, K.J., 2004. Spatiotemporal distribution of marine magnetotactic bacteria in a seasonally stratified coastal salt pond. Appl. Environ.Microbiol. 70, 6230–6239.

Snowball, I.F., Thompson, R., 1988. The occurrence of greigite in sediments from Loch Lomond. J.Quat.Sci 3, 121–125.

Spender, M.R., Coey, J.M.D., Morrish, A.H., 1972. The Magnetic Properties and Mössbauer Spectra of Synthetic Samples of Fe_3S_4. Can. J. Phys. 50, 2313–2326.

Spring, S., Amann, R., Ludwig, W., Schleifer, K.H., Van Gemerden, H., Petersen, N., 1993.

Dominating role of an unusual magnetotactic bacterium in the microaerobic zone of a

freshwater sediment. Appl. Environ. Microbiol. 59, 2397–2403.

Staniland, S., Ward, B., Harrison, A., van der Laan, G., Telling, N., 2007. Rapid magnetosome

formation shown by real-time x-ray magnetic circular dichroism. Proc. Natl. Acad. Sci.

USA. 104, 19524–19528.

Staniland, S., Williams, W., Telling, N., Van Der Laan, G., Harrison, A., Ward, B., 2008.

Controlled cobalt doping of magnetosomes in vivo. Nat. Nanotechnol. 3, 158–162.

Stöhr, J., Siegmann, H.C., 2006. MagnetismFrom Fundamentals to Nanoscale Dynamics.

Springer, Berlin, Germany.

Stöhr, J., 1999. Exploring the microscopic origin of magnetic anisotropies with X-ray magnetic

circular dichroism (XMCD) spectroscopy. J. Magn. Magn. Mater. 200, 470–497.

Stöhr, J., 1995. X-ray magnetic circular dichroism spectroscopy of transition metal thin films. J.

Electron Spectros. Relat. Phenomena 75, 253–272.

Stolz, J.F., Chang, S.-B.R., Kirschvink, J.L., 1986. Magnetotactic bacteria and single-domain

magnetite in hemipelagic sediments. Nature 321, 849–851.

Takahashi, Y., Suzuki, A., Zettsu, N., Kohmura, Y., Yamauchi, K., Ishikawa, T., 2011.

Multiscale element mapping of buried structures by ptychographic x-ray diffraction

microscopy using anomalous scattering. Appl. Phys. Lett. 99, 5–8.

Thibault, P., Dierolf, M., Bunk, O., Menzel, A., Pfeiffer, F., 2009. Probe retrieval in

ptychographic coherent diffractive imaging. Ultramicroscopy 109, 338–343.

Thibault, P., Dierolf, M., Menzel, A., Bunk, O., David, C., Pfeiffer, F., 2008. High-resolution

scanning X-ray diffraction microscopy. Science 321, 379–382.

Thibault, P., Guizar-Sicairos, M., Menzel, A., 2014. Coherent imaging at the diffraction limit. J. Synchrotron Radiat. 21, 1011–1018.

Thomas-Keprta, K.L., Clemett, S.J., Bazylinski, D. a, Kirschvink, J.L., McKay, D.S., Wentworth, S.J., Vali, H., Gibson, E.K., McKay, M.F., Romanek, C.S., 2001. Truncated hexa-octahedral magnetite crystals in ALH84001: presumptive biosignatures. Proc. Natl. Acad. Sci. USA 98, 2164–2169.

Thornhill, R.H., Grant Burgess, J., Sakaguchi, T., Matsunaga, T., 1994. A morphological classification of bacteria containing bullet-shaped magnetic particles. FEMS Microbiol. Lett. 115, 169–176.

Torres de Araujo, F.F., Pires, M.A., Frankel, R.B., Bicudo, C.E.M. 1986. Magnetite and magnetotaxis in bacteria and algae. Biophys. J. 50, 375-378.

Torres de Araujo, F.F., Germano, F.A., Gonçalves, L.L., Pires, M. A, Frankel, R.B., 1990. Magnetic polarity fractions in magnetotactic bacterial populations near the geomagnetic equator. Biophys. J. 58, 549–555.

Towe, K.M., Moench, T.T., 1981. Electron-optical characterization of bacterial magnetite. Earth Planet. Sci. Lett. 52, 213–220.

Tripathi, A., McNulty, I., Shpyrko, O., 2014. Ptychographic overlap constraint errors and the limits of their numerical recovery using conjugate gradient descent methods. Opt. Express 22, 1452–1466.

Tripathi, A., Mohanty, J., Dietze, S.H., Shpyrko, O.G., Shipton, E., Fullerton, E.E., Kim, S.S., McNulty, I., 2011. Dichroic coherent diffractive imaging. Proc. Natl. Acad. Sci. USA. 108, 13393–13398.

Turner, L., Ryu, W.S., Berg, H.C., 2000. Real-time imaging of fluorescent flagellar filaments. J.

Bacteriol. 182, 2793–2801.

Tyliszczak, T., Chou, K.W., 2010. Advances in magnetization dynamics using scanning transmission X-ray microscopy, in: Guo, J. (Ed.), X-Rays in Nanoscience. Wiley-VCH, Weinheim, Germany, pp. 39–78.

Tyliszczak, T., Shiu, H.-W., Chueh, W.C., El Gabaly, F., Shapiro, D., 2014. Soft X-Ray spectromicroscopy using ptychography, in: 12th International Conference on X-ray Microscopy (XRM 2014). p. poster S2–82.

Tyliszczak, T., Warwick, T., Kilcoyne, A.L.D., Fakra, S., Shuh, D.K., Yoon, T.H., Brown Jr., G.E., Andrews, S., Chembrolu, V., Strachan, J., Acremann, Y., 2004. Soft X-ray scanning transmission microscope working in an extended energy range at the Advanced Light Source. AIP Conf. Proc. 1356, 1356–1359.

Ullrich, S., Ullrich, S., Kube, M., Kube, M., Schu, S., Schu, S., Reinhardt, R., Reinhardt, R., Schu, D., Schu, D., 2005. A Hypervariable 130-Kilobase genomic region of microbiology 187, 7176–7184.

Wang, J., 2008. Radiation chemistry by soft X-ray spectromicroscopy. PhD Thesis. McMaster University.

Wang, J., Botton, G.A., West, M.M., Hitchcock, A.P., 2009. Quantitative evaluation of radiation damage to polyethylene terephthalate by soft X-rays and high-energy electrons. J. Phys. Chem. B 113, 1869–76.

Wang, Y., Li, T., Gao, Q., Zhang, S., Shi, Y., 2013. Application of diffractive optical elements for controlling the light beam in ptychography. Opt. Eng. 52, 091720.

Weckert, E., 2015. The potential of future light sources to explore the structure and function of matter. IUCrJ 2, 230–245.

Willmott, P., 2011. An Introduction to Synchrotron Radiation: Techniques and Applications. John Wiley & Sons.

Wiltschko, W., Wiltschko, R., 2005. Magnetic orientation and magnetoreception in birds and other animals. J. Comp. Physiol. A Neuroethol. Sensory, Neural, Behav. Physiol. 191, 675–693.

Winklhofer, M., Abraçado, L.G., Davila, A.F., Keim, C.N., Lins de Barros, H.G.P., 2007. Magnetic optimization in a multicellular magnetotactic organism. Biophys. J. 92, 661–670.

Wolfe, R.S., Thauer, R.K., Pfennig, N., 1987. A "capillary racetrack" method for isolation of magnetotactic bacteria. FEMS Microbiol. Lett. 87, 90039-90045

Xiong, G., Moutanabbir, O., Reiche, M., Harder, R., Robinson, I., 2014. Coherent X-ray diffraction imaging and characterization of strain in silicon-on-insulator nanostructures. Adv. Mater. 26, 7747–7763.

Yamaguchi, K., Matsumoto, K., Fujii, T., 1990. Magnetic anisotropy by ferromagnetic particles alignment in a magnetic field. J. Appl. Phys. 67, 4493–4495.

Yan, L., Zhang, S., Chen, P., Liu, H., Yin, H., Li, H., 2012. Magnetotactic bacteria, magnetosomes and their application. Microbiol. Res. 167, 507–519.

Yu, Y.S., Kim, C., Shapiro, D.A., Farmand, M., Qian, D., Tyliszczak, T., Kilcoyne, A.L.D., Celestre, R., Marchesini, S., Joseph, J., Denes, P., Warwick, T., Strobridge, F.C., Grey, C.P., Padmore, H., Meng, Y.S., Kostecki, R., Cabana, J., 2015. Dependence on crystal size of the nanoscale chemical phase distribution and fracture in LiFePO$_4$. Nano Lett. 15, 4282–4288.

Zhang, B., De Wijs, G.A., De Groot, R.A., 2012. Switchable Fermi surface sheets in greigite. Phys. Rev. B - Condens. Matter Mater. Phys. 86, 2–5.

Zhang, J., Wang, Y., Ji, H., Wei, Y., Wu, N., Zuo, B., Wang, Q., 2005. Magnetic nanocomposite catalysts with high activity and selectivity for selective hydrogenation of ortho-chloronitrobenzene. J. Catal. 229, 114–118.

Zhang, W.J., Chen, C., Li, Y., Song, T., Wu, L.F., 2010. Configuration of redox gradient determines magnetotactic polarity of the marine bacteria MO-1. Environ. Microbiol. Rep. 2, 646–650.

Zhang, Z.J., Chen, X.Y., 2009. Magnetic greigite (Fe_3S_4) nanomaterials: Shape-controlled solvothermal synthesis and their calcination conversion into hematite (α-Fe_2O_3) nanomaterials. J. Alloys Compd. 488, 339–345.

Zhou, K., Zhang, W.Y., Yu-Zhang, K., Pan, H.M., Zhang, S. Da, Zhang, W.J., Yue, H.D., Li, Y., Xiao, T., Wu, L.F., 2012. A novel genus of multicellular magnetotactic prokaryotes from the Yellow Sea. Environ. Microbiol. 14, 405–413.

Zhu, X., Kalirai, S.S., Hitchcock, A.P., Bazylinski, D.A., 2015a. What is the correct Fe $L_{2,3}$ X-ray absorption spectrum of magnetite? J. Electron Spectros. Relat. Phenomena 199, 19–26.

Zhu, X., Hitchcock, A.P., Bittencourt, C., Umek, P., Krüger, P., 2015b. Individual titanate nanoribbons studied by 3D-resolved polarization dependent X-ray absorption spectra measured with scanning transmission X-ray microscopy. J. Phys. Chem. C 119, 24192–24200.

Zhu, X., Tyliszczak, T., Shiu, H.-W., Shapiro, D., Bazylinski, D.A., Lins, U., Hitchcock, A.P., 2016. Magnetic studies of magnetotactic bacteria by soft x-ray STXM and ptychography. AIP Conf. Proc. 1696, 020002.

Appendix A

This appendix presents a brief introduction to ptychography setup at the Advanced Light Source. The general procedures to reconstruct ptychography images and stacks are summarized.

A.1 Ptychography setup at ALS

As mentioned in section 2.4, in ptychography, the sample is scanned through the focused beam of X-rays using overlapped steps. The diffraction data is collected with a CCD camera and the modulus and phase inforamtion of the sample can be retrieved with sophisticated interactive algorithm. Because ptychography has similar setup as conventional STXM, ptychography setup
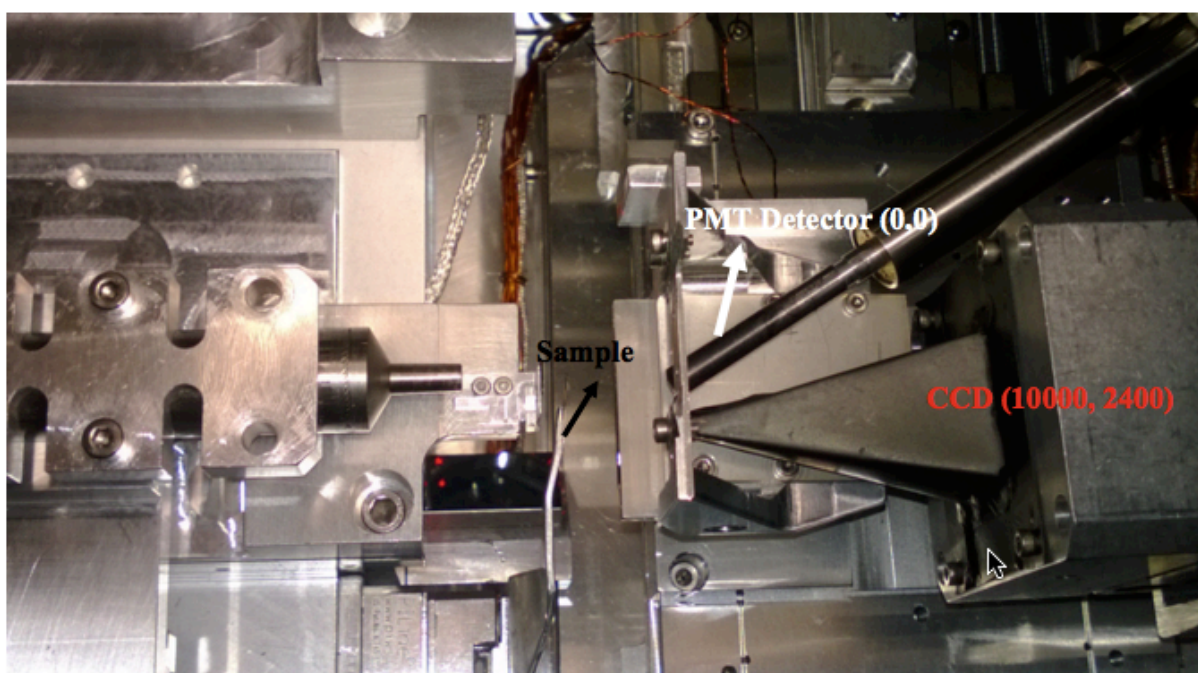
Figure A.1: Ptychography setup at beamline 11.0.2 at ALS.

can be created by modifying existing STXM instrumentation with new hardware. **Figure A-1**

presents a photo of ptychography setup at beamline 11.0.2 at ALS. The biggest difference

between conventional STXM and ptychography is the addition of a CCD camera, which is used

to record 2D diffraction data. A ptychography measurement always starts with a conventional

STXM imaging with a PMT detector, which is used to locate areas for the subsequent

ptychography measurement. Therefore, at beamline 5.3.2.1 and 11.0.2, both PMT detector and

CCD camera are used in ptychography measurement. These two detector can be easily switched

by using different detector coordinates (Detector X, Detector Y), such as, (0,0) for PMT (0, 0)

and (10000, 2400) for the CCD .

A.2 Ptychography reconstruction

At both beamlines 11.0.2 and 5.3.2.1, where the ptychography data was collected in this

thesis, the program "Nanosurveyor" is used to process ptychography data. The general

procedures are described below.

A.2.1 Start "Nanosurveyor" program

1. Go to the "Terminal" on the desktop and type command line: "nanosurveyor". The

Nanosurveyor window should pop up.

2. Three tabs (see **Figure A.2**) are observed at the top of the nanosurveyor program

panel, which are: image viewer, ptychography viewer and reconstruction.
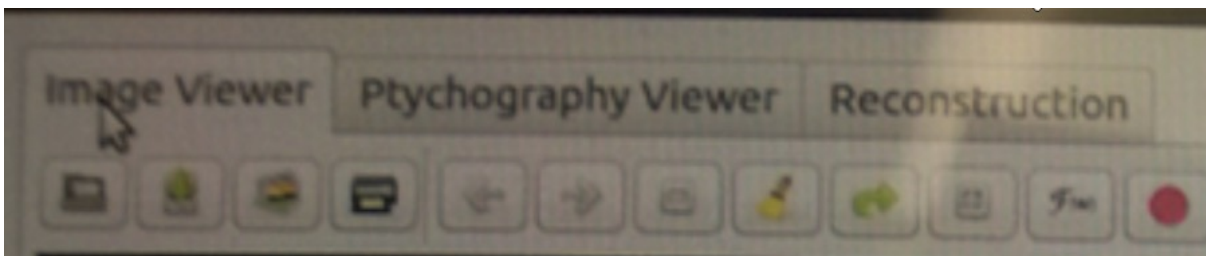
Figure A.2: Three tabs (Image Viewer, Ptychography Viewer and Reconstruction) in Nanosurveyor interface

 (1). Image Viewer Tab: From which, open a bright field image of Zone Plate Image (see below). At the beginning of each reconstruction, a few parameters regarding Zone plate (ZP) need to be determined, such as, its X&Y center pixel and the ZP pupil width

(2). Ptychography Viewer Tab: From which, one can view the reconstructed image and save these images as tif files.

(3). Reconstruction Tab: From which, all the parameters will be input to perform reconstruction. Different than 1102, 5321 nanosurveyor allows users to directly load reconstructed parameters from the STXM scan.

A.2.2 Reconstruction of a single ptychography image

Take an example of ptychography scan, 160521030, which is a single ptychography image of a MV-1 cell. To perform the reconstruction:

1. Load the parameters from the STXM scan: one needs go to "Basic pre-processor"/ "load scan"/ phases-data on phases/160521/NS_160521030.hdr". After hdr is loaded, all the parameters such as step size, exposure time should be the same as the ptychography scan setting.
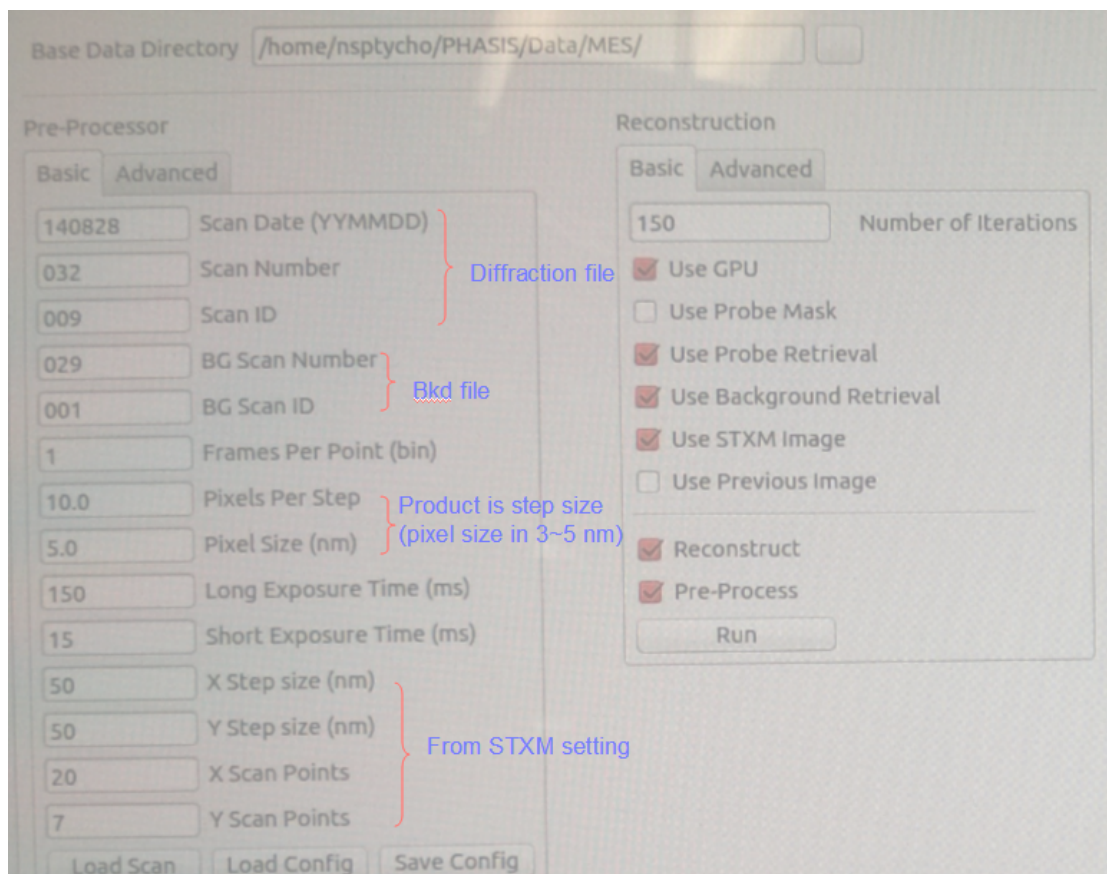
Figure A.2: Parameters for single ptychography image reconstruction with Nanosurveyor

2: Click "Run";

3. One can monitor the process from the "terminal window". Once when the following info is ovserved "writing data to file:/global…/160521/001/160521001.cxi", this means the "cxi" file is already generated;

4. Go to "ptychography viewer" to open the 'cxi' file—at the beginning, a calculated STXM image is generated;

5. Wait until the reconstruction is done, the previous calculated STXM image is <u>replaced</u> by a Ptychogrpahy Amplitude Image.

6. Then, the STXM, Ptychography and Phase images can be saved.

A.2.2 Reconstruction of a ptychography stack

Take an example of ptychography scan, 160521044, which is a ptychography stack of a

MV-1 cell. To perform the reconstruction:

1. Load the parameters from the STXM scan (see **Figure A.3**). One need to go to "Basic

pre-processor"/"load scan"/phases-data on phases/160521/NS_160521044/NS_160521044.hdr".

After hdr is loaded, all the parameters such as step size, exposure time should be the same as the

ptychography scan setting.

2. Click "Save Config" to save the configuration file for the script to process.

Specifically, the configuration should be saved at:/phases-data on

phases/160521/NS_160521044/160521044".
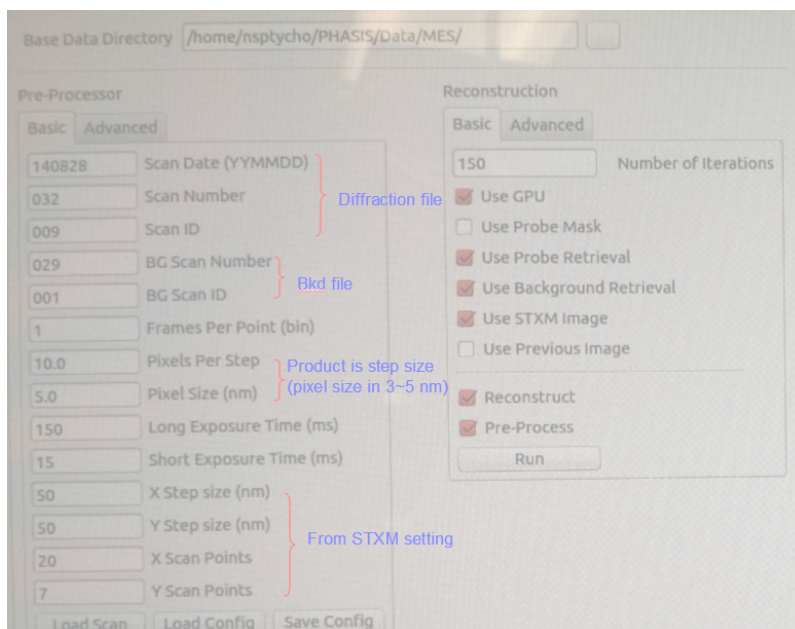
Figure A.3: Parameters for ptychography stack reconstruction with Nanosurveyor

3. Ask for the script "runStack.py" from beamline staff scientist. Once you have it,

change the "scanDate" to "160521" and change the "scanNumber" to "044". Then click "Save".

4. Go the "terminal" window and type "runStack". This will start to process the ptycho-stack;

5. One can monitor the process from the "terminal" window. When the following info is observed "writing data to file:/global…/160521044/001/NS_160521004.cxi", this means the "cxi" file is already generated and saved in the folder 001.

6. Once the reconstruction is done, a folder named "tiffs" can be found at: phases-data on phases/160521/NS_160521044/160521044". The tiffs folder contains 5 sub-folders including complex, intensity, modulus, phase, stxm. If the energy stack has 33 points, one should find 33 files in each sub-folder labelled with the energy point.

Appendix B

This appendix lists publications, and conference presentations and contributions.

B.1 Publications

1. X. Zhu, A. P. Hitchcock, D. A. Bazylinski, P. Denes, J. Joseph, A.L. D. Kilcoyne, U. Lins, S. Marchesini, H.-W. Shiu, T. Tyliszczak and D. A. Shapiro. Measuring spectroscopy and magnetism of extracted and intracellular magnetosomes using soft X-ray ptychography. (PNAS, in revision)

2. X. Zhu, A.P. Hitchcock, D.A. Bazylinski, U. Lins. Chemical and magnetic studies of greigite magnetosomes in multicellular magnetotactic prokaryotes by scanning transmission X-ray microscopy. (To be submitted to Chemical Geology)

3. X. Zhu, A.P. Hitchcock, C. Bittencourt, P. Umek, P. Krüger. Individual Titanate Nanoribbons Studied by 3D-Resolved Polarization Dependent X-ray Absorption Spectra Measured with Scanning Transmission X-ray Microscopy. J. Phys. Chem. C. 2015, 119, 24192-24200.

4. X. Zhu, S.S. Kalirai, A.P. Hitchcock, D.A. Bazylinski. What is the correct Fe $L_{2,3}$ X-ray absorption spectrum of magnetite? J. Electron.Spectrosc.Relat.Phenom. 2015,199,19-26.

5. X. Zhu, T.Tyliszczak, H.-W.Shiu, D. Shapiro, D.A. Bazylinski U. Lins and A.P. Hitchcock. Magnetic studies of magnetotactic bacteria by soft X-ray STXM and ptychography. AIP. Conf. Proc., 2016, 1696 (020002).

6.   X.Zhu, A.P. Hitchcock, T. Tyliszczak, D.A. Bazylinski. Probing magnetic polarities of magnetotactic bacteria by X-ray magnetic circular dichroism in a scanning transmission X-ray microscope. Microsc. Microanal. 2014, 20 (Suppl 3), 1176-1177.

B.2 Conference presentations

1.   X. Zhu, T. Tyliszczak, H.-W. Shiu, D. Shapiro, D.A. Bazylinski , U.Lins, A.P. Hitchcock. "Studying magnetism of magnetotactic bacteria using soft X-ray ptychography and STXM" (Invited talk). XAFS 16 Magnetism Satellite Meeting, Stuttgart, Germany, Aug.30-Sept.2, 2015.

2.   X. Zhu, T. Tyliszczak, H.-W. Shiu, D. Shapiro, D.A. Bazylinski , U.Lins, A.P. Hitchcock. "Biomagnetisim of magnetotactic bacteria studied by soft X-ray STXM and ptychography" (Oral). Microscopical Society of Canada 42nd Annual Meeting, Hamilton, Canada, May 26-29.

3.   X. Zhu, A.P. Hitchcock, C. Bittencourt, P. Umek, P. Krüger. "Individual 1D nanostructures investigated by 3D-resolved polarization dependent X-ray absorption spectra" (Poster). 16th International Conference on X-ray Absorption Fine Structure (XAFS 16), Karlsruhe, Germany, Aug.23-Aug.28, 2015.

4.   X. Zhu, A.P. Hitchcock, T. Tyliszczak, P. E. Leão, D. A. Bazylinski, U. Lins. "Characterization of the chemistry and magnetism of individual magnetotactic bacterial cells using X-ray spectromicroscopy" (Oral). 4th International Meeting on Magnetotactic Bacteria (MTB 2014), Rio de Janeiro, Brazil, Sept.15-19, 2014.

5.   X.Zhu, A.P. Hitchcock, T. Tyliszczak, D.A. Bazylinski. "Probing magnetic polarities of magnetotactic bacteria by X-ray magnetic circular dichroism in a scanning transmission X-

ray microscope" (Oral). Microscopy & Microanalysis 2014 Meeting (M&M 2014), Hartford,

USA, Aug.3-7, 2014.

Appendix C

This appendix lists all software packages used for this thesis

C.1 Software packages used for this thesis

1. axis 2000

   All the STXM data ws analyzed with the software aXis2000, which is written in Interactive Data Language (IDL). It is available free for non-commercial use from http://unicorn.mcmaster.ca/aXis2000.html.

2. Microsoft Office (2003)

   The word processing program Word was used to prepare reports and publications. The presentation program PowerPoint was used to prepare presentations and figures for publications. Excel application was used for data manipulation and analysis.

3. PaintShop Pro, version 4 and 5

   PaintShop Pro, from JASC Incorporated, was used to edit images for presentations and publications

4. SigmaPlot 6.0

   SigmaPlot (by Jandel Scientific) was used to plot spectroscopy data and generate publication quality graphs.

5. STXM_Control

   This program controls all the STXM microscope used in this thesis. It was written and developed by Dr. Tolek Tyliszczak and Peter Hitchcock.